Acoustic Noise Emitted from Overhead Line Conductors

A thesis submitted to

THE UNIVERSITY OF MANCHESTER

for the degree of

DOCTOR OF PHILOSOPHY

In the Faculty of Engineering and Physical Sciences

2013

Qi Li

School of Electrical and Electronic Engineering

LIST OF CONTENTS

LIST OF FIGURES

ABSTRACT

The developments of new types of conductors and increase of voltage level have driven the need to carry out research on evaluating overhead line acoustic noise.

The surface potential gradient of a conductor is a critical design parameter for planning overhead lines, as it determines the level of corona loss (CL), radio interference (RI), and audible noise (AN). The majority of existing models for surface gradient calculation are based on analytical methods which restrict their application in simulating complex surface geometries. This thesis proposes a novel method which utilizes both analytical and numerical procedures to predict the surface gradient. Stranding shape, proximity of tower, protrusions and bundle arrangements are considered within this model. One of UK National Grid's transmission line configurations has been selected as an example to compare the results for different methods. The different stranding shapes are a key variable in determining dry surface fields.

The dynamic behaviour of water droplets subject to AC electric fields is investigated by experiment and finite element modelling. The motion of a water droplet is considered on the surface of a metallic sphere. To understand the consequences of vibration, the FEA model is introduced to study the dynamics of a single droplet in terms of phase shift between vibration and exciting voltage. Moreover, the evolution of electric field within the whole cycle of vibration is investigated. The profile of the electric field and the characteristics of mechanical vibration are evaluated. Surprisingly the phase shift between these characteristics results in the maximum field occurring when the droplet is in a flattened profile rather than when it is ‘pointed’.

Research work on audible noise emitted from overhead line conductors is reviewed, and a unique experimental set up employing a semi-anechoic chamber and corona cage is described. Acoustically, this facility isolates undesirable background noise and provides a free-field test space inside the anechoic chamber. Electrically, the corona cage simulates a 3 m section of 400 kV overhead line conductors by achieving the equivalent surface gradient. UV imaging, acoustic measurements and a partial discharge detection system are employed as instrumentation. The acoustic and electrical performance is demonstrated through a series of experiments. Results are discussed, and the mechanisms for acoustic noise are considered. A strategy for evaluating the noise emission level for overhead line conductors is developed. Comments are made on predicting acoustic noise from overhead lines.

The technical achievements of this thesis are summarized in three aspects. First of all, an FEA model is developed to calculate the surface electric field for overhead line conductors and this has been demonstrated as an efficient tool for power utilities in computing surface electric field especially for dry condition. The second achievement is the droplet vibration study which describes the droplets' behaviour under rain conditions, such as the phase shift between the voltage and the vibration magnitude, the ejection phenomena and the electric field enhancement due to the shape change of droplets. The third contribution is the development of a standardized procedure in assessing noise emission level and the characteristics of noise emissions for various types of existing conductors in National Grid.

DECLARATION

No portion of the work referred to in the thesis has been submitted in support of an application for another degree or qualification of this or any other university or other institute of learning

COPYRIGHT STATEMENT

ACKNOWLEDGEMENT

Firstly, I would like to thank my supervisors, Professor Simon Rowland and Dr Roger Shuttleworth, for their continual encouraging support throughout my studies. Their patience and invaluable guidance lead me through the most difficult time within my research career. Their academic spirit has established an idol within my life and I will always respect and remember.

I would also like to acknowledge the support from Dr Iain Dupere, Professor Stuart Lyon, Professor Zhongdong Wang, Dr Konstantinos Kopsidas and Dr Guobin Zhang for their contribution of advices in carrying out this project. I would like to thank external support offered by colleagues within my office (post graduate research) and manager of high voltage laboratory: Mr. Frank Hogan.

I would like to thank National Grid UK in providing the funding for my PhD and kind assistant in both technical and financial.

Finally I would like to acknowledge my wife Mrs Congcong Zhu who has supported me during the completion of this thesis. Without her care and love, I won't be able to finish this thesis. Also thanks to my parents and friends for their continuous support.

Chapter 1 Introduction

1.1 Background and Project Objectives

Following the rapid increase of voltage level in modern power systems, two environmental impacts of transmission lines are acoustic and electrical noise. These affect the local community in which plant is located, and vary according to local environment, weather conditions and the condition of the plant concerned. The impact of such issues is likely to increase as pressure for compacted tower designs increases. Two new technical developments have increased the need to understand and predict acoustic emissions better. Firstly the development of high temperature low sag conductors, with constructions and materials different from traditional designs, and secondly new compact towers using composite insulation systems instead of metallic construction elements. Each of these will now be considered.

High Temperature Low Sag (HTLS) conductors entered the transmission and distribution market due to their extra power transfer capacity. Figure 1-1 presents the structures of three types of conductors (in the order of left to right): traditional ACSR (Aluminium Conductor Steel Reinforced), newly developed ACCC/CTC (Aluminium Conductor Composite Core) and Gap Type conductor-GZTACSR (Gap Type Super Thermal-resistant ACSR).

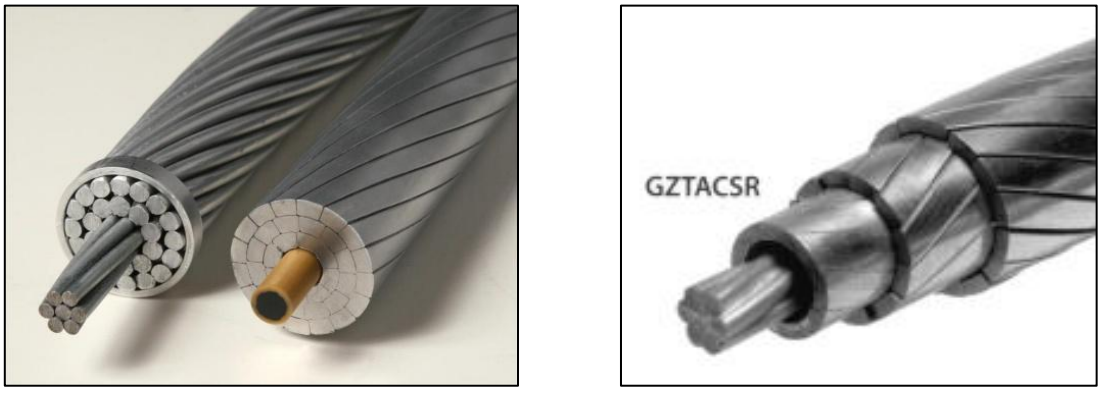

a b

Figure 1-1 Three types of overhead line conductors: a). traditional ACSR (Aluminium Conductor Steel Reinforced) conductor (left) and ACCC/CTC (Aluminium Conductor Composite Core) conductor (right); b). GZTACSR (Gap Type Super Thermal-resistant ACSR) Conductor [1]

ACSR has been utilized in power utilities for more than 50 years. It is constructed with all round shape strands. The outer strands are aluminium, chosen for its excellent

conductivity, low weight and low cost. The centre strands are of steel for the strength required to support the weight. This gives the conductor an overall high tensile strength. Gap Type conductor GZTACSR was developed about 30 years ago and has been installed for more than 2600 km (up to 2004) around the world. It engineered a gap between the inner steel core (round strands) and the thermal-resistant aluminium alloy layer (trapezoidal strands). This gap is filled with grease in manufacturing. This design enables the outer layer and the inner core to move independently. Under high temperature condition the overall design allows the inner core to take all of the expansion force, as a result the thermal expansion characteristics of GZTACSR becomes that of the steel core. This thus allows extreme low sag at high operation temperatures. Most recently developed conductor is ACCC/CTC conductor. It employs aluminium outer layers (trapezoidal strands) to carry current and carbon-glass-fibre composite core to carry the tensioning force. An additional advantage of using this hybrid composite core is to improve the conductivity so as to reduce the overall loss of the line.

However, environmental concerns, such as Corona Loss (CL), Radio Interference (RI) and Audible Noise (AN), are not well understood due to the conductors' different strand shapes and surface conditions (usually filled with silicon oil) compared to traditional conductors. Also the drive to fewer sub-conductors in a bundle at each voltage level is pushing the limits of the existing knowledge.

New towers are being considered to improve the visible aspect of overhead lines. Two examples are the T-Pylon from National Grid and WindTrack from Tennet (Figure 1-2).

a b

Figure 1-2 two innovated pylon design: a). T-Pylon (National Grid); b). WindTrack (Tennet) [2]

There are too many variations to consider all the possibilities, but calculations of noise generation have been included in this project.

A need has been established to be able to reliably predict the acoustic performance of new tower and conductor designs. Concerned for these issues, National Grid UK has appointed University of Manchester to commit a research project titled 'Acoustic Noise Emitted from Overhead Lines'.

This project proposed to undertake research activities aimed at understanding the causes of excessive noise from overhead line conductors and how this might be alleviated. The project included materials' scientists studying metal surfaces and ageing processes. This thesis reports work in the Electrical and Electronic Engineering School characterising noise emissions of conductors.

1.2 Structure of the Project

Figure 1-3 lists three typical experimental approaches to study the audible noise from overhead line conductors. They are distinguished by the length of the noise sources.

Surface gradient calculation was the first step for audible noise research within this project. Within National Grid, there is an existing software (ELECMDL) package to evaluate the surface gradient on overhead line conductors. It was developed in 1992 and has been used by the asset management department for over 20 years. Since computing power has increased dramatically during the last two decades, there is a need to study the possibility of improving the accuracy for this software. Another driver is the newly emerged methodologies for electric field calculation such as finite element methods, which can simulate details of conductor shape and protrusions. Driven by these two motivations, a theoretical study is focused on surface gradient calculations for overhead line conductors. This is described in Chapter 3. Through the theoretical study, the methodologies for the existing tools are understood and their accuracy analyzed. A novel method combining both analytical and numerical methods is developed to obtain information on the surface gradient distribution. With this advanced model, surface stranding shape, protrusions and the effect of the towers can be taken into consideration.

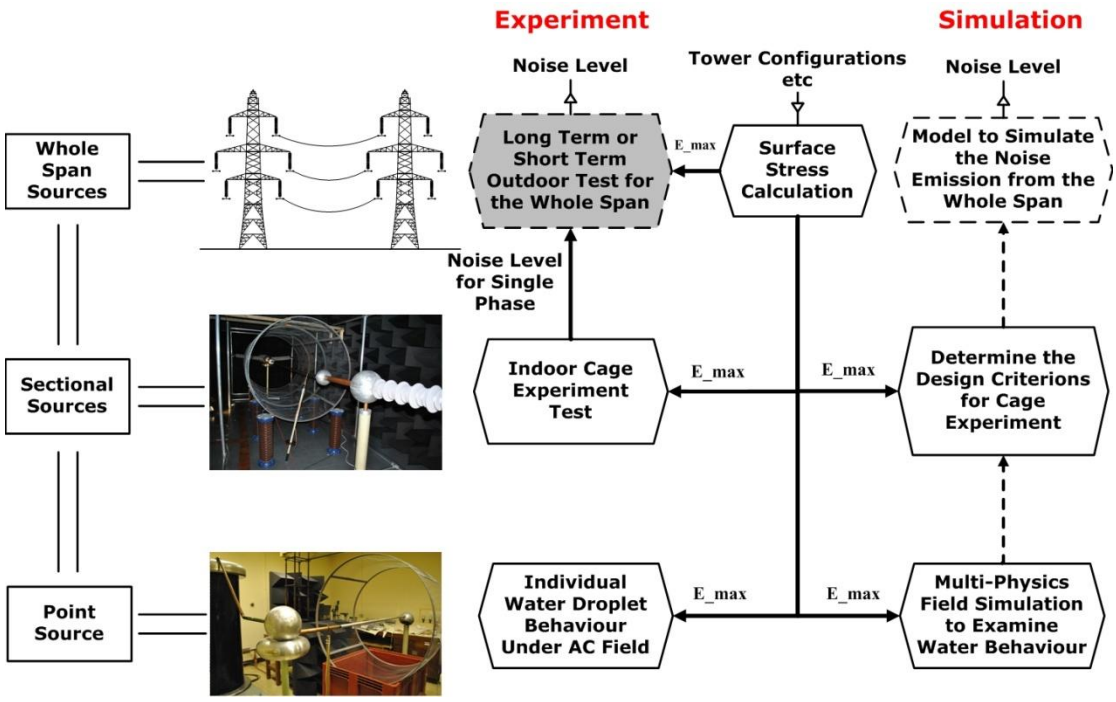

Figure 1-3 Structure of the Project

In the second aspect of the project, a small testing rig (a sphere-plane experiment introduced in Chapter 4) is designed to study the behaviour of a single droplet under AC electric fields. The axisymmetric geometry provides the convenience of being able to capture the shape change from one direction using a high speed camera. The electric field strength on the surface of the sphere simulates the surface stress on the overhead line conductors (17-18 kV/cm under dry conditions).

The term ‘hum noise’ refers to tonal emission which has a fundamental of twice the power frequency, thus 100 Hz in Europe and 120 Hz in North America. Since ‘hum noise’ produced from an overhead line [3] was noticed by Taylor, Chartier and Rice in 1960, its physical mechanism remains a mystery. Although a number of scientific hypotheses [4-12] have been introduced to explain the nature of this phenomena, relevant experimental work is still insufficient to identify the primary cause. Chapter 5 describes the experimental design. The design was influenced by existing literature on audible noise from overhead line conductors (as reviewed in Section 2.2). In addition a noise seminar was also organized in the University of Manchester to gather experience in this research field. These contributed to the design of experimental set-up and selection of instrumentations.

One difficulty for experimental verification is due to the fact that the 100 Hz content cannot be accurately measured in the laboratory environment. This is for following two reasons: first of all, the frequency spectrum of the background noise in laboratory environment contains peaks at 100 Hz and its harmonics (refer to the background noise measurement results in Chapter 5); secondly, the level of 'hum noise' produced by transformer increases significantly with the level of the leakage current. In order to mitigate the influence of these, an anechoic chamber was commissioned inside the high voltage laboratory in the University of Manchester. This pioneering testing facility allows accurate detection of the 'hum noise' from overhead line conductors and is an effective tool to identify the mechanism of the 'hum noise'. A medium-sized testing rig (cage experiment as shown in Figure 1-3) was designed to simulate the electric field surrounding the overhead line conductors thus reproducing the audible noise levels from the overhead line conductors. The criterion was to control the surface gradient to be as same as the overhead line conductors (17-18 kV/cm under dry conditions). It was developed for the purpose of characterising the noise performance of different types of conductors.

As introduced in Chapter 6, various samples, in various states of ageing, from various suppliers have been fully characterised. Manual spray and continuous spray have been used for the experiment. A methodology of comparison (ratings for different conductors introduced in Section 6.5.2) has been developed which enables direct comparison of conductor types. This part of the work is being utilized by National Grid in selecting conductors for new tower.

Chapter 7 discussed the results generated in Chapter 6. Chapter 8 concludes the outcomes of this part of the project and also describes potential future work. A comprehensive set of results are presented in Appendix, so that these can be used in future for forecasting conductor behaviour. Only illustrative and summaries of results are presented in the main text to enable clarity of presentation, and to provide supportive examples of work.

Chapter 2 Literature Review

2.1 Introduction

Research work on audible noise from overhead line conductors can be classified into three main areas: surface gradient (surface electric field) calculations, cage experiments and physical mechanism studies. Surface gradient calculation is the first step for overhead line designs within power utilities. It is critical in assessing the potential noise level before an overhead line is commissioned. Cage experiments are a well-developed laboratory tool to reproduce the electrical environment of overhead line conductors. Physical mechanism studies tend to explain the cause of low frequency 'hum noise' (100 Hz, 200 Hz and their harmonic) distinct from the high frequency 'crackling noise'. This chapter presents literature reviews from these three areas.

The first section summarizes the main methods employed by previous researchers to evaluate transmission line conductor surface voltage gradients. Five major methods are reviewed in detail.

After this, publications about cage experiments and noise prediction methods are discussed in the second section. Not only outdoor measurements which are carried out close to whole spans of overhead line, but also indoor measurements which employ cage configurations to simulate sections of overhead line have been reviewed.

In the third section, published articles concerning mechanisms of 'hum noise' are discussed.

2.2 Review of Existing Methods for Surface Gradient Calculation

Different methods for calculating field strength are classified as either analytical methods or numerical methods according to their principles.

Analytical methods described here are (in order of increasing complexity):

- Maxwell's Potential Coefficient Method
- Markt and Mengele's Method and its Extension

Numerical methods considered are:

- Successive Images Method
- Charge Simulation Method
- Finite Element Method

2.2.1 Simplified Model

The major factors affecting conductor surface stress for an overhead line, as shown in Figure 2-1, are:

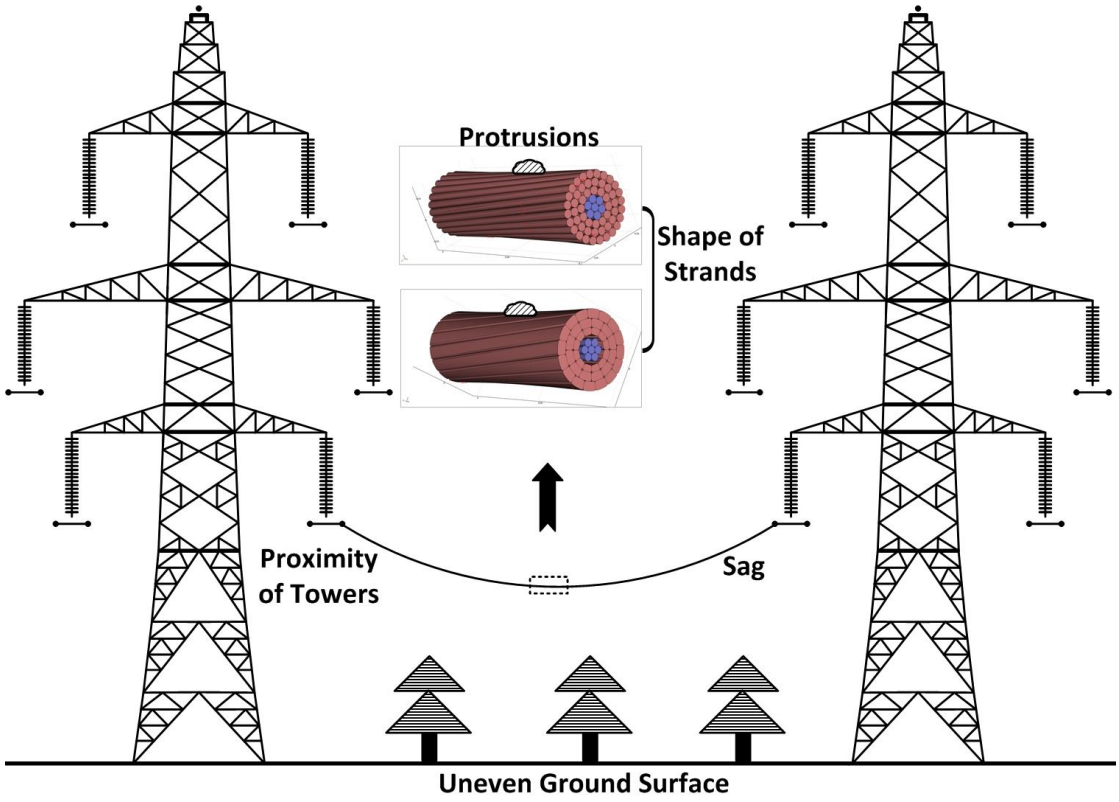

Figure 2-1 Diagrammatic drawing of a transmission line span between two 400kV towers (L6)

- Conductor sag
- Proximity of towers
- Uneven ground surface
- Finite ground conductivity
- Conductor stranding and protrusions (such as insects and raindrops) [6]

By ignoring all the factors listed above, a simplified transmission line model can be produced which comprises a series of cylindrical conductors with infinite length, parallel to each other and placed above a smooth ground plane. The three-dimensional transmission line is thus represented by a two-dimensional model.

2.2.2 Maxwell's Potential Coefficient Method

The first publication on the calculation of conductor surface stress was in 1948 when Temoshok introduced Maxwell's Potential Coefficient to calculate the charge density for each conductor within a transmission line system [13]. More systemic processes for this method can be found from Adams' example of a single conductor transmission line (1955) [14].

In order to explain the principle of Maxwell's Potential Coefficient Method, an isolated single conductor case is considered first:

As in Figure 2-2, the single cylindrical conductor with radius r_0 and electric potential U is considered as an isolated conductor (the distance between conductor and the ground plane being large compared to conductor radius).

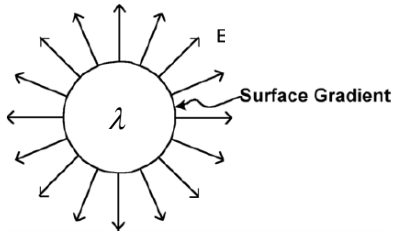

Figure 2-2 Isolated single conductor

Any charge on the conductor surface is assumed to be distributed uniformly around the conductor surface as well as along the length of the conductor. The conductor can

thus be represented by a line charge (with the same amount of charge) distributed on the central axis of the conductor.

Assume that the density of the line charge is λ C/m along the length of conductor. According to Gauss's law (integral form) [15],

$$\varepsilon_0 \int_{surface} E \cdot ds = \int_{volume} \rho dv \tag{2-1}$$

$$\Rightarrow \varepsilon_0 E \cdot 2\pi r = \lambda \tag{2-2}$$

Where $\mathcal{E}_0$ is the permittivity of vacuum, E is electric field strength, and ρ is charge density.

The electric stress on the surface of the conductor is therefore:

$$E = \frac{\lambda}{2\pi\varepsilon_0 r} \tag{2-3}$$

Assume the electric potential is Φ. The electric field strength E is then:

$$E = -\nabla\Phi = -\frac{d\Phi}{dr}u_r \tag{2-4}$$

Where u_r is the unit vector which has the direction as E.

Substituting Equation(2-4) into Equation(2-3) and integrating with respect to r from D (D is the distance from conductor surface to ground) to the surface of the conductor, r_0, the potential of the conductor U is obtained as:

$$\int_D^{r_0} -\frac{d\Phi}{dr}u_r \cdot dr = \int_D^{r_0} \frac{\lambda}{2\pi\varepsilon_0 r} \cdot dr \tag{2-5}$$

$$\Rightarrow U = -\int_D^{r_0} \frac{\lambda}{2\pi\varepsilon_0} \cdot \frac{1}{r} dr = \frac{\lambda}{2\pi\varepsilon_0} \ln\frac{D}{r_0} \tag{2-6}$$

The electric field strength on the conductor surface E can be expressed as a function of potential U as:

$$E = \frac{\lambda}{2\pi\varepsilon_0 r} = \frac{U}{r \ln\frac{D}{r_0}} \tag{2-7}$$

Maxwell's Potential Coefficient Method [14] assumes that surface charges are distributed uniformly around each conductor. In this circumstance, a multi-conductor system with ground plane is equivalent to a multi-line charge system (λ_1~λ_6 are defined in Figure 2-3). The ground plane acts as a mirror producing a reflection of the line charges, as shown in Section 2.2.4.

According to Equation(2-3), the electric field strength can be calculated by charge densities λ_1~λ_6. Charge densities are calculated from:

$$[\lambda]=[P]^{-1}[U] \tag{2-8}$$

Where the *P* matrix is Maxwell's potential coefficient matrix, given as:

$$P_{kk}=\frac{1}{2\pi\varepsilon_0}\ln\frac{2h_k}{r_k}, k=1,2,...n \tag{2-9}$$

$$P_{km}=\frac{1}{2\pi\varepsilon_0}\ln\frac{D_{km}}{d_{km}}, k=1,2,...n, m=1,2,...n, k\neq m \tag{2-10}$$

In which $D_{km}=\sqrt{(x_k-x_m)^2+(y_k+y_m)^2}$ and $d_{km}=\sqrt{(x_k-x_m)^2+(y_k-y_m)^2}$

The analytical solution for electric field strength at any location is thus obtained by vector superposition.

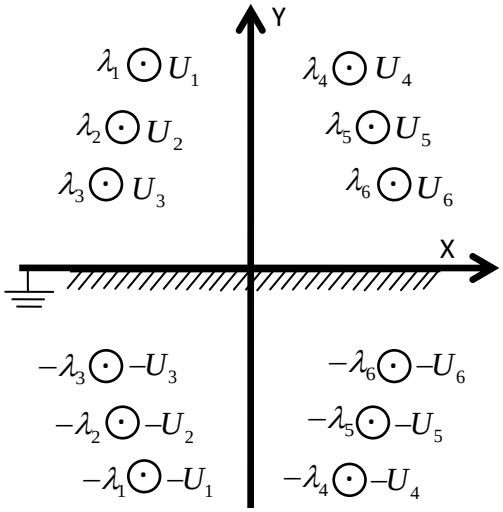

Figure 2-3 Multi conductors above ground

Unfortunately Maxwell's Potential Coefficient Method is limited to calculation of multi-conductor systems with large spacing. Using a single line charge to replace a conductor's surface charge distribution implies a uniform charge and electric field distribution around the conductor surface. Such an assumption becomes inadequate in the case of transmission lines using bundle conductors since the sub-conductor spacing in a bundle is of the order of only 10-40 times the sub-conductor radius.

2.2.3 Markt and Mengele's Method

Markt and Mengele [16] were the first to suggest a method of calculating the conductor surface electric field of a bundle conductor in transmission lines [17]. This method can be treated as an extension of Maxwell's Potential Coefficient Method. The calculating process can be divided into three steps:

Step 1-Replacing sub-conductors by a single conductor

The sub-conductors within each bundle are initially replaced by a single conductor, representing the whole bundle, with an electrically equivalent radius. The equivalent radius of the bundle is calculated as:

$$r_{eq} = \left[n \cdot r \cdot (R)^{n-1} \right]^{\frac{1}{n}} \tag{2-11}$$

Where r is the radius of sub-conductors within the bundle; R is the radius of the bundle as shown in Figure 2-4; and n is the total number of sub-conductors within one bundle.

Step 2-Calculating charge densities using the Maxwell's Potential Coefficient Matrix

The line charge density is calculated using the same procedure as the previous method (Maxwell's Potential Coefficient Method) shown in Equation(2-8).

Step 3-Calculating electric field within each bundle

Sub-conductors within a bundle are assumed to be placed far enough apart that each can be approximated by a line charge located at the central point of the cylinder (Figure 2-4).

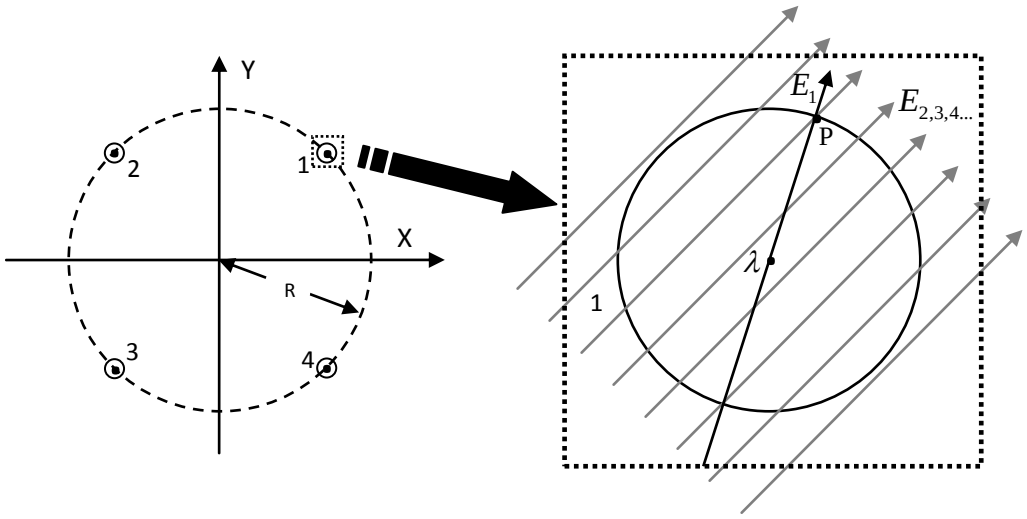

Figure 2-4 Quad bundle conductor

Since the radius of the bundle is much larger than the radius of a single conductor ($R>>r$), the field strength induced by other conductors ($E_{2,3,4}$) on conductor 1 can be approximated to a superimposed electric field. As shown in Figure 2-4, P is a point located at the surface of conductor 1. The electric field strength at P can thus be calculated by vector superposition of $E_{2,3,4}$ and E_1 which is obtained by Equation (2-12):

$$E_n = \frac{\lambda_n}{2\pi\varepsilon_0 d_n} \tag{2-12}$$

Where E_n is the field at a distance d_n created by the line charge λ_n.

Markt and Mengele's Method is well known as an accurate analytical method for field calculation in transmission lines. However, at higher voltage levels, bundle conductors are widely utilized in modern transmission line design. The distance between sub-conductors is relatively small compared to the distance between different phases. As a result, line-charge simplification introduces large errors in calculating electric field distributions within bundles. Further improvement of calculation accuracy is thus required for bundle conductors.

An improvement was introduced by King who suggested that the line charge used to replace each sub-conductor should not be located at its central point but at a small distance away from its central point [18]. This small distance is a function of the

bundle's geometry. King further improved this method by replacing a sub-conductor by two line charges symmetrically displaced from the centre of the conductor [19].

2.2.4 Successive Images Method

The Image Method comes from Lord Kelvin's publication [20] in 1848 when he discovered that the electric field of a charge in front of a conducting plane can be calculated by the charge and its mirror image. By using this basic idea of the image method, Hammond [21] presented a cylindrical conductor example which connected the 'image method' to transmission line field calculations. Based on this, Sarma and Janischewskyj published a paper [22] in 1969 on electrostatic field calculation for parallel cylindrical conductors. This is also recognized as the most classic publication on the Successive Images Method.

a) Theory of 'Successive Images Method'

The successive image method initially uses the central line charge simplification, introduced in Maxwell's Potential Method, to calculate the charge density of each conductor, and then considers the non-uniform distribution of those charges around the surface of each conductor. An iterative method is employed to approach the correct value of the electric field.

The theory behind the Successive Images Method is the Uniqueness Theorem, which can be stated as: if one can find a solution which meets the Poisson Equation or Laplace Equation with boundary conditions satisfied, this will be the only solution for the specific electrostatics problem [23].

An explanation of the Uniqueness Theorem is that conductive material can be used to fill the inside of any volume surrounded by an equal potential surface without modifying the electric field outside the equal potential surface (the net charge of that volume must remain the same).

As shown in Figure 2-5, the arbitrary charges: 'q_1', 'q_2', 'q_3'… 'q_n' determine an equal potential surface S. The electric field distribution outside the surface S will remain the same if the inside of S is filled with a conductor charged 'q_1+q_2'[24].

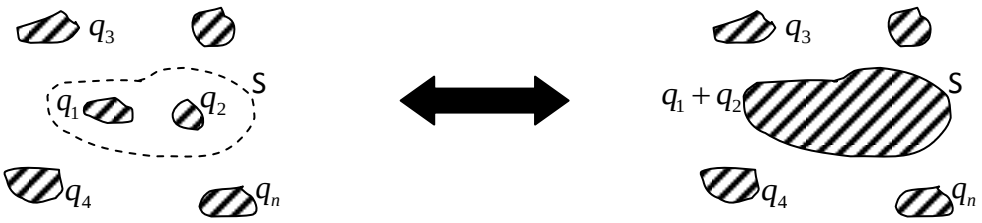

Figure 2-5 Application of 'uniqueness theorem'-fill equipotential surface with a conductor

This general conclusion can be applied to the cylindrical conductor case as in Figure 2-6: the non-uniformly distributed charges on the conductor surface can be replaced by a line charge -λ located at a distance $\delta=r^2/D$ away from its centre. The electric field outside the cylindrical conductor can thus be calculated by consideration of line charges $+\lambda$ and -λ instead.

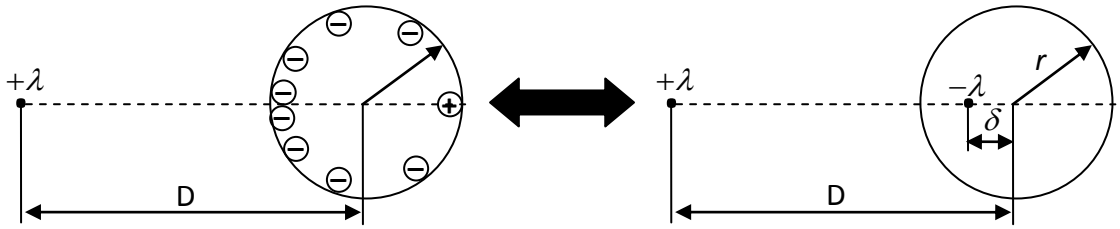

Figure 2-6 Line charge near a cylindrical conductor

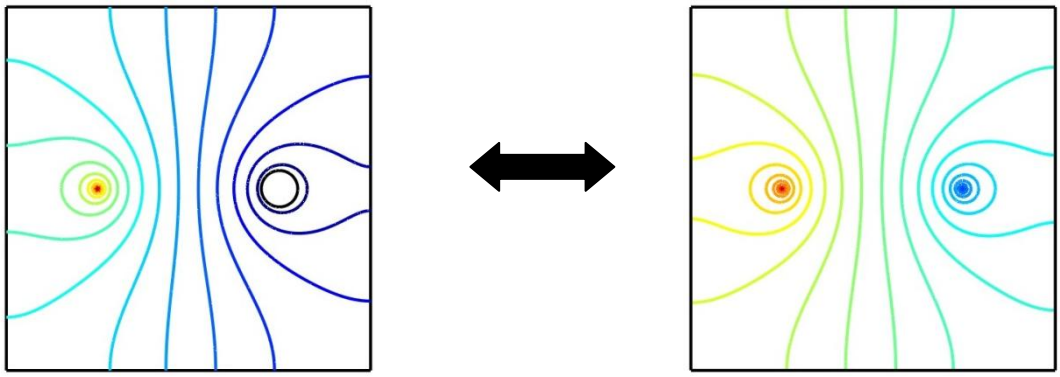

Figure 2-7 Equal potential for line charge and cylindrical conductor (left) and two line charges (right)

The simulation result (from COMSOL) presented in Figure 2-7 verifies the conclusion that the electric field remains the same when using a line charge to replace the conductor. An equi-potential plot is employed to reflect the electric field distribution.

This conclusion can be easily extended to the case of isolated two-conductor bundles.

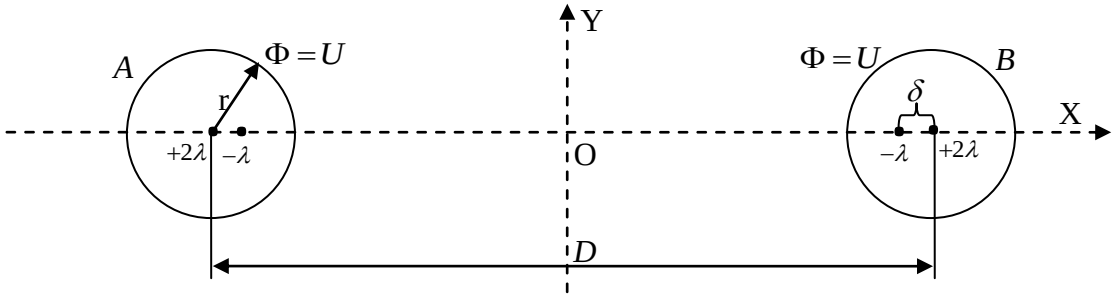

Figure 2-8 isolated two-conductor bundle

As shown in Figure 2-8, if the distance D between two conductors is much larger than their radius ($D \gg r$), these two conductors can be represented as two line charges located at their centre ($+\lambda$), this conclusion is obtained from the following derivation:

From the Uniqueness Theorem, the solution of this electric field problem is to find a charge distribution which maintains the potential of the ground plane at zero and that of the conductors A and B to be U.

Assume the charge density of each conductor is $+\lambda$. When considering the potential of the ground plane, the two conductors can be approximated as a single line charge with charge density $+2\lambda$ and located infinitely distant from it. According to image theory, charges induced on the ground plane will have the same effect as a -2λ reflection situated under the ground plane, and infinitely apart from A and B. By introducing this -2λ line charge, the potential of the ground plane is maintained at zero. Now, we need to maintain the surface of A and B at potential U. For conductor A, there are two line charges outside its surface: the image with a charge -2λ, and the net charge on B with value $+\lambda$. Both charges can be considered to be a long distance away from A. Using the proven conclusion above, 'line-charge induced charges on the surface of a cylindrical conductor can be replaced by a charge of the opposite polarity and located $\delta = r^2/D$ from the centre', the image -2λ induces a charge $+2\lambda$ at distance δ from the centre of A (in the case $\delta = 0$) while the net charge of B, $+\lambda$, introduces a charge $-\lambda$ at the distance δ from the centre of A. As $D \to \infty$, $\delta \to 0$, so the total introduced charge is $+2\lambda - \lambda = +\lambda$ located at the centre of A. By the same derivation, there is $+\lambda$ located at the centre of B as well.

If the situation becomes more complex, by considering that $D/r \neq \infty$, we have the same image line charge -2λ. As conductors *A* and *B* are now closer together, the derivation changes to the following:

We now need to maintain the surfaces of *A* and *B* to be equi-potential. Because $D \gg r$ is no longer true, we have now $+2\lambda$ located at the centre of *A* and *B* after considering the ground plane's charge effect. In order to maintain *A* to be equi-potential (we assume *B* is initially in the same situation), an image charge of -2λ, located $\delta_1 = r^2/D$ from the centre of *A*, is introduced. Now conductor *A*'s surface is maintained at equi-potential by these line charges: two $+2\lambda$ line charges in the centres of *A* and *B*, -2λ line charge located at $\delta_1 = r^2/D$ from the centre of *A*. In order to maintain conductor *B* at an equi-potential, we have to introduce another two line charges: -2λ located $\delta_1 = r^2/D$ from the centre of *B* and $+2\lambda$ located at $\delta_2 = \frac{r^2}{D-\delta_1} = \frac{r^2}{D - r^2/D}$ from the centre of *B*. These line charges maintain the equal potential surface of *B* while modifying the equi-potential situation of conductor *A*, so another two line charges have to be introduced inside *A*, and so on…

By reiteratively maintaining *A* and *B* to be equi-potential surfaces, a series of line charges can be introduced inside each conductor. Assume that after *n* times of iteration, the distance between the last two images becomes negligible ($\delta_n - \delta_{n-1} \approx 0$), then adding another two images -2λ and $+2\lambda$ is equivalent as adding no charge, and does not change the charge distribution. This process can thus be terminated at an appropriate level of accuracy. However, the net charge must be maintained at $+\lambda$ in each conductor. We can achieve this by adding $+\lambda$ at δ_n apart from their centres in both conductors as the effect can be cancelled by their images.

Simulations were carried out in order to verify this method. As shown in Figure 2-9, a series of line charges were employed to represent the conductor surface charge. The black circles in the simulation results are conductors, the green contours are potential contours. It can be seen from the simulation results that the contour near the conductor surface (green circle) has a good fit with the conductor surface (black circle). This is a good evidence of the applicability of the Successive Image Method. It is also demonstrated in simulation that for a typical National Grid twin bundle (400

mm spacing), after the first set of fictitious line charges are introduced, another step of iteration only contributes less than 1% improvement in terms of the accuracy.

There have been many applications of the Successive Images Method during the last 40 years [25-27].

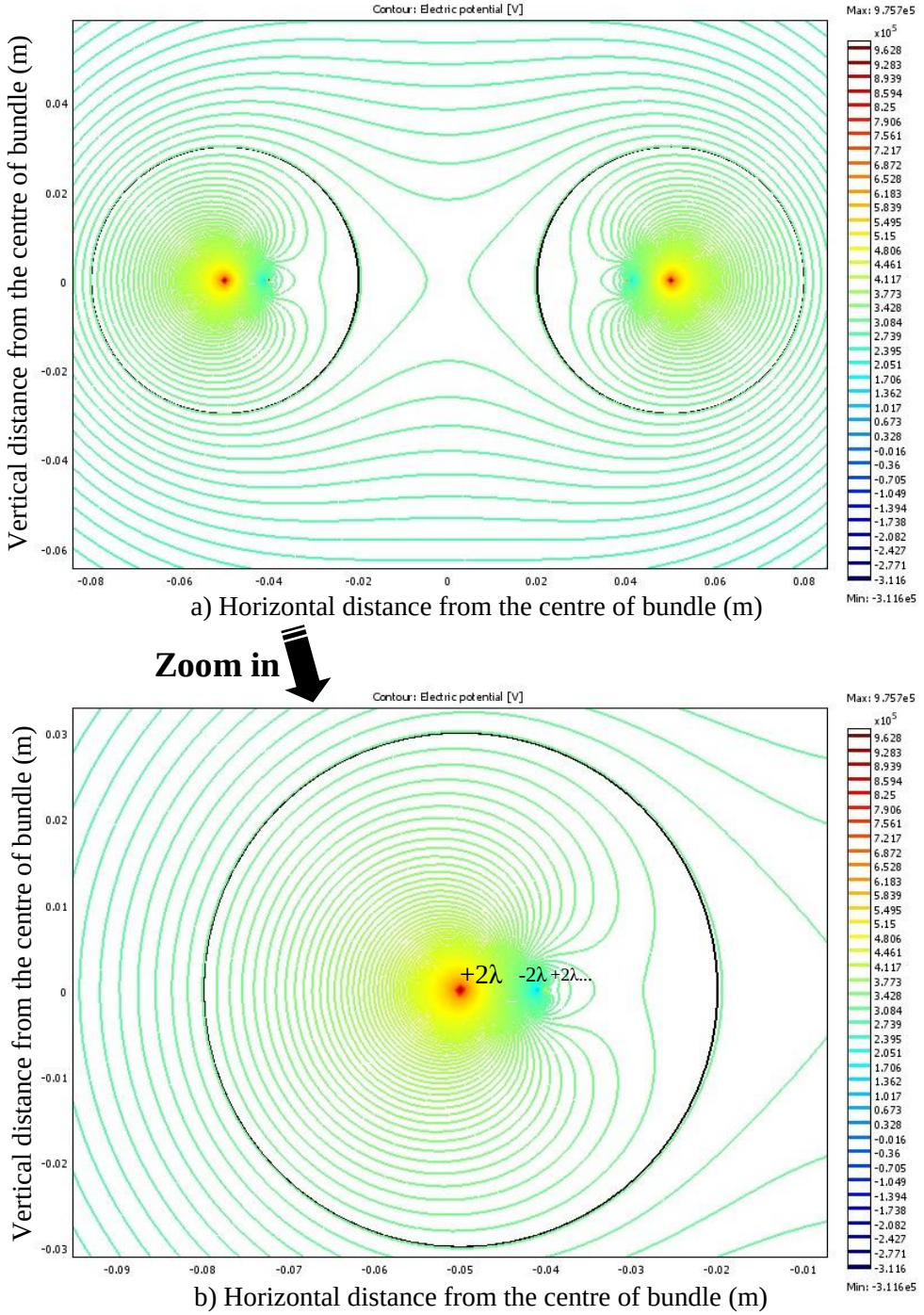

Figure 2-9 Equipotential plot for isolated two-conductor bundle

Application to Transmission Line Calculations

A single conductor transmission line is employed to explain the calculating processes:

Step 1 Use Maxwell's Potential Matrix to calculate the net charge of each conductor. 7 line charges and 7 images are obtained as shown in Figure 2-10.

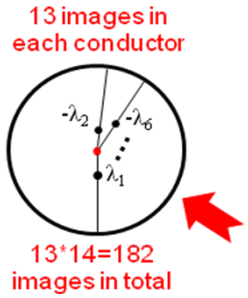

Step 2 Consider one conductor (λ_1 in Figure 2-10), there are 13 line charges in total outside the conductor surface. In order to maintain the surface at an equal potential, 13 images are introduced inside λ_1. The same process is applied to the other conductors. 182 images in total are obtained after the first iteration while 2366 images in total are obtained after the second iteration process.

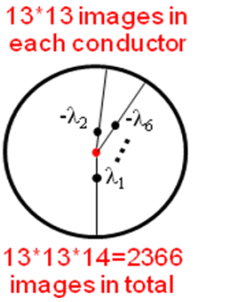

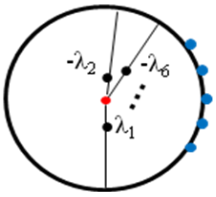

Step 3 As line charge densities are obtained as above, an analytical solution for the electric field strength of any location is thus obtained by vector superposition from:

$$E = \frac{\lambda}{2\pi\varepsilon_0 r}$$

A certain number of points can be selected on the surface of each conductor to represent the surface field distribution.

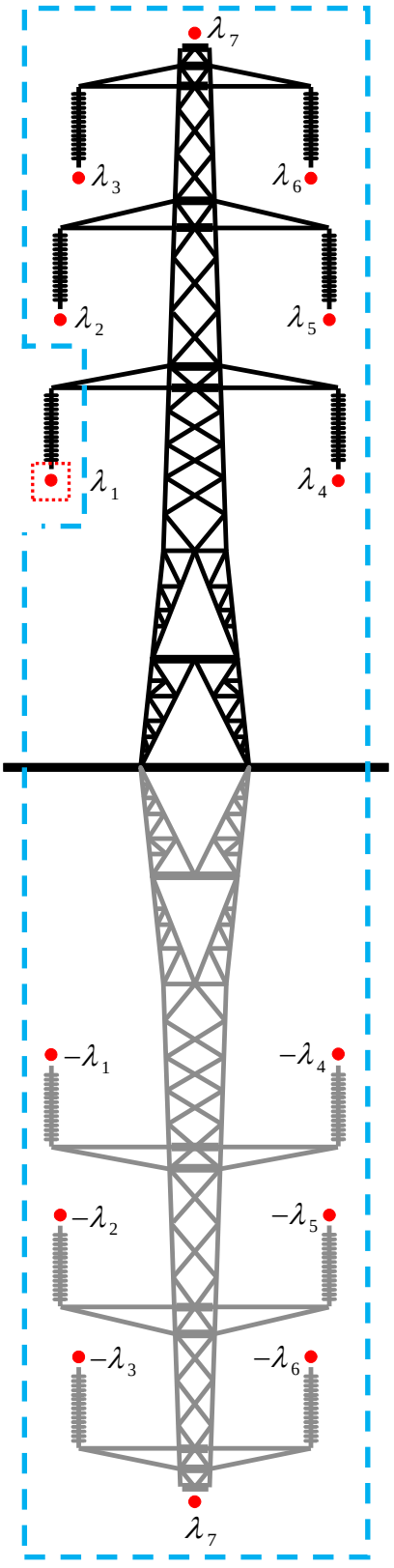

Figure 2-10 Transmission Line Case

The above process demonstrates calculating procedure for a certain time instance. Since the whole calculation is time dependent, this procedure is repeated.

2.2.5 Charge Simulation Method

The Charge Simulation Method (CSM) has been commonly employed to analyze electric field problems in high voltage insulation systems. The method dates back to 1969 when Abou Seada and Nasser employed CSM to evaluate the field strength in a twin cylindrical conductor [28]. Subsequently, Singer, Steinbigler and Weiss published a comprehensive paper [29] on the details of CSM. They extended the applicability of CSM from two dimensions to three dimensions, and gave an example of the calculation of electric field strength near a transmission line tower, using CSM. 'An optimized charge simulation method' was discussed by Yializis, Kuffel and Alexander in 1978 [30], and techniques for optimizing calculation speed by flexibly selecting simulation charge shapes were presented. More recent work employing CSM calculates the surface field of a ±800 kV UHVDC transmission line in China [31].

The principle of the Charge Simulation Method can be explained as 'using discrete fictitious charges to replace the non-uniformly distributed surface charge' [28]. Like the Successive Images Method, it is a numerical method based on fictitious charges. However, the difference is that the images introduced in the Successive Images Method are fixed at a certain position with a certain shape and charge density, while the fictitious charges introduced in CSM are flexible in both location and shape. Providing the fictitious charges have been set up, the charge densities can be calculated so that their integrated effect satisfies the boundary conditions. This is explained through a simplified example as follows:

As shown in Figure 2-11, N line charges have been introduced to simulate the surface charge distribution of a twin cylindrical bundle. The boundary conditions are satisfied by selecting N test points on the surface (red points) and assuming their potential to be the conductor's voltage. As the potentials of the test points can be calculated by superposition of fictitious line charges, N equations can thus be constructed with N unknown variables (fictitious line charge densities):

$$[P][\lambda] = [U] \tag{2-13}$$

The line charge densities can be found by matrix inversion:

$$[\lambda]=[P]^{-1}[U] \tag{2-14}$$

The electric field can thus be calculated from Equation(2-3).

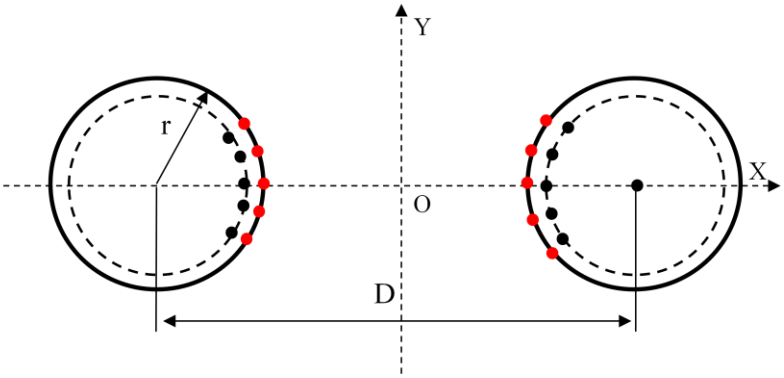

Figure 2-11 isolated two-conductor bundle

2.2.6 Software Methods

Two software packages, ELECMODL and SES-ENVIRO, have the capability to calculate surface electric stress for transmission lines. ELECMODL was written by Richard Stone from National Grid in 1992. They are MS-DOS programs especially designed for surface field calculation. Configurations such as height of each phase, bundle spacing, conductor radius are input parameters. Average and maximum surface gradient for each sub-conductor are the outputs. The interface is shown in Figure 2-12.

SES-ENVIRO was designed as an analytical tool for estimating environmental impact on the surroundings of overhead lines. It was developed to evaluate environmental emissions from overhead lines such as: Audible Noise, Radio Interference, and Corona Loss. The sub-module within SES-ENVIRO calculates the surface stress as an input for audible noise analysis.

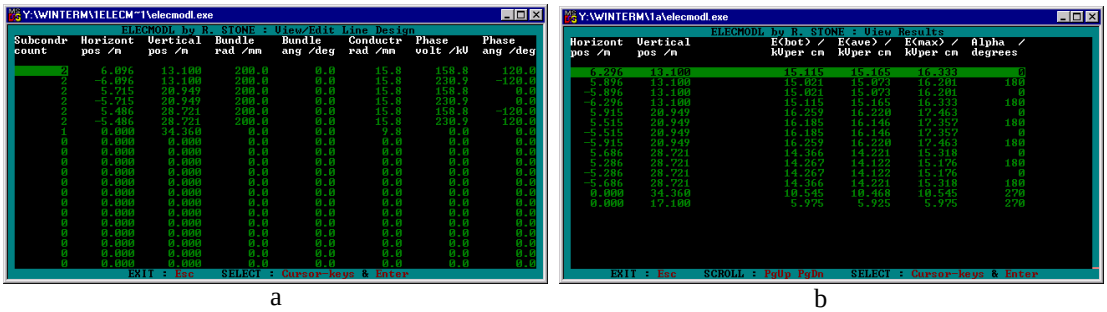

a b

Figure 2-12 Interfaces of ELECMODL: a). input parameters; b). results

SES-ENVIRO employs the Successive Images Method to calculate the electric surface stress. The technical basis of this programme is the classic paper by Sarma and Janischewskyj [22] as introduced in the previous section. Both ELECMODL and SES-ENVIRO calculate the surface stresses based on the simplified model introduced in Section 2.2.1. In SES-ENVIRO, surface roughness can be included to calculate the audible noise level. However, the sub-module for surface stress calculation within SES-ENVIRO ignores surface roughness due to stranding, protrusions, etc.

2.2.7 Summary of Existing Methods

Table 2-1 summarises the methods used to calculate conductor surface stress, described earlier.

Table 2-1 Characteristics for different calculating methods

Methods	Advantages	Disadvantages	Application
Maxwell's Potential Coefficient Method	• Simple and easy • Fast	• Low accuracy • Not capable for multi-bundle case calculation	Only capable of single conductor transmission line system
Markt and Mengele's Method	• Relatively simple • Relatively high accuracy	• 8% deviation from CSM • Not capable for bundle configurations above 'Quad'	Tolerable accuracy can be achieved for single, twin, and triple bundles (<10%) but not for quad bundles or above…
Successive Images Method	• It can achieve any degree of accuracy (depends on iterations) • Relatively fast compared to other numerical methods	• The method employed to calculate net charge introduces errors • Ignores deviation for smooth cylindrical surfaces	It is an accurate method designed to handle any bundle configurations for overhead line system but based on simplified models as above
Charge Simulation Method	• A numerical method with high degree of accuracy (depends on calculating power) • Can be further applied to multi-dimensional and irregular shapes	• Large errors can be introduced when too few fictitious line charges are employed • Higher computing power is needed compared to Successive Images	It is an accurate method designed to handle any bundle configurations for overhead line systems. Further applications are possible with different geometries of conductor and 3-D analysis
Finite Element Method	• Capable of various shape and dimensions analysis • Multi-physical filed coupling allows various analysis: thermal, vibration, etc	• Limited by the scale of simulation environment, because of the computer capability • Purely numerical analysis based on the physics	It is the only methods that can couple multi-physics fields with various shapes of simulation domain. Mainly limited by the range of scales of simulation geometry. Specially used for smaller scale analysis such as stranding.

2.3 Review for Cage Experiments

2.3.1 Outdoor and Indoor Testing Lines for Audible Noise

The first systematic paper on 'audible noise from transmission lines' was published in 1969 by Taylor, Chartier and Rice [3]. During the following 40 years, sequential

works have been carried out by various utilities and universities. Intensive publications can be found around the 1980s when EHV transmission lines were in the testing stage. Testing lines for audible noise after 1990 tend to evaluate the noise emission level for novel configurations such as asymmetrical bundles, non-parallel bundles etc. Most recent work can be found from China's HVDC test lines.

Taylor, Chartier and Rice [32] were the first to measure noise level from transmission lines. Their results were obtained from both outdoor and indoor tests under or after rainy conditions. Outdoor tests were carried out at the Apple Grove 750 kV test site, while indoor tests were made on very small dry wires and tubes in the shielded room of the Westinghouse RI Lab. The voltage level for their indoor experiment was 80 kV. The authors concluded that "the major effect of voltage gradient on the sound level occurs in the high range of the frequency spectrum". However, because no effort had been made to mitigate the background noise (especially the 80 kV transformer 'hum'), Teich and Weber queried this conclusion in their publication of 2002 [33]. Within Taylor's publication, authors were trying to relate the audible noise level with surface potential gradient. However, the method employed for calculating surface gradient is not an accurate method which affects the results and conclusions. There is also no field control method within the indoor test set-up (Figure 2-13) within this early work such as an earthed cage etc.

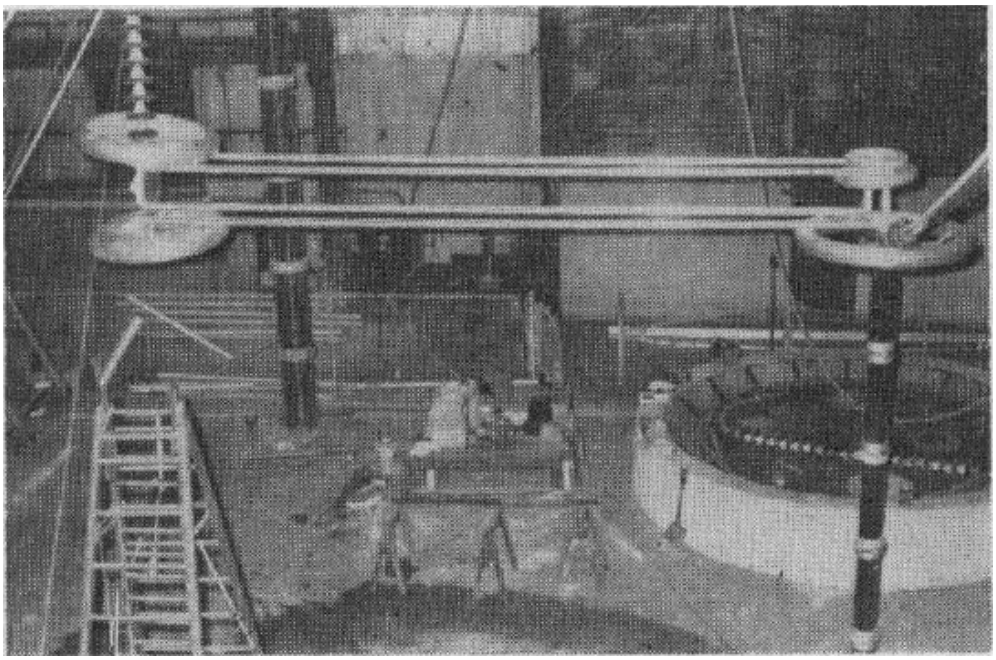

Figure 2-13 Test Set-up used in HV Lab [3]

Subsequent work was carried on by Juette and Zaffanella in 1970 [34, 35]. In this a test cage (Figure 2-14) was employed to control the electric field and test results were utilized to determine Radio noise, audible noise and corona loss effects for UHV lines (Bonneville Testing Line).

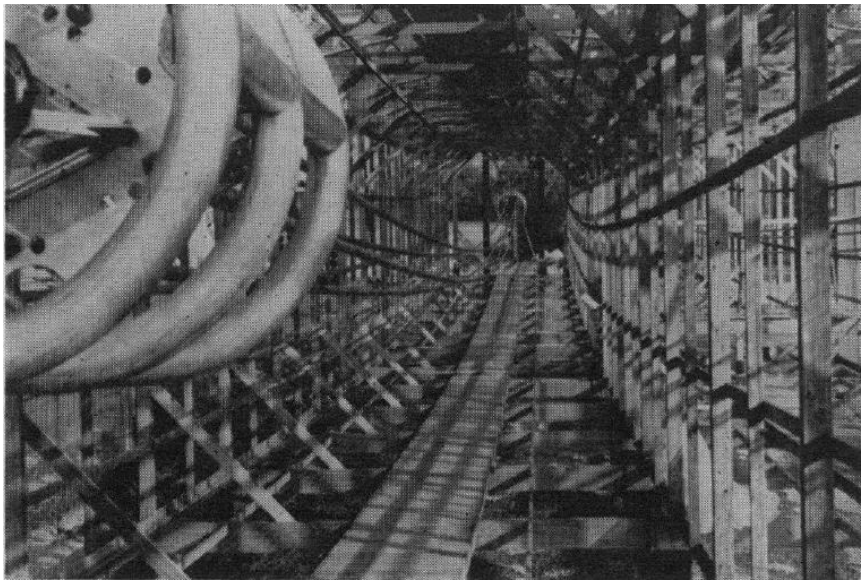

Figure 2-14 Test Set-up for controlled-field cage [34]

Within these early works, all these tests were on single phase lines with various bundle configuration and conductor radii. Their testing results are believed to be extendable to evaluate the 'Audible Noise level' for real three phase transmission lines with different bundle arrangements [3, 32-34]. The calculation methods are developed in "Transmission Line Reference Book-345 kV and Above" [36].

However, a few researchers hold the different opinion that single-phase tests in the laboratory were not properly simulating the electric field in the immediate vicinity of the conductor and that the corona discharge and associated streamer lengths on the test conductor were not representative of conditions in the field [37].

After that, a three-phase UHV testing line (Figure 2-15) was energized in General Electric in 1979, and novel configurations have been tested in this field [38]. Furthermore, long term testing was carried on in order to examine the effect of conductor ageing. It has been found that: for a particular case of bundles of 8*3.31 cm conductors operating at approximately 15 kV/cm, noise reductions of 2 dB were noted after 5 months of exposure, 4 dB after 10 months and 8 dB after almost 3 years [39].

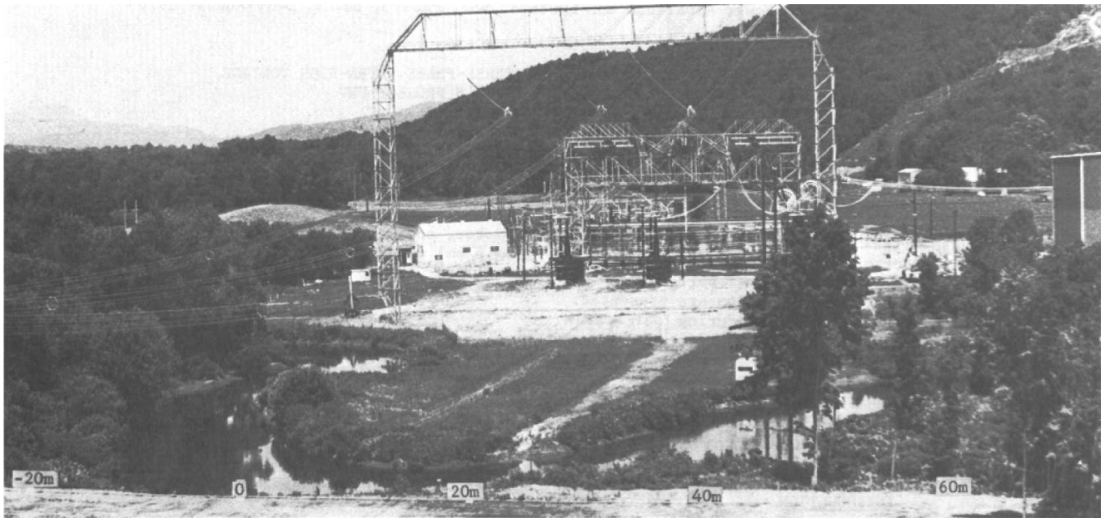

Figure 2-15 Three Phase Outdoor Testing Line—UHV Project in GE [38]

Another outcome from the cage experiments is the correlation between noise level and bundle geometry. Pokorny, Schlomann and Barnes [40] first concluded their publication with: "for a given applied voltage, an increase in the number of sub-conductors will produce a corresponding reduction in audible noise". Comber and Zaffanella [41, 42] concluded that significant noise can be abated by optimizing the geometry of bundle conductors. Higher voltage levels have been applied in a similar test by Trinh, Maruvada and Poirier [43].

As shown in Figure 2-16, Sforzini et al [44] were the first to mitigate background noise and noise reflection by introducing an anechoic chamber in a cage experiment. Within the conclusion, 100 Hz hum noise was noted. The authors also noted that the anechoic chamber is an effective facility to mitigate background noise.

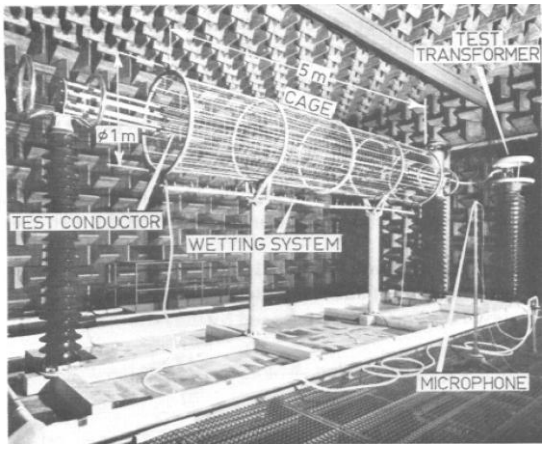

Figure 2-16 Anechoic Chamber Cage [44]

From 1976, intensive research work focusing on 'the correlation between asymmetrical bundles and noise generation' was carried out [45, 46]. However, this multi-bundle geometry is applied to higher voltage levels above 700 kV (UHV and EHV) which is not presently adapted to the UK's transmission system which is mainly comprised of 400 kV transmission lines.

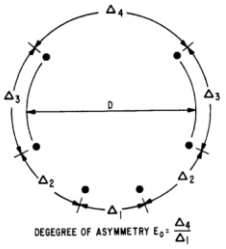

Figure 2-17 Asymmetric bundle arrangements [46]

2.3.2 Outcomes from the 'Experts' Noise Seminar'

In order to gain experience from other researchers, an 'Experts' Noise Seminar' was organized in June 2011 at the University of Manchester. The design criterion for cage experiments was discussed in detail. Table 2-2 summarized the design parameters provided by attendees from four leading research institutes and also the parameters decided for the facility in Manchester, more detail of which is given in the following chapter.

Table 2-2 Corona Cage Design Parameters

	Tsinghua (China)	ETH (Switzerland)	Eskom (South Africa)	JPS (Japan)	Manchester (UK)
Length of Conductor	4m (overall) 3m (effective)	6m (overall)	Not mentioned	7.5m (overall)	4m (overall)
Cage Size	Square 1.7m*1.7m	12 edge shape ~1.5m radius	Not mentioned	Cylinder 1m radius	Cylinder 0.75 m radius
Voltage Level	90~130kV	166.6kV	Not mentioned	Max 150kV	90~150kV
Surface Stress	23~32kV/cm	17.6kV/cm	14~22kV/cm	10~17kV/cm	16~25kV/cm
Acoustic Noise Control	Indoor with no specific noise control	Indoor with correction (background)	Outdoor with no specific noise control	Outdoor with no specific noise control	Anechoic chamber with 22.5dBA(100Hz) reduction
Tensioning Design	Maximum 2 tons	No tension force for straighten	Not mentioned	Load cell unit for tension	Maximum 1 ton
Electrical Measurements	PD, RIV	Leakage current	Not mentioned	No	PD, RIV, Leakage current
Acoustic Measurements	Sound level meter	Sound level meter with FFT	Not mentioned	Microphone with FFT	Brüel & Kjær PULSE platform for analysis

The involved affiliates include Tsinghua University (China) [47, 48], ETH (Switzerland) [8-11, 49, 50], ESKOM (South Africa) [6, 51], JPS (Japan) [52-56] and the University of Manchester (UK).

The experimental set-ups from these affiliates are shown in Figure 2-18.

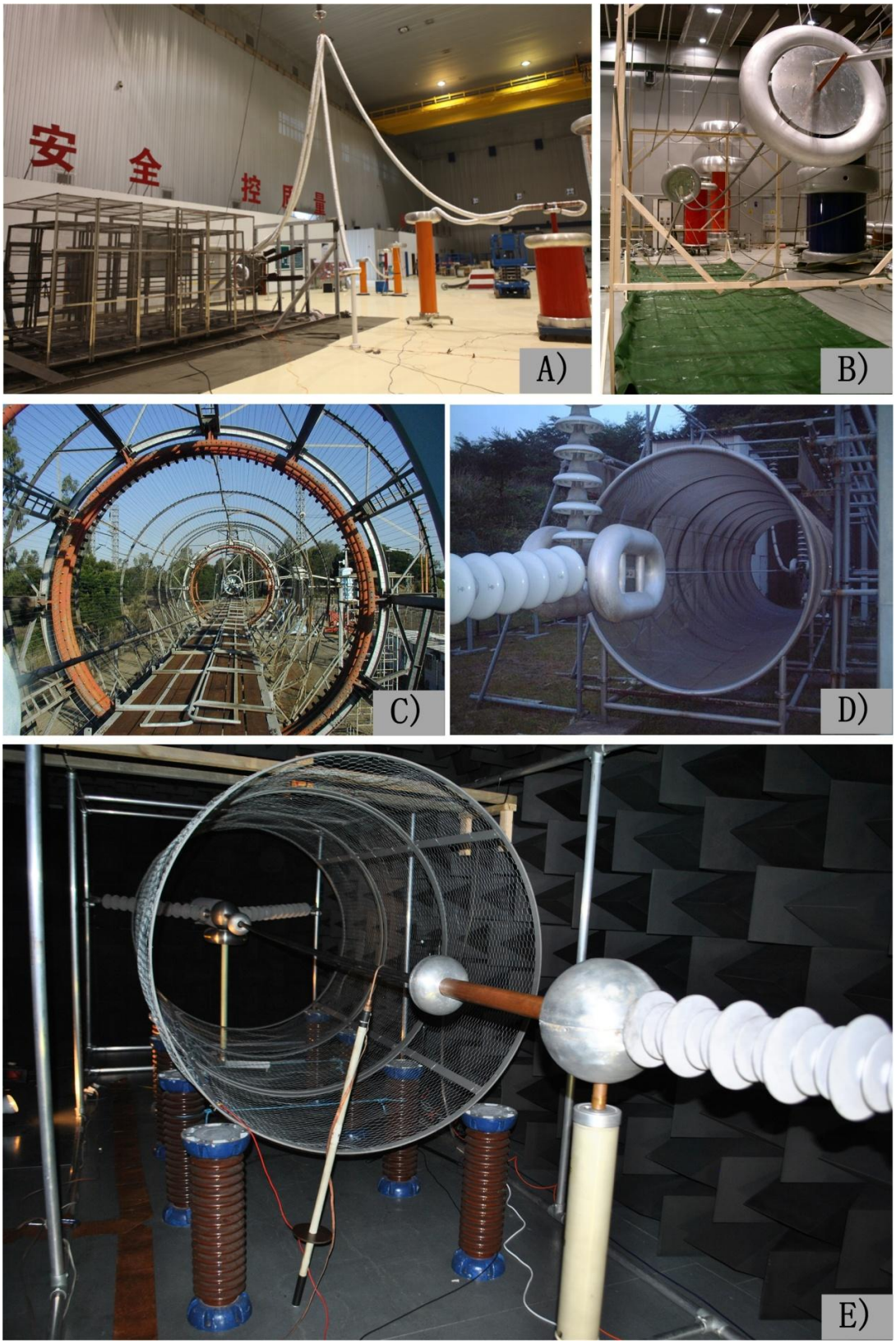

Figure 2-18 Experimental Facilities from Different Affiliates: A) Tsinghua (China); B) ETH (Swiss); C) ESKOM (South Africa); D) JPS (Japan); E) Manchester (UK) [6, 8-11, 48, 50-52, 54-56]

2.3.3 Calculation Methods for Audible Noise Level Prediction

In general, transmission lines are designed to prevent corona discharges under dry conditions. Compared with the performance under foul weather, noise generation under fair weather conditions is usually negligible. The design criterion for transmission lines is thus fixed on the noise performance under wet conditions. Because the mechanisms of audible noise from transmission lines are still debatable, only empirical formulae are widely employed to calculate the audible noise level. This section covers existing methods for audible noise level calculations.

EPRI's "*Transmission Line Reference Book-200 kV and Above(Third Edition)*" [6] introduced two major methods for calculating the audible noise level-'EPRI Method' and 'BPA Method'. Both of them employed empirical formulae which are derived from cage testing results.

a) EPRI Method

The empirical equations are derived from testing results on a large number of bundle configurations and conductor types [34, 35]:

For sub-conductor number $n < 3$:

$$P = 20\log n + 44\log d - 665/E_{\max} + K_n + 75.2 - 10\log D - 0.02D$$

For sub-conductor number $n \geq 3$:

$$P = 20\log n + 44\log d - 665/E_{\max} + (22.9(n-1)d/B) + 67.9 - 10\log D - 0.02D$$

Where:

P is the audible noise in dBA above 20 μPa.

n is the number of sub-conductor in the bundle.

d is the sub-conductor diameter in cm.

$E_{\max}$ is the maximum conductor surface gradient in kV/cm, calculated for the average height above ground assumed equal to the minimum height plus 1/3 of the sag.

d_{eq} is the bundle diameter in cm.

D is the distance from the phase to the measuring point in m.

K_n is equal to 7.5 dB for $n=1$ and 2.6 dB for $n=2$.

b) BPA Method

The BPA refers to "Bonneville Power Administration" which organized a series of testing work on overhead power lines between 1975 and 1985 [57]. BPA method based on long-term statistical data collected from aged overhead testing lines:

For sub-conductor number $n<3$:

$$P=55\log d+120\log E_{\max}+Alt./300-115.4-11.4\log D$$

For sub-conductor number $n\geq 3$:

$$P=26.4\log n+55\log d+120\log E_{\max}+Alt./300-128.4-11.4\log D$$

Where:

P is the audible noise in dBA above 20 μPa.

n is the number of sub-conductor in the bundle.

d is the sub-conductor diameter in cm.

$E_{\max}$ is the maximum surface gradient in kV/cm, calculated for an average height above ground equal to the minimum height plus 1/3 of the sag.

$Alt.$ is the altitude above sea level in m

D is the distance from the phase to the measuring point in m.

2.4 Publications on 'Mechanisms of Hum Noise'

The mechanism of "hum noise" is a topic still being debated. Publications in this area are rare, and no consensus has been reached as to the mechanism of hum production. By reviewing the existing work, two potential mechanisms for 'hum noise' are manifested as the most recognized ones:

- Vibration of space charge surrounding conductors
- Vibration of charged water droplets

2.4.1 Vibration of space charge surrounding conductors

Vibration of space charge surrounding conductors has been described as the main mechanism by many publications.

'Hum noise' has been described as the result of a pressure wave caused by the movement of air ions alternatively attracted to and repelled from the conductors [6]. The positive-polarity corona discharges, initiated when the electric field at the surface of the conductor reaches some critical positive value, create electrons that are attracted to the conductor and positive ions that are pushed away from the conductors by the electric field. When the electric field changes sign, the positive ions return towards the conductor. Similarly, negative-polarity corona discharges, initiated at some critical negative electric field value, create electrons that attach to air molecules to form negative ions that are pushed away from the conductor. When the electric field changes sign, the negative ions return to the conductor. Ion movement causes alternative changes in air density and air pressure twice each power frequency cycle. A sound pressure wave with frequency twice the power frequency is then established.

More detailed evidence on the "vibration of space charge" can be found on Maruvada's book about corona from overhead transmission lines [7]. Hum noise is described as a production of the oscillatory movement, towards and away from the conductor, of the ionic space charge created during both the positive and negative half-cycles of the voltage. This movement of space charge, which in turn transfers energy to the air molecules through collisions, gives rise to an acoustic pure tone, at a frequency twice that of the supply voltage.

2.4.2 Vibration of charged water droplets

A recent publication by Teich and Weber [33] in 2002 stated their view on the 'space charge oscillation mechanism'. They suspected that the oscillation of water droplets is the dominant cause of the 2f (100 Hz) emission. An experiment was designed by Teich and Weber to examine the oscillation of pendant water droplets under 100 kV supply voltage (as attached in Figure 2-19). The high voltage rod used in this experiment is hydrophilic.

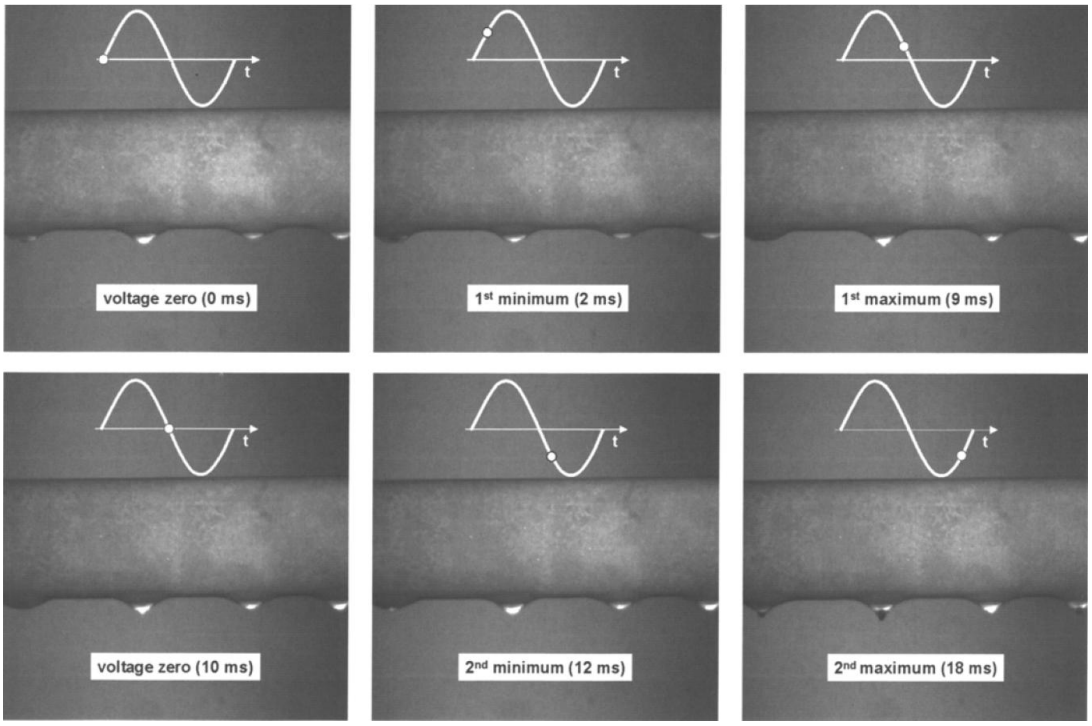

Figure 2-19 Water droplet shape change during one cycle captured by Teich and Weber [33]

However, Straumann and Semmler expressed opposed opinions on their publication [11] in 2004. Metallic protrusions were employed by them to simulate the water droplet shape, and hum noise can still be captured. So they conclude that the mechanical vibration of water droplets cannot explain 2f hum noise. In the meantime, they employed a plasma model [4, 5] to explain 2f tonal emission. Further support on this can be found in a later publication [10].

Chapter 3 Improved Calculations of Surface Field Gradients

3.1 Introduction

The most important factor influencing generation of corona is electric field distribution in the vicinity of the conductor surface [7]. Thus calculation of the electric field strength on the surface of HV conductors is of high importance when studying corona phenomena and designing high voltage overhead line infrastructure.

As described in Section 2.2, most of the existing methods were developed in 1960s when the computing resources were limited. This constraint made it unfeasible to evaluate the surface electric field distribution when considering the shape of strands, protrusions and proximity effect of towers. The fast development of both hardware and software in computer technology during the past decades has made it feasible to perform large scale computation in an affordable cost. The Finite Element Method has been widely utilized in calculating electromagnetic fields. It is an effective tool to compute electric field distribution on a complex geometry. These hardware and software developments provided a foundation to carry out further research on surface gradient calculations.

On the other hand, various types of conductors have recently entered the electrical power market to fulfil the capacity needs. Conductors with different shapes of strands (typically round and trapezoidal shapes) exist in power utilities. The lack of knowledge about the field distribution on these types of conductors has pushed the power utility to seek for new methods to predict the conductors' field distribution before their use.

This chapter proposes a novel method which utilizes both analytical and numerical procedures to predict the surface gradient. With this method, stranding shape, protrusions, the proximity of tower, the type of tower, bundle spacing and bundle arrangement can be taken into consideration when calculating surface potential gradients.

3.2 New Techniques for Surface Gradient Calculation

3.2.1 Modified Successive Images Method

In the Successive Images Method, to allow the first iteration to start, the net charge of each sub-conductor must be initially calculated. The original calculating method for the net charge employed by Sarma and Janischewskyj [22] is the Maxwell's Coefficient Method which assumes that charge is distributed uniformly on the conductor surface. When bundle conductors are introduced, the surface charge is no longer uniformly distributed due to the effect of the other sub-conductors within the same bundle. This assumption causes unsatisfactory errors in surface stress calculations.

As presented in Section 2.2, the first step is to calculate the net charge densities: $\lambda_1 \sim \lambda_{13}$ as shown in Figure 3-1. Maxwell's Potential Method assumes that the surface charge of each conductor can be replaced by a single line charge at the conductor centre. This converts the problem to a calculation of stress from multi-line charges (in this case 26 line charges with 13 unknown variables): $[\lambda] = [P]^{-1}[U]$

However, this simplification ignores the effect caused by non-uniformly distributed surface charge.

A new approach to maintain accuracy is to define a series of unknown variables of charge densities as $\lambda_1 \sim \lambda_{13}$, and use these variables rather than actual values to carry on the iterative process. When the first iterative process is finished, there are 25 line charges inside each sub-conductor. The line charge system becomes 25 line charges in 26 conductors which results in a 650 multi-line-charge system. At this stage, charge densities $\lambda_1 \sim \lambda_{13}$ can be recalculated using the Maxwell's Coefficient Matrix.

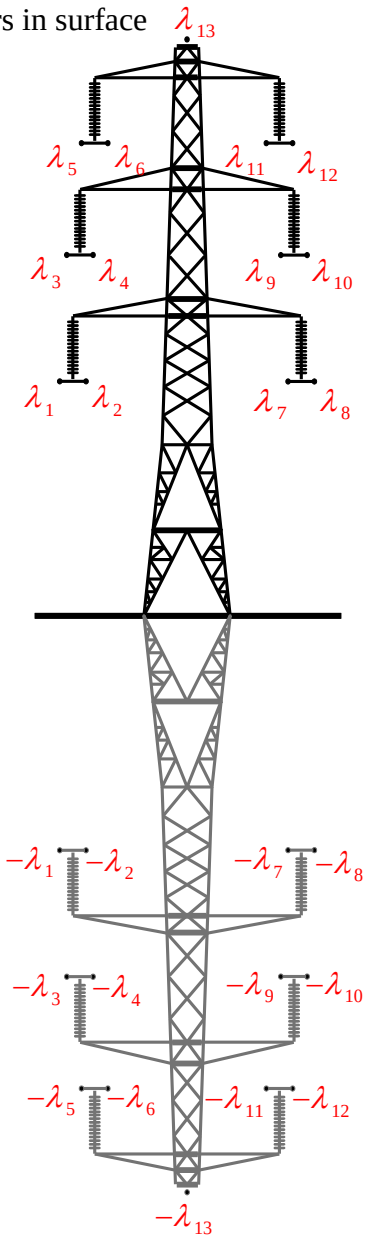

Figure 3-1 Multiple Line Charges

By this adjustment, 650 line charges rather than 1 are used to represent the surface charge distribution.

The calculation results from the original and the modified Successive Images Method are compared in Figure 3-2.

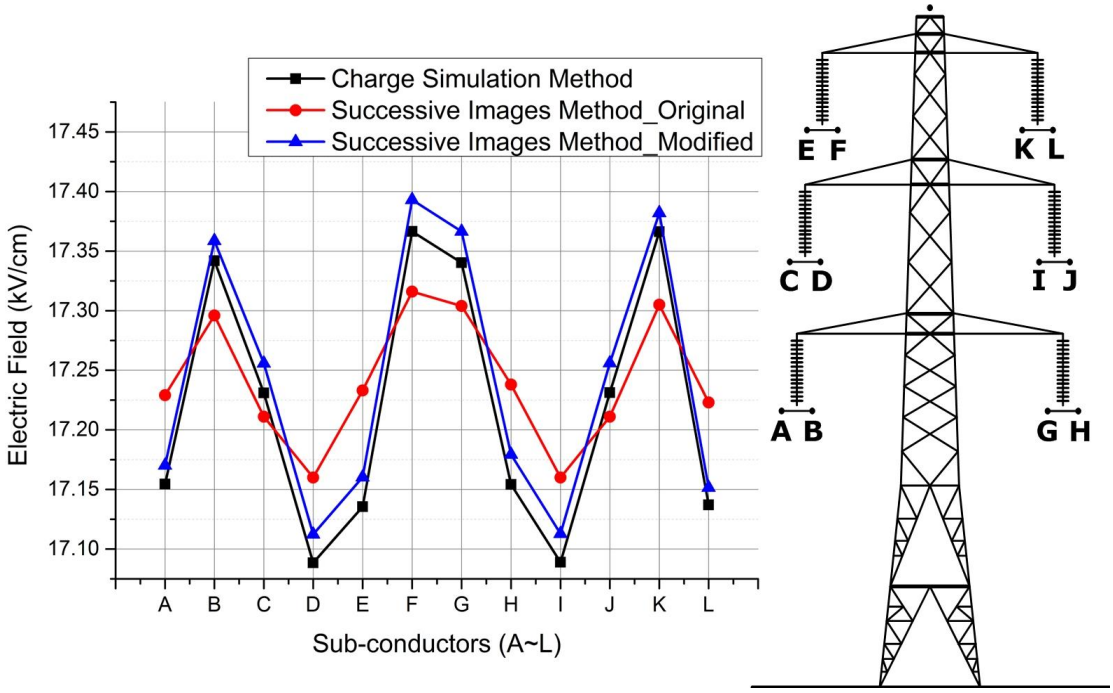

Figure 3-2 Comparison between Original and Modified Successive Images Method

The results from the Charge Simulation Method (the blue line) are used as a reference. The reason it (CSM) has been chosen as a reference method is that National Grid uses it to evaluate line noise. Results from the Modified Successive Images Method and the CSM follow the same trend for all sub-conductors. For each sub-conductor, the CSM result is about 0.01 kV/cm, or 0.06%, lower than the Modified Successive Images Method. However, for the original Successive Images Method, the result is not as close to the CSM result (with an average of 1% deviation). For sub-conductor **D**, the maximum surface gradient from the Original Successive Images Method is higher than from the CSM, while in sub-conductor **F**, the situation is reversed. In general, the Modified Successive Images Method is in closer agreement with ELECMDL for maximum gradient than with the 'Original Successive Images Method'.

3.2.2 Accuracy Analysis of Charge Simulation Method

The basic theoretical background and calculation procedure for the Charge Simulation Method were introduced in Section 2.2.5. In this section, factors which influence the accuracy of CSM and the methods employed to evaluate the degree of accuracy are discussed in detail for a specific case, L2_RUBUS. For comparison, results from the Modified Successive Images Method are treated as reference values here.

Referring to Figure 3-3, N fictitious line charges are located on a circle with radius r inside the conductor surface. As introduced in Section 2.2.5, to calculate the charge densities for those fictitious line charges, N potential reference points are introduced on the surface of the conductor. Testing points (arbitrarily distributed) on the surface of conductor are employed to examine the potential values calculated from the N fictitious line charges. The degree of agreement between calculated potential values at the testing points and the real value (the conductor voltage) is an important indicator for the accuracy of the Charge Simulation Method[29].

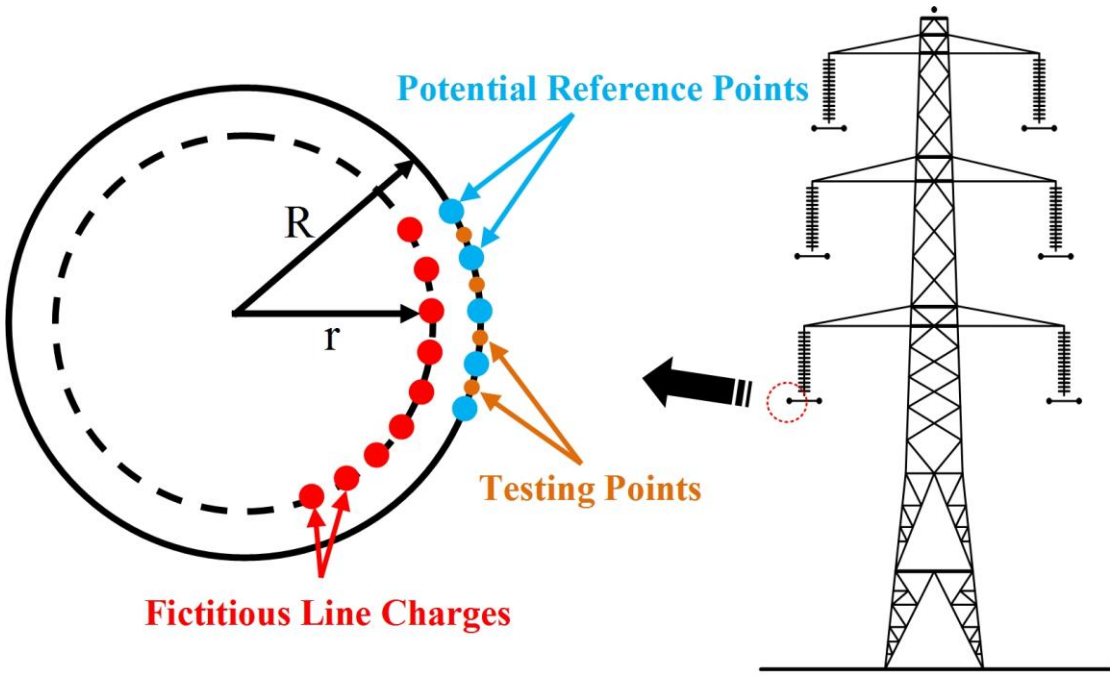

Figure 3-3 Analysis of Parameters selected for Charge Simulation Method

As illustrated in Figure 3-3, two parameters affect the calculation accuracy for the Charge Simulation Method:

- The ratio between the inner circle's radius (r) and the conductor radius (R): r / R
- The number of fictitious line charges: N

In general, the more fictitious line charges introduced, the higher the degree of accuracy obtained. However, the number N is limited by the computing power available. For example in the 'L2_RUBUS' case, a 13*N by 13*N matrix P needs to be inversed to obtain the line charge densities as:

$$[\lambda] = [P]^{-1}[U] \tag{3-1}$$

So for N=100, a 1300 by 1300 matrix needs to be inversed, and if N=1000, a 13000 by 13000 matrix must be inversed. The maximum size which can be inversed by MATLAB is limited by the size of RAM. For an 8 GB RAM PC, a matrix size of 10000 by 10000 is approximately the upper limit for computing power.

In the first study, the ratio: r / R was fixed at 0.98. N was varied from 50 to 300. As plotted in Figure 3-4, the dotted line is the voltage on the surface of sub-conductor No.1 at time 0 and is 230.94kV. It can be seen that as N increases from 50 to 300, the calculated voltage at testing points around the conductor surface tends towards the dotted line.

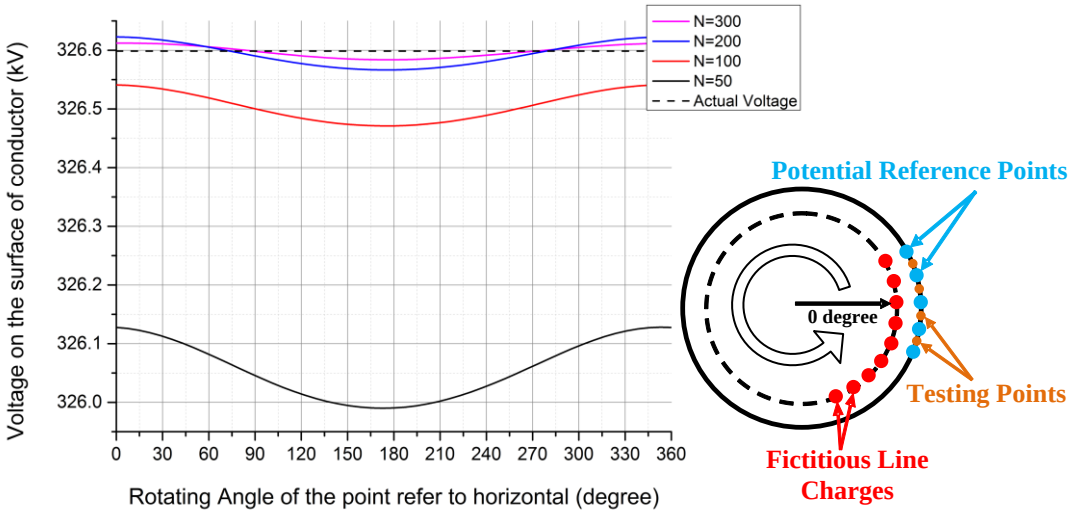

Figure 3-4 Surface potential plot with different number of fictitious line charges (CSM)

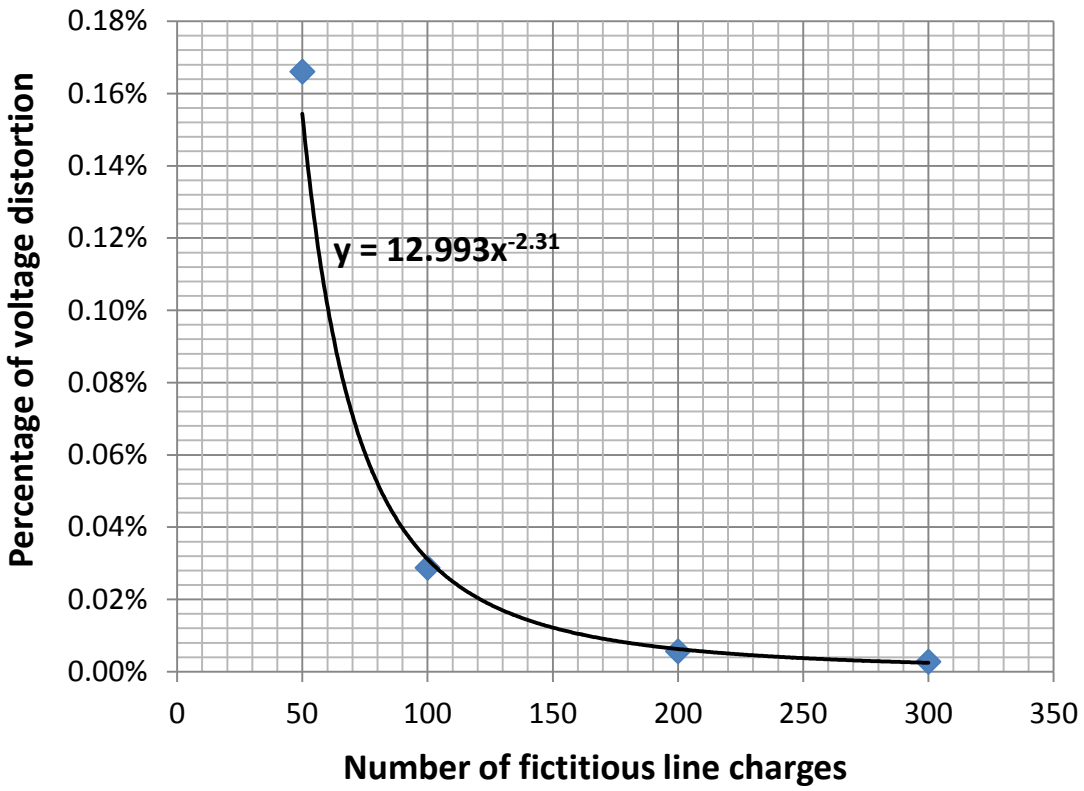

Figure 3-5 Surface potential distortion with different number of fictitious line charges (CSM)

The second study is to examine the effect of ratio *r/R*. This time, N is fixed at 300. The ratio *r/R* is varied from: 0.9 to 0.98. The dotted straight line is the actual voltage of the conductor. The degree of agreement between calculated potential value and actual conductor voltage increases with the ratio *r/R* (from 0.9 to 0.98). One exception is when *r/R* reaches 0.99, the accuracy reduced. This is explained in the later conclusion.

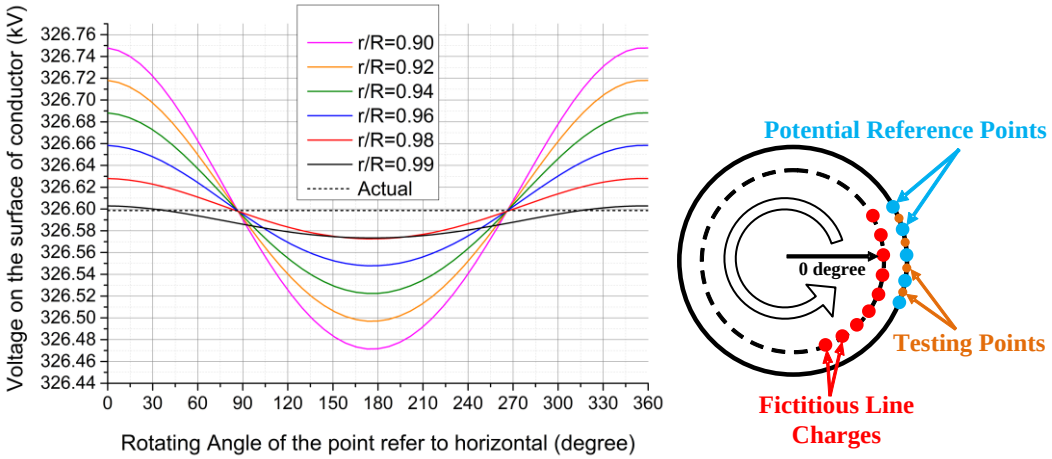

Figure 3-6 Potential plot with different positions of fictitious line charges (CSM)

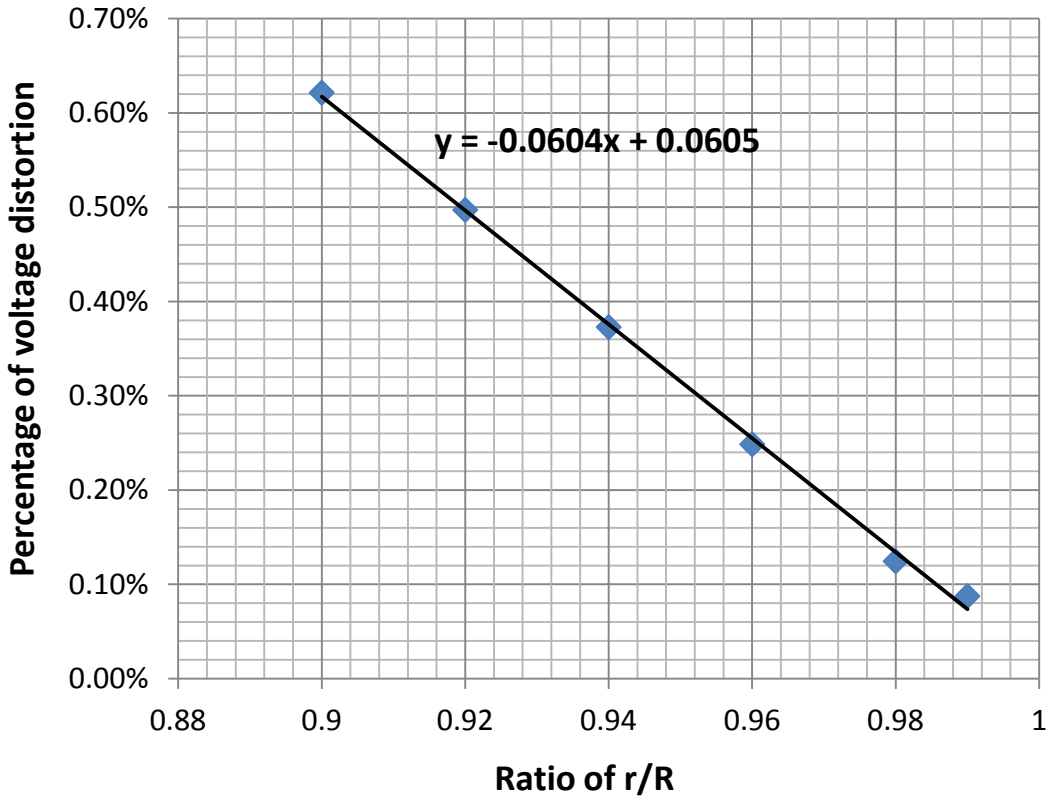

Figure 3-7 Surface potential distortion with different positions of fictitious line charges (CSM)

The results shown in Figure 3-8 are the calculated surface stresses with different parameters:

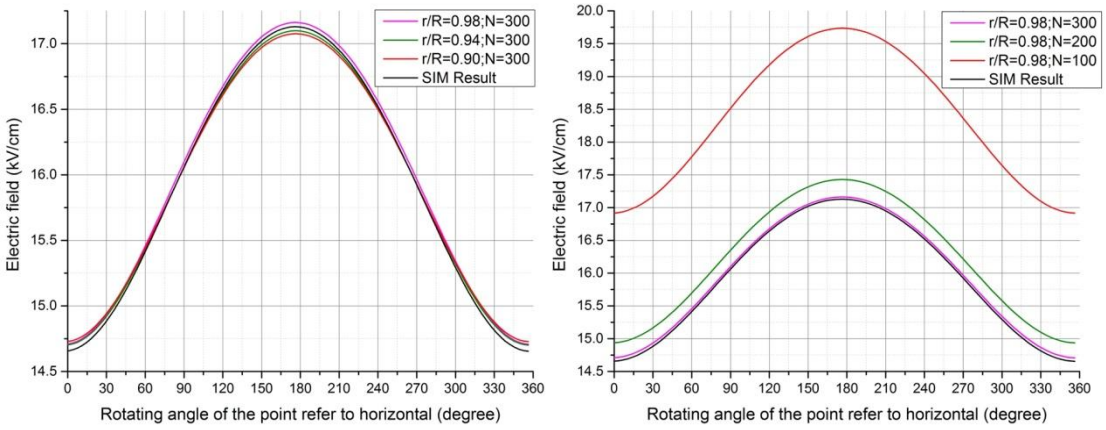

Figure 3-8 Surface Stress varied with N (left) and ratio *r/R* (right) for Charge Simulation Method

The accuracy of CSM is normally examined by the degree of fit between calculated potential values at test points and the actual conductor voltage [29]:

- By introducing more fictitious line charges (increasing N), better accuracy can be achieved: deviation of potential reduced from 0.17% to 0.003% as N increased from 50 to 300 (Figure 3-5).

- As N is increased above 200, it becomes difficult to further increase the accuracy. N=300 gives only 0.003% deviation from actual potential value (Figure 3-5).

- In general, as the ratio *r/R* is increased, a higher accuracy can be achieved (Figure 3-7). However, the 0.99 ratio gives a large error since the distances between fictitious line charges and test points are smaller than the gap between adjacent fictitious line charges. Overall, N=300 with Ratio=0.98 gives the best accuracy for CSM, with the available PC.

3.2.3 A Novel Method for Surface Gradient Calculation

As introduced in Section 2.2.1, all existing methods for transmission line surface stress calculations are based on a simplified model ignoring (as presented in Figure 5-1):

- Conductor sag
- Proximity of towers
- Uneven ground surface
- Finite ground conductivity
- Conductor stranding and protrusions such as insects and raindrops

By considering these ignored effects, a higher degree of accuracy can be achieved in surface stress calculations. By studying the calculation methods, the characteristics of the different calculation methods have been obtained and these are listed in Section 2.2.7 and Table 2-1.

As shown in Table 2-1, the different methods have different advantages in surface stress analysis. By making best use of the advantages, and bypassing the disadvantages of each, a comprehensive method which employs the CSM, the Successive Images Method and the Finite Element Method was developed.

FEM can analyze geometries with irregular shapes coupled with multi-physics fields. However it is limited by the scale of geometries it can simulate. For example, in the transmission line simulation case L2_RUBUS, the largest mesh elements an 8 GB PC can handle is 1 million. The volume of the entire simulation is approximately 80000 m^3 (40*40*50). The size of each individual mesh is approximately $(80000/10^6)^{1/3}$=0.43 m (43 cm). This result indicates that for a uniform FEA meshing, there are only 0.023 simulation elements over a 1cm length on the conductor surface. This number can be increased by using a finer mesh size at the conductor surface. However it manifests the limitation of FEA in simulating simultaneously the large and small scale transmission line environments. On the other hand, the Successive Images Method can only simulate regular cylindrical conductors with smooth surfaces and only in a relatively large scale as for L2_RUBUS. The CSM has the advantage that it can be extended to simulate the three-dimensional effect of sag.

It is possible to combine the three methods together to analyze surface stranding effects within the whole scale of the transmission line environment.

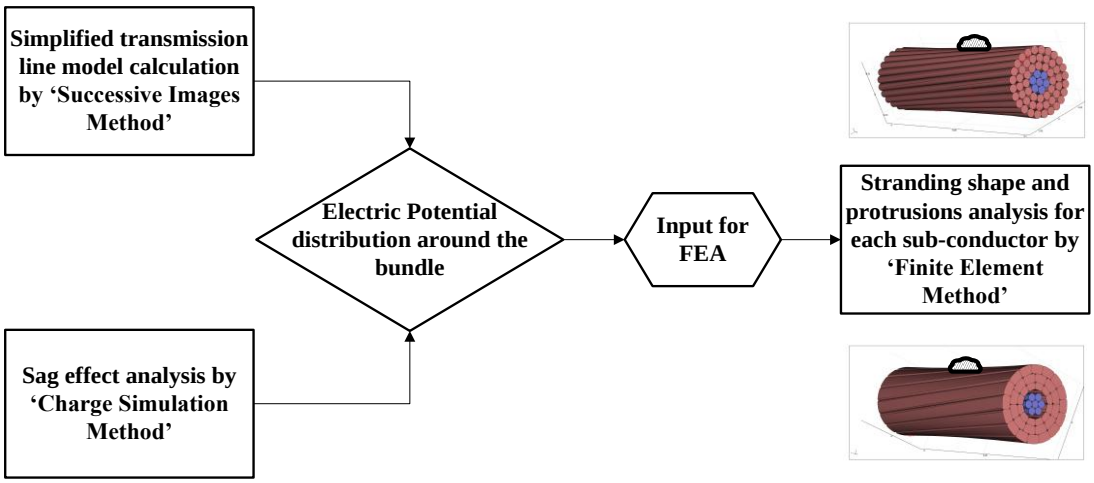

Figure 3-9 Comprehensive method for surface stress calculation

The flow chart of Figure 3-9 shows how the three methods can be combined to analyze the surface field distribution. The Successive Images Method and Charge Simulation Method are employed to calculate the electric potential distribution on a relatively large scale (a whole span of a transmission line). Within this large scale, the surface protrusion effects are negligible, so the calculation results obtained are sufficiently accurate. Once the large-scale results are obtained, a smaller domain (around a section of conductor) is extracted as a boundary condition for the FEA

process. This comprehensive process allows the FEA software to analyze the surface stress within the large scale of a transmission line environment.

For the particular case presented in Section 2.2 (L2_RUBUS), the equipotential surface surrounding a twin bundle can be obtained by either the Successive Images Method or the Charge Simulation Method. By taking a suitable potential contour as a boundary condition, it is straightforward to construct a small scale FE model using software such as COMSOL. The transmission line is then converted to a relatively small scale geometry to analyze the surface stress. Not only stranding shapes but also the effects of protrusions, dust and water droplets can be further analyzed.

As an example of the technique, the simulation result for a twin bundle in L2_RUBUS is presented in Figure 3-10. The stranding effect of the GAP type Matthew conductor has been taken into consideration in this figure.

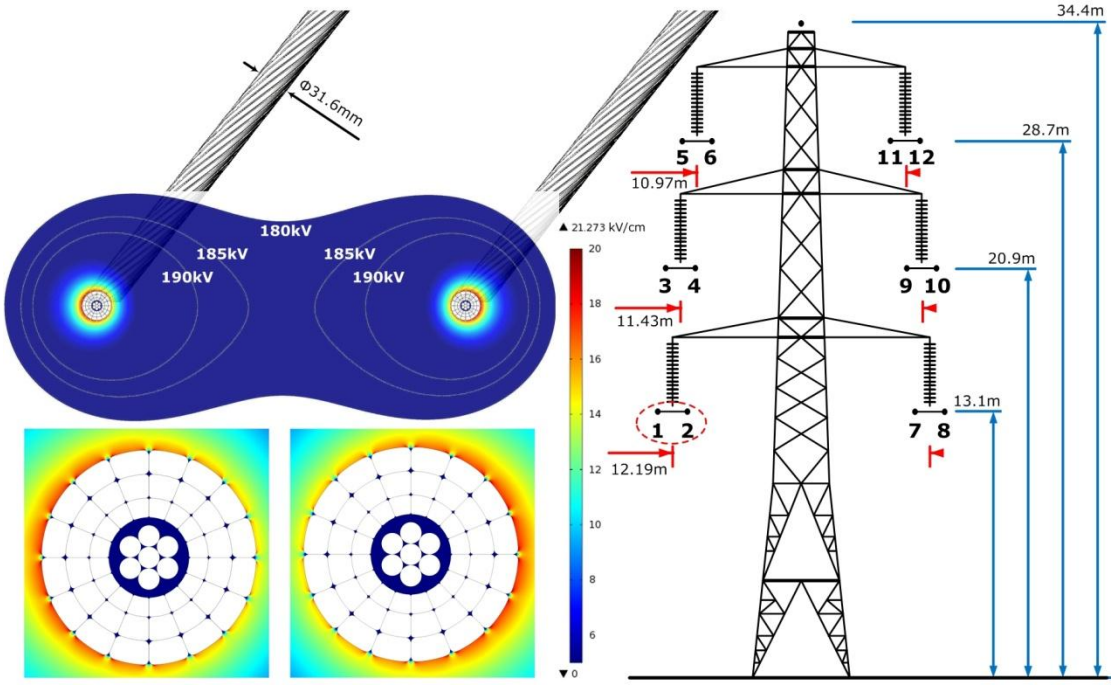

Figure 3-10 Calculation procedure for novel method

3.2.4 Meshing Techniques for FEM

In order to evaluate the surface gradient enhancement when overhead line conductors pass the supporting tower, a holistic FEA model has been constructed using commercial software to simulate the tower, insulators and conductors (Figure 3-11).

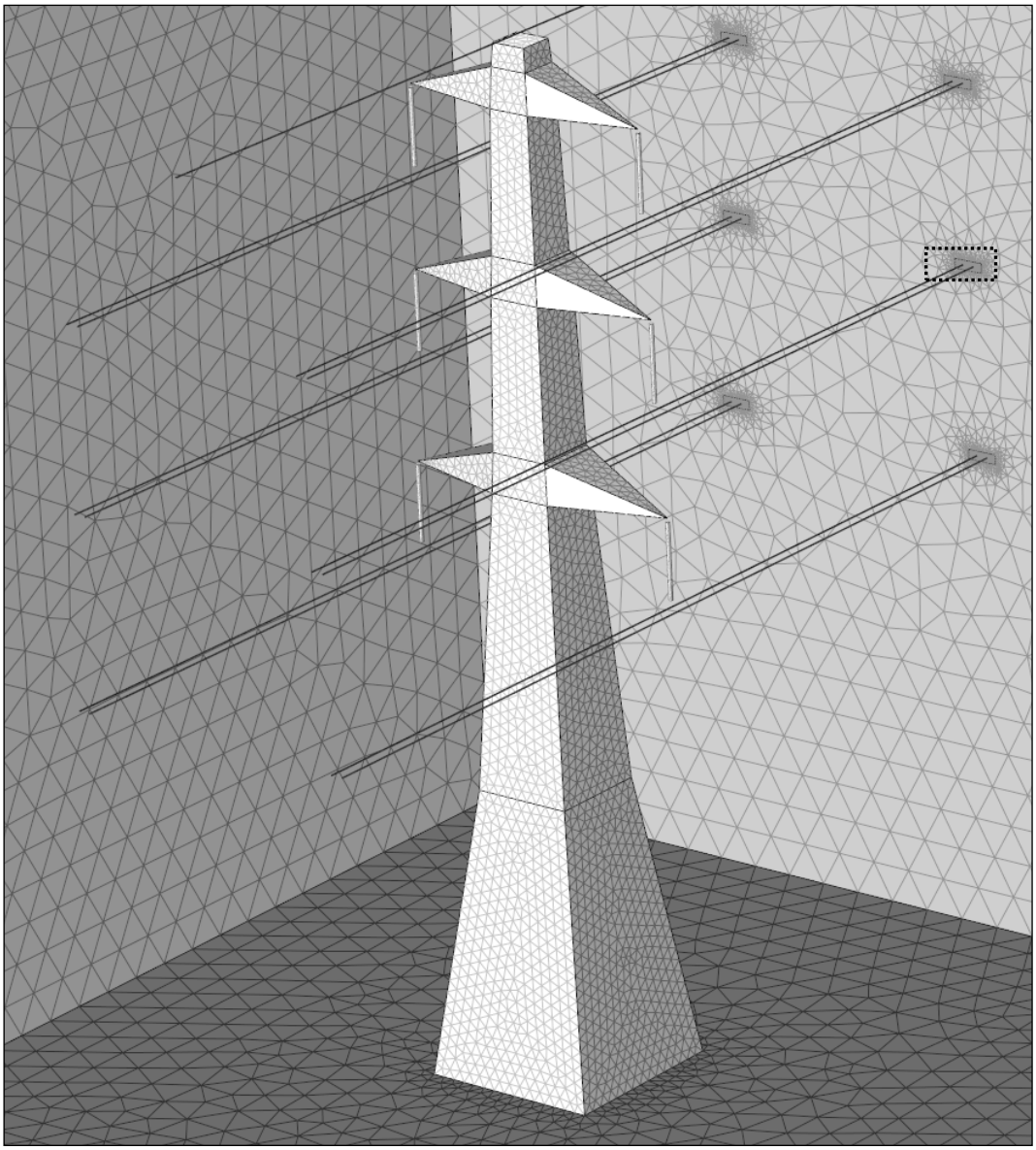

Figure 3-11 Mesh for the L2 tower

The challenge of performing holistic simulations using FEM is forming a proper strategy for mesh generation. The scale factor (μ) is defined as:

$$\mu = \frac{l_{\max}}{l_{\min}} \tag{3-2}$$

Where l_{max} and l_{min} refer to the maximum and minimum length of the geometry within the whole simulation

The minimum size within the geometry is set by conductors which have a diameter of 3.2 cm while the maximum size is the tower structure which is about 40 m tall. This results in a scale factor of more than 1000.

A large scale factor requires a large computing memory in order to obtain an accurate result. This issue is addressed by combining structured and unstructured mesh and controlling the growth rate of the mesh layer around the overhead line conductors, as shown in Figure 3-12.

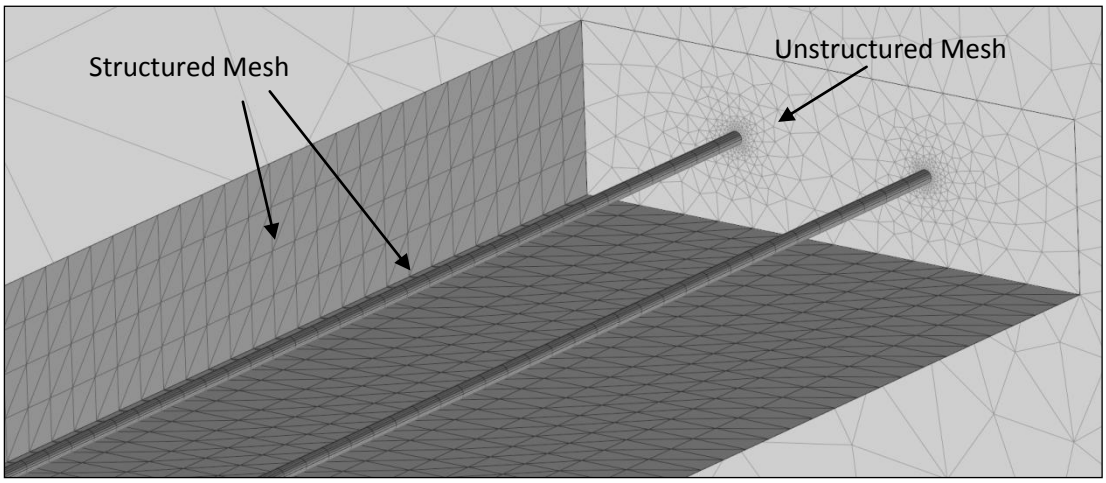

Figure 3-12 Zoom in view of L2 tower mesh

Meshing details for this simulation are listed in Table 3-1.

Table 3-1 Mesh Statistics

Element Type	Element Number	Domain Mesh Parameter	Statistics
Tetrahedral Elements	1745046	Number of elements	4700846
Pyramid Elements	233000	Mesh volume	80000.0 m^3
Prism Elements	2722800	Maximum growth rate	10.68
Triangular Elements	267350	Average growth rate	1.584
Quadrilateral Elements	130000		
Edge Elements	43194		
Vertex Elements	234		

3.3 Results and Discussion

3.3.1 Case Study for National Grid 400 kV OHL (L2)

A specific transmission line configuration—'L2 RUBUS'—was selected as a standard model to compare the results of the different calculation methods introduced in Section 2.2.

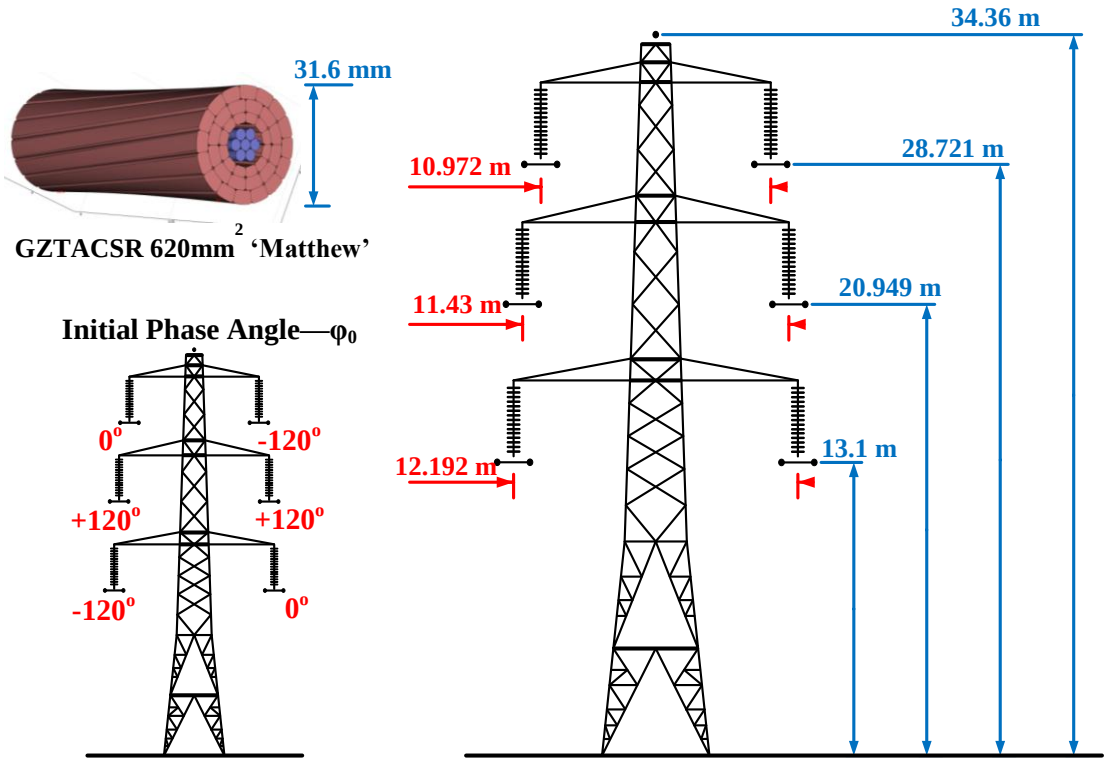

Figure 3-13 Parameters for L2 tower

'L2 RUBUS' as presented in Figure 3-13 is a specific configuration which National Grid received complaints about due to excessive audible noise. It is a double circuit twin-bundle line with GAP-Type Matthew conductor. The phase arrangement is relatively complex as not only is the transposed phase arrangement used, but also the un-transposed arrangement is employed. The effect of different phase arrangements on surface field strength will be discussed in the next Chapter. Within this case study, the phase arrangement shown in Figure 3-13 has been assumed. As introduced previously, Maxwell's Potential Coefficient Method is limited to calculations for a single conductor transmission line system, and so it will not be used or compared with the others here.

The Markt and Mengele's Method, Successive Images Method, Charge Simulation Method, and National Grid's software method are tested here for comparison. As surface stress varies through the power cycle in a sinusoidal manner, the variation of the surface field strength has first been analyzed through a 0.02 second cycle. The surface stress of the left sub-conductor of the bottom left-hand bundle, 'A', is plotted in Figure 3-14. The calculation results show a close agreement between the Successive Images Method and the Charge Simulation Method, both of them being relatively accurate numerical methods. The analytical Markt and Mengele's Method has a similar average result but shows less variation around the circumference in comparison with the other two methods.

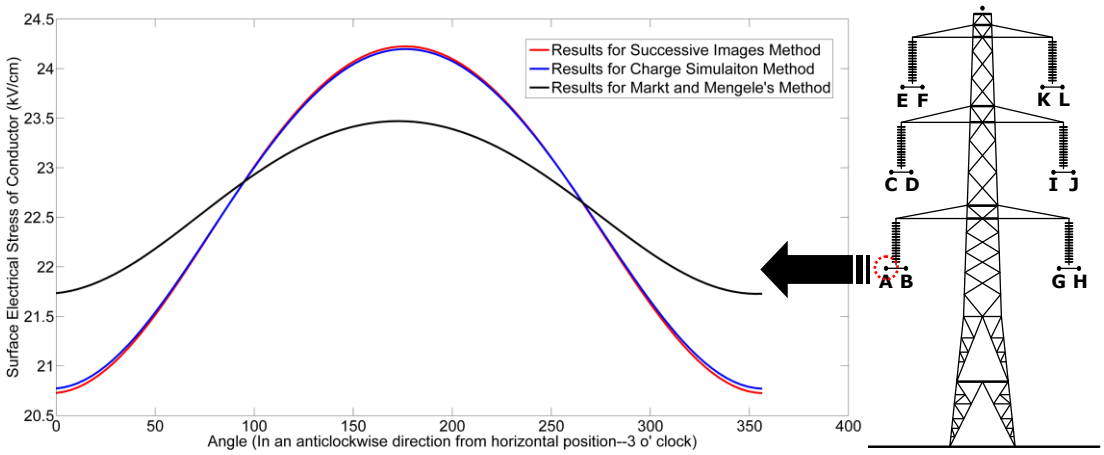

Figure 3-14 Configurations of 'L2 RUBUS' from National Grid

The surface stresses of the rest sub-conductors (conductors 'B~M' as named in Figure 3-14) at time t=0 (phase angles shown in Figure 3-13) are presented from Figure 3-15 to Figure 3-26. The highest field strengths are found in the left bottom bundle and the right top bundle at this instant in the cycle. Inverted profiles can be seen for the other sub-conductor within each bundle. This effect occurs because charges with the same polarity repel each other and consequently the highest charge density on the surface of each sub-conductor is always located further away from the centre of the bundle. As surface charge density defines electric field strength, the highest field strength can always be found at position furthest from the centre of the bundle. However, the profiles for the two sub-conductors within the same bundle are not symmetrically reversed as their maximum surface stress is different. The small variation of maximum surface stress is caused by the other conductors outside the bundle.

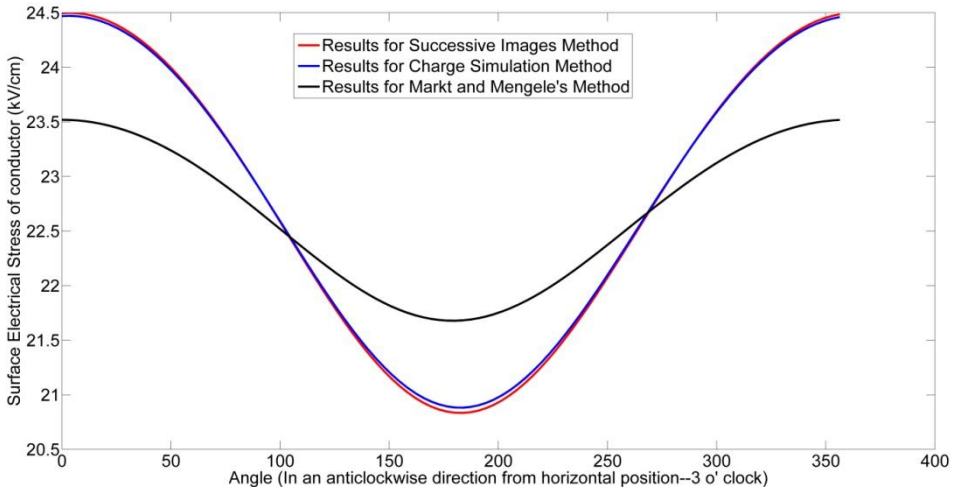

Figure 3-15 Surface electric field for conductor 'B' (named in Figure 3-14) at ‘time 0’

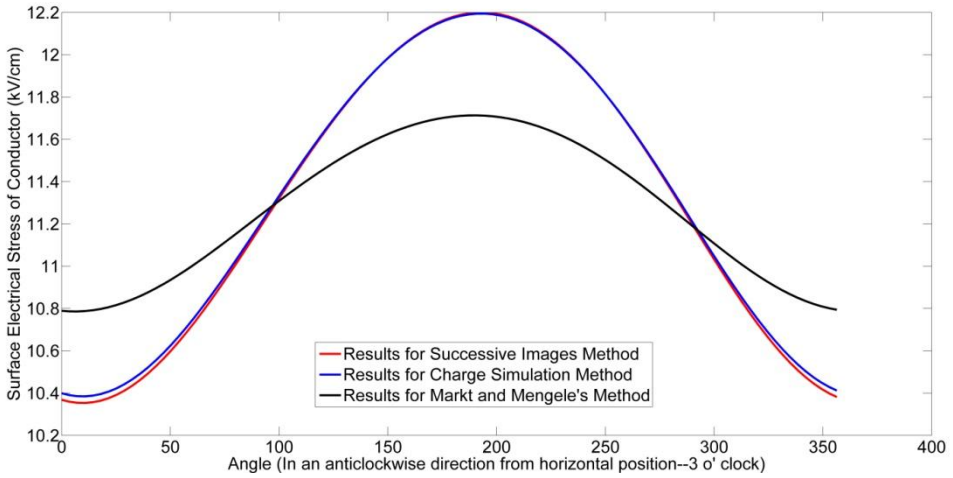

Figure 3-16 Surface electric field for conductor 'C' (named in Figure 3-14) at ‘time 0’

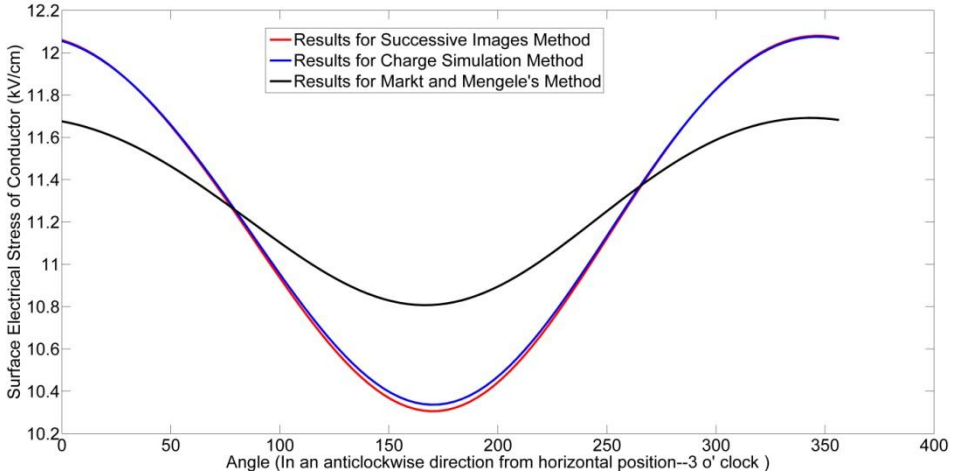

Figure 3-17 Surface electric field for conductor 'D' (named in Figure 3-14) at ‘time 0’

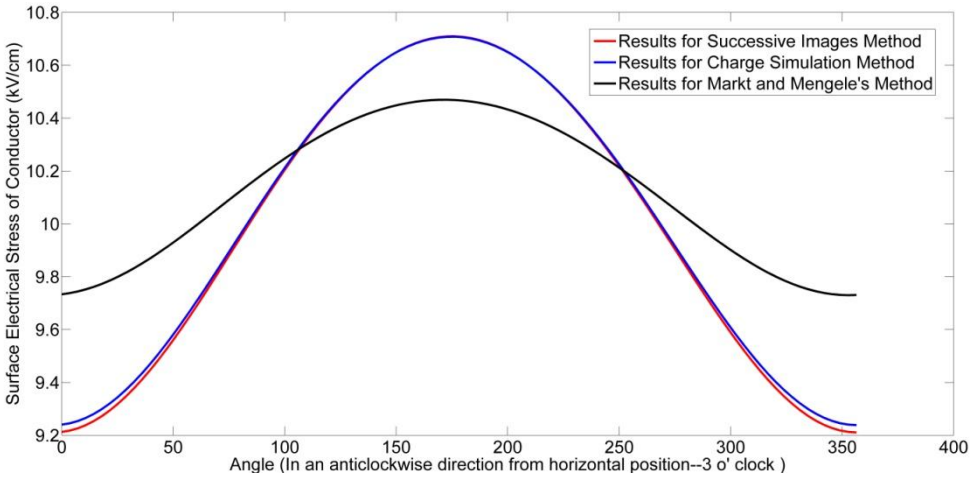

Figure 3-18 Surface electric field for conductor 'E' (named in Figure 3-14) at ‘time 0’

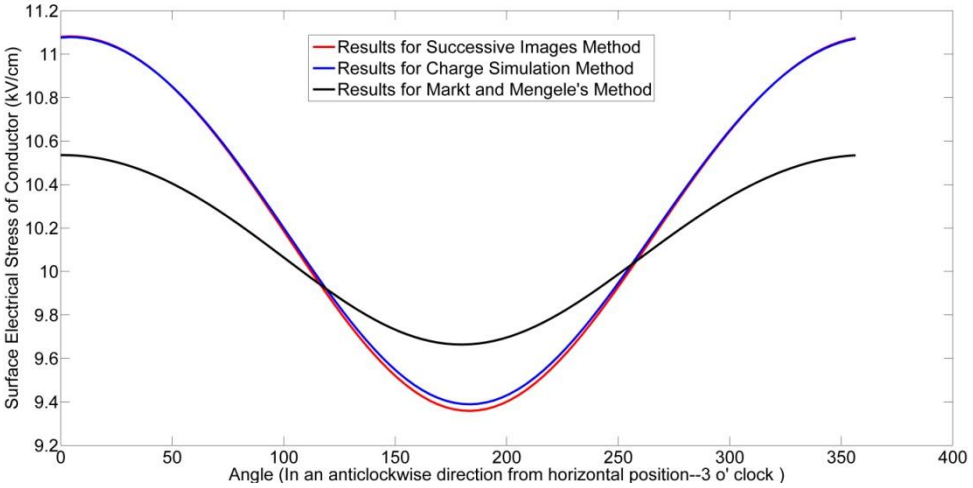

Figure 3-19 Surface electric field for conductor 'F' (named in Figure 3-14) at ‘time 0’

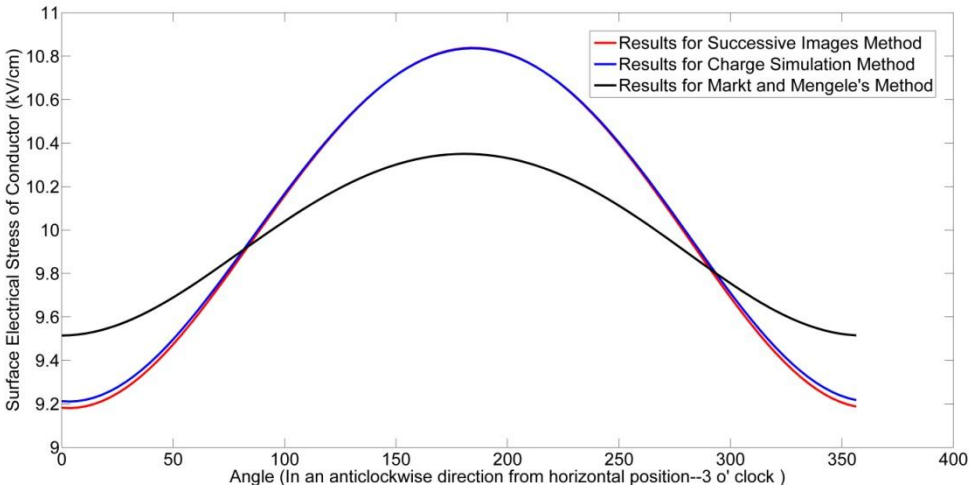

Figure 3-20 Surface electric field for conductor 'G' (named in Figure 3-14) at ‘time 0’

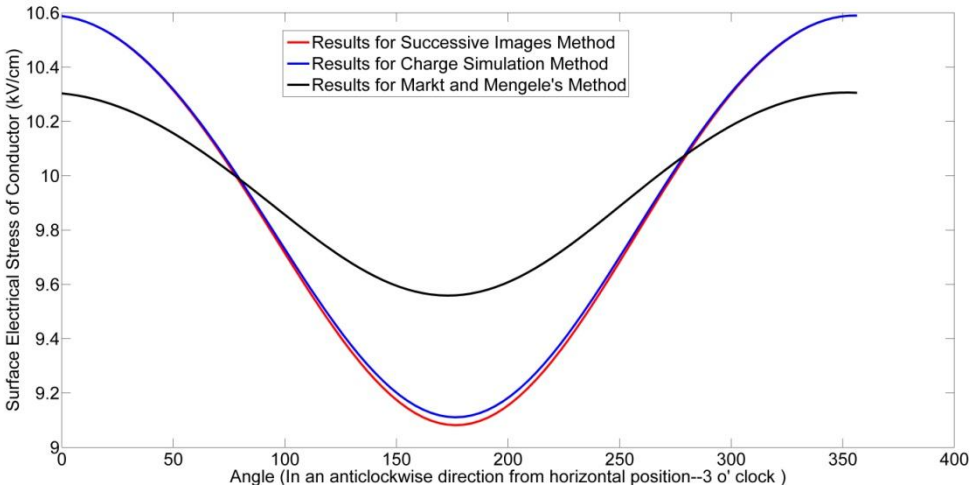

Figure 3-21 Surface electric field for conductor 'H' (named in Figure 3-14) at ‘time 0’

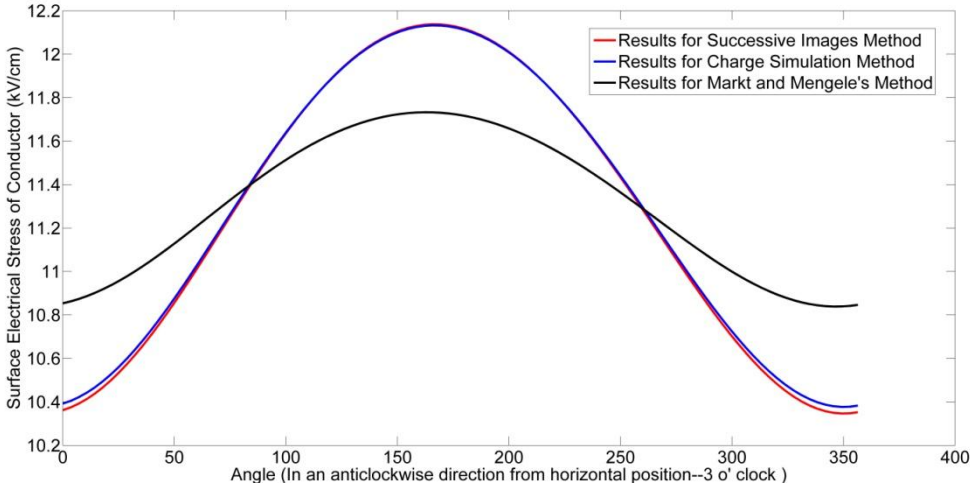

Figure 3-22 Surface electric field for conductor 'I' (named in Figure 3-14) at ‘time 0’

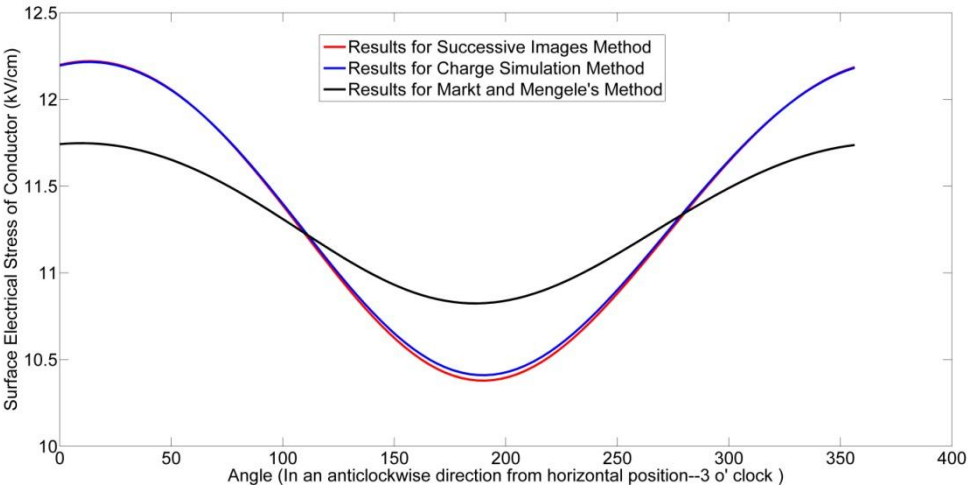

Figure 3-23 Surface electric field for conductor 'J' (named in Figure 3-14) at ‘time 0’

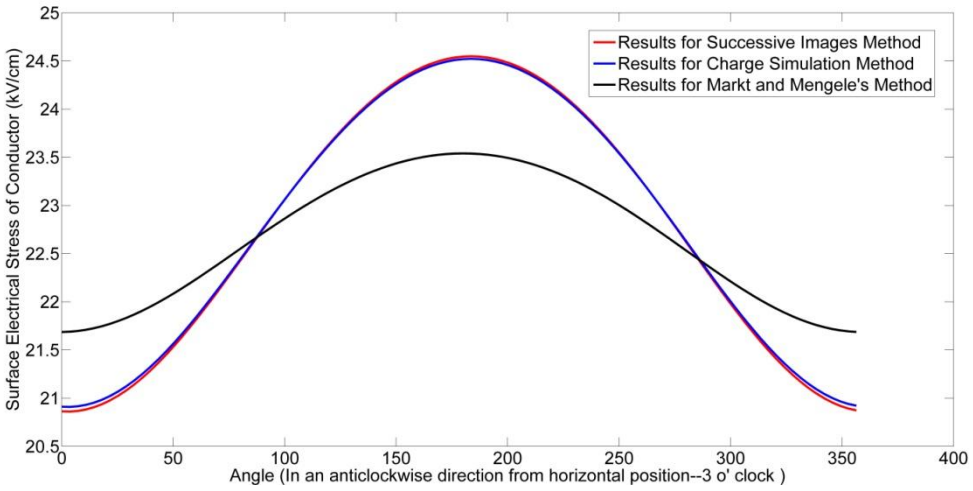

Figure 3-24 Surface electric field for conductor 'K' (named in Figure 3-14) at ‘time 0’

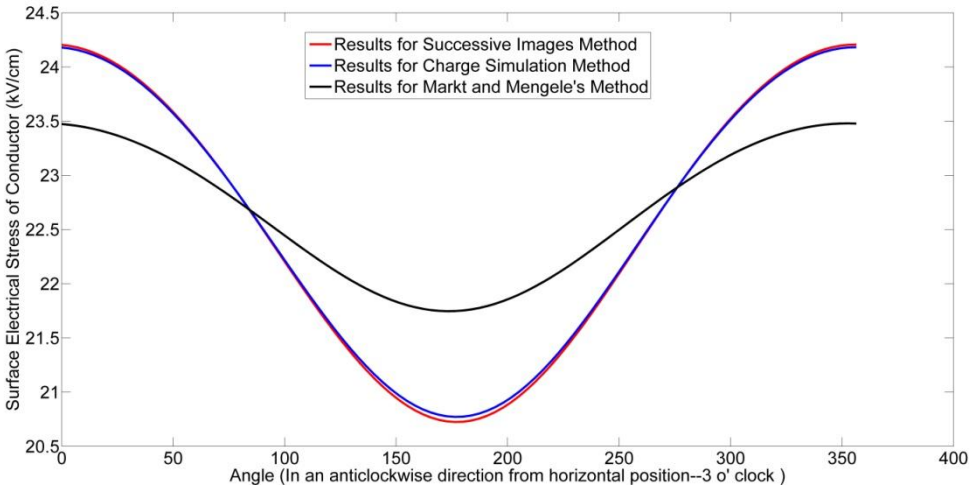

Figure 3-25 Surface electric field for conductor 'L' (named in Figure 3-14) at ‘time 0’

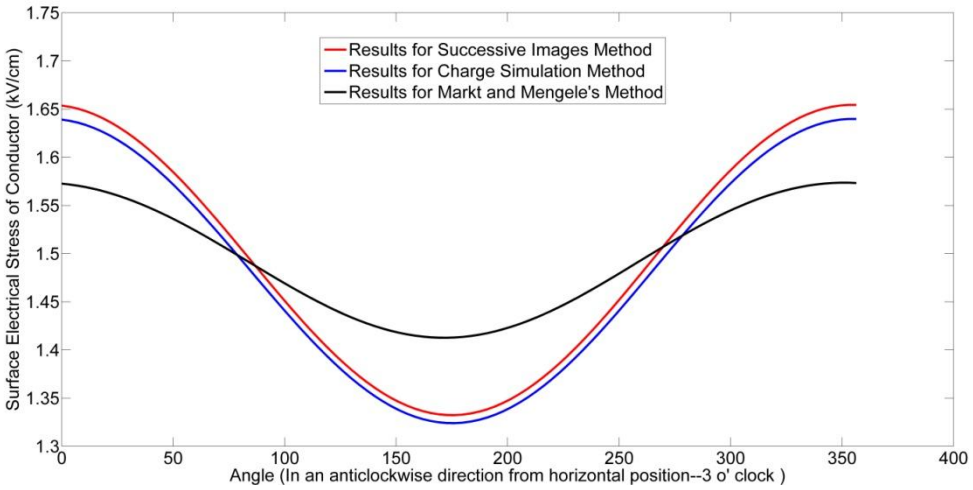

Figure 3-26 Surface electric field for conductor 'M' (named in Figure 3-14) at ‘time 0’

The surface stress profile varies with time in a sinusoidal shape and is presented in the 3D plot of Figure 3-27. The X-axis represents time from 0 to 0.02s with 200 steps. The Y-axis refers to the 100 points selected around the surface and the Z-axis is the surface electrical stress in kV/cm. Two contour surfaces (Z=±22 kV/cm) are employed as a reference plane.

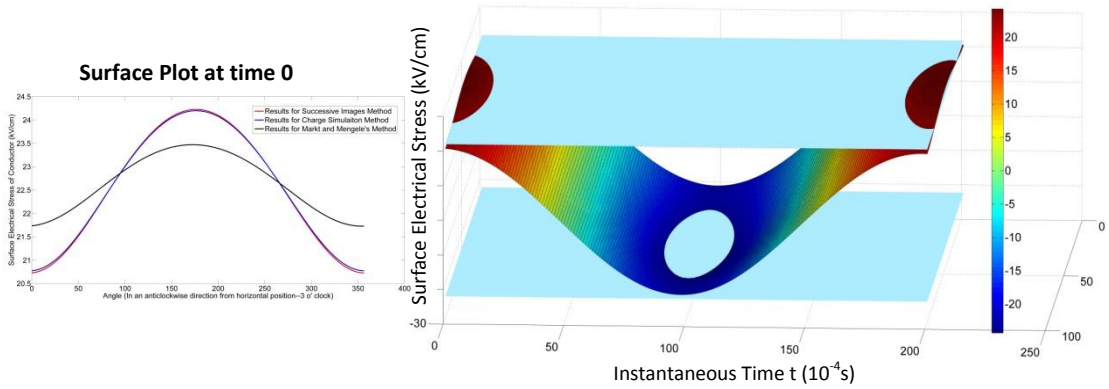

a b

Figure 3-27 surface stress variation with time: a). surface electric field plot at 0s; b). 3D plot for a cycle

This 3D plot contains the stress profile around the conductor surface for a whole cycle. For each sub-conductor, the RMS value of surface potential gradient can be obtained by integrating the instantaneous surface gradient value with respect to time for the whole cycle. In Figure 3-28, the point at the 180^{o} position on the surface has been selected to plot the stress variation through a cycle (red curve). The RMS value (blue line) has been calculated as:

$$E_{RMS} = \sqrt{\frac{\int_0^{0.02} \left(E(t)\right)^2 dt}{0.02}} \qquad (3\text{-}3)$$

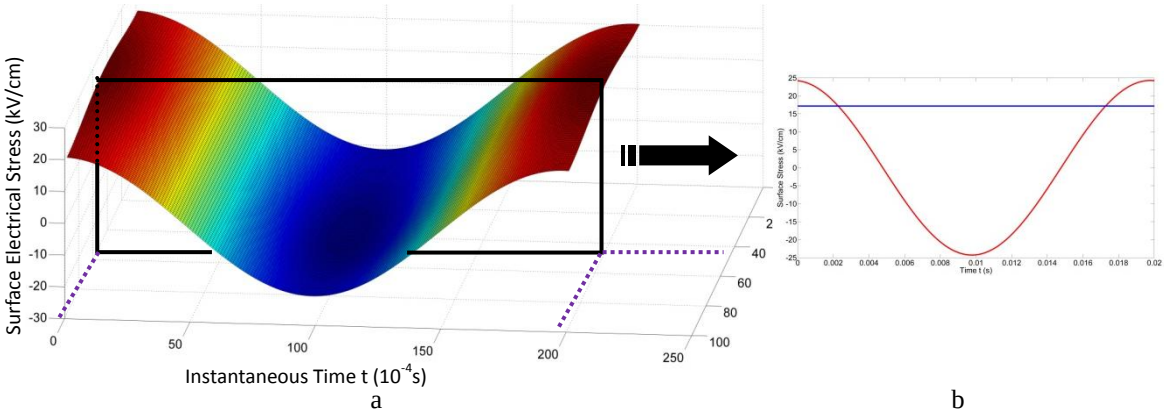

a b

Figure 3-28 procedure to compute rms value: a). 3D field variation during one cycle; b). cut plot of a).

For each conductor, the RMS values for electric stress around the surface can be obtained by the same process. The maximum RMS value, also known as the Maximum RMS Surface Gradient, exists at a certain point on the surface. The Maximum Surface Gradient is a critical parameter because it reflects the intensity of undesired effects in overhead lines, such as: Radio Interference, Corona Loss and Audible Noise. This parameter is also employed here to compare the results from different calculation methods.

As presented in Figure 3-29, one analytical method (Markt and Mengele's Method), two numerical methods (Successive Images Method and Charge Simulation Method), and one software method (ELECMODL) have been studied and the 'Maximum Surface Gradient' (RMS) for each is compared. The line graph in Figure 3-29 describes the maximum gradient for sub-conductors No.1 to No.12. The plot (Figure 3-29) shows that sub-conductors **B**, **F**, **G**, and **K** sustain higher surface stresses while sub-conductors 4 and 9 create lower stresses. The points are joined by lines in this figure to illustrate the consistent relative behaviour of the models.

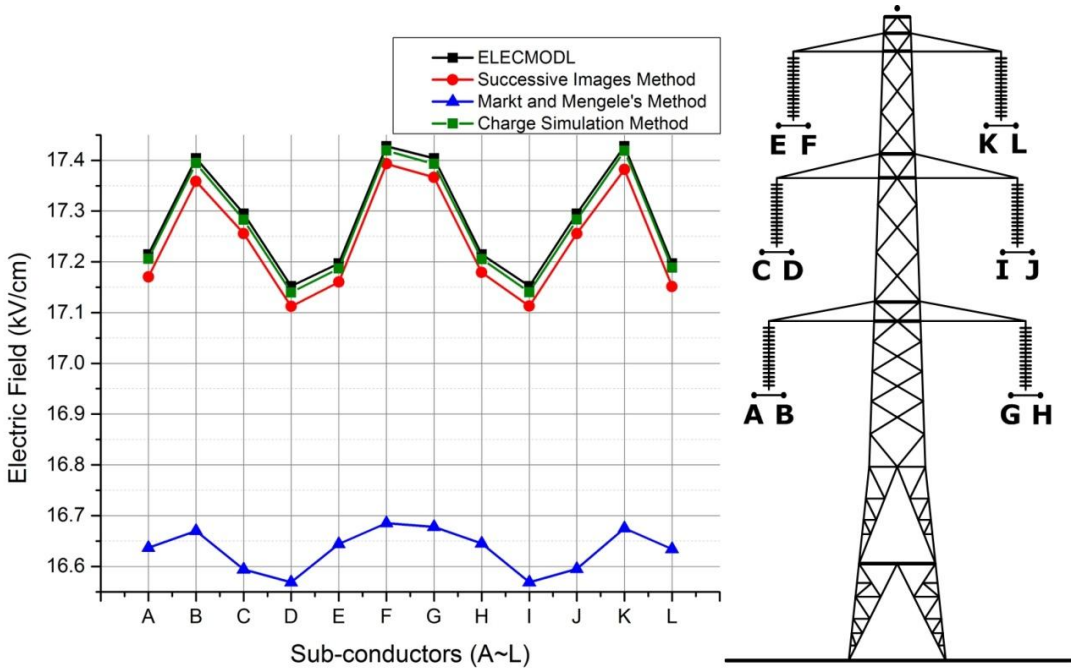

Figure 3-29 'Maximum Surface Gradients' for different methods

When comparing the different methods, the Markt and Mengele's Method generated a relatively lower value of surface stress compared to the other methods. This inaccuracy is due to neglecting non-uniform charge density on the surface of each

sub-conductor. Both the Successive Images Method and the Charge Simulation Method are classified as numerical methods, and employ iterative processes to approach an accurate solution. As in Figure 3-29, the three lines are following consistent trends, and the difference for each conductor is tolerable (being under 0.05 kV/cm which is around 0.3%). This leads to the conclusion that both the Successive Images Method and the Charge Simulation Method can generate sufficiently accurate results for a simplified calculation in transmission lines system.

3.3.2 Effect of Stranding Shape

With the advance of manufacturing techniques, various types of conductor have been created to fulfil the needs of modern power systems. For example, trapezoidal shaped strands achieve a higher fill factor (as shown in Figure 3-30), and are more efficient in current transmission compared to traditional round strands. The increasing use of trapezoidal shaped conductors pushes the need to study the surface gradient because all previous models have used heuristics based on circular strand cross-sections.

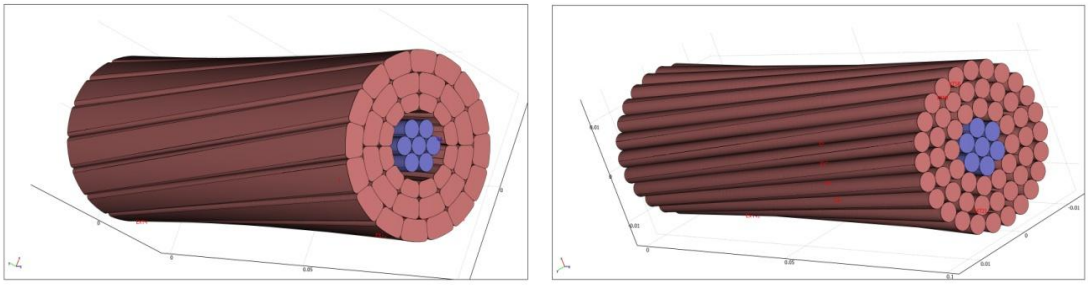

a b

Figure 3-30 GZTACSR ‘Matthew’ (a) and ACSR ZEBRA-260 (b) for 400 kV OHL

As introduced previously, existing methods for surface gradient calculations ignored the shape of the strands. A cylinder was employed to represent all types of overhead line conductors. In order to obtain more information on surface gradients for different shapes of strand, a novel method developed here is applied to a typical tower configuration, L2 (Figure 3-13). The left sub-conductor (conductor 'A' in Figure 3-14) is analyzed. Internal strands are not considered in this simulation, illustrated in Figure 3-31, only the external surface geometry is modelled.

From the electric field plot along the surface of the conductor, the following conclusions can be obtained:

- The round stranded conductor has a higher maximum surface gradient compared to a trapezoidal stranded conductor
- The maximum electric field for a trapezoidal shaped strand is located at the corners while the maximum electric field for a round shape strand is located at the tip of the circle furthest from the conductor centre
- On the circumference of a conductor fabricated with trapezoidal strands, there are large continuous lengths with approximately same surface voltage gradient
- On the surface of the round strands, the surface gradient varies along the strand surface and there is no continuous area with same voltage gradient

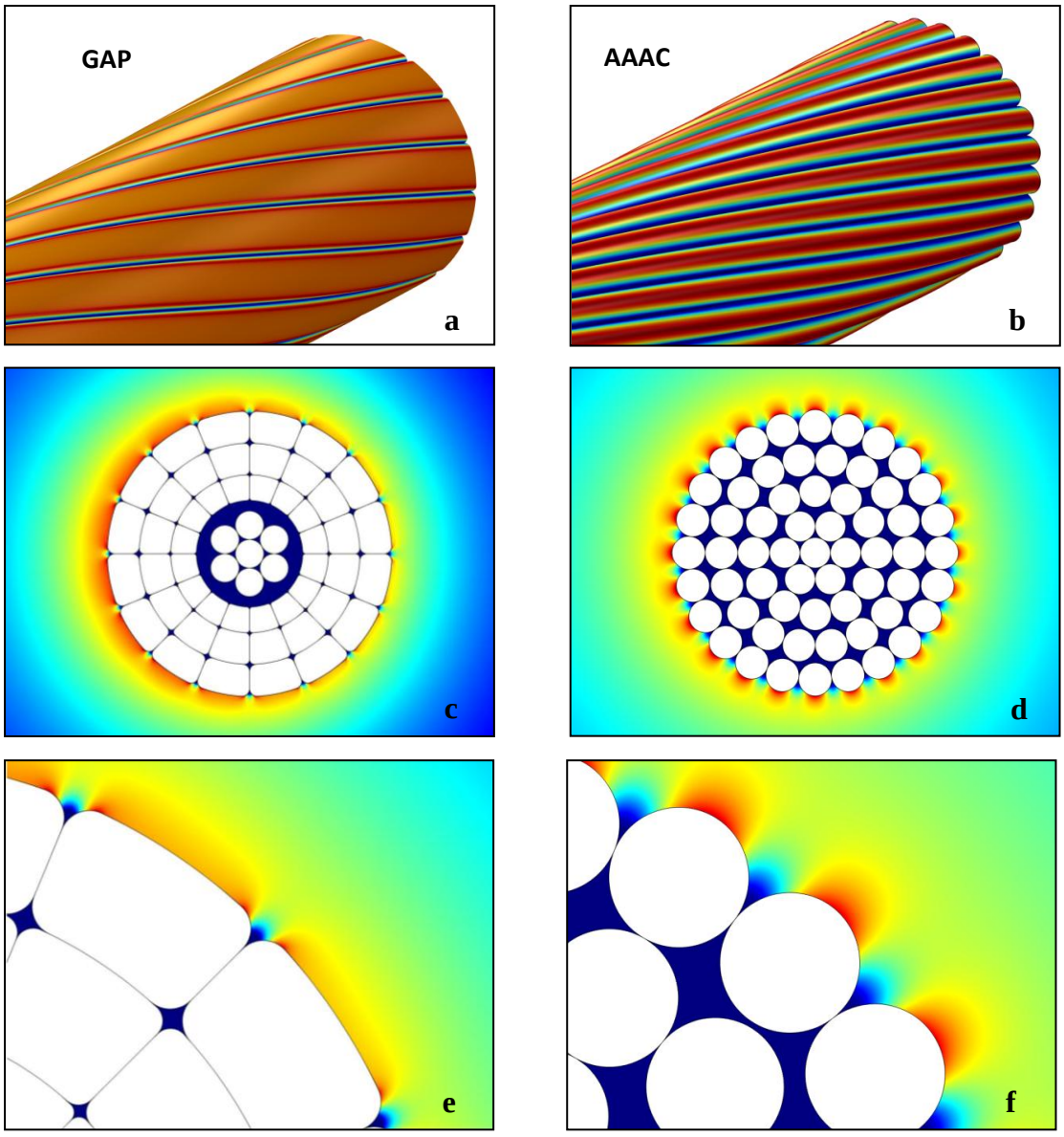

Figure 3-31 Trapezoidal strands (GAP) and round strands (AAAC) comparison (a, c and e are plots for the segmented strand case while b, d and f are plots for the round strand case)

In Figure 3-32, the arc length along the edge of conductor strands is chosen to represent the surface distribution of electric field. The horizontal axis refers to the electric field strength and the vertical axis represents the integrated arc length which has a surface gradient value above a certain level. If 16 kV/cm is selected (dashed line in Figure 3-32) as a typical level to examine the field distribution, the trapezoidal stranded conductor has approximately 88 mm circumference above this level while the round stranded conductor has about 59 mm circumference above 16 kV/cm. If a higher level of electric field is selected as the threshold, take 20 kV/cm as an example, the round stranded conductor has a larger area above this value than the trapezoidal stranded one.

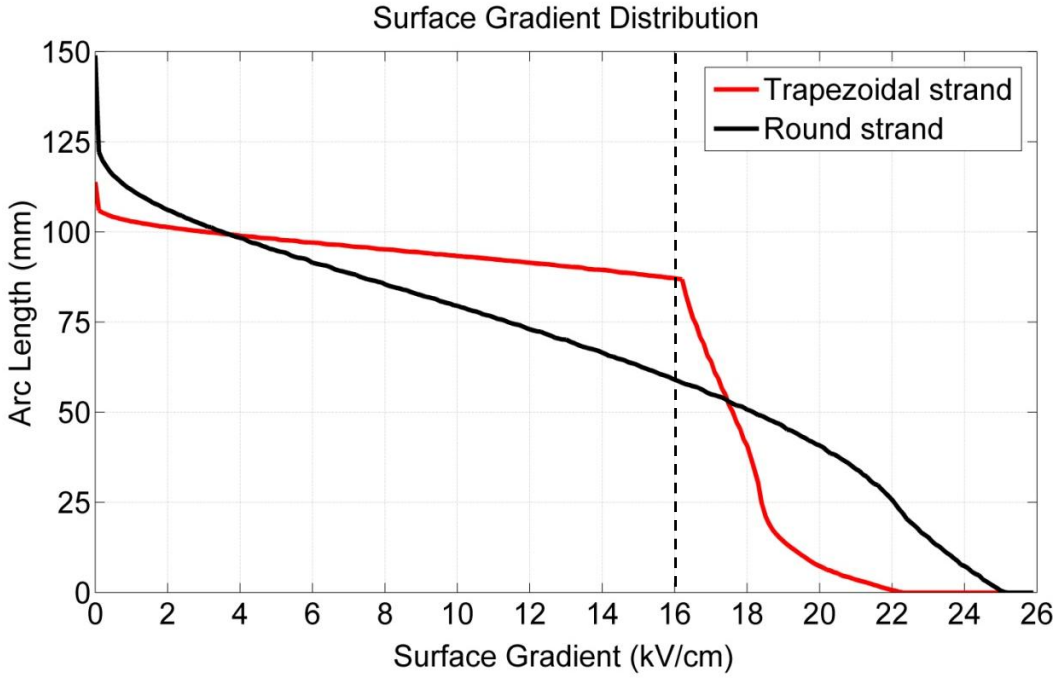

Figure 3-32 Arc length with surface gradient above a certain level

3.3.3 Effect of Protrusions

Figure 3-32 described the circumferential length above a threshold value of voltage gradient. The next step is to decide the threshold value to be considered important.

A hemispherical protrusion is introduced to the existing model to compute the enhancement of electric field. As presented in Figure 3-33, when a protrusion is applied to the surface of the conductor, the local electric field is increased due to the relatively large curvature created by the protrusion. This field enhancement is not

only determined by the shape and size of the protrusion but also depends on the location of the protrusion.

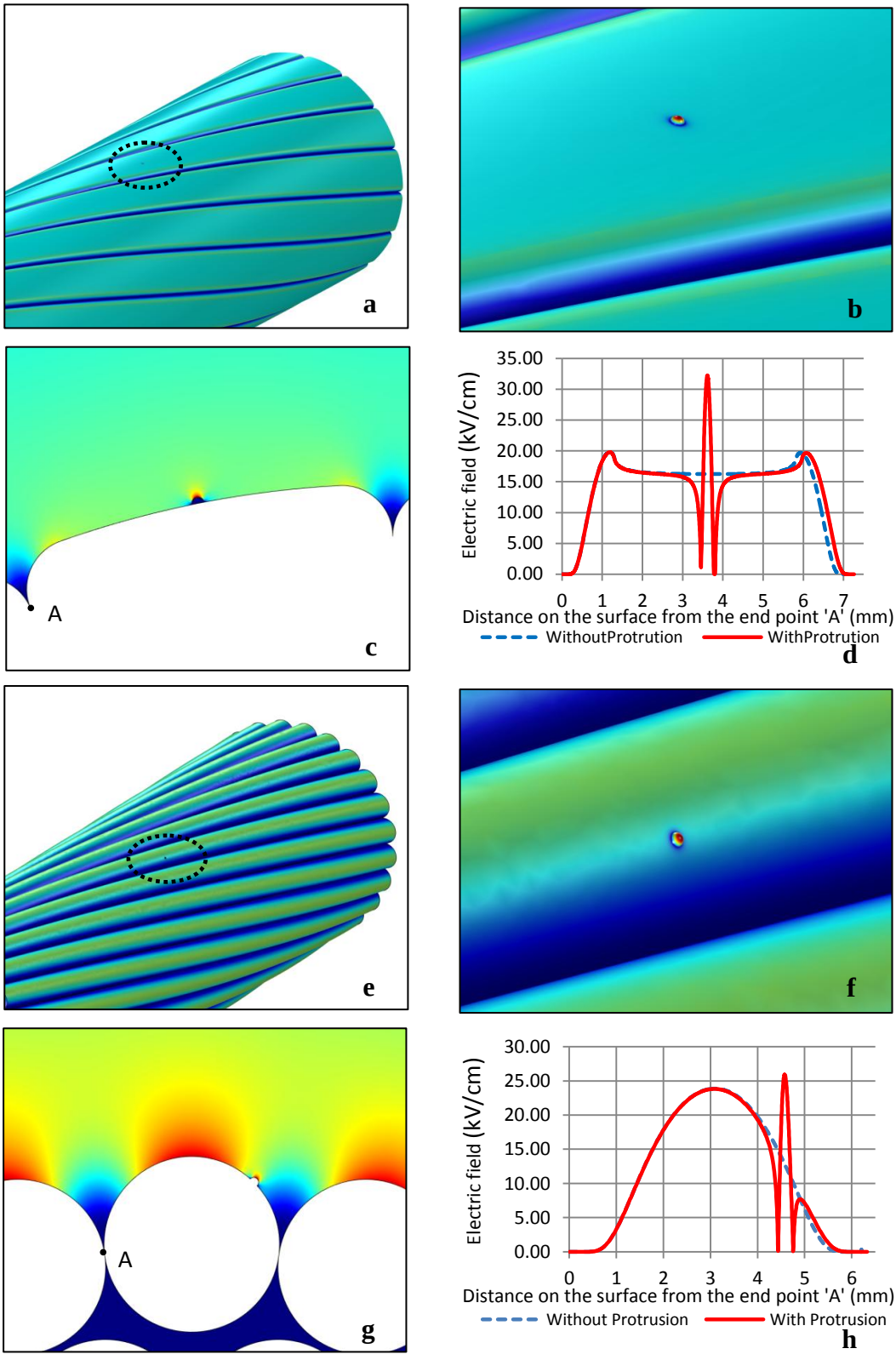

Figure 3-33 Protrusions on different types of conductors (a~d: colour plots and field plot for trapezoidal stranded conductors; e~h: colour plots and field plot for round stranded conductors)

A hemispherical protrusion with a range of sizes (radius: 10um, 50um, 100um and 200um) was applied on both trapezoidal strands and round strands. The finite element method was employed to evaluate the electric field enhancement. By varying the location where the protrusion sits, the relationship between surface gradient with protrusion and without protrusion was established in Figure 3-34 and Figure 3-35. The distorted curve in Figure 3-35 is mainly due to numerical errors.

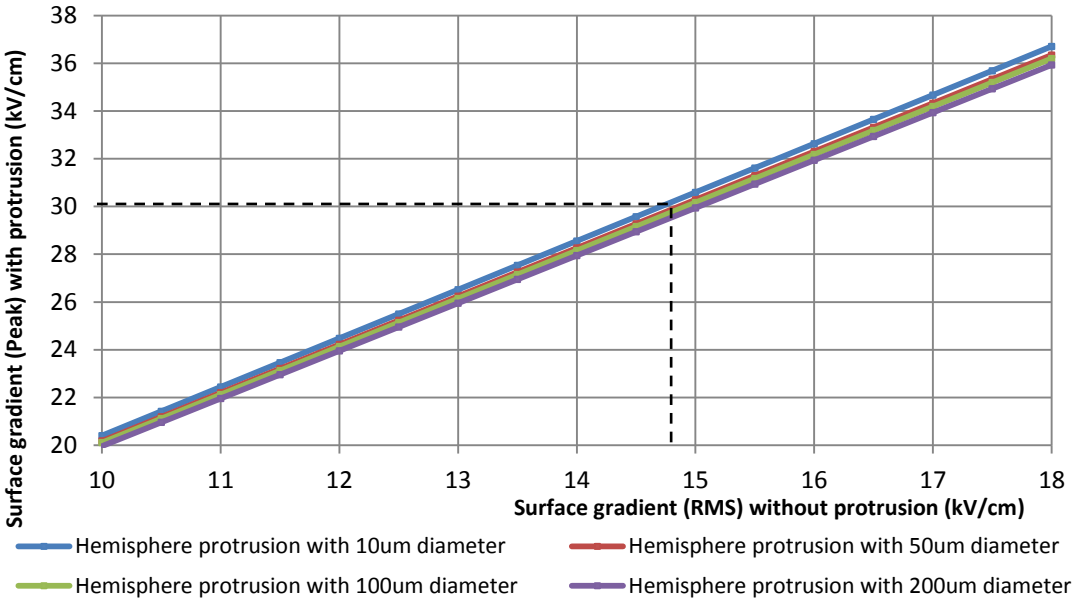

Figure 3-34 Surface Gradient Enhancement by protrusion for Trapezoidal Stranded Conductor

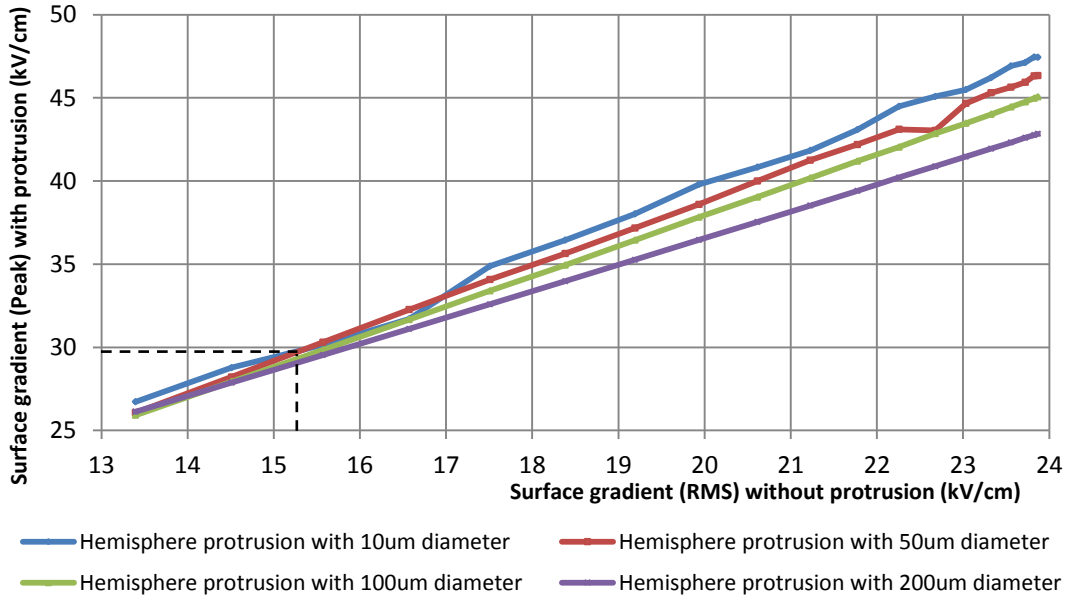

Figure 3-35 Surface Gradient Enhancement by protrusion for Round Stranded Conductor

Here it is assumed that corona is initiated when the local stress exceeds 30 kV/cm. From Figure 3-34 and Figure 3-35, if the worst scenario was considered (the surface gradient with protrusion achieves 30 kV/cm), the threshold value for surface gradient without a protrusion is marked by a dashed line (14.7 kV/cm for trapezoidal strands and 15.3 kV/cm for round strands). Referring to Figure 3-32, the critical surface arc length for trapezoidal shape strands is approximately 88 mm while the critical surface arc length for round shape strands is approximately 62 mm.

3.3.4 Field Enhancement Caused By the Proximity of Tower

When overhead line conductors pass a metallic structured tower, the electric field on the surface of conductors is enhanced due to the short distance to ground potential (tower). In order to evaluate this effect, a novel finite element model has been built, taking into consideration tower shape, insulator strings, and conductor bundles.

a) Assumptions

The following simplifications are made in order to perform the large scale simulation:

- the metallic tower structure is a solid body rather than a lattice structure
- the insulator strings are simplified to a cylindrical shape of radius 100 mm and relative dielectric permittivity of 4
- conductors are simplified as cylinders
- the ground is assumed to be a perfect conductive plane
- the small degree of sag within the first 20 meters span is ignored
- the whole simulation extends 20 meters from the tower to both sides
- electrostatic analysis is performed and the time is selected at 0 s for evaluation

b) Voltage Gradient Distribution at 'Time 0'

The results are displayed at instantaneous time 0. The phase arrangement as introduced in Figure 3-13 is a typical untransposed phase in National Grid. The voltage applied on each phase is listed in Table 3-2.

Table 3-2 Phase angle and phase voltage at time 0

	Left bottom	Left middle	Left top	Right bottom	Right middle	Right top
Phase angle	-120^{o}	$+120^{o}$	0^{o}	0^{o}	$+120^{o}$	-120^{o}
Voltage (kV)	-163.3	-163.3	326.6	326.6	-163.3	-163.3

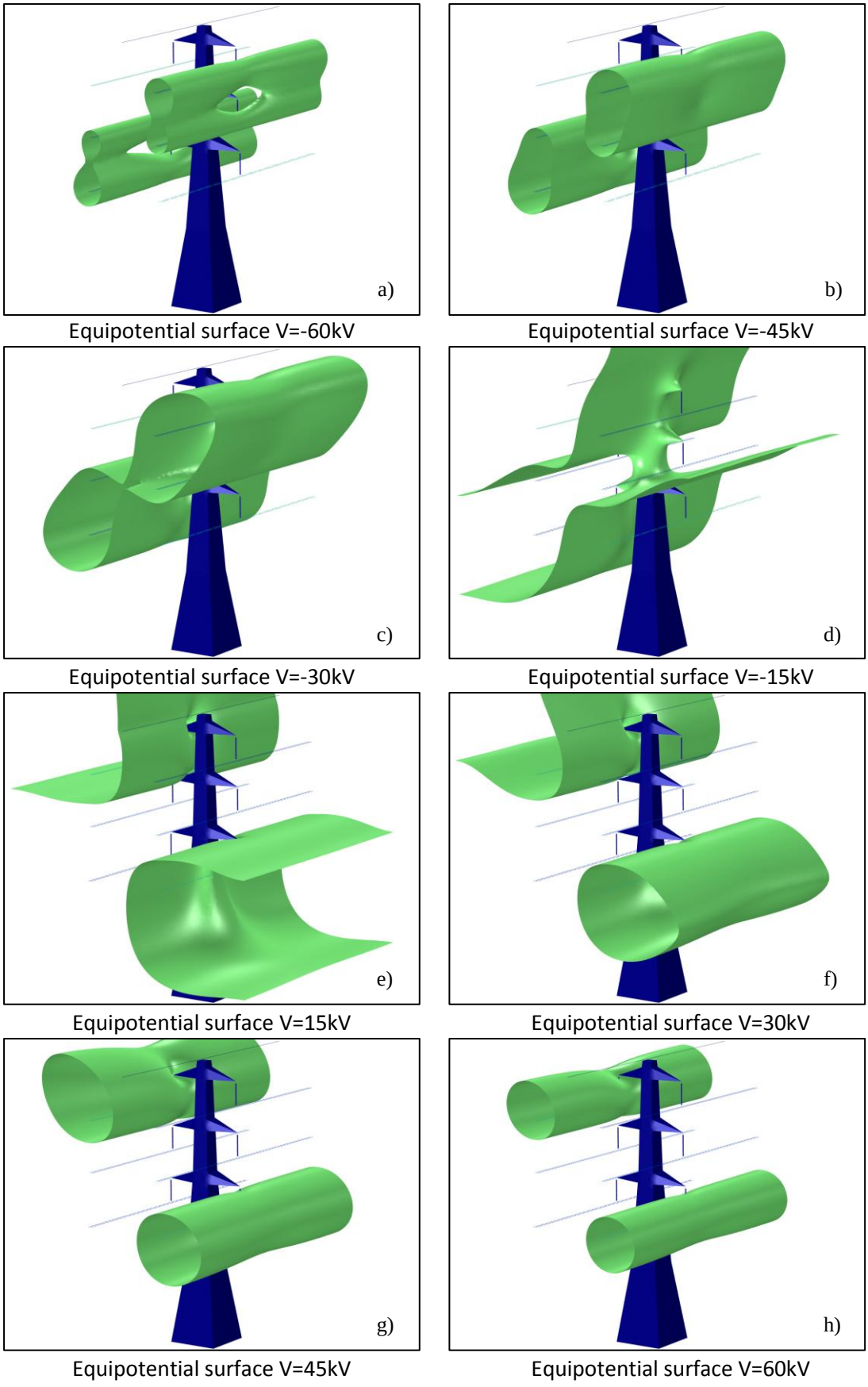

Figure 3-36 Equipotential Surfaces Surrounding a 400kV L2 Tower

c) Electric Field Enhancement

As described in Section 2.2.1, when a simplified model was considered, the potential distribution does not vary along the axial direction of the conductors. Any equipotential surface in three-dimension is thus an extrusion of the equivalent two-dimensional equipotential line. As shown in Figure 3-36, due to the effect of the metallic tower adjacent to the overhead conductors, the equipotential surface is distorted. As a result, the electric field on the conductor surface is enhanced. For instance, on the plot 'equipotential surface V=45 kV', the potential drop from the top left phase to the equipotential surface is approximately 282 kV. According to electrostatic theory, when the potential drop remains constant, the shorter the clearance is, the higher the electric field on surface of the conductor will be.

The electric field along the surface of a single conductor ('conductor F' in Figure 3-29) as distance from the tower increases at time 0 is plotted in Figure 3-37, as a worst scenario. The surface gradient without the tower (shown as a dashed line) is approximately 24.7 kV/cm (peak). When the L2 tower is included, the surface gradient increases to a peak of 26 kV/cm (peak). This plot applies along a horizontal line on the surface of conductor (red dot in the figure).

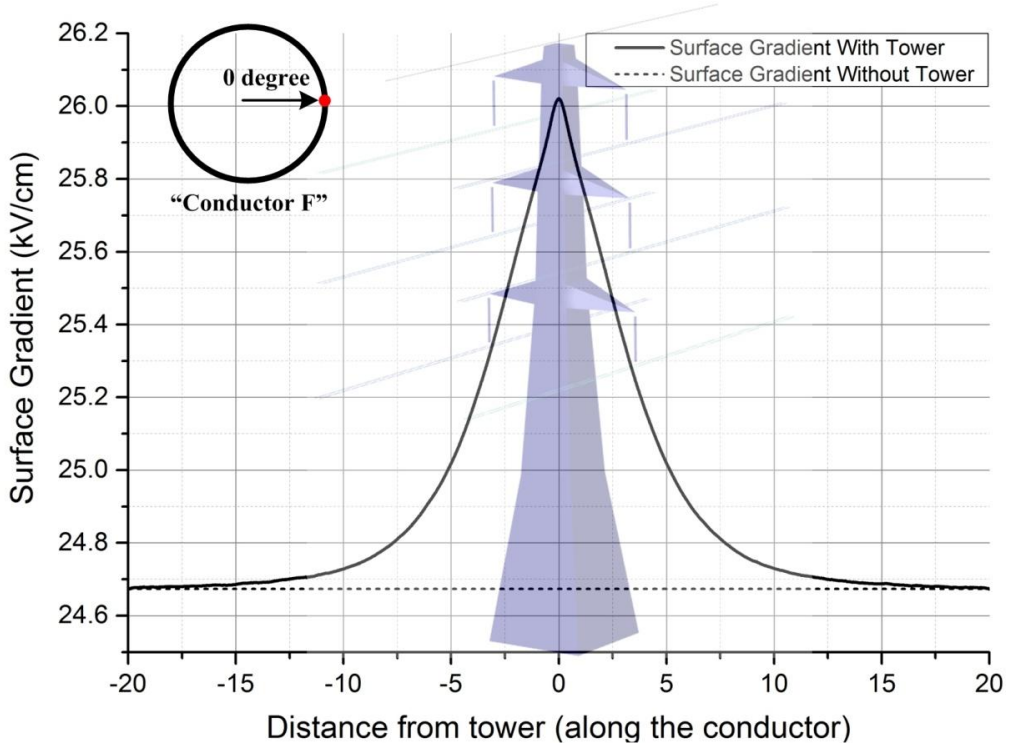

Figure 3-37 Electric Field Enhancement by Tower (x axis gives distance from the tower)

As a conclusion, the field enhancement on "conductor F" due to the proximity of tower is around 1.4 kV/cm (6%) maximum. If we assume that the electric field varies as sinusoidal wave within one cycle, the increased surface gradient in RMS term is thus calculated from peak value as 1 kV/cm.

3.3.5 Effect of the Conductor Orientation

The conductor orientation varies due to the following factors:

- different types of tower (such as L2, L6, and the recently designed T-Pylon)
- different spacing arrangements (such as 300 mm, 400 mm and 500 mm)
- different bundle arrangements (single, twin, triple and quad bundles)

This section examines the sensitivity of the surface gradient values of overhead line conductors to these geometric factors. As the relatively large scale is the main concern, the simplified model with no sag and no tower effect (Section 2.2.1) is utilized to conduct surface gradient calculations in this part.

a) Different Types of Tower

As introduced in Section 3.3.1, a typical L2 tower is described in Figure 3-13. The new tower design, T-Pylon, is shown in Figure 3-38. These two configurations are used to study the effect of different types of tower configurations on surface gradient calculations. For comparison, all other parameters, such as conductor size (31.6 mm diameter), bundle spacing (twin 400 mm), voltage level (400 kV) and phase arrangement (untransposed), are kept the same for both calculations.

Table 3-3 Comparison (T-Pylon with L2)

Conductor Number	*L2*		*T-Pylon*	
	E_max (kV/cm)	*E_ave (kV/cm)*	*E_max (kV/cm)*	*E_ave (kV/cm)*
1	17.43	16.46	18.19	17.15
2	17.64	16.62	**18.26**	**17.20**
3	17.54	16.53	17.57	16.48
4	17.37	16.41	16.75	15.88
5	17.41	16.44	17.39	16.47
6	**17.67**	**16.64**	18.07	16.97
7	17.64	16.61	**18.26**	**17.20**
8	17.43	16.46	18.19	17.15
9	17.37	16.41	18.07	16.96
10	17.54	16.53	17.39	16.47
11	**17.67**	**16.64**	16.75	15.88
12	17.41	16.44	17.57	16.47
Average	**17.51**	**16.52**	**17.71**	**16.69**
Maximum	**17.67**	**16.64**	**18.26**	**17.20**

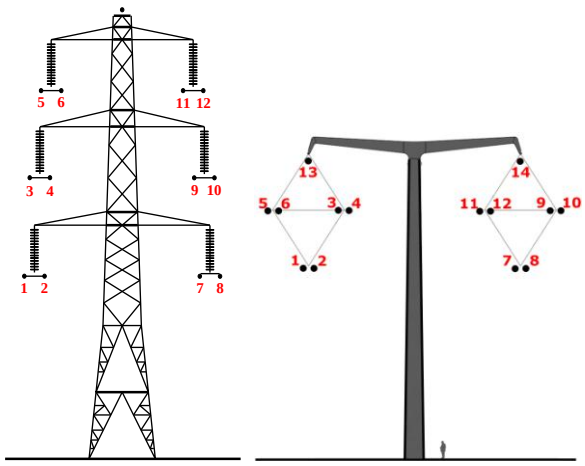

By observing Table 3-3, the following conclusions are drawn:

- L2 tower has lower surface gradients both in maximum and average value among all sub-conductors. The difference between these values on the L2 and T Pylon are approximately 1% (0.2 kV/cm) for average value and 3% (0.6 kV/cm) for maximum value
- If the variation between maximum and minimum values of surface gradient among all sub-conductors is taken into consideration, T-Pylon has a larger variation (8.3%) when compared with the L2 tower (1.7%).

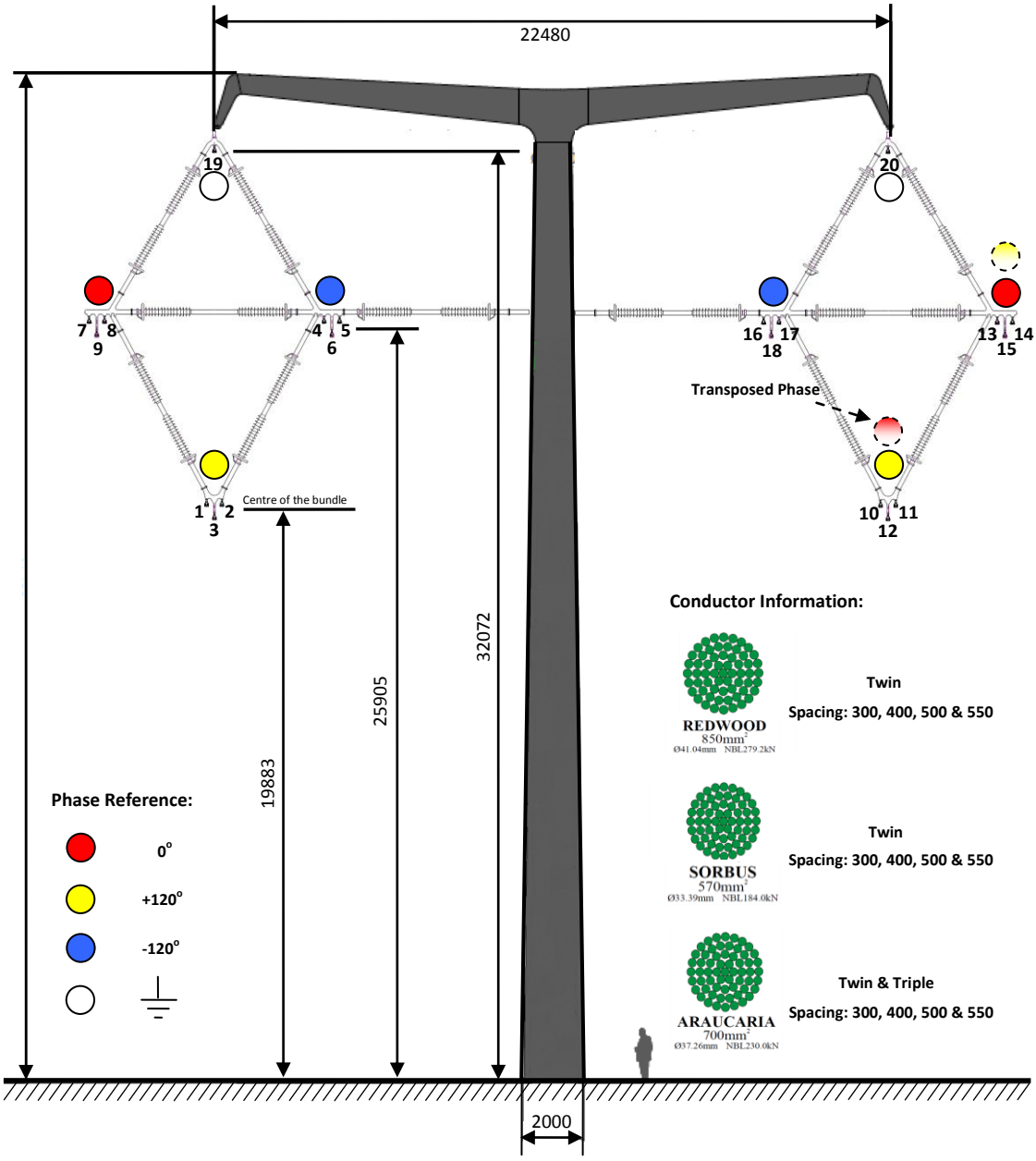

Figure 3-38 Parameters for 'T-Pylon'

b) Bundle-Spacing

Bundle spacing is the distance between the centres of two adjacent sub-conductors. Within National Grid UK, the bundle spacing varies from 300 mm to 550 mm according to voltage levels and tower configurations. In order to evaluate the effect of spacing on surface gradient values, a L2 RUBUS twin bundle (as shown in Figure 3-13) is taken as a prototype for stress computation. The spacing is increased from 50 mm to 550 mm at 10 mm intervals.

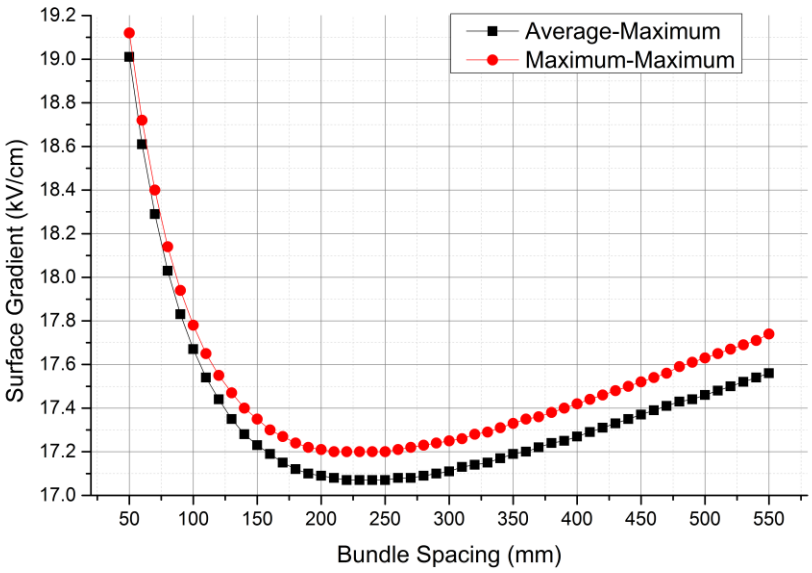

Figure 3-39 Maximum Surface Gradient with Bundle Separation

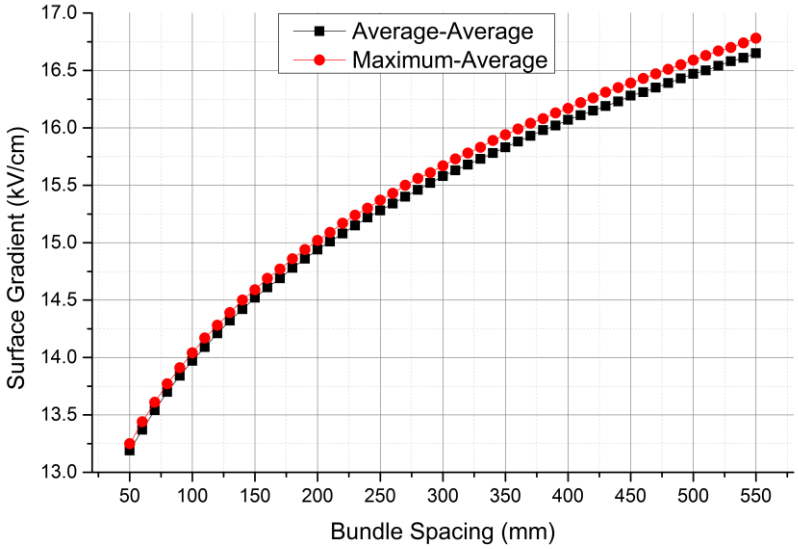

Figure 3-40 Average Surface Gradient with Bundle Separation

In Figure 3-39, the maximum value is first taken from the surface of each sub-conductor. The maximum and average values are then taken among all those sub-conductors. For example, the 'average-maximum' value means the following process:

- The maximum surface gradient is first measured around the whole circle of each sub-conductor. 13 maximum values are generated as there are 13 sub-conductors within the whole system.
- The mean value is taken among those 13 maximum values to obtain a single value to indicate the surface gradient level within this calculation.

Similarly, in Figure 3-40, the average value is first taken around each sub-conductor. The maximum and average values are then generated.

It is observed that:

- Both 'maximum-maximum' and 'average-maximum' values reduce rapidly from 50 mm to 230 mm (Figure 3-39), but increase from 230 mm to 550 mm. So the surface gradient in this case is minimized at about 230 mm spacing. An increased bundle spacing or reduced bundle spacing from 230 mm will cause the maximum value of surface gradient to rise.
- If the bundle spacing is reduced from 550 mm to 230 mm, there is approximately a 3.5% drop on the maximum surface gradient value.
- In contrast to Figure 3-39, the 'maximum-average' and 'average-average' values increase when the bundle separation increases (Figure 3-40).
- If the bundle spacing is reduced from 550 mm to 50 mm, there is approximately 27% drop in average surface gradient value.

c) Different Bundle Arrangements

The highest voltage level in the transmission system in the UK is 400 kV. The bundle arrangements include single, twin, triple and quad. Twin and triple bundles are most widely used in overhead line conductors. To evaluate the reduction of surface gradient values from twin bundle to triple bundle, L2 RUBUS (shown in Figure 3-13) is chosen as a benchmark model. The bundle spacing is fixed at 500 mm, surface stress calculations for both twin and triple bundles are calculated. The results are compared

in Table 3-4. By introducing one more sub-conductor (from twin to triple), the surface gradient reduces by approximately 20% (3.5 kV/cm).

Table 3-4 Comparison for Surface Gradient (RMS values between twin and triple)

Conductor Number	*Twin*		*Triple*	
	E_max (kV/cm)	*E_ave (kV/cm)*	*E_max (kV/cm)*	*E_ave (kV/cm)*
1	17.43	16.46	13.99	12.64
2	17.64	16.62	14.23	12.82
3	17.54	16.53	13.68	12.41
4	17.37	16.41	14.06	12.70
5	17.41	16.44	13.88	12.57
6	**17.67**	**16.64**	13.99	12.64
7	17.64	16.61	13.66	12.39
8	17.43	16.46	13.95	12.61
9	17.37	16.41	**14.29**	**12.87**
10	17.54	16.53	14.23	12.82
11	**17.67**	**16.64**	13.99	12.64
12	17.41	16.44	13.68	12.41
13	-	-	13.88	12.57
14	-	-	14.06	12.70
15	-	-	13.99	12.64
16	-	-	13.95	12.61
17	-	-	13.66	12.39
18	-	-	**14.29**	**12.87**
Average	**17.51**	**16.52**	**13.97**	**12.63**
Maximum	**17.67**	**16.64**	**14.29**	**12.87**

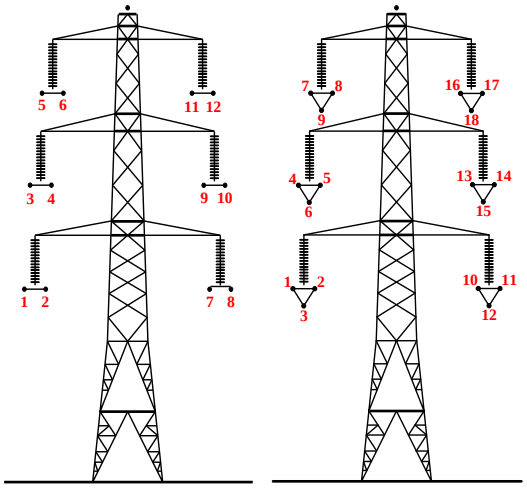

3.3.6 Stratagem for Evaluating Surface Gradient

Existing methods for surface gradient calculation on overhead line conductor only consider a maximum value assuming cylindrical conductors. However, it is not the maximum value but the distribution of surface gradient which determines the corona generation on a conductor. The distribution of surface potential gradient can be affected by both micro and macro factors such as: stranding shape, protrusions on the strands, tower proximity, tower geometry, intra bundle spacing and bundle separation.

In order to examine the sensitivity of different factors to surface potential gradient distribution, the following strategy is proposed. The electric field strength is first calculated assuming a protrusion is applied at a specific location on the surface of the overhead line conductor. If this calculated maximum electric field exceeds 30 kV/cm, this area is then counted as 'above the threshold electric field'. A reference length of conductor (1 m) is examined, and the area 'above threshold electric field' is identified to reflect the potential area that can initiate corona discharges.

For comparison purpose, indexes for different factors are defined on a 0 to 1 scale, as shown in Table 3-5.

Table 3-5 Factors and Their Definitions

Factors	Range	Min	Max	Increment
Stranding Shape	0, 1	round	trapezoidal	1
Protrusion Size	0, 1	r=10 um	r=200 um	
Proximity of Tower	0, 1	D=0 m	D=10 m	
Type of Towers	0, 1	L2	T	1
Bundle Spacing	0, 1	50	550	
Bundle Arrange	0, 1	twin	triple	

The surface area above threshold electric field is computed and divided by a reference value to obtain the results in Figure 3-41. The abscissa is the index increment as defined in Table 3-5.

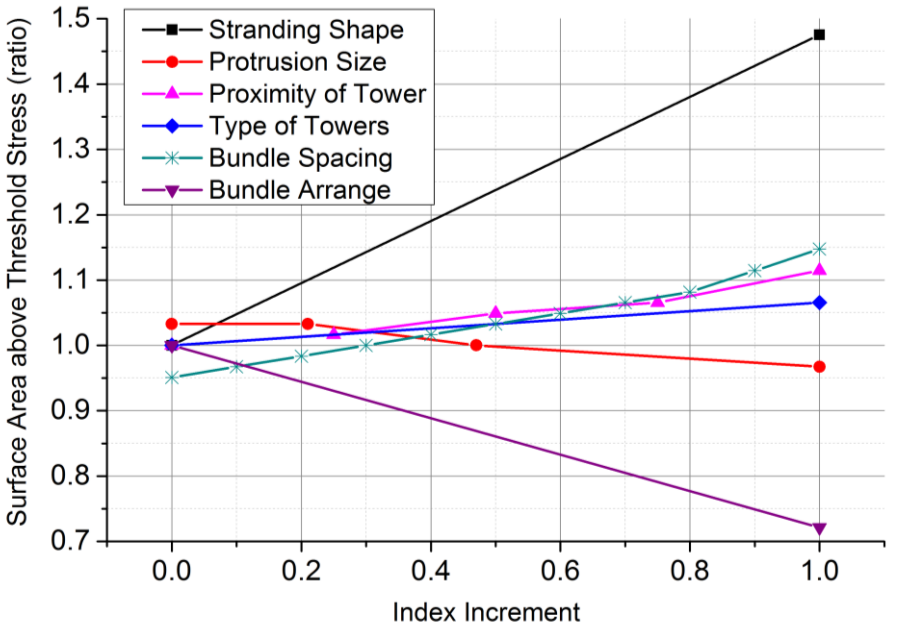

Figure 3-41 Sensitivities of Factors for Surface Gradient Calculation

The following conclusions are drawn:

- The most sensitive factor is the stranding shape, since when the shape of strands is changed from round to trapezoidal, the area of surface which can initiate corona discharge increases about 50%.

- The second sensitive factor is the bundle arrangement. For example if the conductor bundle is changed from twin to triple, the area of corona discharge is reduced by approximately 30%.
- When the bundle spacing is reduced from 550 mm to 50 mm, there is a 20% reduction of surface area with excessive corona discharge.
- The maximum enhancement of field due to the proximity of the tower is about a 12% increase in surface area with corona, but this value reduces to a negligible level 10 metres away from the tower.
- Larger protrusions produce a smaller area with corona discharge (9% reduction from 10 um to 200 um).

3.4 Conclusion

A new model has been demonstrated for surface gradient calculation on overhead line conductors. It enables full consideration of strand shape, protrusions, proximity of towers, types of tower, bundle spacing and bundle separation. It is found that the surface gradient distribution is sensitive to both stranding shape and the bundle arrangement (twin or triple). Other factors have relatively small influence on the field distribution.

This part of study gives a comprehensive evaluation of surface gradient distribution of overhead line conductors under dry conditions. When a wet condition is considered, the presence and movement of moisture modifies the electric field. This is studied in the next chapter.

Chapter 4 Droplet Behavior under Electric Field

4.1 Introduction

Knowledge about surface gradient for overhead line conductors under dry condition has been established in the last chapter. This chapter focuses on phenomena when conductor is subject to rain condition.

The dynamic behaviour of water droplets subject to AC electric fields is investigated by experiment and finite element modelling in this chapter. The motion of a water droplet is considered on the surface of a metallic sphere. To understand the consequences of vibration, an FEA model is introduced to study the dynamics of a single droplet in terms of phase shift between vibration and the exciting voltage. Moreover, the evolution of electric field within the whole cycle of vibration is investigated.

4.2 Single Droplet under an AC Field

To study the mechanical and electrical behaviour of droplets under alternating electric fields, a sphere-to-plane set up is used. The advantage of using a sphere-to-plane geometry is that the axial-rotational symmetry can avoid three-dimensional effects (depending on the mode of droplet vibration). A high speed camera is synchronised to both voltage and leakage current signals (as shown in Figure 4-1) to study the dynamics of a single droplet. The entire high voltage system is designed to avoid corona discharges from any unwanted locations. The experiment was designed using FEA software to determine a suitable gap distance and sphere diameter.

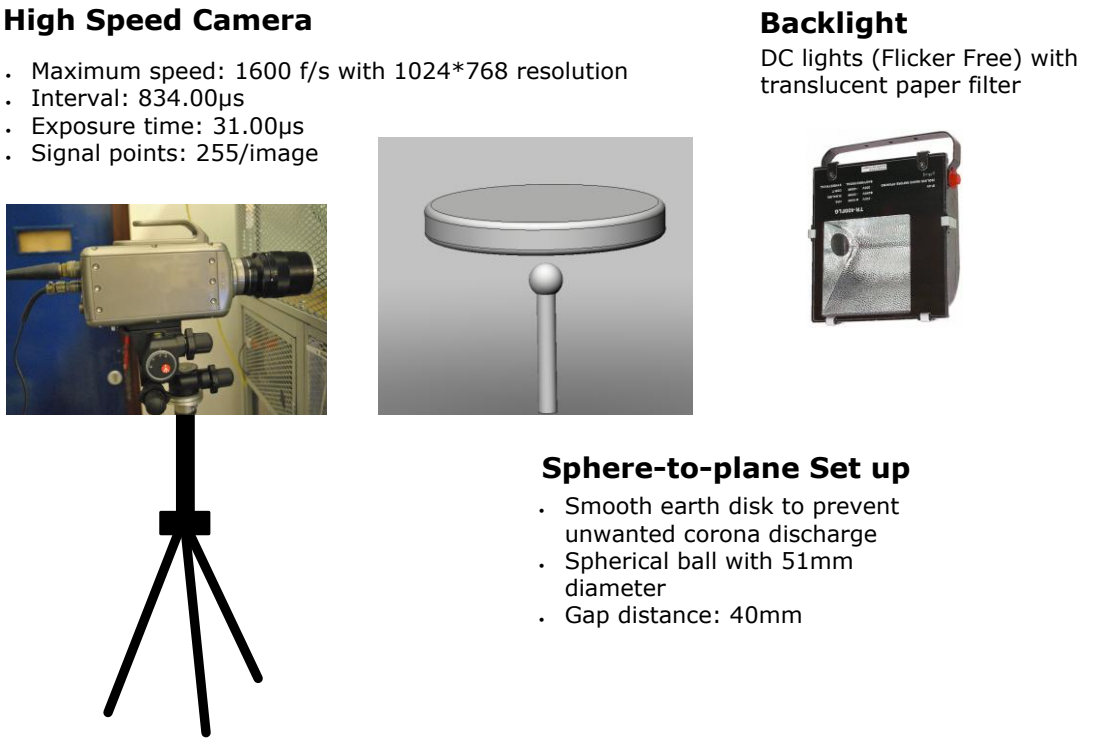

Figure 4-1 Sphere-to-plane set up

4.2.1 Experimental Set-up and Instrumentation

a) High Speed Camera

A high speed video camera (Phantom V5.1 as shown in Figure 4-1) is utilized to capture the shape of the water droplet vibration under AC field. The settings of the camera are:

- 1200 frame per second recording speed with resolution of 1024*768

- time interval between two adjacent images: 834 µs
- exposure time: 31 µs
- an external signal is used to trigger the camera

b) Enclosed Chamber

The purpose of this experiment is to capture the dynamic movement of a single water droplet subject to an AC electric field. As water droplets are sensitive to any external wind flow, turbulent air flow is prevented by enclosing the whole set-up with a sufficiently large metallic chamber.

c) Sphere-to-plane Gap

As mentioned above, in order to generate an axial-symmetrical electric field, a sphere and a round plate are selected as HV and earth electrode respectively. The earth plate has smooth round edges to prevent undesired corona discharges (Figure 4-2).

The critical design parameters which determine the distribution of the electric field surrounding the sphere are:

- the diameter of the aluminium sphere
- the distance of the gap between sphere and electrode
- the diameter of the plane electrode

Figure 4-2 Sphere-to-plane Gap

An FEA model has been developed to determine the electric field distribution for various sphere diameters, gap distances and dimensions of earth plate. Results are compared to the protrusion example described in Section 3.3.3. These parameters are optimized so that the electric field distribution is closest to the overhead line

conductor case. Although in this case of a sphere the field is divergent in two planes not one as for a conductor/cylinder.

d) Backlight

The key design features for backlight controls (Figure 4-3) are:

- A DC voltage source for the light to prevent flickering
- A flat paper sheet attached to the light screen to achieve an intense and uniform illuminating source

Figure 4-3 Back Light Control for High Speed Imaging

e) Electric Circuit

The circuit diagram is shown in Figure 4-4.

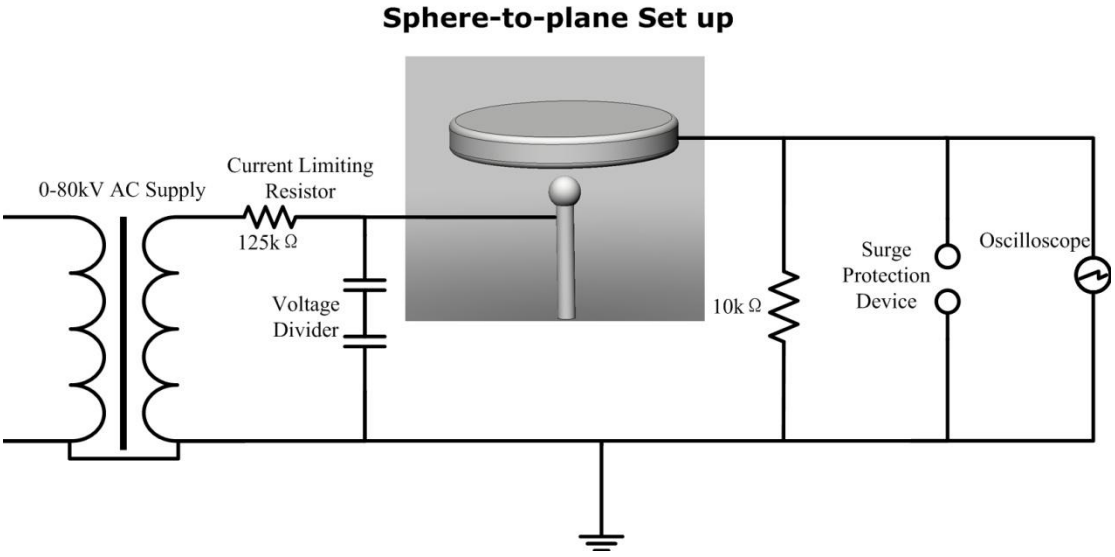

Figure 4-4 Electrical Diagram of Sphere-to-plane Set up

Within this test, a 0-80 kV transformer is employed as the HV supply. The current limiting resistor is selected as 125 kΩ to limiting the flash over current. A surge

protection device (spark gap) is introduced to protect the oscilloscope as well as the leakage current measurement circuit. A voltage divider is used to accurately measure the supplied voltage value on the HV sphere.

4.2.2 Synchronization

The images captured from the high speed camera are synchronized with the electrical measurement results (applied voltage value and leakage current value). As shown in Figure 4-5, this is achieved by introducing a signal buffer and a data acquisition board.

The signals from the voltage divider and leakage current measurement device are transmitted through a signal buffer first. There are two functions of signal buffer:

- to buffer the signal to be able to match the speed of image recording
- to mitigate the DC offset produced from the whole electronic circuit by matching the input impedance

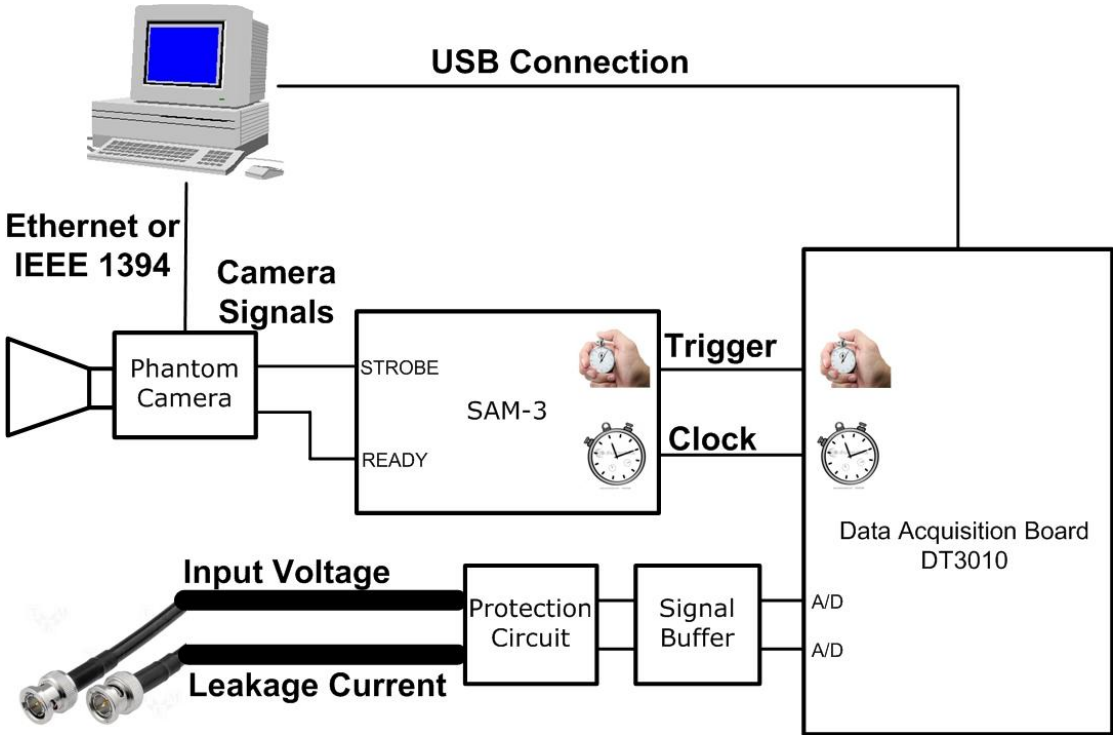

Figure 4-5 Connections for Synchronization

After buffering, the analogue signals are converted to digital signals and assigned to individual channels within the data acquisition board. By synchronizing the internal clock within the high speed camera and the data acquisition board, the digital signal

of the voltage and leakage current is attached to individual images captured by the high speed camera.

As the measurement accuracy of this experiment relies on the synchronization between images and signals, a calibration procedure has been carried out to examine the performance of the whole set up. To do this, the instantaneous times of a series of breakdown activities is measured by high speed recording and then compared with voltage and current measurement results.

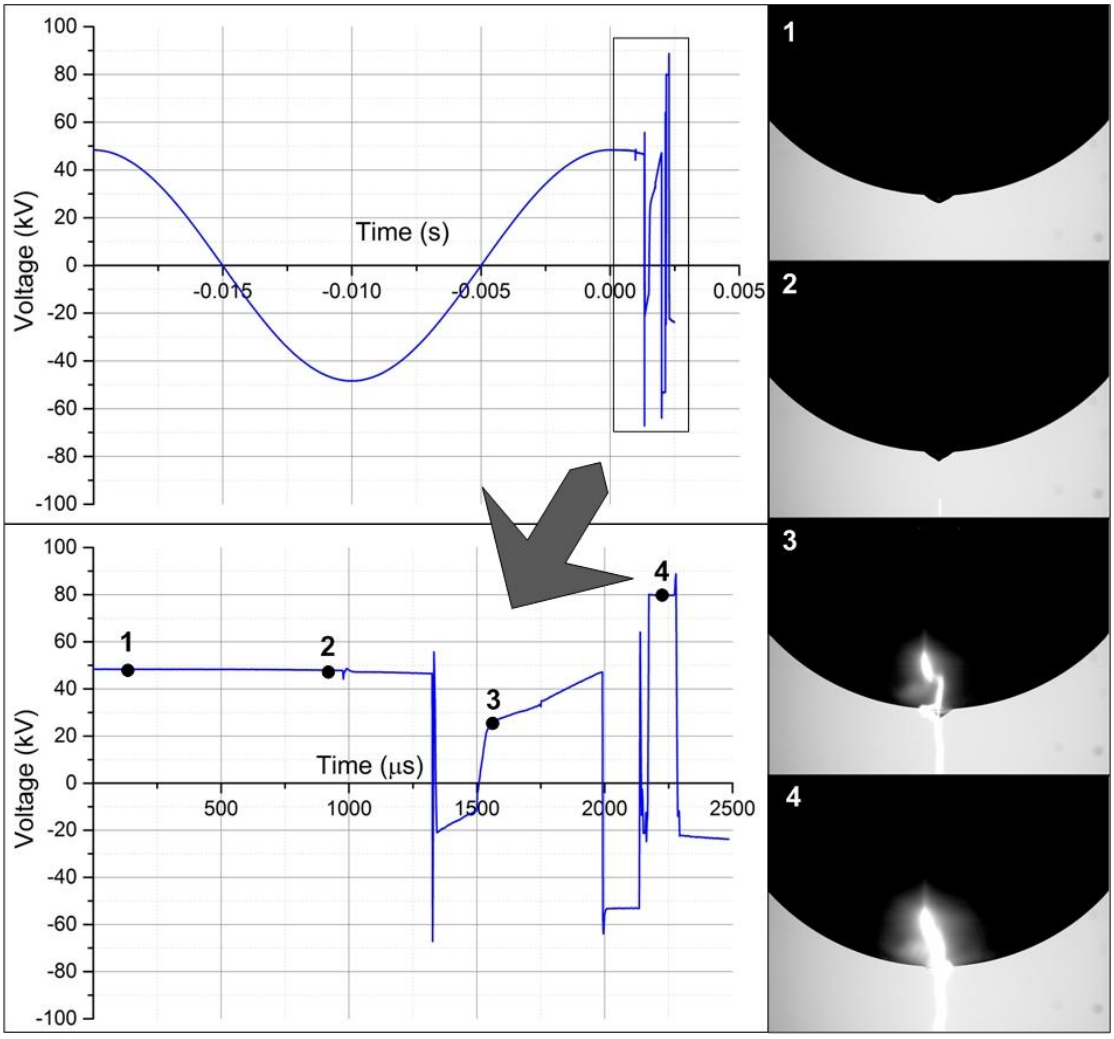

Figure 4-6 Calibration for Synchronization (The bottom graph is an expansion of part of the top chart)

As shown in Figure 4-6, the first voltage drop was detected at 1300 µs while the first discharge is detected at about 1550 µs. This time difference is because that images are captured every 831 µs. It demonstrates that the error of the synchronization system is lower than the capturing time interval (831 µs).

4.2.3 Results and Discussion

Both sessile and pendent droplets are tested within an AC electric field. The shape of droplet, voltage and leakage current are shown in Figure 4-7 and Figure 4-8.

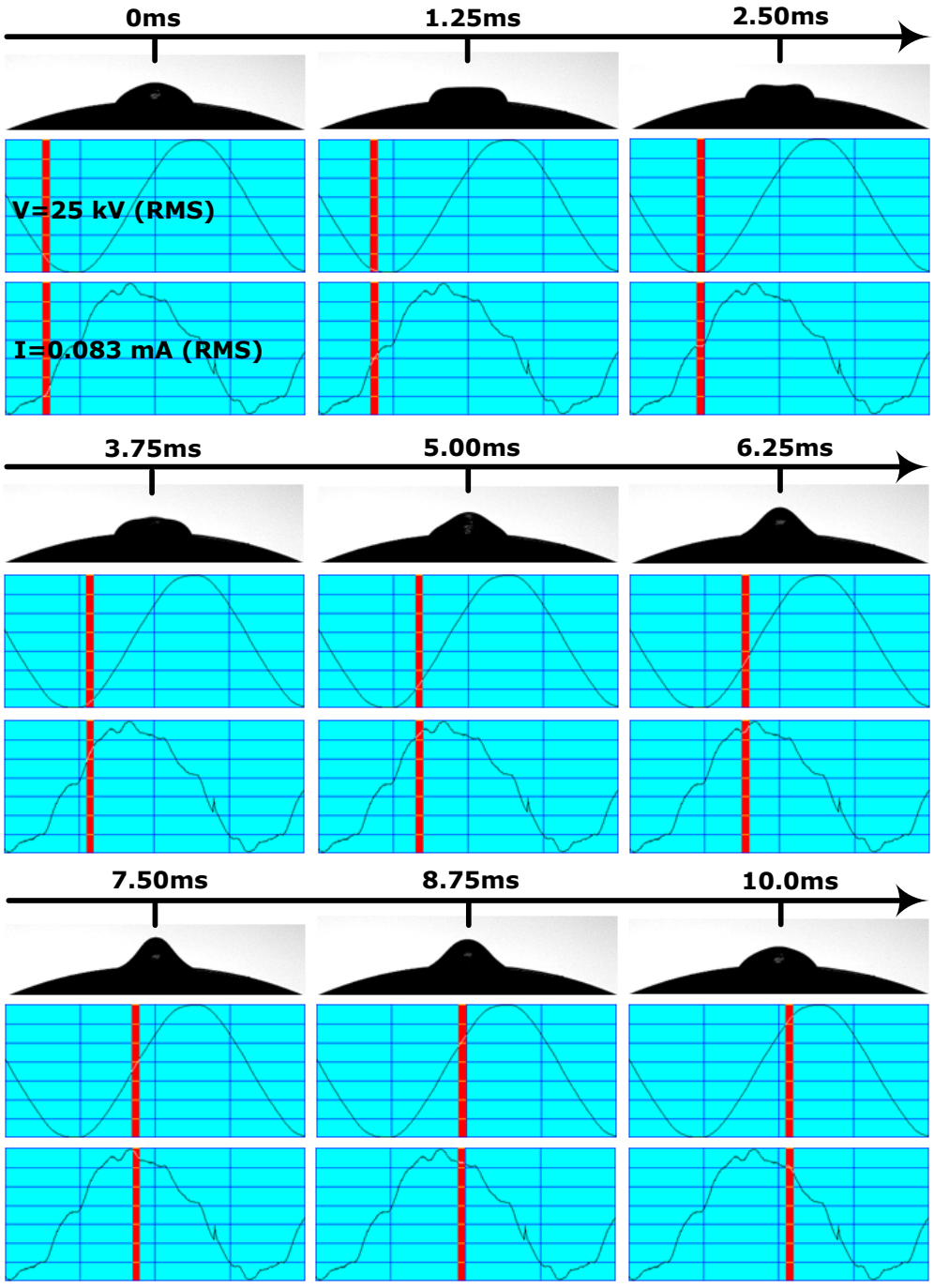

Figure 4-7 Droplet Motion (sessile drop)

Rain water collected in Manchester was found to have an average conductivity of 80μs/cm, and so that value was used in this experiment.

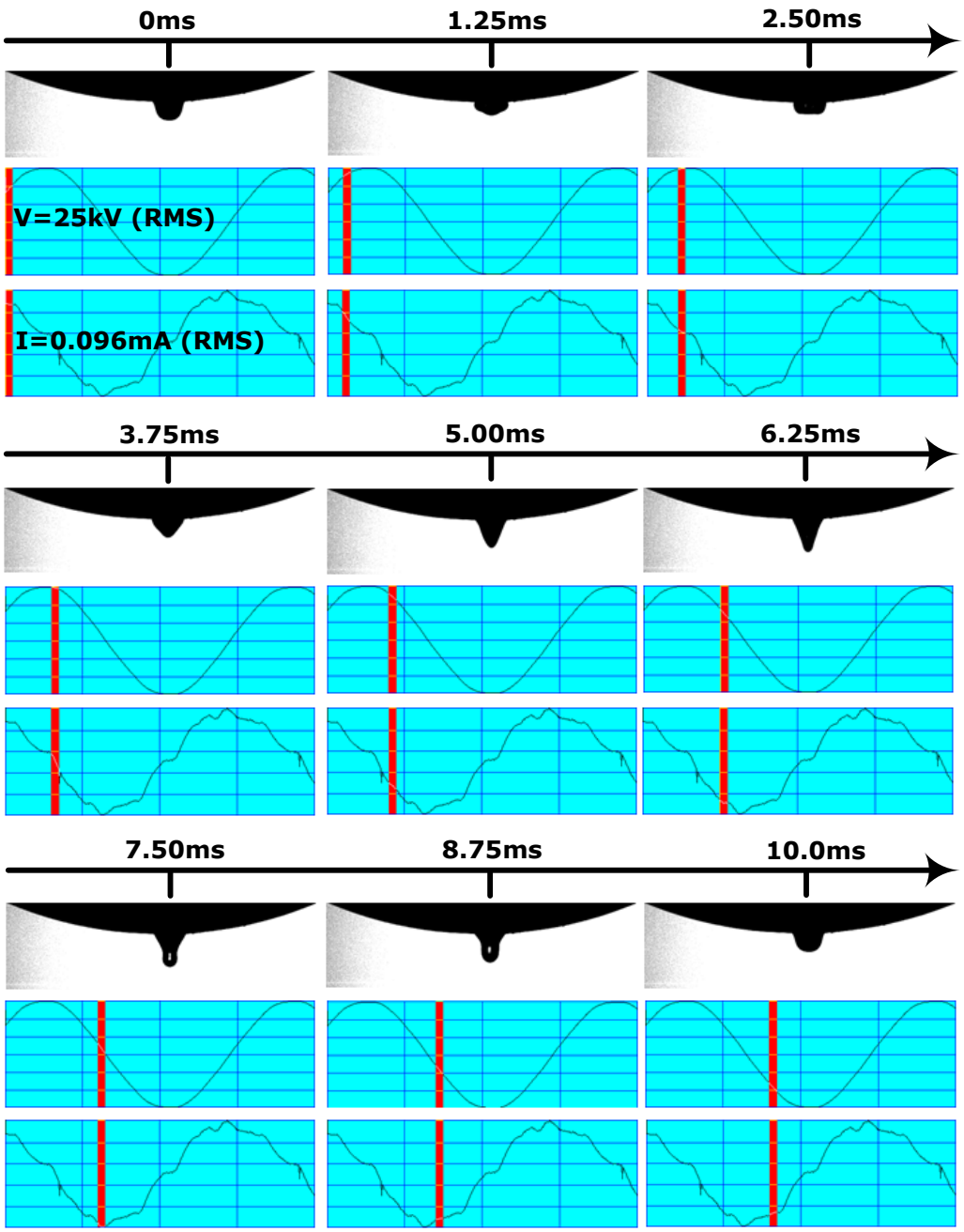

Figure 4-8 Droplet Motion (pendent drop)

It is found that the motion of water droplet is periodic, and the frequency of 100 Hz is twice the supply frequency. The droplet experiences a stretching process and a compression process within each period of 0.01 s. Nine images have been selected to present the vibration characteristics for both sessile and pendent droplets (Figure 4-7 and Figure 4-8). The time interval between two adjacent images is 1.25 ms. The shape of the droplet alters through each half power cycle between three states or outline shapes: semi-spherical, flattened, and conical.

It can be observed that the applied voltage reaches its maximum when the shape of water droplet is flattened, and minimum when the droplet is approaching the conical shape. From a vibration point of view, this phenomenon can be explained by a ninety degree phase shift between excitation force and response [58].

4.2.4 Electric Field Evaluation

As introduced in Section 4.2.2, the applied voltage is measured simultaneously with high speed video. It allows the accurate calculation of electric field distribution for any instant. It is assumed that the shape of water droplet is axial-symmetrical.

The surface gradient of a sessile drop has been computed by the Finite Element Method. FEA models within two popular commercial software packages (ANSYS and COMSOL) have been built. By comparing the results, and noting their similarity, give confidence in the simulation results. It is also ensured that the numerical errors within FEA procedure (due to mesh, geometry modeling etc) are minimized.

Geometry Modelling

As mentioned in Section 4.2.1, high resolution images are captured from a high speed camera. This allows accurate reconstruction of the shape of the water droplet. Taking advantage of MATLAB's reconstruction function, a model of a droplet at various instants has been built in both 2-D symmetrical and 3D as shown in Figure 4-9.

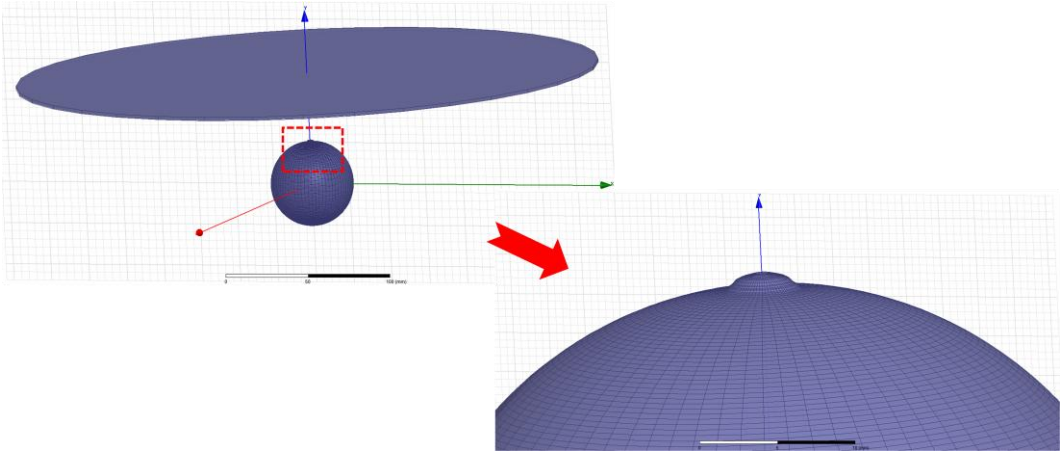

Figure 4-9 Geometry Model for a Water Droplet

Two methods to reconstruct the shape of water droplet have been tested:

- utilizing MATLAB's Boundary Reconstruction function (curve fitting)
- utilizing AutoCAD's Bezier Curve function

The standard deviations are evaluated, and it is proved that MATLAB's Boundary Reconstruction method gives higher accuracy in this case, and is utilized as geometry modeling method.

Meshing

With the advanced function of the software, 'adaptive meshing' (Figure 4-10), the numerical residual is reduced to a minimum when the maximum computing power is deployed.

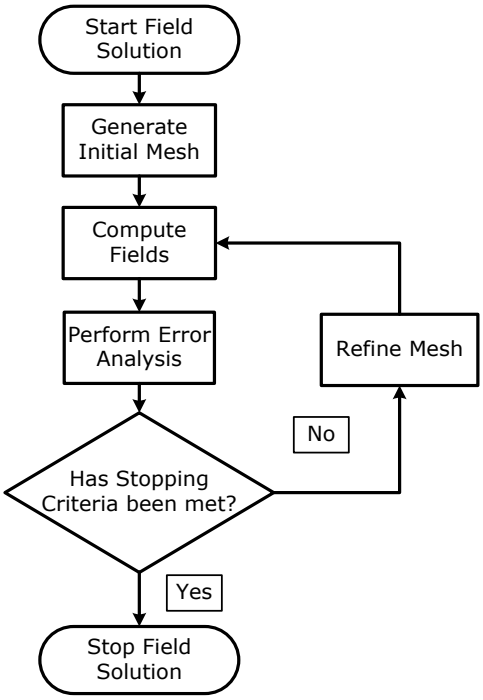

Figure 4-10 the Adaptive Meshing Algorithm [59]

Post-process

The axial-symmetrical simulation is performed, and the 2D axial-symmetrical result is revolved to reconstruct the surface field distribution of the single droplet as shown in Figure 4-11. For reference, the original image from the high speed camera is attached in the first row. The second row shows the electric field distribution within the air surrounding the water droplet. The third row plots the 3-D surface electric field.

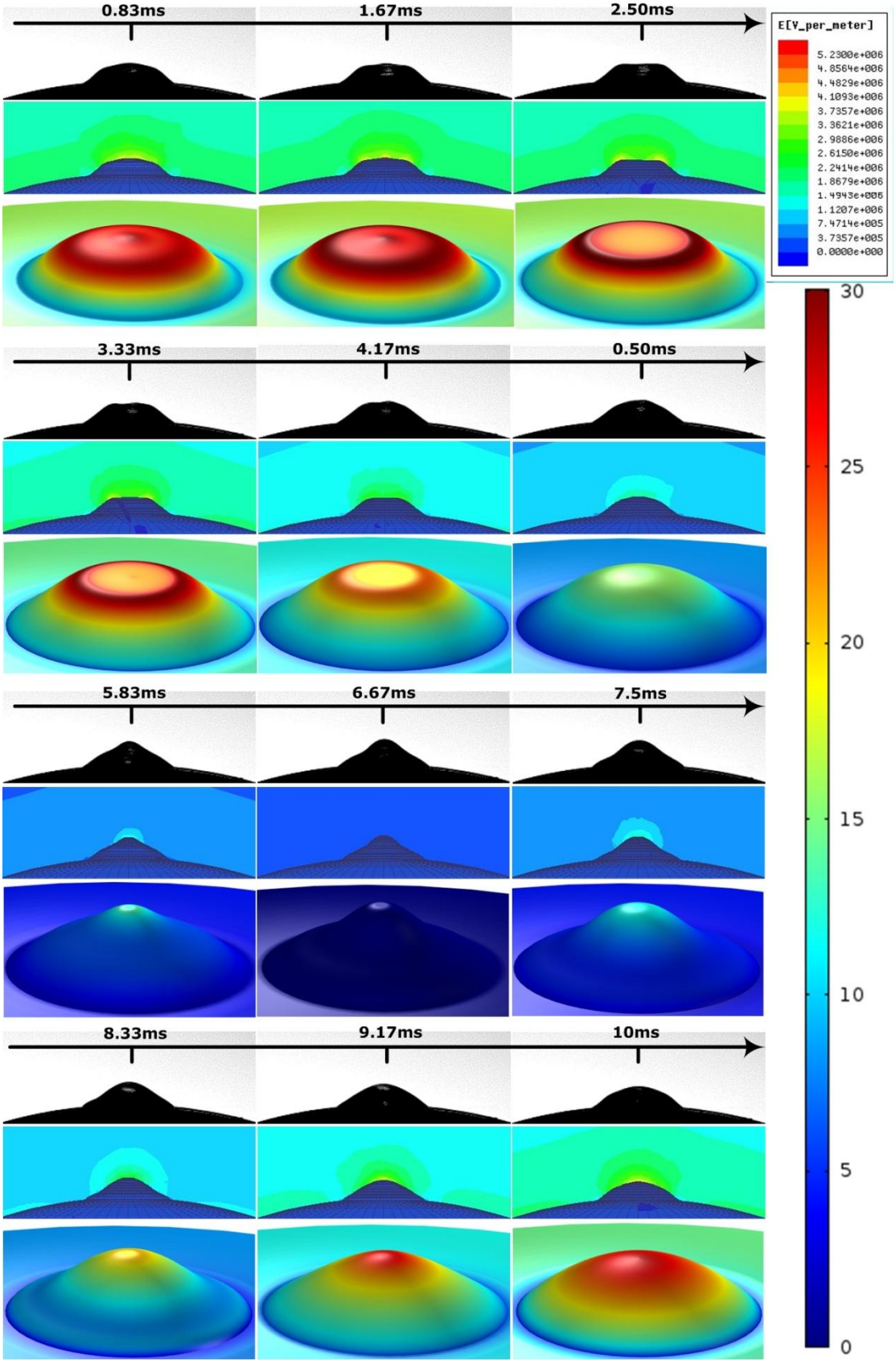

Figure 4-11 Electric Field Evolution within One Vibration Cycle (half a power cycle)

It is observed that the electric field varies with both droplet shape and applied voltage. The electric stress reaches its maximum when the shape of water droplet is flattened while encountered a minimum when the droplet is approaching the conical shape.

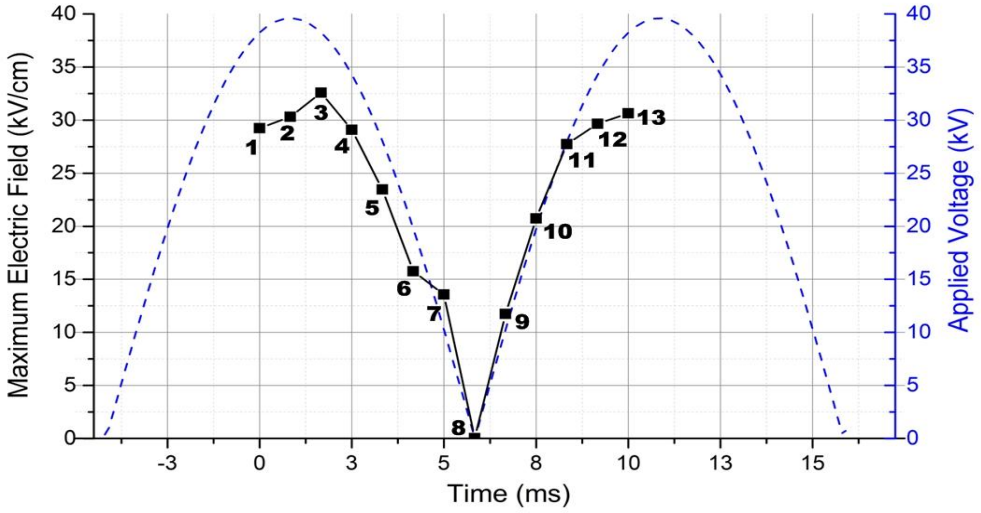

Figure 4-12 Electric Field and Applied Voltage within One Cycle

In Figure 4-12, the maximum electric field is plotted with applied voltage against the time. Each black point and associated number describes the maximum electric field strength for one FEA simulation as shown in Figure 4-11.

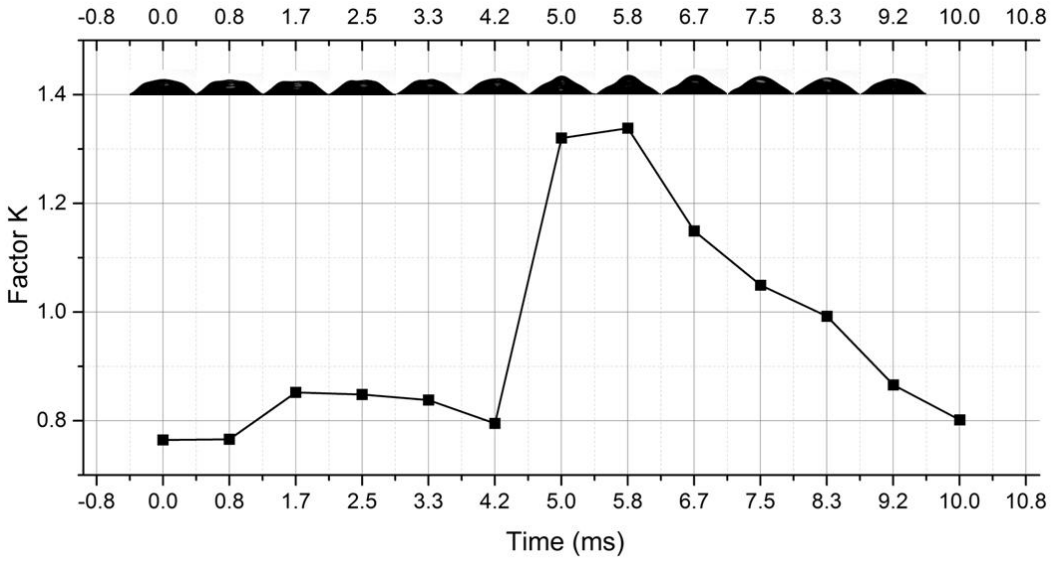

Figure 4-13 Electric Field Enhancement Factor (K) for Different Shapes

Figure 4-13 describes the impact that the shape has on the electric field. A natural shape is first selected (position 12) as a reference $E_{max}(t_0)$, and a constant DC voltage

level is applied to the different shape of droplet. The field enhancement factor, only due to the shape of the drop, is then computed from:

$$K(t) = \frac{E_{\max}(t)}{E_{\max}(t_0)} \tag{4-1}$$

As stated in Section 4.2.3, the shape of droplet is characterised as three types: flattened, semi-spherical, and conical. In Figure 4-12, positions 1-5 and 13 can be classified as flattened. Positions 6 and 12 are semi-spherical shape. Positions 7-11 are conical shape. In Figure 4-13, the field enhancement factor can be seen to be approximately 0.8 for both flattened and semi-spherical shapes and increases to 1.3 for the conical shape. This means that the shape of water droplet can enhance the surface electric field by 30% in the worst scenario in this case. At higher fields, it is expected that the factor *K(t)* will take more extreme values (i.e. the droplet will become more flattened and pointed). Ultimately there will be a field at which a droplet will become unstable as discussed in Section4.2.5. These values will also be dependent on water droplet size. *K(t)* might then be written as a function of filed, *E*, and droplet volume, *V*, as *K(t, E, V)*.

4.2.5 Ejection phenomenon

It is observed that:

- When the voltage increases to a certain level, the droplet start to eject smaller secondary droplets;
- The ejection phenomena can be observed from different sizes of drops;
- Not only pendent but also sessile drops can produce ejection phenomena;
- After separation from the main body, those small secondary droplets vibrate under AC electric field (move backwards and forwards in space).

The ejection process for sessile droplet is shown in Figure 4-14. When the shape of the droplet become conical, the inertia of the top part of water overcomes the surface tension and is separated from the main body. A similar process is observed on a pendent droplet as shown in Figure 4-15. In this case two secondary droplets can be seen, each of which returns to the main droplet on field reversal. This implies the

secondary droplet is charged, since electric force is strong in this field, it causes the droplet to reverse direction.

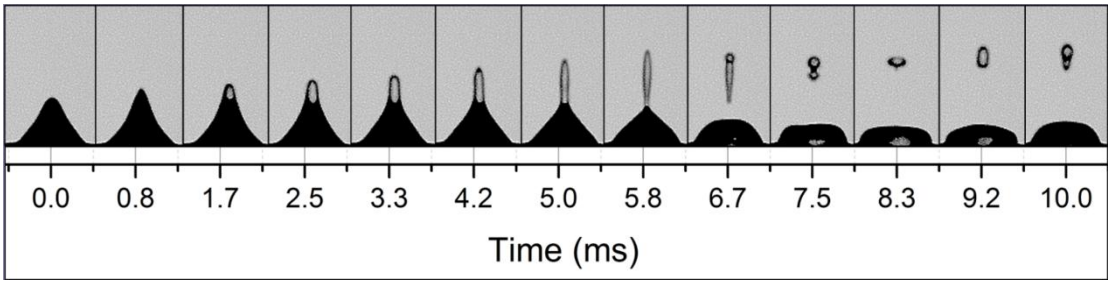

Figure 4-14 Ejection Phenomenon on Sessile Droplet

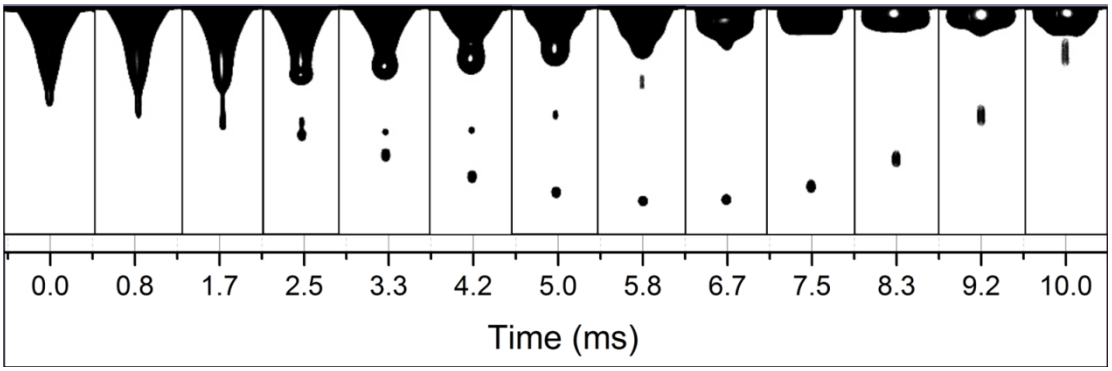

Figure 4-15 Ejection Phenomenon from Pendent Droplet

4.3 Droplets' Motion on Conductors

In Section 4.2, the vibration characteristics of a single droplet on sphere-to-plane set-up were presented. For simplicity, the experiment was designed to be axis-symmetrical. In reality, water droplets are located on the surface of overhead line conductors. A controlled experiment has been performed on high voltage overhead line conductor to study the vibration of large population of water droplets in a more representative geometry.

A micrometer syringe was used to control droplet sizes. Twenty sessile drops and twenty pendent drops (50 mm^3 in volume) are manually applied on a 20 cm length of conductor. The applied voltage increases from 0 kV to 110 kV within ten seconds for each experiment and then remains constant at 110 kV (equivalent surface gradient: 18 kV/cm) for 5 minutes when equilibrium state has been reached. The high speed camera with 1200 frames per second was used to record the motion during each

vibrating cycle. As shown in Figure 4-16, the images captured are processed in MATLAB. A specific MATLAB code is created for both pre-process and post-process. The pre-process employs 'Image Deblurring Algorithms' and 'Edge-Detection Algorithms' to accurately define the boundary of droplets.

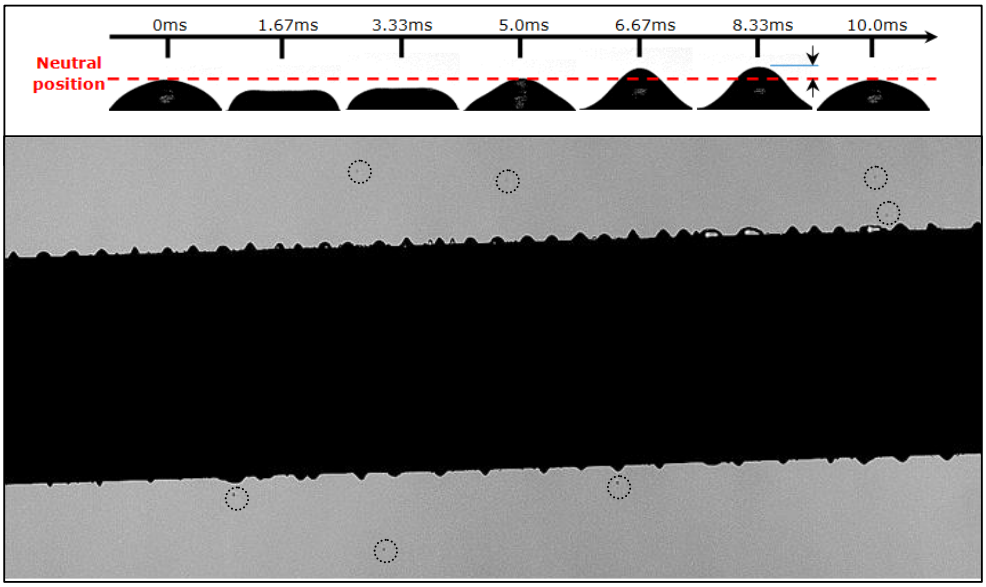

Figure 4-16 High Speed Image for a Row of Droplets-seven ejected sub-droplets can be seen in the dashed circles

Ejection phenomena can be observed from GAP type conductors as fine particles continuously being created from the tip of water droplets. These are highlighted in Figure 4-16. For AAAC type conductors however, there are no ejection phenomena. Thirty-four sessile drops and twenty-one pendent drops are seen on the images for the GAP type conductor while twenty sessile drops and eighteen pendent drops are seen on the AAAC type conductor. However, in both cases twenty sessile and twenty pendant droplets were applied initially to both GAP and AAAC conductor lengths. This has led to the conclusion that the GAP conductor tends to increase the population of drops while reducing the individual average volume. AAAC conductor retains the droplets approximately in their initial condition.

The displacement of the vertex of each droplet has been traced from its neutral position and is presented in Figure 4-16. The frequency of the droplet vibration is then computed by counting the number of times the vertex passes the neutral position. The conductor has been energised for 5 minutes long in order to ensure equilibrium state.

Each calculation for frequency covers 20 cycles in order to ensure the reproducibility. Results for frequency distribution are shown in Figure 4-17.

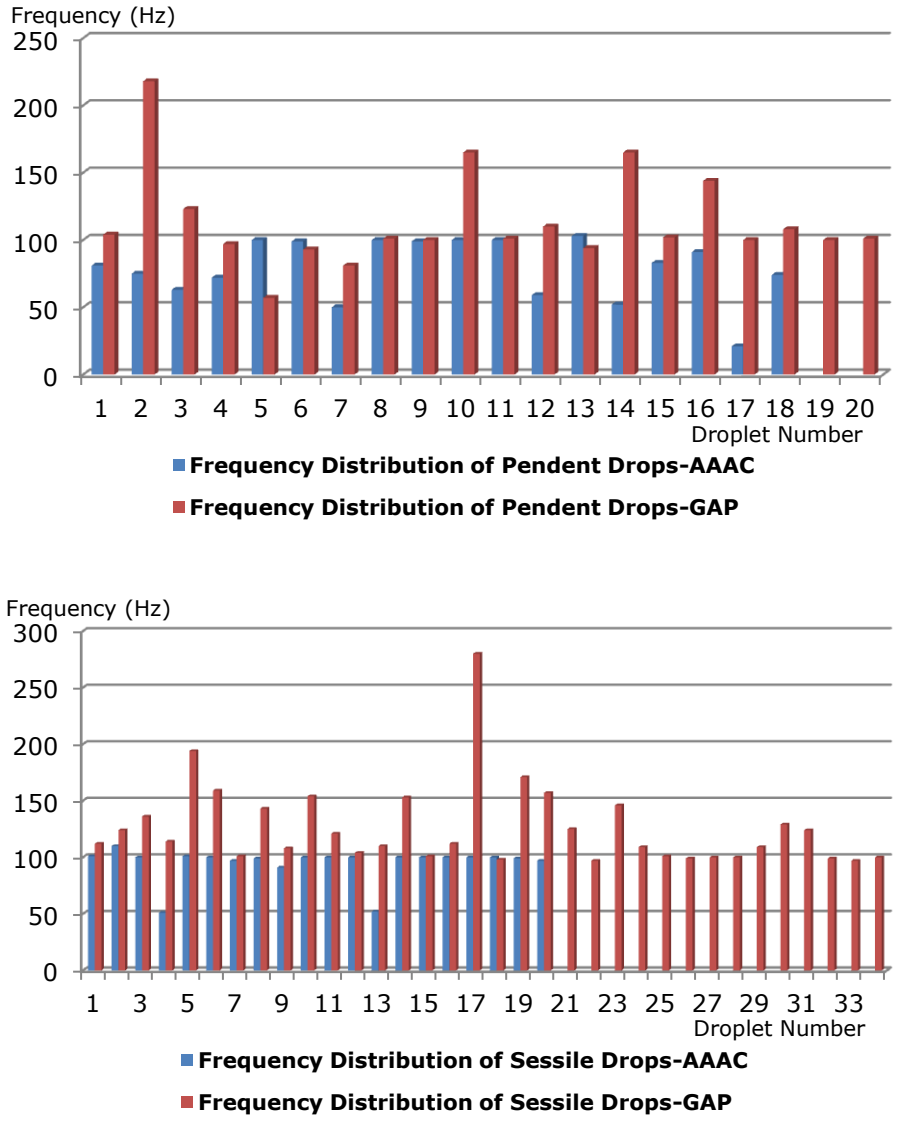

Figure 4-17 Frequency of pendant and sessile vibrating droplets on AAAC and GAP conductor

It is found that:

- Drops on AAAC vibrate in lower frequency band than drops on GAP
- The majority of drops vibrates under harmonics of the power frequency (50, 100, and 150 Hz)
- Sessile droplets have higher vibration frequencies than pendent

4.4 Conclusion

Using the small-scale sphere to plane experiment, a single droplet subject to AC electric field has been investigated. It is observed that droplet vibrates from a conical shape to flattened shape at twice the power frequency (100 Hz).

By synchronising the voltage signal with the high speed images, the electric field at each image can be calculated from FEA model. The calculations have shown that the electric field varies with both droplet shape and applied voltage. It is observed that the electric stress reaches its maximum when the shape of water droplet is flattened while encounters a minimum when the droplet is approaching the conical shape. The computation results also identified that the shapes of the droplet can either reduce or enhance the electric field. The maximum field a conical shape droplet can have is 1.3 times higher than its natural shape. Similar results can be found in a literature [33].

Similar experiments have been carried out on a section of real conductor with a number of pendent and sessile droplets. The vibration frequencies of these droplets are detected under steady state. Results have shown that most of droplets were vibrating at 100 Hz while some droplets were vibrating at harmonics frequencies of the main supply (200 Hz typically).

Ejection phenomena are observed on droplets under AC excitation. Large droplets eject sub-droplets to reduce their mass until stability has been reached. This indicates that although the rain droplets can form randomly as an initial condition, their sizes are tend to approach a certain value which is the threshold value under which droplets can vibrate stably without losing any mass.

To summarize: the droplet's shape can enhance its surface electric field by about 30%. This enhancement of field leads to larger corona discharges due to the higher electrostatic fields. Vibration frequencies of droplets are observed to be distributed mainly at 100 Hz while some are at 200 Hz. Droplets can reduce their mass by ejection until a steady state vibration process is reached.

To study the noise output of conductor from wetted condition, a controlled experiment will be presented in the next chapter.

Chapter 5 Experimental Design and Instrumentation

5.1 Introduction

In this chapter the method of determining the acoustic output from individual conductors is described. Cylindrical cage experiments are an effective, proven way to study the environmental impact of transmission line conductors (see Section 2.3). A cage experiment for audible noise examination is introduced in this chapter. An anechoic chamber has been designed to isolate the background noise as well as the transformer hum noise. It prevents reflections inside the chamber which eventually produced a free field environment for noise measurement.

An appropriate cage radius was first selected by considering the various conductor configurations likely to be tested. Results from Chapter 3 are used as reference electric field values to determine the proper dimension of the whole set up.

The instrumentations for acoustic, electrical and high speed imaging are introduced within this chapter.

5.2 Design Criterion for the Anechoic Chamber

There are two main background low frequency noise sources inside a high voltage laboratory:

- Electrical switching devices, such as contactors, produce acoustic noise at 100 Hz and its harmonics.
- High voltage transformers produce 'hum' (mainly 100 Hz and its harmonics) due to the 'magnetostriction effect'.

In order to insulate the system from the background noise, the first challenge for an anechoic chamber is to effectively reduce low frequencies. This is achieved by constructing an enclosure using acoustic insulation material.

The second objective is to prevent sound reflections inside the chamber, and thereby create a 'free field' for sound measurements. Wedges with sound absorbing material are employed to address this. The manufacturer of the anechoic chamber (AGS Noise Control Ltd) was selected from a range of commercial suppliers on price, delivery and performance. The specific reason of selecting AGS is that they could supply a demountable solution for use inside the high voltage laboratory of the University of Manchester.

5.2.1 Sound Insulation Panels

The sound insulation panels (Figure 5-1) have a sheet metal thickness of 0.7 mm and a 50 mm core of cross-layered mineral wool. In the single-sided perforated configuration, this panel achieves sound reduction of 36 dB Rw and attains absorption class A (according to the standard for building acoustics ISO 140-4).

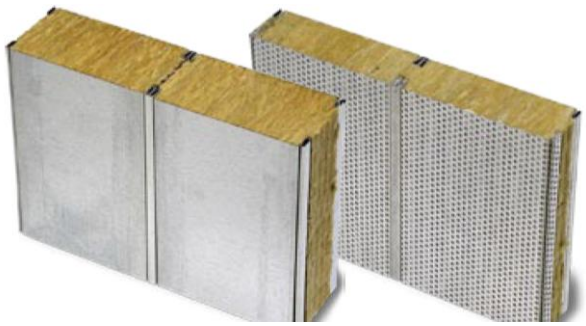

Figure 5-1 Panels for acoustic insulation

5.2.2 Foam wedges

The foam wedges (Figure 5-2) are designed in a way to maximize the ability to absorb sound waves and prevent reflections. They are designed specifically for low frequency sound ranging from 100 Hz to 300 Hz.

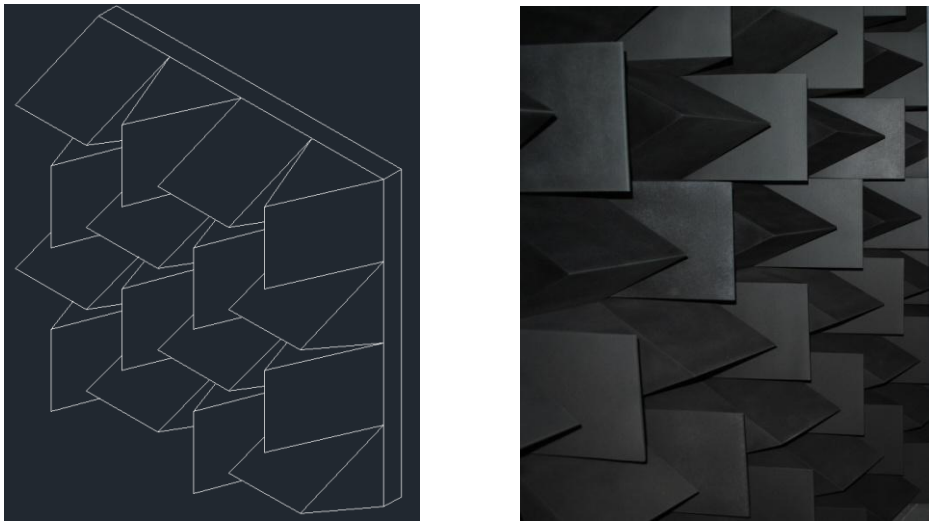

a) b)

Figure 5-2 Foam wedges (a) and attached on the wall of the anechoic chamber (b)

These wedges are filled with porous foam to absorb sound waves. The surface is coated with carbon to maximize the effective contact area with air thus achieve high degree of sound absorption. The shape of the wedge is arranged in a way, that when low frequency sound wave approached it, the majority of the sound energy will be consumed by absorption and diffuse reflection. As a result, the reflection of a sound wave from the surrounding walls is prevented inside the anechoic chamber.

5.2.3 Construction of the Anechoic Chamber

Limited by the laboratory space and the high cost of sound insulation material, the dimensions of anechoic chamber were selected as: 10.5 m (length) * 4.3 m (width) * 3 m (height). As shown in Figure 5-3, the anechoic chamber consists of the following components:

- Framework including vertical and horizontal beams
- Sound insulation panels
- Foam wedges
- Accessories such as doors and an aperture for wiring

a). frames for anechoic chamber

b). installation for the frame

c). fit in panels

d). half-assembled anechoic chamber

e). last side-panel fitted in

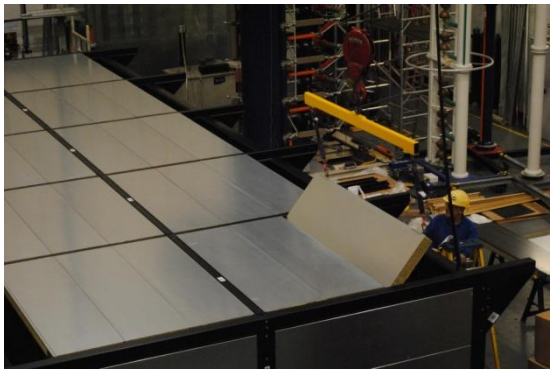

f). last roof-panel fitted in

g). installation for the doors

h). attach the wedges

Figure 5-3 Construction of the anechoic chamber

The assembling of the anechoic chamber is supervised by an experienced noise control engineer to ensure the designed parameters are achieved (Figure 5-4).

a). outside view of the anechoic chamber

b). outside view of the anechoic chamber

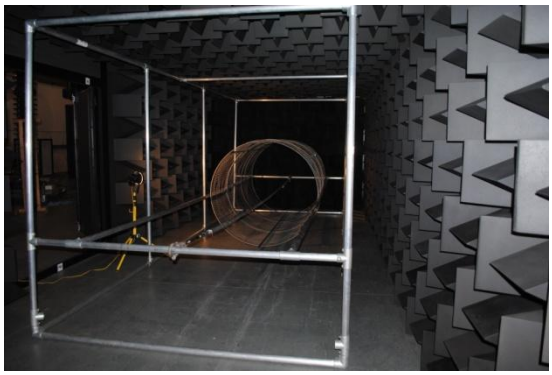

c). inside view of the anechoic chamber

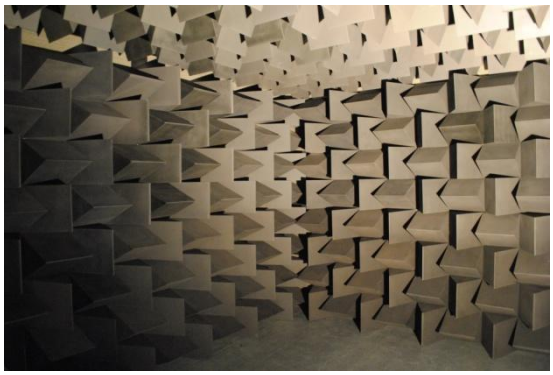

d). inside view of the anechoic chamber

Figure 5-4 Completed view of the anechoic chamber

5.2.4 The Acoustic Performance of the Anechoic Chamber

A series of acoustic measurements were carried out to evaluate the performance of the anechoic chamber. There is no existing standard to regulate the measurement for an anechoic chamber, so most of the measurements carried out here refer to the standard for building acoustics (ISO 140-4). The most representative measurements are:

1) sound insulation measurements for background noise

Measurements are taken in ten selected positions, and an average result is obtained.

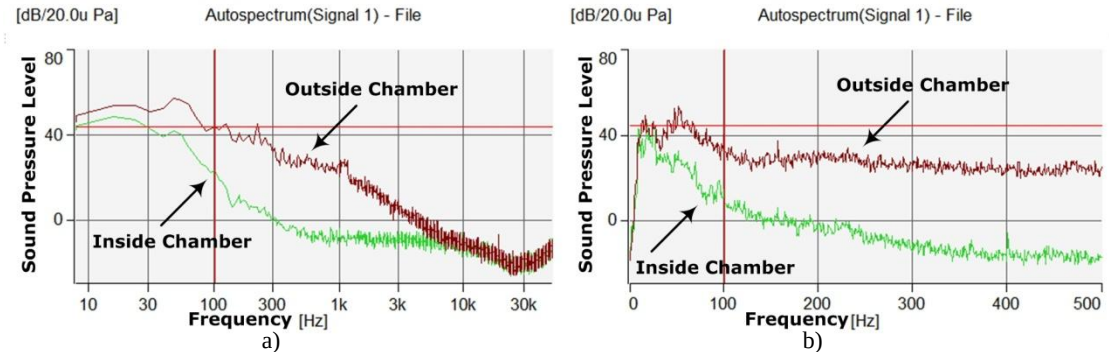

Figure 5-5 Background noise mitigation by anechoic chamber-one of the ten measurements

As shown in Figure 5-5, one of the ten measurements is selected as an example. There is approximately 22 dB reduction in average for the 100 Hz noise. The A-weighted overall sound pressure level is reduced by 35 dBA from the background level.

2) reverberation time measurement

The reverberation time is the decay time for sound within the chamber after an impulsive excitation. It is a significant index for the performance of the sound absorbing wedges inside the anechoic chamber. An impulsive sound signal is first applied on a standardized sound source for a short period of time, and then is stopped instantaneously. The microphone is utilized to record the sound pressure level for the whole period time to capture the decay curve of sound.

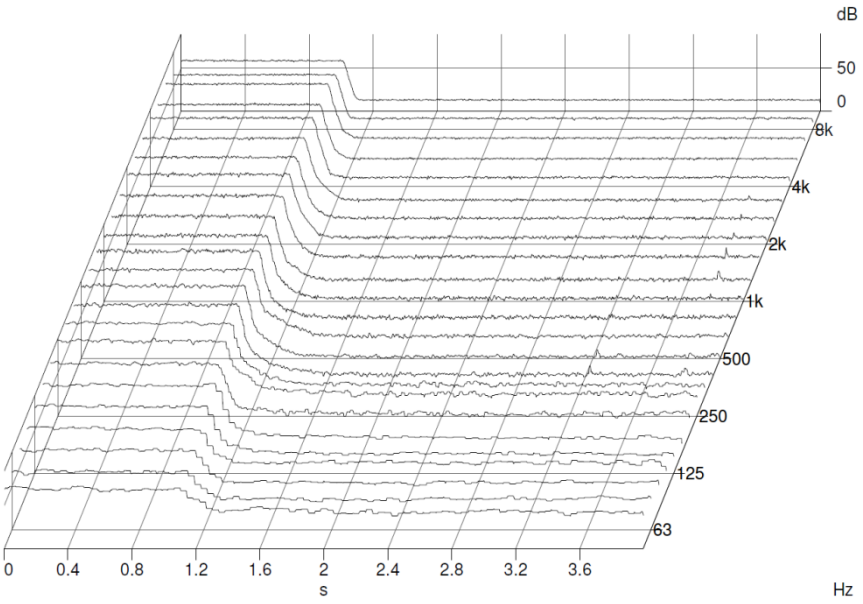

Figure 5-6 Reverberation time plot for various frequencies (x-axis: time; y-axis: frequency; z-axis: SPL)

As shown in Figure 5-6 the impulsive sound signal stops at 1s and experienced decay after that. The decay curve for high frequency components (6 kHz) is more rapid than for the low frequency component (63 Hz) indicating that the low frequency acoustic wave decays more slowly than the high frequency acoustic wave. The detailed information of reverberation decay time is listed in Table 5-1. As a comparison, the reverberation time at 250 Hz for a conference room with the same volume is 1.14 s which is ten times higher than the anechoic chamber. In acoustic measurement, lower reverberation time indicates higher accuracy especially in measuring low frequency noise.

Table 5-1 Reverberation Decay Time for Various Frequencies

Frequency(Hz)	50	63	80	100	125	160	200	250	315	400	500	630
Decay Time(s)	0.65	0.45	0.28	0.20	0.23	0.20	0.14	0.11	0.13	0.08	0.08	0.09
Frequency(Hz)	800	1k	1.25k	1.6k	2k	2.5k	3.15k	4k	5k	6.3k	8k	10k
Decay Time(s)	0.06	0.07	0.07	0.07	0.08	0.07	0.09	0.08	0.09	0.08	0.09	0.10

5.3 Design Criterion for the Cage Experiment

The 'Cage experiment' is an HV laboratory set-up especially for corona study. Figure 5-7 shows a prototype cage experiment set-up in the Manchester HV lab. The high voltage is applied on the inner conductor (it can be replaced by various types of conductors including: AAAC, ACCC/CTC, GAP etc), while the outer meshed cage is earthed. This arrangement enhances the surface electric stress by the presence of the cage. An intense electric field on the surface of inner conductor can then be achieved at lower voltage levels. For example, by reducing the cage radius to 0.75 m, only a 150 kV single phase supply is required to obtain the similar surface field strength seen by 400 kV system transmission line conductors.

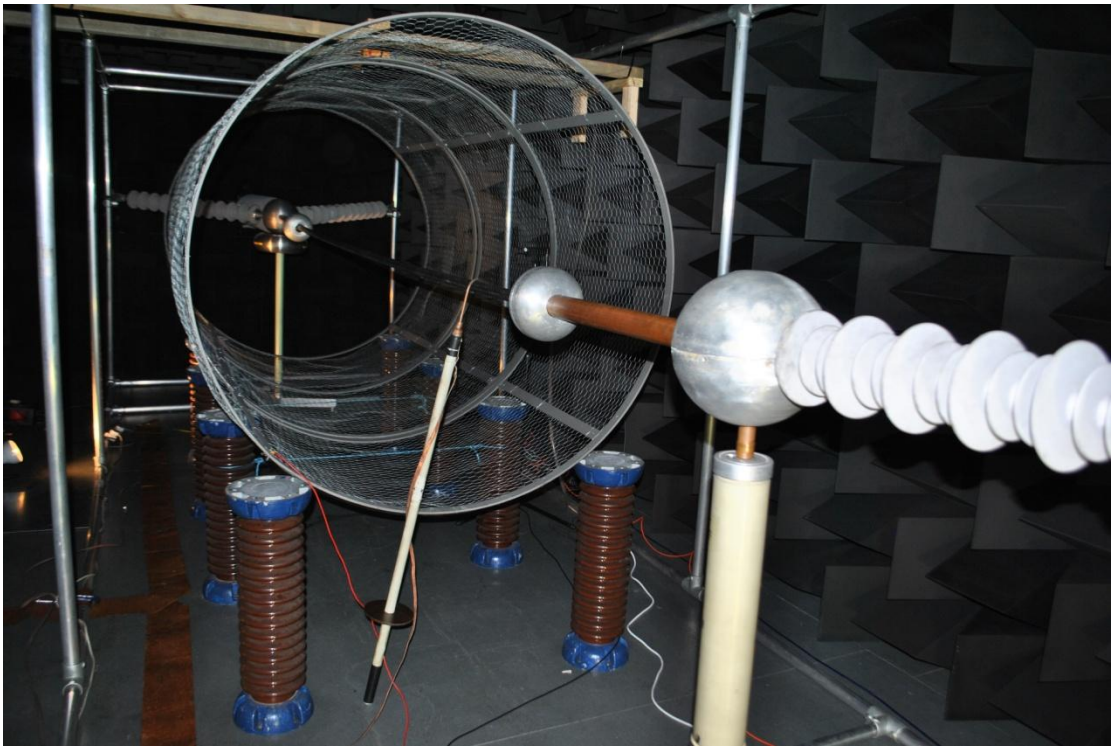

Figure 5-7 Cage experiment for studying the conductor audible noise

As presented in Figure 5-8, three critical parameters need to be defined:

- Radius of the Cage

- Radius of the End sphere
- Length of the conductor within the cage section

The cage radius needs to be defined properly to not only provide enough surface field strength, but also to prevent flash over between the conductor and the cage. Stress relief devices are introduced to mitigate the excessive corona discharges due to end effects. As the dashed lines show in Figure 5-8, the cage has been divided into three sections. The end sections have non-uniformly distributed electric fields due to end effects while the middle section can be approximately treated as having a uniformly distributed divergent field. In general, the longer the end sections are, the lower degree of distortion will be seen in the middle section. In the experimental set-up, in order to generate enough acoustic noise, the middle section needs to be as long as possible. However, the entire length is limited to around 6.5 meters due to the restricted space inside the anechoic chamber. There will thus be a trade-off when determining the length of the end and the mid sections. The experimental rig has been built so the cage length can be readily extended.

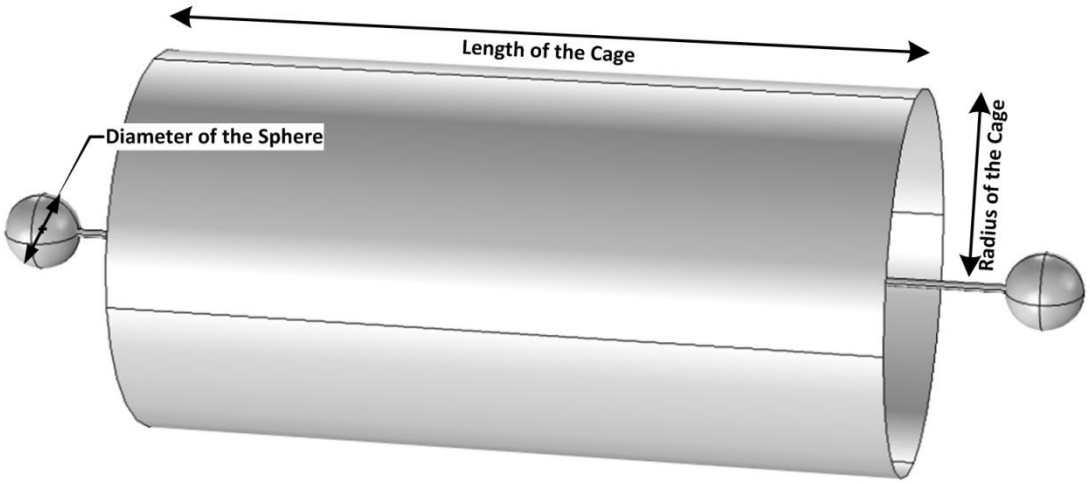

Figure 5-8 Sketch of 'Cage Experiment'

Following the theoretical study of existing methods in Section 2.2, the next section analyzes the possibilities for improving the calculation accuracy, and proposes a new method in computing surface gradient which combines finite element method and charge simulation method.

5.3.1 Cage Radius Consideration

The design objective was to build up a cage which allows experiments on single, twin, triple and quad bundle. At the same time, the surface electric stress must be controlled to be higher than 16kV/cm which is recognized as the corona inception gradient [14].

a) Single conductor

A single conductor inside a cage has a coaxial geometry as shown in Figure 5-9. If the electric potential of the inner cylinder is U, and the outer cylinder is at zero potential, then the electric field strength on the surface of inner cylinder is:

$$E = \frac{U}{r \times \ln(R/r)}$$

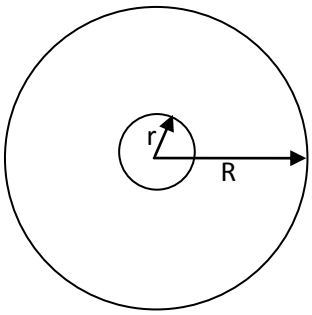

Figure 5-9 'Coaxial Geometry'

The contour plot for surface gradient with respect to conductor and cage radius is shown in Figure 5-10. The following notes depicted from Figure 5-10 to Figure 5-17.

- $E_{average}$ mean value of electric field over the whole surface of the sub-conductor
- $E_{maximum}$ max value of electric field over the whole surface of the sub-conductor

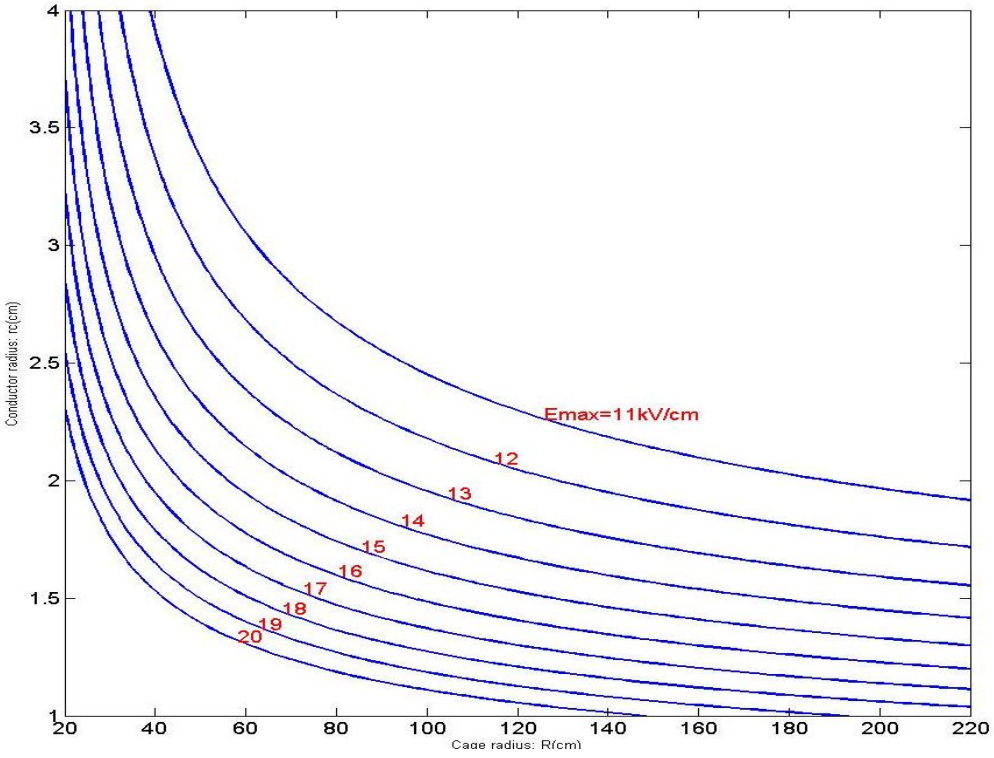

Figure 5-10 Contour plots for 100 kV supply (single conductor)

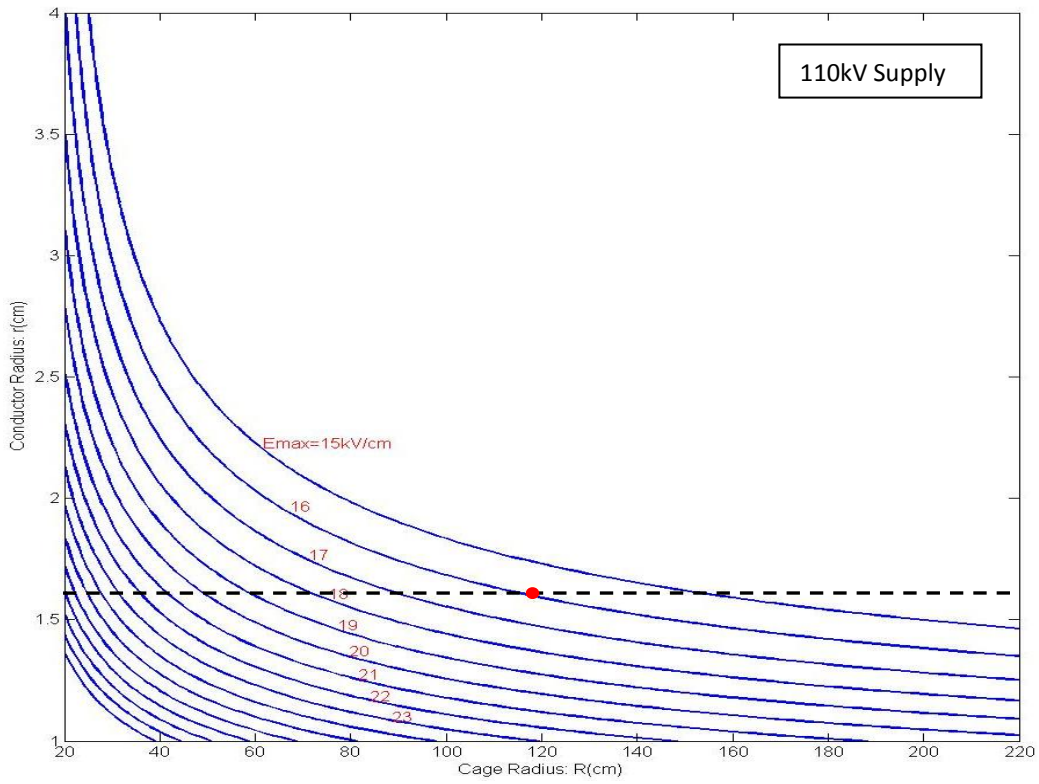

Figure 5-11 Contour plot for 110 kV supply (single conductor)

From Figure 5-10 and Figure 5-11, for a fixed conductor radius of 16 mm, in order to obtain 16 kV/cm of surface gradient, the cage radius must be lower than 80 cm for a 100 kV supply, and 120 cm for a 110 kV supply. This analysis assumes cylindrical (i.e. not stranded) conductors.

b) Twin bundle

For a twin bundle, there is no existing analytical formula to calculate the surface stress. Simulation work on FEA software-COMSOL has been carried out to obtain a series of surface stress values relating both bundle spacing and cage radius.

The conductor radius was fixed at 16mm. By varying the conductor spacing and the cage radius, different field strengths can be achieved. The voltage was fixed at 100kV. In Figure 5-12, the right hand plot gives the electric potential plot for a twin bundle within a cage. The left plot is the field strength plot around the surface of the left-hand sub-conductor. Similar processes were carried out for various bundle spacing and cage radius. Figure 5-13 was obtained as a contour plot.

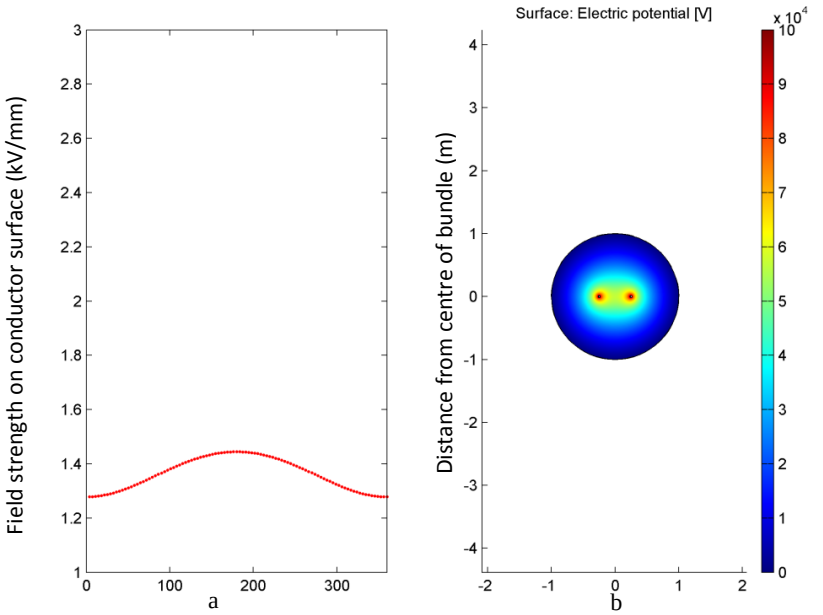

Figure 5-12 Surface stress plot of left-hand sub-conductor (a); electric potential plot for a twin bundle (b)

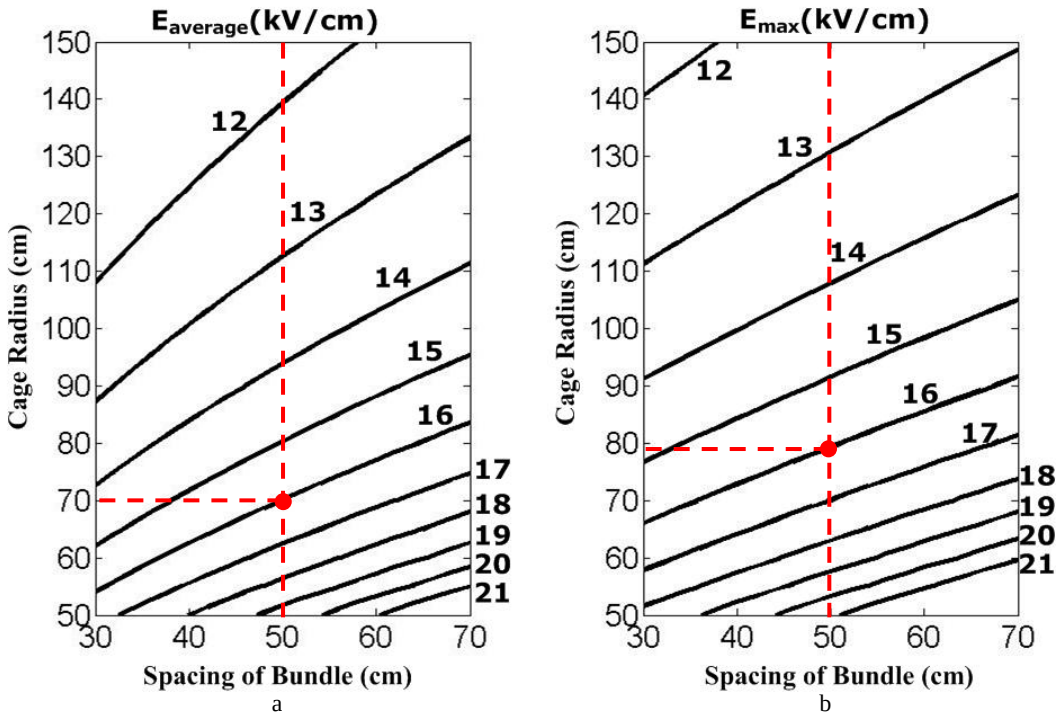

Figure 5-13 Average (a) and maximum (b) contour plot for a twin bundle inside a cage (100 kV supply)

In Figure 5-13, the dashed red line showed the cage radius needed for 500 mm spacing bundle to generate 16 kV/cm (cylindrical shape assumed, RMS value) electric stress.

c) Triple bundle

Similar processes were followed for a triple bundle to obtain the contour plot as presented in Figure 5-14 and Figure 5-15 show the simulation results and the surface electric stress distribution for each sub-conductor with a 100 kV supply.

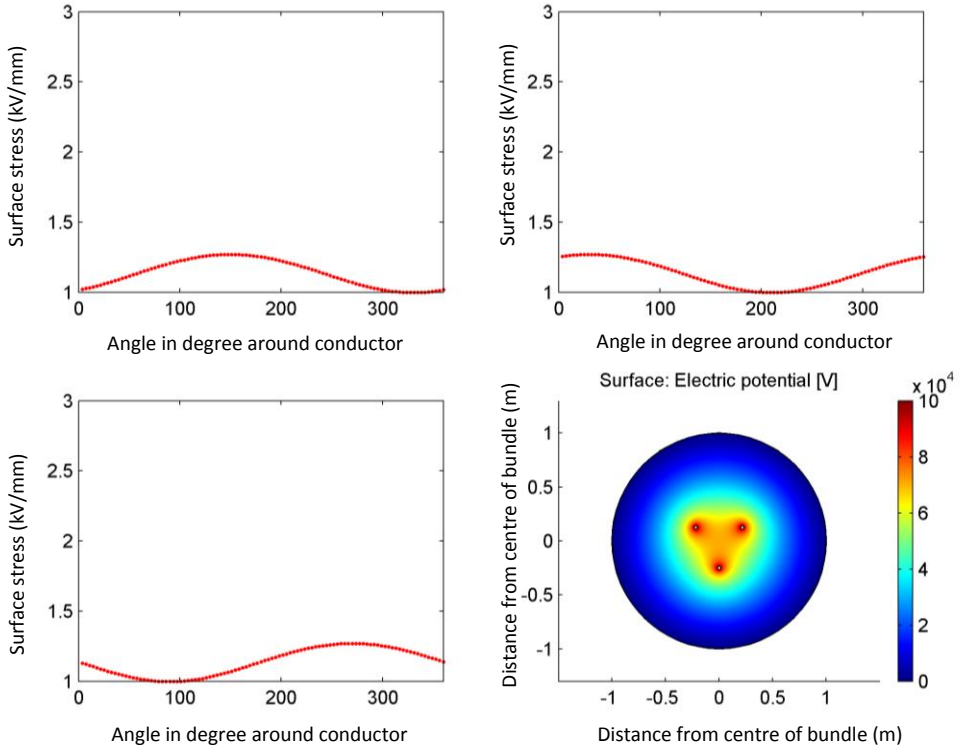

Figure 5-14 Surface stress plot of sub-conductors and electric potential plot for a triple bundle

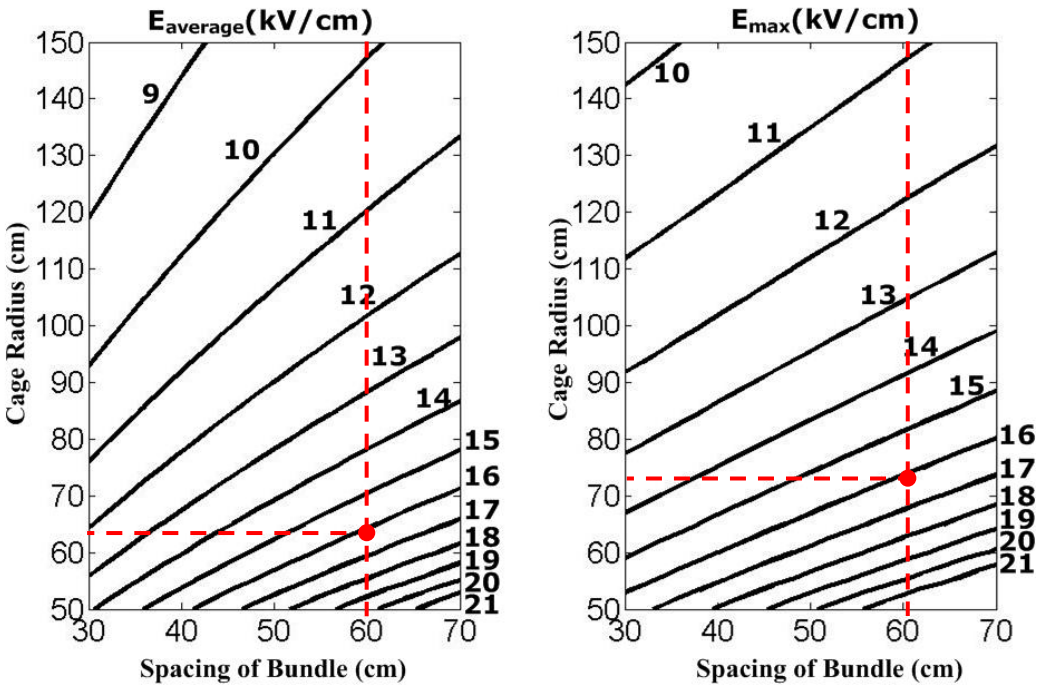

Figure 5-15 Average (L) and maximum (R) contour plot for a triple bundle inside a cage (100 kV)

d) Quad bundle

Similar processes were followed for the quad bundles to obtain the contour plot presented in Figure 5-16 and Figure 5-17give the simulation results and distributions for each sub-conductor.

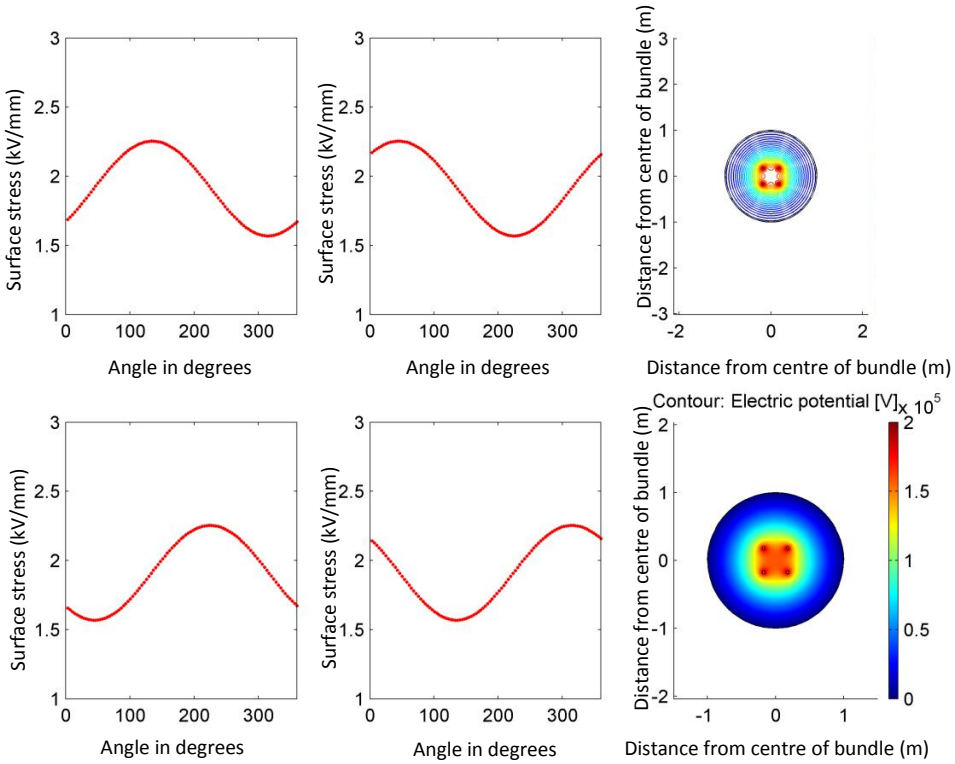

Figure 5-16 Surface stress plot of sub-conductors (left and middle); electric potential plot (lower right) and electric potential contour (upper right) for a quad bundle

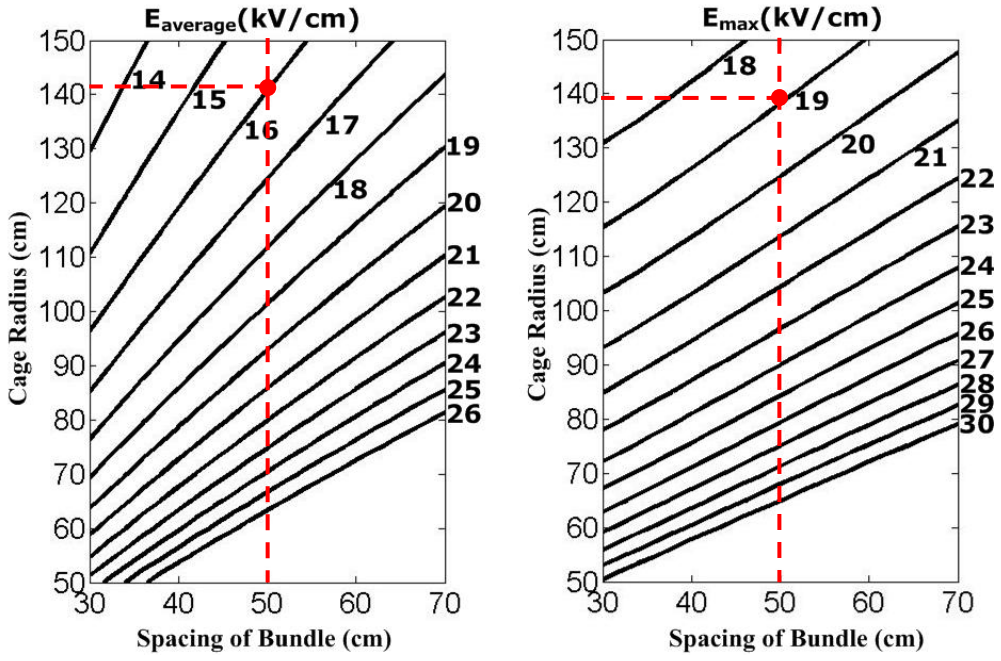

Figure 5-17 Average (left) and maximum (right) contour plot for a quad bundle inside a cage (200 kV supply)

It was found that if the value for cage radius is relatively low (such as 0.5 m), the field distribution on the surface of each sub-conductor is distorted due to the proximity of cage. In this circumstance, the experimental results of electric field on the surface of sub-conductors cannot represent the quad bundle in transmission lines. Figure 5-18 shows the simulation result for a quad bundle (conductor radius 16mm with 500mm spacing) in a cage of 0.5 m radius and 150 kV supply voltage. Figure 5-19 shows results for an isolated quad bundle with 10 times the spacing used as the radius of the simulation boundary condition and a 400 kV supply voltage.

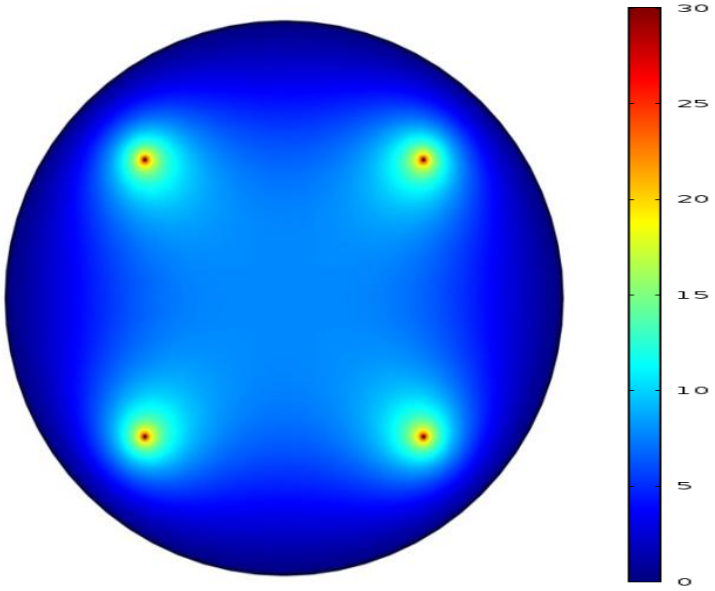

Figure 5-18 Simulation results for cage experiment with cage radius 0.5 m (150 kV supply)

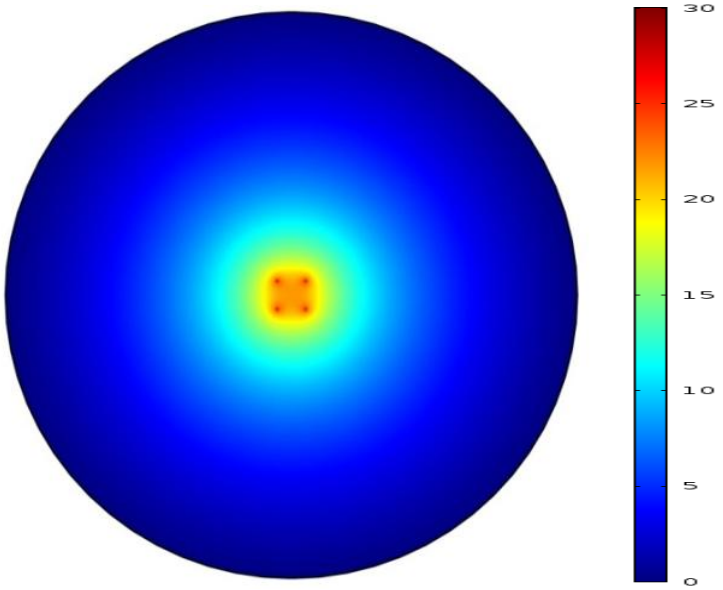

Figure 5-19 Simulation results for isolated quad bundle (400 kV with 10 times spacing as boundary condition)

In order to assess the field distortion in the small radius cage, the surface field strength of each sub-conductor was plotted in these two simulations, see Figure 5-20.

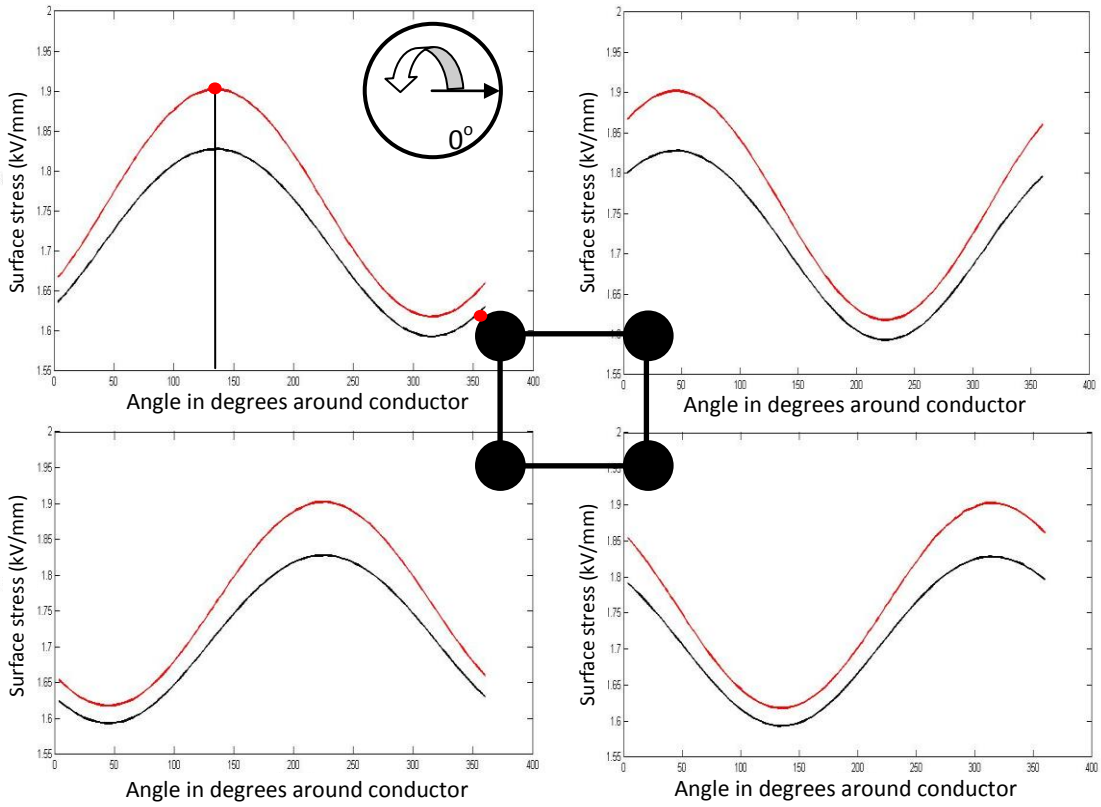

Figure 5-20 Surface field distribution comparison between small cage radius (0.5 m) (the red curves) and isolated quad bundle (the black curves) for each of the conductors in the bundle

In Figure 5-20, the red curve represents the surface field in a small radius cage with a quad-bundle, and the black one is the surface field plot of a 400 kV isolated quad-bundle. It can be observed that for a small radius cage quad bundle (red curve) the surface stress variation is larger than for the isolated quad-bundle (black curve). This would not be an appropriate experimental model because the whole surface of each conductor could not be accurately modelled.

In Figure 5-21, the dotted curve is the isolated 400 kV case with maximum surface stress at 18.28 kV/cm; the solid curves are the electric field distribution on one sub-conductor with different cage radii (0.55-2 m) at an appropriate voltage level to maintain surface stress to be the same as 400 kV real transmission line (18.28 kV/cm). It can be concluded that a cage radius higher than 0.75 m gives sufficient agreement to the isolated 400 kV case (1% deviation). However, note has to be made that the analysis presented here only considers the electric field on the surface of a conductor,

the field distribution away from the conductor is different compared to the real 400 kV overhead lines. This is an inherent limitation for cage experiment.

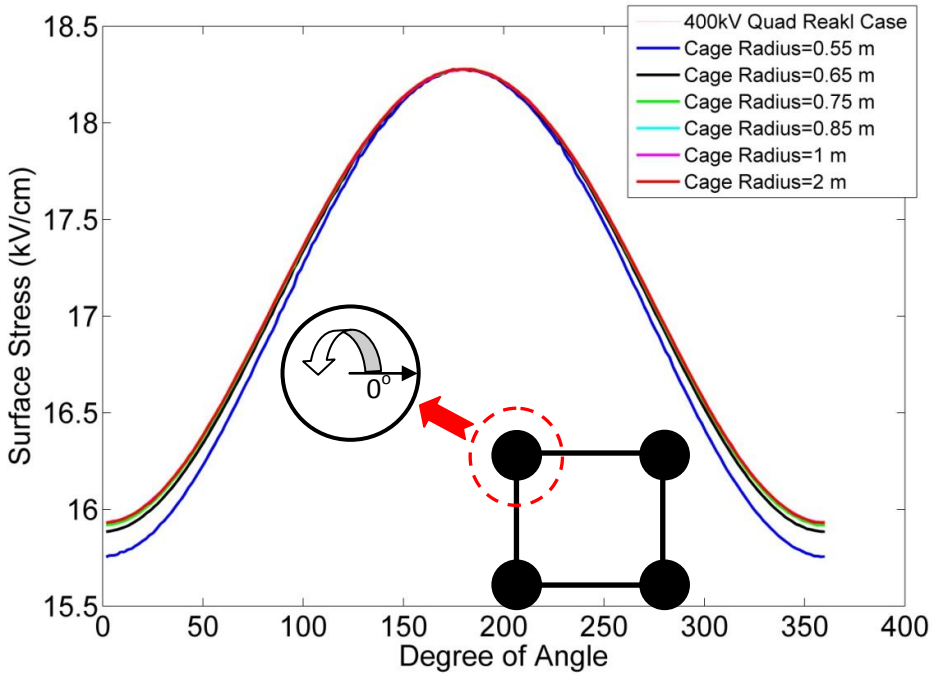

Figure 5-21 Surface field distribution comparison between small cage radius (0.5 m) and quad bundle

5.3.2 End Effect Considerations

Corona discharges are most likely to initiate at sharp edges or protrusions. In the cage experiment, each end of the cylindrical conductor will introduce a divergent electric field as presented in Figure 5-22. This enhanced field will then initiate excessive corona discharges which is not desirable. By introducing a spherical guard at each end, the electric field can be controlled so that the middle section has higher surface stress.

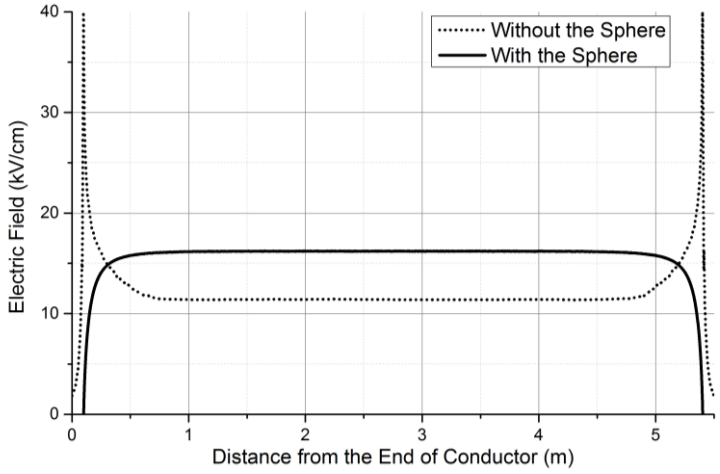

Figure 5-22 Surface field strength plot for a cylindrical conductor with and without corona guard

In Figure 5-22 (right) spherical guards with radius of 10 cm effectively reduced the divergent field at each end of conductor.

Figure 5-23 shows a plot from COMSOL for both potential and electric field strength.

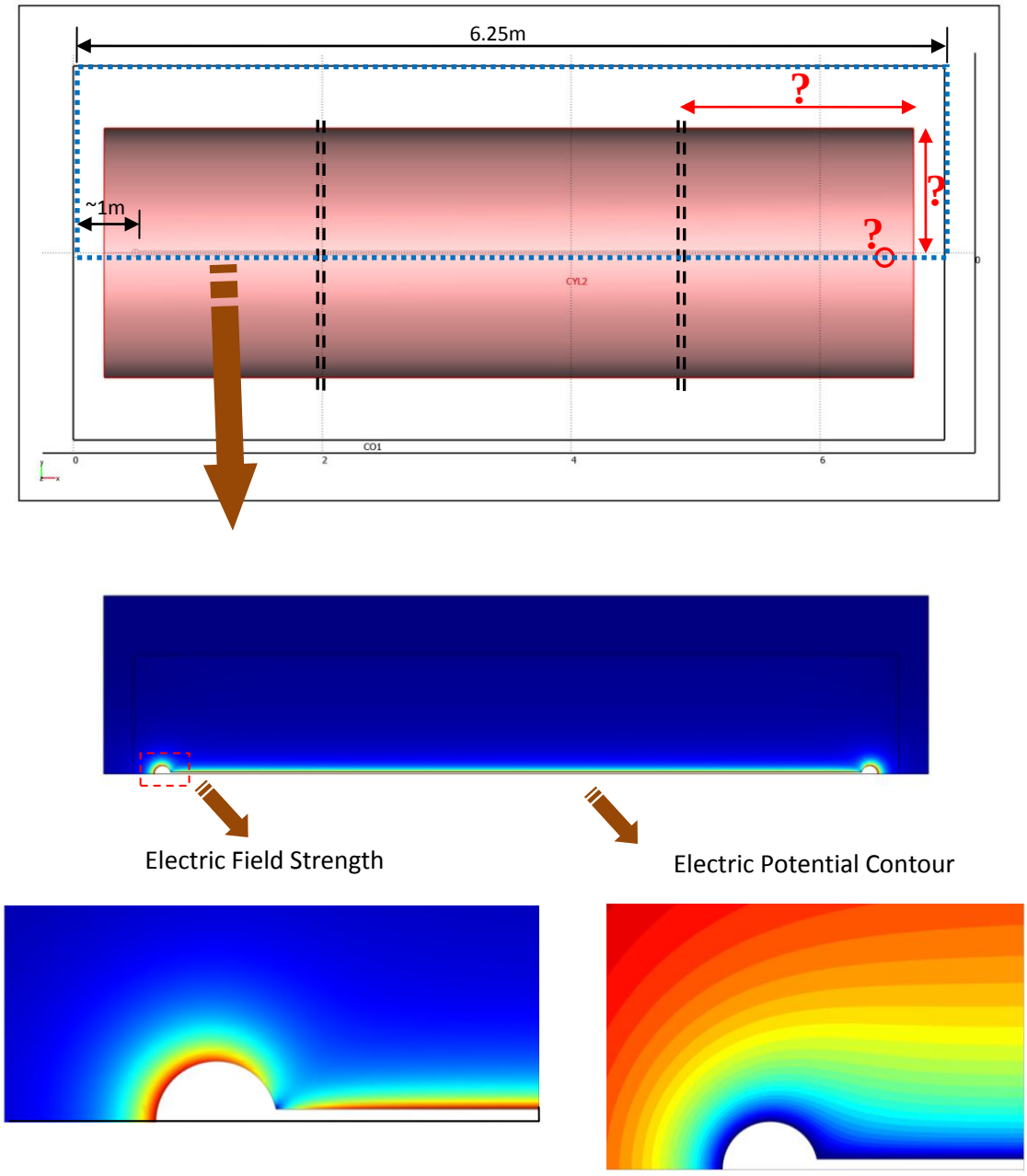

Figure 5-23 Surface stress distribution and electric potential contour

5.3.3 Evaluation of the Field Distortion

As presented in Fig 5.18, in order to determine the overall length of the cage in the maximum 7 metres length environment, 6 simulations with a cage length from 4 m to

6.5 m were carried out in COMSOL. By comparing the field distortion within the dashed area as in Figure 5-24, the 6.5 m cage was found to have the lowest degree of distortion due to end effects. The overall length for the cage was thus chosen as 6.5 m, to mitigate end effects.

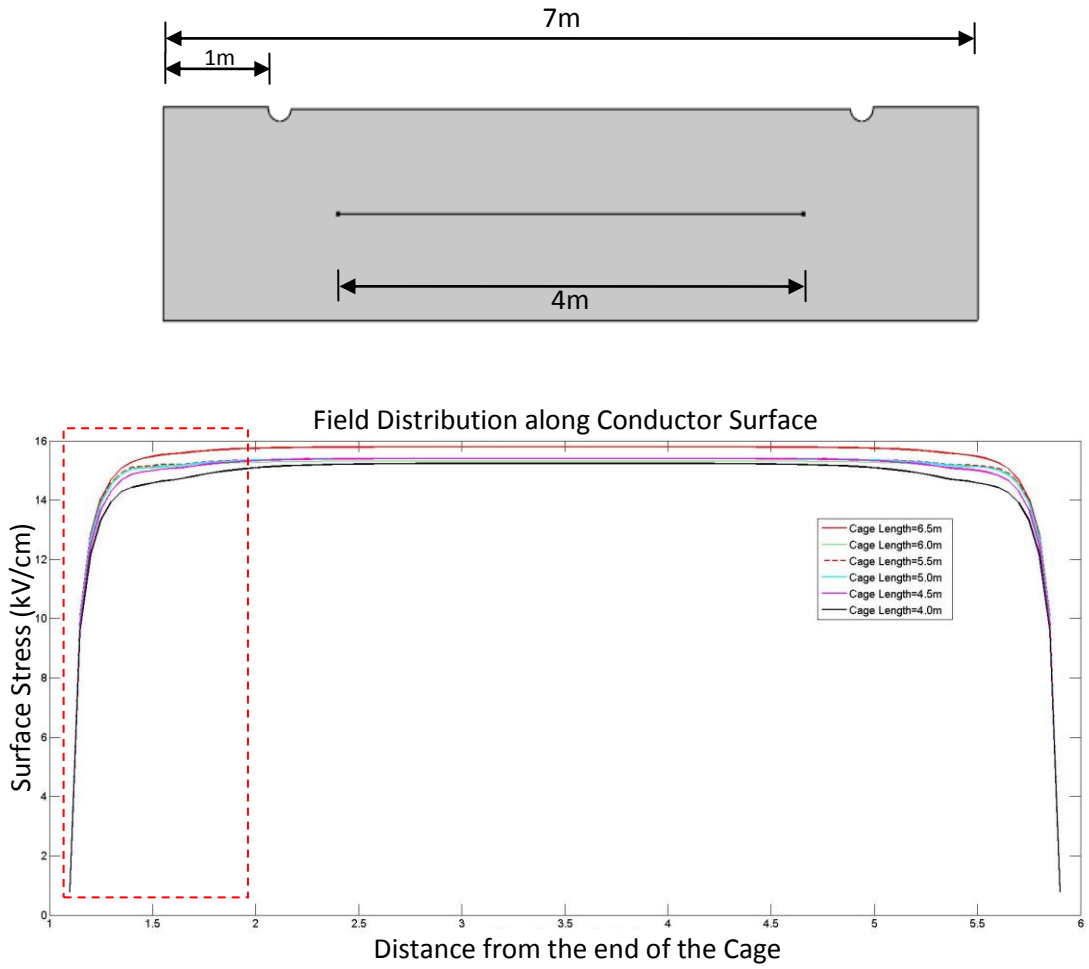

Figure 5-24 Surface field distribution comparison between small cage radius (0.5 m) and isolated quad bundle

As shown in Figure 5-25, the other parameter needing to be defined is the length of the middle cage section. As the middle section is the section in which the electric field distribution of practical transmission line conductors will be simulated. The design criterion is to maintain uniformity of the surface gradient in the middle section.

As in Figure 5-25, this simulation is based on a cage experiment with 1.5 m diameter cage, a conductor length of 6 m and a cage length of 6.5 m. The supplied voltage is 100 kV.

The plot and tabled data (Figure 5-25) present the surface gradient distribution along the conductor surface in kV/cm. The surface gradient is varying rapidly in each end of conductor, but maintained at a constant value in the middle section (to within 0.01%).

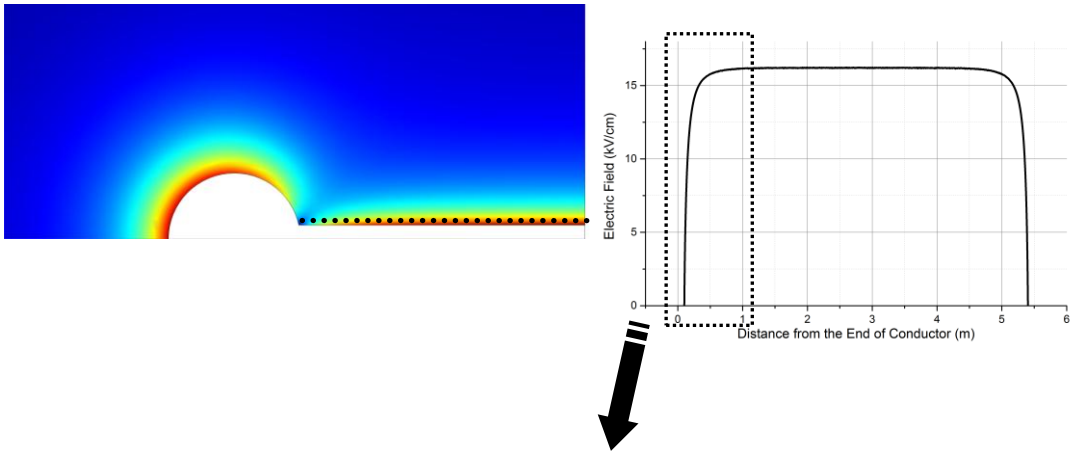

Point Number	1	2	3	4	5	6	7	8	9	10
Distance (m)	0.600	0.658	0.716	0.774	0.832	0.890	0.948	1.006	1.064	1.122
E-field (kV/cm)	0.71	10.65	13.25	14.36	14.93	15.25	15.44	15.57	15.65	15.71
Percentage (%)	4.50	67.10	83.50	90.50	94.90	96.10	97.30	98.10	98.60	99.00

Point Number	11	12	13	14	15	16	17	18	19	20
Distance (m)	**1.180**	1.238	**1.296**	1.354	1.412	1.470	1.528	1.586	1.644	1.702
E-field (kV/cm)	**15.74**	15.77	**15.79**	15.81	15.82	15.83	15.84	15.84	15.85	15.85
Percentage (%)	**99.20**	99.40	**99.60**	99.70	99.70	99.80	99.80	99.85	99.88	99.90

Point Number	21	22	23	24	25	26	27	28	29	30
Distance (m)	**1.760**	1.818	1.876	1.934	1.992	2.050	2.108	2.166	2.224	2.282
E-field (kV/cm)	**15.85**	15.85	15.86	15.86	15.86	15.86	15.86	15.86	15.86	15.86
Percentage (%)	**99.92**	99.94	99.94	99.95	99.96	99.97	99.98	99.98	99.98	99.99

Point Number	31	32	33	34	35	36	37	38	39	40
Distance (m)	2.340	**2.398**	2.456	2.514	2.572	2.630	2.688	2.746	2.804	2.862
E-field (kV/cm)	15.86	**15.86**	15.86	15.86	15.86	15.86	15.86	15.87	15.87	15.87
Percentage (%)	99.99	**99.99**	100	100	100	100	100	100	100	100

Figure 5-25 Surface field distribution along the conductor surface (Field strength and percentage of maximum field strength are given)

The data in the table shows that 1.18 m is required for the end section length in order to keep the distortion percentage lower than 1%, 1.296 m for 0.5% distortion, 1.76 m for 0.1%, and 2.398 m for 0.01%.

5.3.4 Corona Inspection

The design criterion for corona fittings is to reduce unwanted corona discharges while maintaining the adequate voltage level for experimental needs. Any protrusions on the high voltage body initiate corona discharges, especially at connections and terminations. As shown in Figure 5-26, two corona rings and spheres (1, 2, 3, and 4) are introduced to mitigate corona discharge from joints and terminations. These stress relief devices are tested under high potential. Corona activity is visually detected by UV camera.

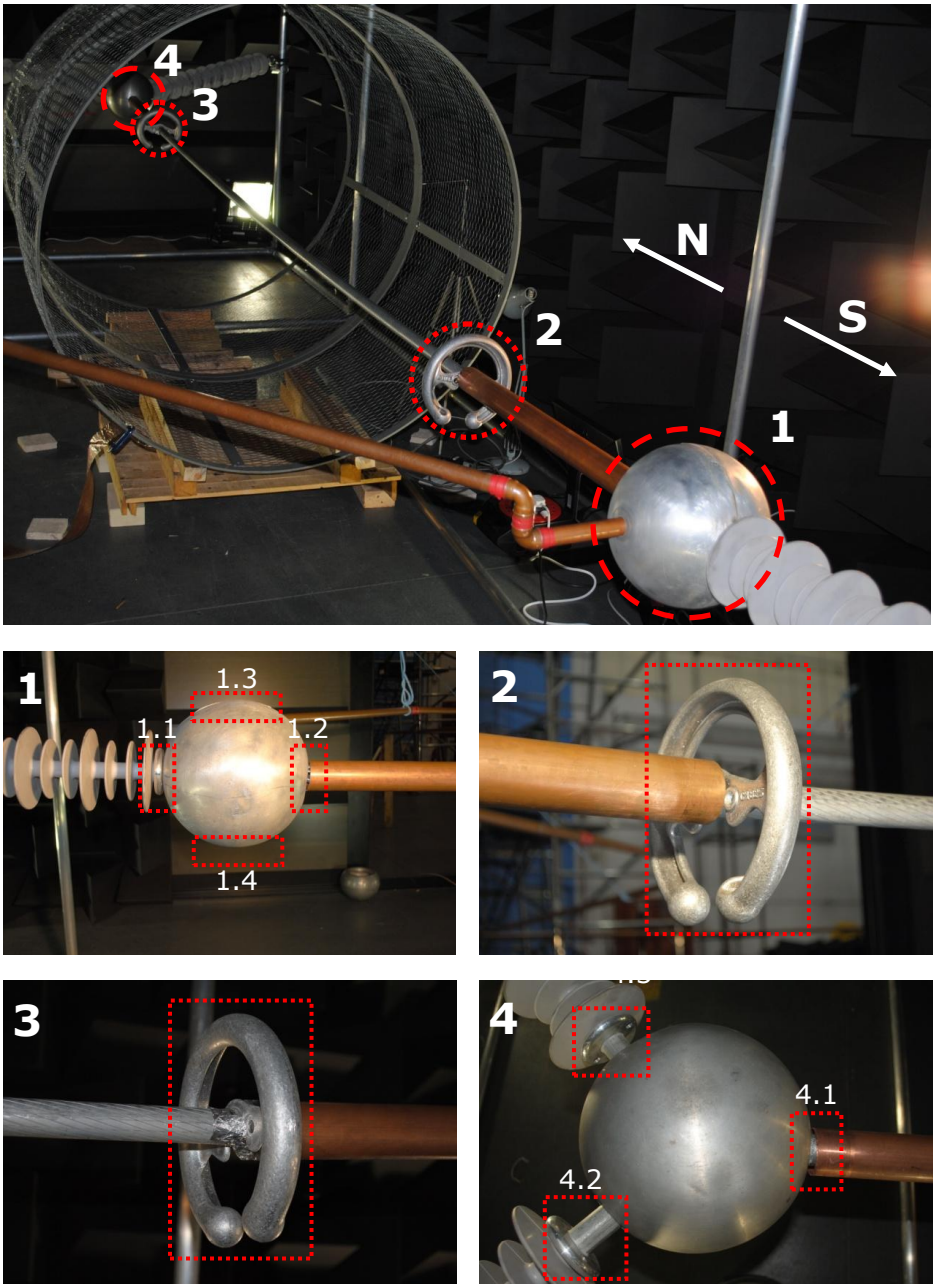

Figure 5-26 Testing positions for cage experiment

The UV images are presented in Figure 5-27, and the inception voltage levels are summarized in Table 5-2. As introduced in Section 5.3.1, the voltage level needed to simulate the overhead line is around 110 kV, and is thereby 30 kV lower than the corona inception from fittings. This gives a corona-free environment to test conductors inside the cage with up to 25 kV/cm surface stress.

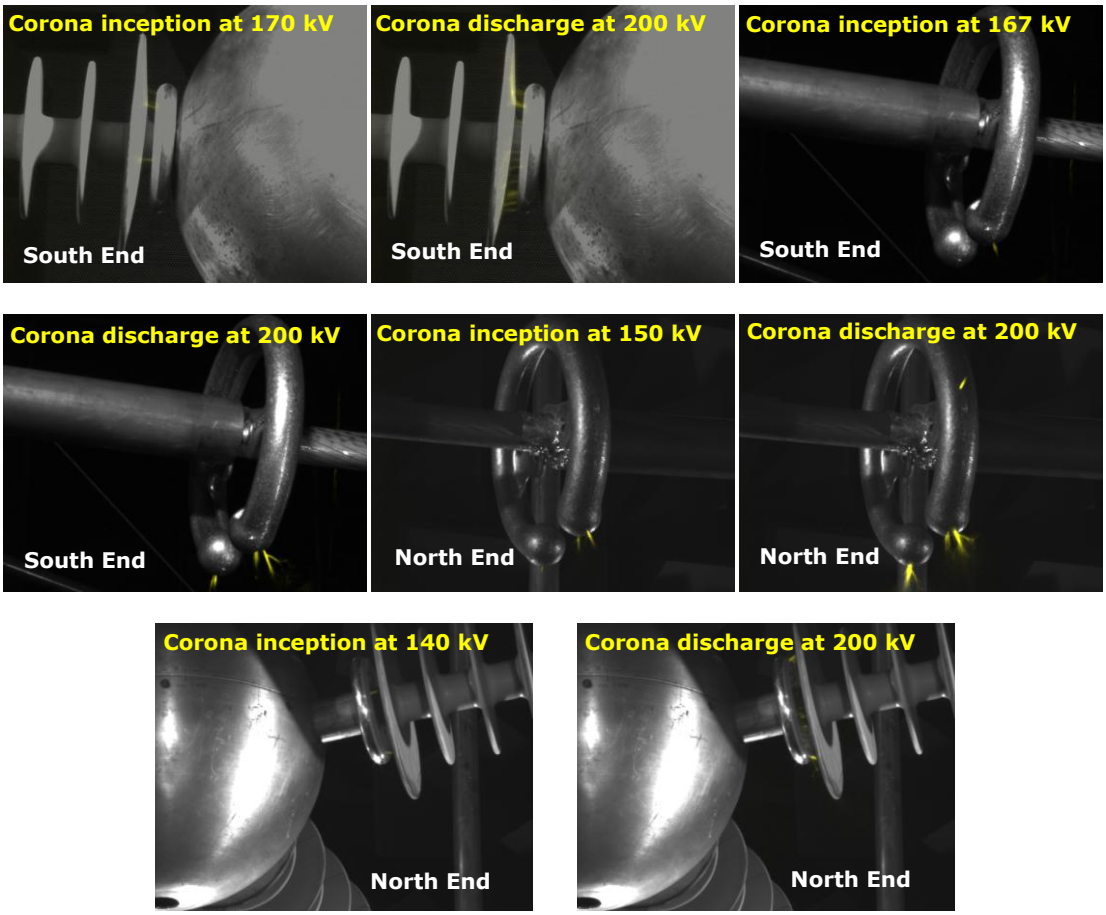

Figure 5-27 UV images for corona detection

Table 5-2 Corona Inception Voltage for Stress Relief Devices

Stress relief devices	South-end corona ring	North-end corona ring
Corona inception voltage	167kV	150kV

Stress relief devices	South-end sphere	North-end sphere
Corona inception voltage	172kV	140kV

The next stage is to decide the voltage level needed to simulate the surface gradient of overhead line conductors. Two methods are employed to select the voltage level:

1. Calculation of the surface stress;
2. Experimental observation of corona inception and development inside the cage section.

Results for the surface gradient calculation on a 400kV overhead line (L2-RUBUS) are shown in Figure 5-28 (for details refer to Section 3.3.1).

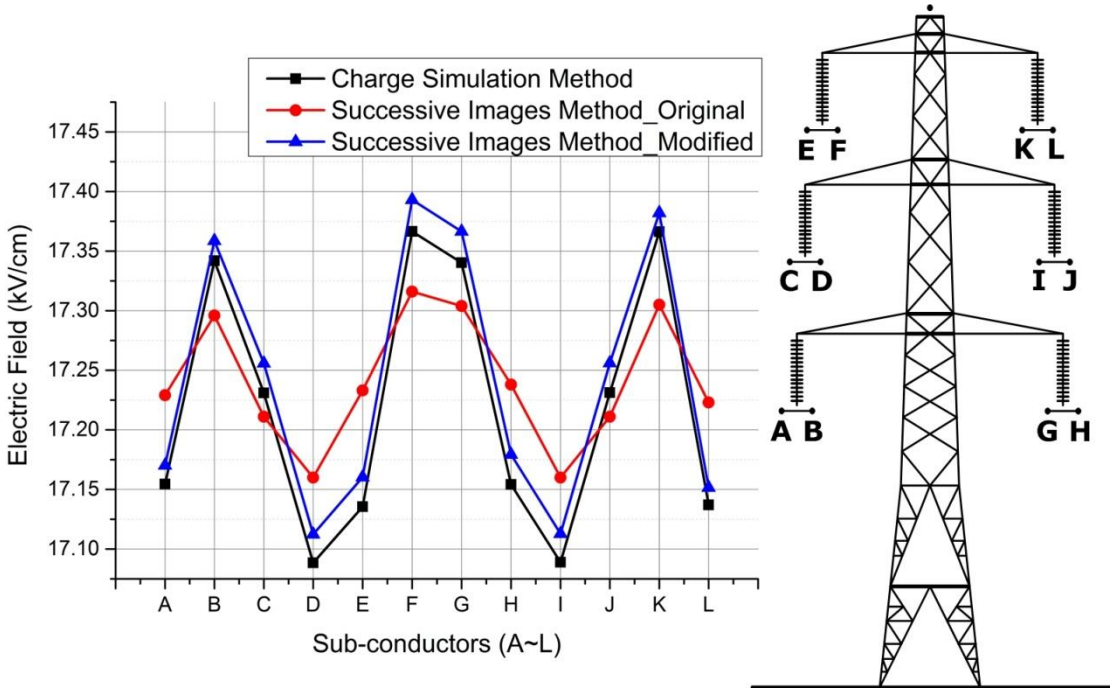

Figure 5-28 Case Study Results (maximum stress for cylindrical assumption) for 400kV Overhead Line

The surface stresses of 12 sub-conductors sit around "17.3 kV/cm" from Figure 5-28. In order to relate this value to the voltage level, the surface gradient for cage experiment is plotted with applied voltages as shown in Figure 5-29.

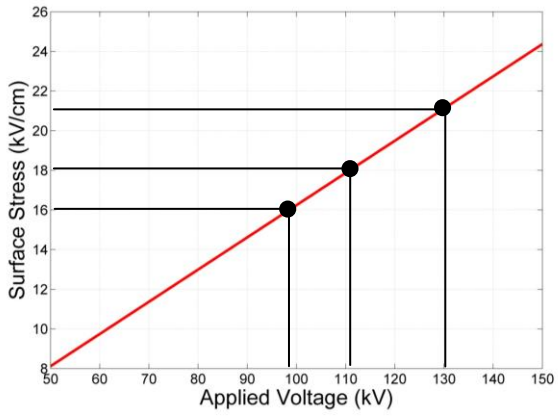

Figure 5-29 Surface stress for cage experimental set-up in anechoic chamber

As shown in Figure 5-29, if 16-18 kV/cm is selected as the range of operational surface gradient in a 400 kV overhead line, the voltage required for the cage experiment is between 98 and 110 kV. It is also interesting to increase the voltage

level up to 130 kV to simulate the surface stress of "21 kV/cm" which reflects an extreme condition for overhead lines in service, beyond service conditions.

Another way to evaluate the proper voltage level is the experimental observation by UV camera as shown in Figure 5-30.

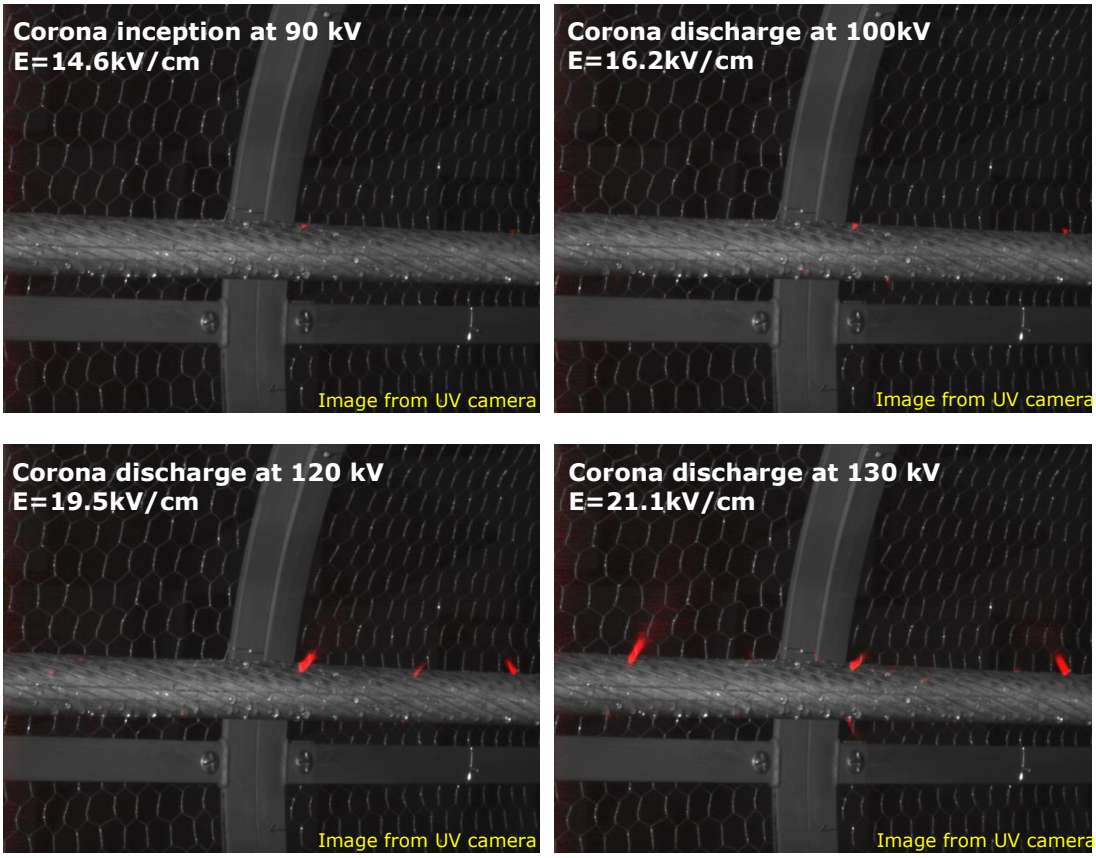

Figure 5-30 UV detection for corona in the section inside cage

The corona inception voltage is 90 kV, while stable corona is established when voltage rise above 100 kV. Excessive corona discharge is detected at 130 kV.

5.3.5 Partial Discharge Evaluation for the Bushing

As introduced previously, in order to achieve the acoustic insulation, a chamber enclosed with sound proof panels is essential. This enclosed chamber is at ground potential and requires a bushing to lead the high voltage through the sound proof panel without violating the acoustic insulation of the anechoic chamber (Figure 5-31).

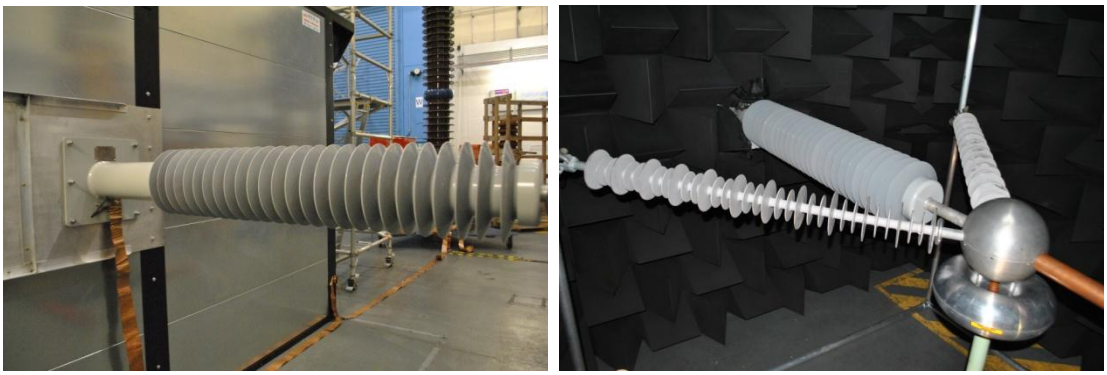

Figure 5-31 250kV HV bushing: outside view of bushing (Left); inside view of bushing (Right)

The partial discharge (PD) measurement system is employed to detect the PD index from the whole HV supply. Apart from the corona discharge on the surface of conductor sample, there is potential PD activity from undesired places such as the HV bushing. The PD signal from the HV bushing can be treated as background noise when evaluating the corona discharge level from the conductor sample. Measurements have been carried out to evaluate background PD level when the high voltage supply is solely applied to the HV bushing, and no conductor is under test.

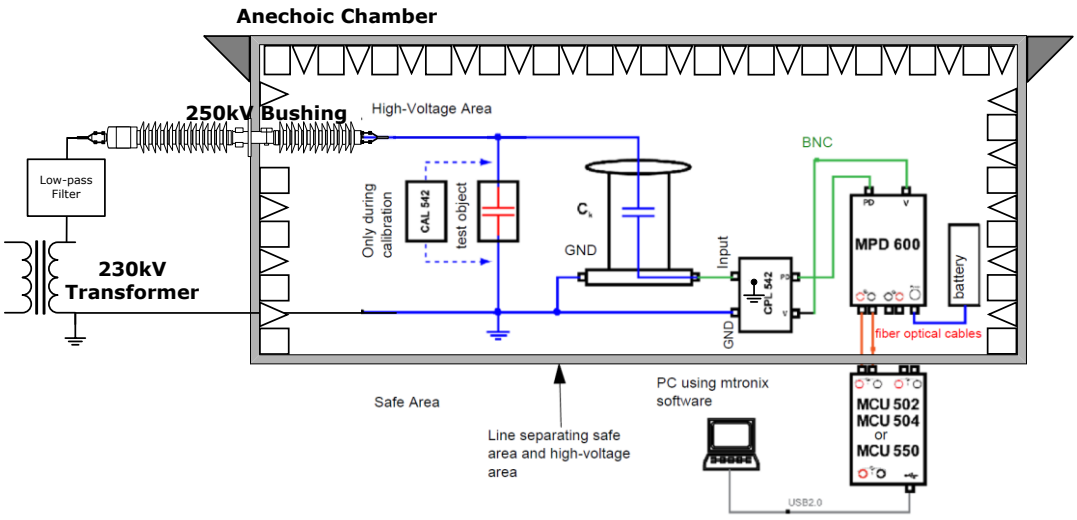

Figure 5-32 PD Measurement Circuits for Bushing

The measurement circuit is shown in Figure 5-32. From the phase-resolved diagram (Figure 5-33), the maximum single discharge has an equivalent charge of approximately 1 nC while other discharge activities are below 1 nC. If Q_{IEC} is plotted against the applied voltage (Figure 5-34), the apparent charge according to IEC standard is below 1 nC, below 140 kV. This indicates that PDs from the HV bushing contribute apparent charge less than 1 nC.

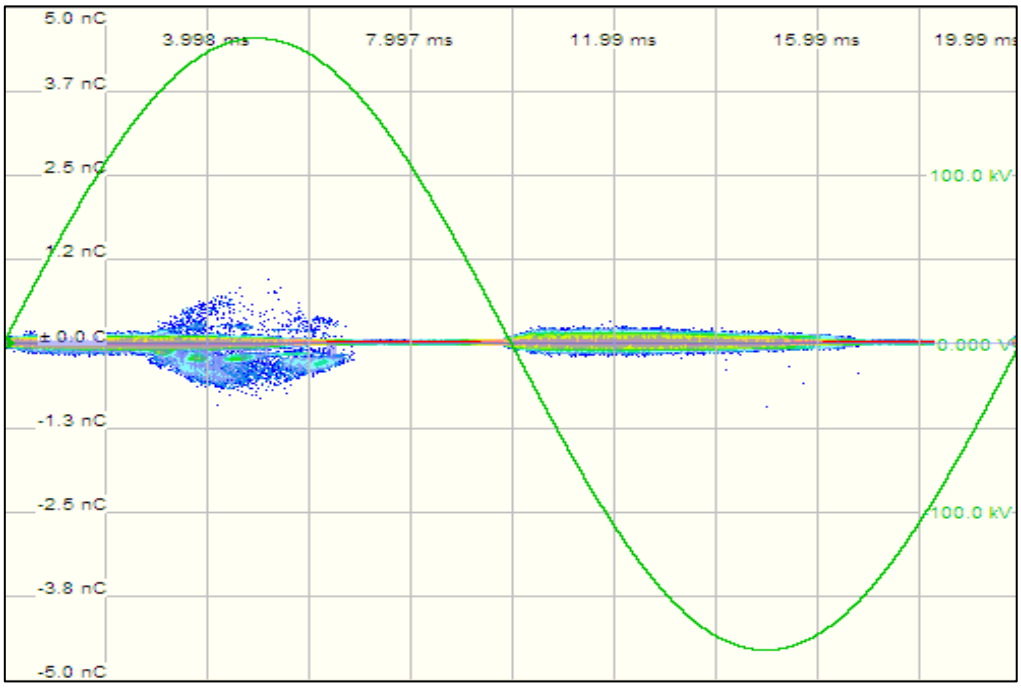

Figure 5-33 Phase resolve diagram for bushing test

Based on the PD bushing test, it is appropriate to choose 1 nC as the threshold value for conductor samples. The corona discharge inception voltage is defined as the voltage that leads to PD levels exceeding the threshold value.

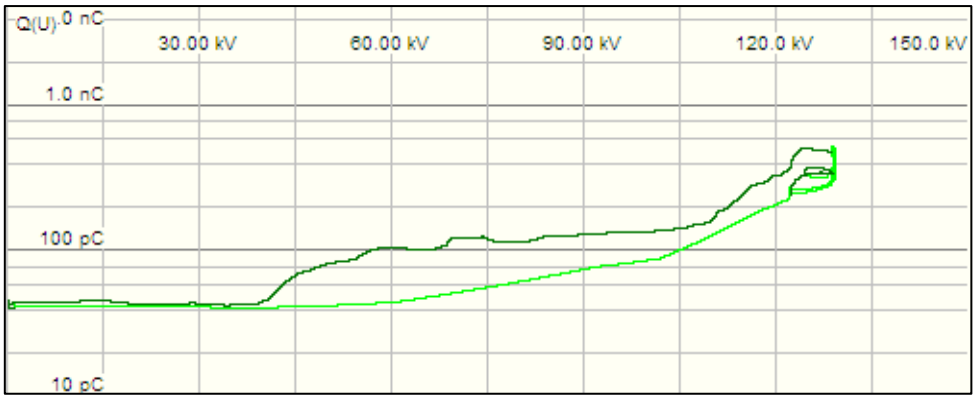

Figure 5-34 Q_{IEC} amplitude with applied voltage level

5.3.6 Design of the Tensioning System

In order to tension a section of overhead line conductor, a rigid framework (Figure 5-35) was built from aluminium scaffolding. It was extended to a dimension to fit the overall length of conductor and accessories.

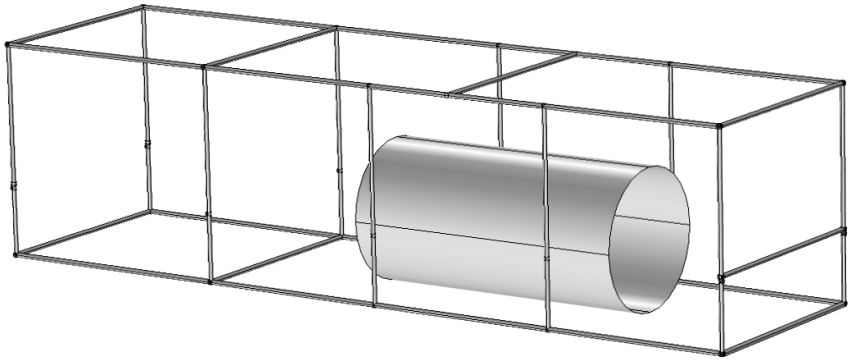

Figure 5-35 Sketch of the Scaffolding Frame

Two sets of mechanical devices, cable grips and turnbuckles, were then introduced to finish the connection.

The maximum tensioning force for the cable grip is 12800 lbs (5806 kg) while the safe working load for turnbuckle is 11 kN (1122 kg). So together there is a possibility to apply around 1 Tonne force on the overhead line conductor for this tensioning system (Figure 5-36).

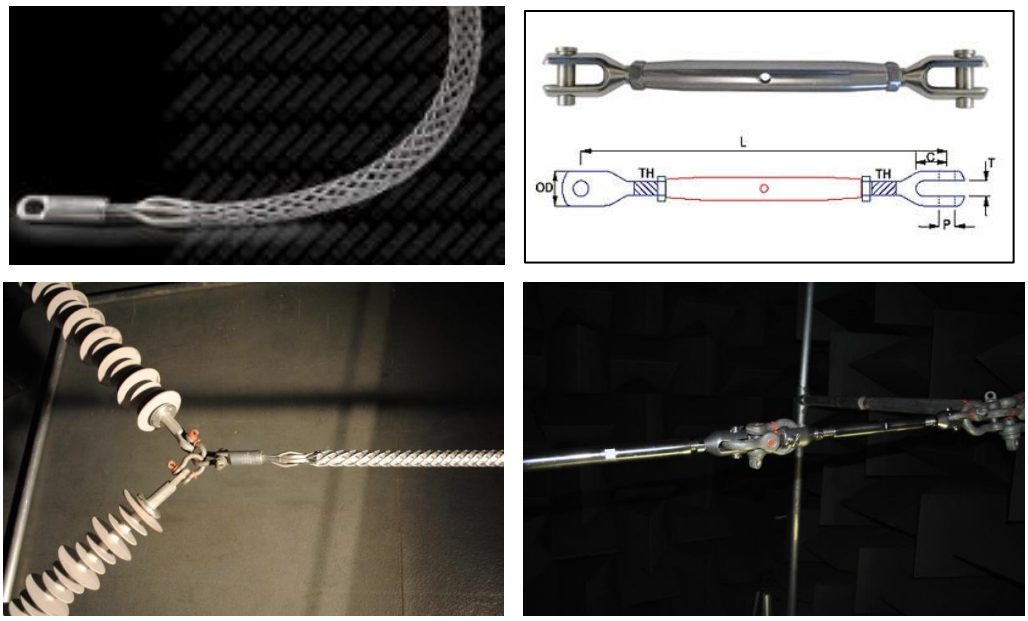

Figure 5-36 Cable Sock (top left); Turnbuckle (top right); Tensioning Connection (bottom)

5.3.7 Spray Conditions

There are three wetting conditions used within the experimental facility routinely:

a) Manual Spray

Uses a bottle sprayer to manually wet the conductor sample on a one-off basis, to apply excessive water droplets on the whole surface of conductor sample as shown in Figure 5-37 (both sessile and pendent drops are formed).

Figure 5-37 A Section of Conductor after Manual Spray Process

b) Continuous Light Spray

Containers are filled with water and pre-pressurized before experiment. Four nozzles are arranged to provide spray to cover the whole length of conductor sample. The spray can last consistently for ten minutes. The precipitation rate is 21 mm per hour as measured by the standardized rain gauge (Figure 5-39).

c) Continuous Heavy Spray

Pressurized water feeds four nozzles, covering the whole length of conductor sample. The precipitation rate is 50-60 mm per hour as measured by the standardized rain gauge. The profile is visually compared with light spray in Figure 5-38.

Figure 5-38 Light Spray Condition (left) Compared to Heavy Spray Condition (right)

Figure 5-39 Calibration for the Spray System (Precipitation Rate Measurement)

5.3.8 Measurement Instruments and Overview of the Cage Experiment

As highlighted in Figure 5-40, measurement devices employed in cage experiment include:

- Two ultra violet cameras
- Two free-field microphones
- A high speed camera
- A partial discharge detection system

The UV cameras are employed to visually detect the corona discharges. They are also important tools when mitigating unwanted corona from joints and high voltage terminations.

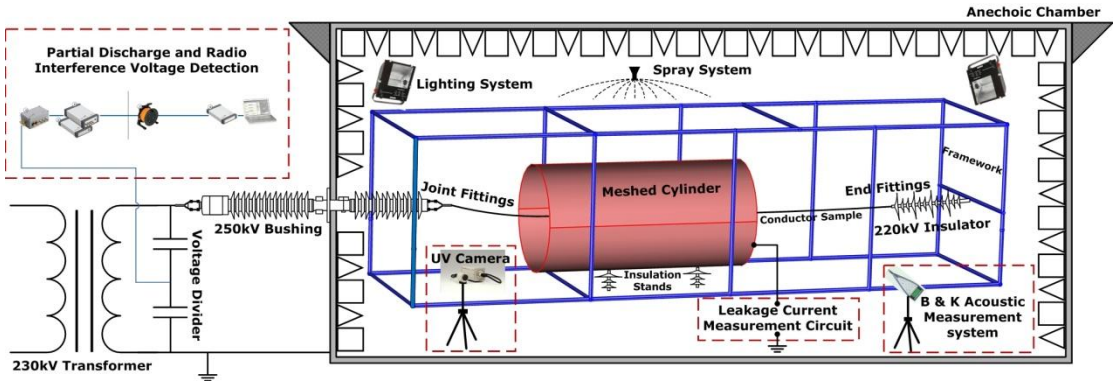

Figure 5-40 Overview of the Cage Experiment

The two microphones are introduced for acoustic measurements. This set-up allows not only sound pressure level measurements but also sound intensity measurements.

Signals are integrated by a data processing front-end which enables FFT analysis and sound intensity computation.

The high speed camera (up to 1600 frames per second for a resolution of 1024x768) produces slow motion video of water droplets behaviour within the AC electric field.

The partial discharge detection system is introduced for two functions:

- To detect the discharge level of the bushing and supply circuit (an undesired noise source).
- To quantify the apparent charge Q_{IEC} of corona discharges from wet conductor.

5.4 Acoustic Measurement

The characteristic of the noise itself is the most important consideration when choosing suitable instrumentation. The critical characteristics of the noise are:

- Noise spectrum: wide-band, narrow-band, or highly tonal
- Level variation with time: constant, highly time dependent, or intermittent

These characteristics determine the choice of microphone.

In addition, the acoustic measurement process is closely linked to the characteristics of the sound source and the propagation of the sound produced. For example, a tonal noise requires a narrow-band frequency analysis as well as an analysis for higher order harmonics, while a wide-band noise requires A-weighted or one-third octave band sound pressure level evaluation. A microphone suitable for free field use is known as a free-field sound level meter, and mainly measures sound waves perpendicular to the sensor plate, while for diffuse fields, a general pressure sound meter is preferred to capture sound waves from all directions.

5.4.1 Selection of Microphone for Sound Measurements

Audible noise from overhead line conductors contains two components: a high frequency crackling noise and a low frequency hum noise. The frequency of the crackling noise ranges from 1 kHz to 20 kHz while the hum noise is mainly a 100 and/or 200 Hz pure tone. The measured acoustic noise within the experiment is a

mixture of these two components as well as some broadband background noise. As a result, the microphone is required to cover a wide frequency range from 80Hz to 20 kHz.

As a frequency spectrum analysis is required for the sound signal, the sensitivity of the microphone within the low frequency range (specifically at 100Hz and 200Hz) should be as high as possible.

Within a laboratory environment, the sound field is unpredictable, so the microphone must be capable of producing accurate measurement results within a complex sound field.

The anechoic chamber is approximately 10m in length but only 2.5m in width, while the sound source within the chamber is a cylindrical conductor of 3m length. So the maximum measurement distance between microphone and the sound source is around 1m. Thus the microphone is performing a 'near field' measurement. This constraint requires the microphone to be able to measure near field sound pressure levels with satisfactory accuracy.

Figure 5-41 Brüel & Kjær 4961 multi-field microphone

To fulfil the requirements listed above, a high performance microphone Brüel & Kjær 4961 multi-field microphone was selected as a sound level meter for experiments, see Figure 5-41. It has the following advantages:

- it is capable of measuring noise in unpredictable sound-field conditions
- it can perform near-field measurements
- its integrated function allows accurate measurement not only in a free field but also in a diffuse field

- it is not particularly sensitive to the sound incidence angle which allows a flexible allocation of microphone position within the high voltage laboratory
- it has a degree of electromagnetic immunity which is critical inside a high voltage laboratory

The main microphone technical specifications are listed in Table 5-3.

Table 5-3 Technical Specifications for the Brüel & Kjær 4961 multi-field microphone

Specifications	Value
Sensitivity (250Hz)	-24.4 ±2 dB re 1V/Pa, 60 mV/Pa
Free-field response 0^o incidence	±2 dB 12 Hz-20 kHz
Lower Limiting Frequency (-3 dB)	3-6 Hz
Upper Limit of Dynamic Range (3% Distortion)	>130 dB SPL
Clipping Limit	>133 dB (peak)
Max. Sound Pressure Level	>150 dB (peak)
Magnetic Field Sensitivity	No detectable influence from a 50 A/m, 50Hz magnetic field

5.4.2 FFT Analysis for Frequency Spectrum Evaluation

As introduced in the previous section (5.4.1), the sound emitted from overhead line conductors contains not only a high frequency noise (wide band from 1 kHz to 20 kHz) but also pure tonal noise (typically at 100 and 200 Hz). These characteristics of the audible noise from overhead line conductors require a high degree of accuracy when generating a frequency spectrum by a Fast Fourier Transform.

a) Pitfalls of an FFT Analyser

It is well understood that the following effects in a FFT process can introduce errors in the derived frequency spectrum:

- Aliasing
- Leakage
- "Picket Fence" Effect

b) Aliasing

Aliasing is an error produced in a FFT when sampling time signals. As shown in Figure 5-42, analogue signals (green curves) are filtered by a fixed sampling frequency "f_s". From top to bottom, the four analogue signals are:

a) constant signal (0 Hz)
b) sinusoidal signal with x Hz
c) sinusoidal signal with f_s Hz
d) sinusoidal signal with X+f_s Hz

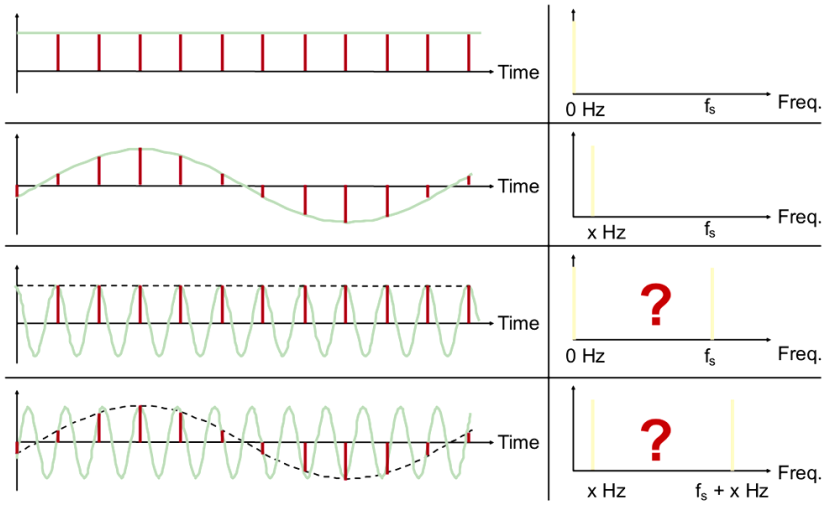

Figure 5-42 Explanation of Aliasing

The red sampling points are taken to perform FFT, and the frequency distribution is shown on the right hand side. Clearly, a) has a frequency of 0 Hz, and the result obtained for frequency is correct. Occasionally, all the sampling points obtained constant values within c), this happened due to the reason that the sampling frequency is the same as the frequency of the analogue signal. The frequency components after FFT are 0 Hz and f_s Hz. Obviously, 0 Hz component is an error of FFT process. Similar results are seen on b) and d), again d) generates a fake frequency component due to the reason that sampling frequency is lower than the signal frequency. This type of error introduced is named aliasing for FFT.

There are two techniques which can avoid this error:

- introduce a low-pass filter which attenuates high frequency components of the signal, so that there is no signal with a frequency greater than $f_s/2$
- increase the sampling frequency to ensure the sampling frequency is at least two times higher than the upper frequency limit of the low-pass filter

By applying appropriate settings to the FFT analyzer, the aliasing effect can be avoided within the commercial B and K PULSE (acoustic analysis) platform.

c) Leakage

One of the features of a FFT is that a signal is required between negative infinity time and positive infinity time. In most cases, the measurement time is a short period, so extending a short time signal into an infinite time signal is essential in FFT. A commonly used method is to stitch two periods of signals together and repeat the process. This works when the time signal is periodic, and the last value of the first period is the same as the first value of the second period. However, if the time signal is not periodic, when two periods of signal are stitched into one, discontinuity is caused. The discontinuity can cause the FFT results to contain frequency errors.

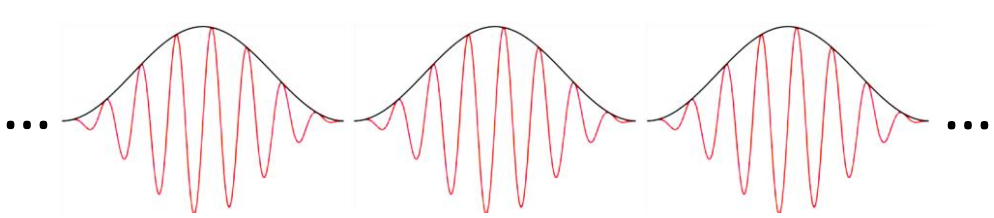

Figure 5-43 Time signal stitched using Hanning Window

In order to deal with this, a signal windowing technique (Hanning Window) is used. As shown in Figure 5-43, after passing the signal through a Hanning Window, the discrete signal becomes continuous, and the accuracy of the FFT is improved.

d) Picket Fence Effect

In the FFT process, discrete frequency components are obtained as final results. This is known as sampling in frequency. In Figure 5-44, the yellow curve is the actual frequency spectrum of a signal, and the red points are frequency sampling points. It can be seen that information about the frequency distribution is lost since the frequency sampling rate is low. This is undesirable especially if a pure tone is in the acoustic signal. When measuring acoustic noise from overhead line conductors, any

100 Hz peak is critical in evaluating noise performance, so the Picket Fence Effect must be avoided to obtain an accurate result.

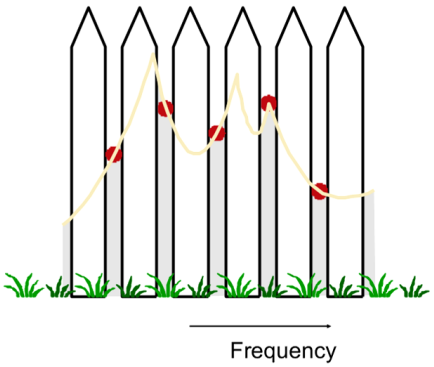

Figure 5-44 Picket Fence Effect

5.4.3 Octave Bands Analyzer and Overall Level Analyzer

a) Octave Bands

In order to obtain sound signal information in the frequency domain, the energy of the signal is electronically separated into various frequency bands. Octave bands are used to divide the frequency domain so that each band covers a 2-to-1 range of frequencies. For example, the 1000 Hz band (1000 Hz as the central frequency) ranges from 707 to 1414 Hz (upper frequency boundary is twice the lower boundary). The frequency bands for octave bands are listed in Table 5-4. The older bands were widely used in the past. In order to compare with publications of the 1960s or even older, knowledge of the old type of band separation is valuable.

Table 5-4 Octave Bands (new and old standardized frequency range)

New	**Centre Frequencies (Hz)**	**31.5**	**63**	**125**	**250**	**500**	**1000**	**2000**	**4000**	**8000**	**16000**
	Lower Band Limit (Hz)	22	44	88	177	354	707	1414	2828	5657	11314
	Upper Band Limit (Hz)	44	88	177	354	707	1414	2828	5657	11314	22627
Old	**Centre Frequencies (Hz)**	**-**	**-**	**113**	**225**	**450**	**900**	**1800**	**3600**	**7200**	**-**
	Lower Band Limit (Hz)	-	-	75	150	300	600	1200	2400	4800	-
	Upper Band Limit (Hz)	-	-	150	300	600	1200	2400	4800	9600	-

For more detailed analysis of sound energy distribution, each octave band is further divided into three parts to obtain 1/3 octave bands. For example, the first octave band in Table 5-4 ranges from 22 to 44 Hz, but in a 1/3 octave band, it is divided into three bands: 22-28 Hz, 28-35 Hz and 35-44 Hz.

In the PULSE platform which is an integrated post-process module from Brüel & Kjær there is a flexibility to perform any of the listed frequency band analyses above.

b) Overall Level

If details of sound energy frequency distribution are not required, a single value can indicate the noise level. This is known as an overall level and is a weighting of the sound pressure level over the whole frequency span. Depending on which frequency is emphasized, there are weighting functions which apply different gains at different frequencies. The most commonly used weighting function is A-weighting. The A-weighted sound level, expressed in dB(A), has been shown to correlate well with human subjective response. This character makes it widely recognized as a standardized weighting procedure.

In addition to A-weighting, there are various weighting functions for overall level:

- ***B-weighting:*** corresponds to a contour of medium sound pressure levels (SPLs)
- ***C-weighting*****:** corresponds to an equal loudness contour at high SPLs
- ***D-weighting*****:** has been standardized for aircraft noise measurements

5.5 Partial Discharge Measurement

Partial discharge measurement is an assistive measurement technique to quantify the level of corona discharge. A common challenge in PD measurement is the effect of background noise. However, within the cage experiment, partial discharge from corona can be readily distinguished from background noise. For example, as introduced in Section 5.3.5, the background apparent charge level Q_{IEC} is less than 600 pC with 140kV applied voltage, which is very much less than the corona discharge level Q_{IEC} of 60 nC.

The PD test equipment employed in this experiment is an OMICRON MPD 600 PD detecting system. It fulfils the requirements listed in British Standard (BS) 60270, and uses the basic test circuit specified in BS 60270 as shown in Figure 5-45. A 500 pF discharge-free capacitor is used as a coupling capacitor. A high voltage supply, with a low level of background noise is used. The high-voltage connections are designed to

have negligible PD emission level. As introduced in Section 5.3.4, this is achieved by introducing electric field relief devices in joints and at the conductor ends.

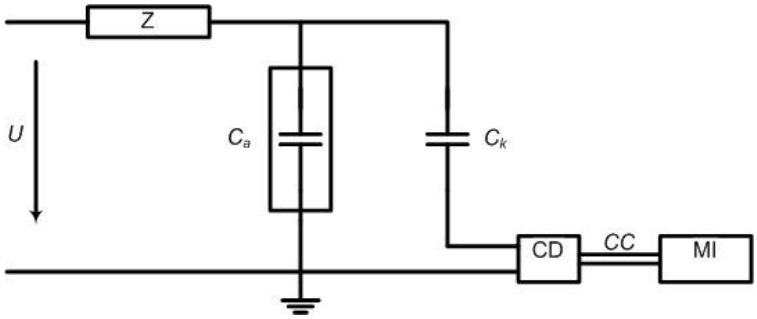

Components:

U	high-Voltage Supply
Z_{mi}	input impedance of measuring system
CC	connecting cable
C_a	test object
C_k	coupling capacitor
CD	coupling device
MI	measuring instrument
Z	filter

Figure 5-45 Basic partial discharge test circuit

5.6 Conclusion

An experimental set up for measuring the noise from overhead line conductors has been described in this chapter. Sound insulation is provided by designing and constructing an anechoic chamber around the coaxial arrangement. The electrical design is aimed to simulate the electric field of a 400 kV transmission line conductor. Measurement instrumentation has been introduced and the extended capability of this exceeds any other known facilities.

The introduction of this set-up leads to the measured results from a range of conductors which will be presented in the next chapter.

Chapter 6 Test Procedure and Results

6.1 Introduction

This chapter firstly introduces the sample preparation and test procedure for cage experiments. The procedure for generating noise and PD results are described after the first section. Results are discussed and compared in the last section.

6.2 Test Procedure

Due to the nature of high voltage tests, the test procedure is critical to the results. Careful design of the test procedure includes the following:

- sample preparation
- reproducibility of testing conditions
- measurement procedure

The standardized test procedure is tailored by either studying the literature or from experience in the lab. The finalized procedure is established aimed at producing as much information as possible within a limited availability of HV lab. The expectations of these tests are:

- characterise the audible noise emission from different types of conductor
- to understand the key factors for noise generation

6.2.1 Sample Preparation

Conductor samples are obtained from two routes:

- transported from National Grid UK and prepared in the university
- prepared by the manufacturer and transported from overseas

Two critical factors affect the reproducibility of test results:

1. Surface damage during transportation or cutting: The material of the outer layer of conductor samples is either aluminium or aluminium alloy. This results a high possibility of surface scratches. A damaged surface has a higher possibility to generate successive corona discharges due to the divergent electric field surrounding the sharp edges.
2. When tensioning forces are low, the strands may become loose. In the reality of an overhead line span (usually 400 meters long), the conductor is subject to massive tensioning forces (typically 3 tons). The strands are then held in the compact configuration. However, when the conductor is cut into short samples (5 metres long) and less tension is applied (usually 0.3 tons), the strands may no longer maintain the compact geometry. Either the displacement of

individual strand or increase of the overall diameter affects the reproducibility of measurement results.

Extra caution is paid on both cutting and transporting the sample. Protection is used to cover a conductor surface to prevent scratches and mechanical fittings (jubilee clips) are used to retain the compact shape of the conductor. These actions attempt to reduce as much as possible the experimental errors caused by sample preparation.

Delivered conductor samples are usually a few times longer than the actual required length. For example, a typical sample delivered is 25 meters long while only 4.88 meters is required for the experiment. This gives the opportunity to prepare multiple samples for each type of conductor as a backup.

The following samples (Table 6-1) have been tested within the cage experiment inside the anechoic chamber.

Table 6-1 Conductor Sample List for Cage Experiment

Name	History	From	Diameter	Age
Aged GAP Matthew	Matthew GAP from the ZO (strung in 2003, removed in 2006, stored since then)	National Grid	31.5 mm	In service for 3 years, then stored for 5 years
Aged AAAC	Aged Sorbus (AAAC 570mm^2) from the ZE (strung in 1993, removed 2012)	National Grid	33.39 mm	In service for 19 years
New ACCC/CTC	New CTC/Lamafil ACCC from storage at Staythorpe ('London')	National Grid	34 mm	Not in service, stored for about a year
3M	3M 'Curlew' conductor from Didcot stores	National Grid	31.5 mm	Stored for 2 years after manufacture
Midel	Manufactured from Middle East	National Grid	31.5 mm	Stored for 2 years after manufacture
New JPS (Round)	Stored for a year	JPS Japan	31.5 mm	Stored for 2 years after manufacture
New JPS (Trap)	Stored for a year	JPS Japan	31.5 mm	Stored for 2 years after manufacture

Information is attached to each sample by an explicit label on arrival to prevent confusion.

6.2.2 Reproducibility

In order to maintain the reproducibility, each time the anechoic chamber is built in the same procedure and the instrumentation inside set-up followed exactly the same arrangement. As introduced in Chapter 5, the position of anechoic chamber, metallic

frame, and measurement devices is kept the same within the HV lab when rebuilding the rig.

6.2.3 Measurement Procedure

The set-up of test rig is introduced in Chapter 5, the test procedures to generating measurement results are described briefly as following:

1. Sound Pressure Level recording for various voltage gradient
   A. Manually fill water and apply the pressure to all sprayers;
   B. Manually wet the conductor sample to achieve a pre-wetted condition;
   C. Run the spray system for 10-12 minutes (constant spray can be achieved within 7-10 minutes, thereafter the spray rate is reducing gradually);
   D. Apply voltage immediately after the spray starts, and adjust the voltage to the appropriate level (to achieve 6 kV/cm, 7 kV/cm, … 22 kV/cm);
   E. Record the sound signal for 10 minutes (sound recorder);
   F. Stop recording;
   G. Switch off the high voltage supply;
   H. Post-process for the recorded signal to obtain the SPL for 100Hz, 200Hz, and overall level in dBA.
2. Sound Pressure Level decay tests
   A. Manually fill water and apply the pressure to all sprayers;
   B. Manually wet the conductor sample to achieve a pre-wetted condition;
   C. Run the spray system for one hour (constant spray can only lasts for about 7-10 minutes, so the remaining time is the drying process);
   D. Apply voltage immediately after the spray starts, and adjust the voltage level to achieve 18 kV/cm surface gradient;
   E. Record the sound signal and PD signal (OMICRON) for one hour (sound recorder only capture the time signal);
   F. Stop recording;
   G. Switch off the high voltage supply;
   H. Post-process for the recorded signal to obtain the decay curve of 100 Hz, 200 Hz and overall sound pressure level in dBA; PD signal analysis to obtain the Q_{IEC} variation within 1h.
3. Corona Inception and Extinguishing tests

A. Manually fill water and apply the pressure to all sprayers;
B. Manually wet the conductor sample to achieve a pre-wetted condition;
C. Calibration process for OMICRON, charge calibration and voltage calibration;
D. Run the spray system for 10-12 minutes (continuous spray can be achieved within 7-10 minutes, the spray rate is reducing gradually);
E. Increase the voltage from 0 to 133 kV (refer to 22 kV/cm surface gradient) in a rate of approximately 2.5 kV/s and stay constant for 5 seconds, then reduce the voltage in a rate of 2.5 kV/s till 0;
F. Record the PD patterns for the whole testing time;
G. Repeat E,F for extra four times until the spray is not sufficient;
H. Repeat A-G once in order to maintain the reproducibility;
I. Post-process to obtain the PD level variation and the inception stress and extinguishing stress.

6.3 Data Analysis for Acoustic Noise

The key function of anechoic chamber is to accurately measure sound pressure levels from a section of high voltage conductor. With all the efforts in design and commissioning (as introduced in Chapter 5), this facility has become a critical tool for the power utility (National Grid) to select quieter conductors before selection for new overhead lines. A specific rating strategy has been developed to compare different samples. This section demonstrates the standardized procedure in post-processing measurement data.

6.3.1 Electric Field Normalization

Within the cage experiment, a voltage level is applied on the overhead line conductor to achieve equivalent electric field strength on the surface. The cage set-up can be simplified as a coaxial geometry. As explained in Section 5.3.1, the equivalent electric field strength can be calculated as:

$$E = \frac{U}{r \times \ln\left(R / r\right)} \tag{7-1}$$

Where U is the applied voltage, r is the average conductor radius and R is the cage radius.

This means different conductor radii will result in different electric field strengths on the surface even if the applied voltage was the same. In order to compare conductors with a wide range of geometries, the electric field strength is selected as a reference rather than the applied voltage. In the experiment, the voltage is adjusted to the appropriate value in order to achieve a certain level of electric field (Section 5.3.4). The electric field is increased from 6 kV/cm to 21 kV/cm with a 1 kV/cm interval. Referring to Table 6-1, there are four other conductors (3M, Midel, JPS-Round and JPS-Trap) with the same average radii as Aged Matthew. Their applied voltage is as same as the values listed for Matthew in Table 6-2.

Table 6-2 Electric Field-Voltage Table for Cage Experiment

Electric Field (kV/cm)	6	7	8	9	10	11	12	13
Voltage for Matt (kV)	36.51	42.59	48.68	54.76	60.85	66.93	73.02	79.10
Voltage for AAAC (kV)	38.12	44.48	50.83	57.18	63.54	69.89	76.25	82.60
Voltage for ACCC (kV)	38.63	45.06	51.50	57.94	64.38	70.81	77.25	83.69
Electric Field (kV/cm)	14	15	16	17	18	19	20	21
Voltage for Matt (kV)	85.18	91.27	97.35	103.4	109.5	115.6	121.7	127.8
Voltage for AAAC (kV)	88.95	95.31	101.7	108.0	114.4	120.7	127.1	133.4
Voltage for ACCC (kV)	90.13	96.56	103.0	109.4	115.9	122.3	128.8	135.2

6.3.2 Acoustic Data Analysis for One Test

With the support from the world's most recognized acoustic measurement company (Brüel & Kjær), a specific post-process platform for results from the anechoic chamber has been created (Figure 6-1).

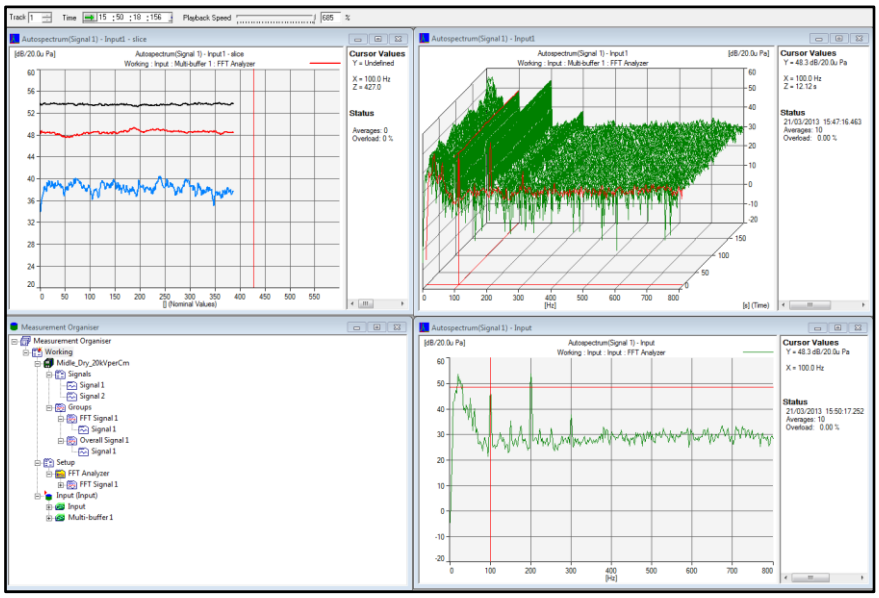

Figure 6-1 FFT Analyzer for Post-processing Sound Signals

This post-process module analyzes the recorded time varying data from the experiments, and generates two types of index:

- sound pressure level in 100, 200, 300 Hz from the FFT analyzer
- overall level with specific weighting (A-weighting is used)

The key parameters for the FFT analyzer are listed in Table 6-3.

Table 6-3 FFT Settings for Post-process

Frequency Span	0-800 Hz
Central Frequency	400 Hz
Resolution for Frequency Plots	Df=800 Hz/6400 Lines=125 mHz
Time Period	T=8 s
Sampling Time (rate)	dt=488.3 μs

The selection of these parameters is to achieve highest resolutions on the frequency domain. In general, the original sound record lasts for approximately 160 seconds. It is divided into short pieces with 8 seconds interval. Within each piece of time signal, FFT is performed to obtain frequency characteristics for that particular time interval. About 20 results are obtained from the whole recorded length. These results are input to statistical analysis tool to obtain more information.

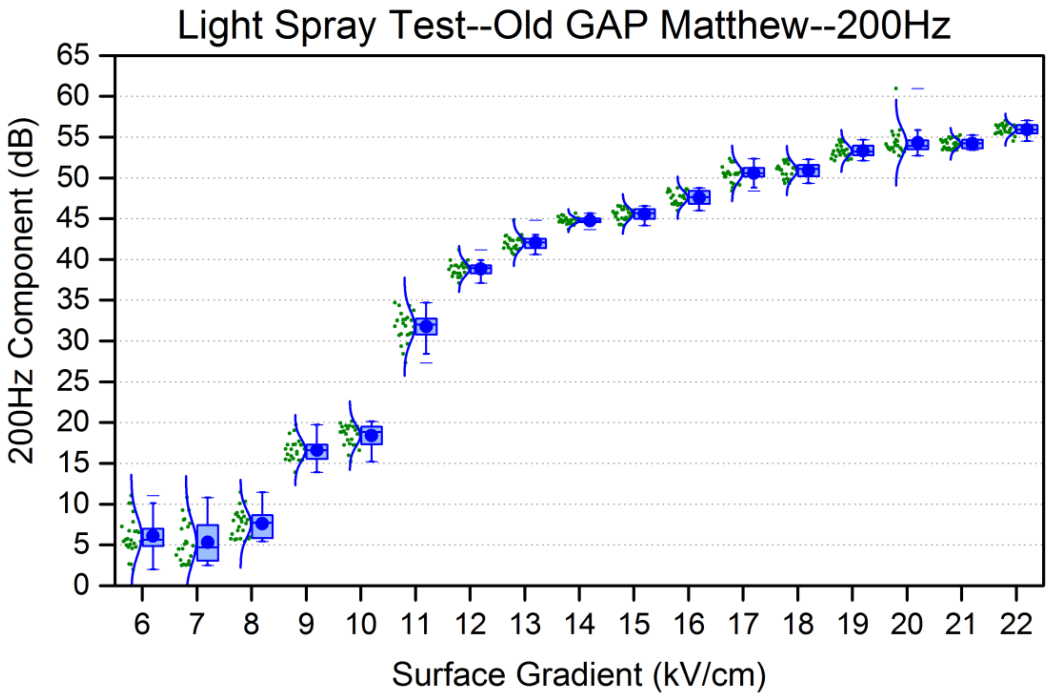

Figure 6-2 Statistical Plot of Measurement Results for 200Hz SPL from Aged Matthew Conductor

As shown in Figure 6-2, the following key values are summarized within the plot:

- the curve is a fitted normal distribution while the blue dot point is the mean value
- the position of blue box covers the range from 25% to 75% of the fitted distribution
- the positions of top and bottom whisker (short line) refer to maximum and minimum measured values respectively, and the line within box refers to the median

6.4 PD Measurements

As described in Section 5.5, a commercial module (OMICRON MPD 600) is utilized to quantify the level of corona discharge within the cage experiment. A typical measurement result is described here and a table of summarized inception level is presented.

6.4.1 Corona Inception Detection for One Type of Conductor Sample

Followed by the test procedure described in Section 6.2.3, the PD data is recorded through the commercial module. It is then analyzed in a post-processing platform to detect the inception voltages.

For comparison purpose, the electric field strength rather than the voltage level is selected as a reference to display the PD level. In order to maintain the reproducibility of measurements, a repeated test (five measurements under same condition) is performed on each type of conductor. The average value over five measurements can then be taken as the corona inception level.

In Section 5.3.5, the background level (bushing and other PD sources) was measured. 1 nC was selected as a threshold for corona inception on conductors. As presented in Figure 6-3, five measurements are taken on a typical conductor sample (Aged Matthew conductor) under a light spray condition. The apparent charge according to IEC Standard is plotted against the electric field strength assuming a cylindrical shape. The dashed line showed the threshold value (1 nC) for PD level. It is observed that the

measurement results have small variations among five measurements and all five measurements follow the same trend.

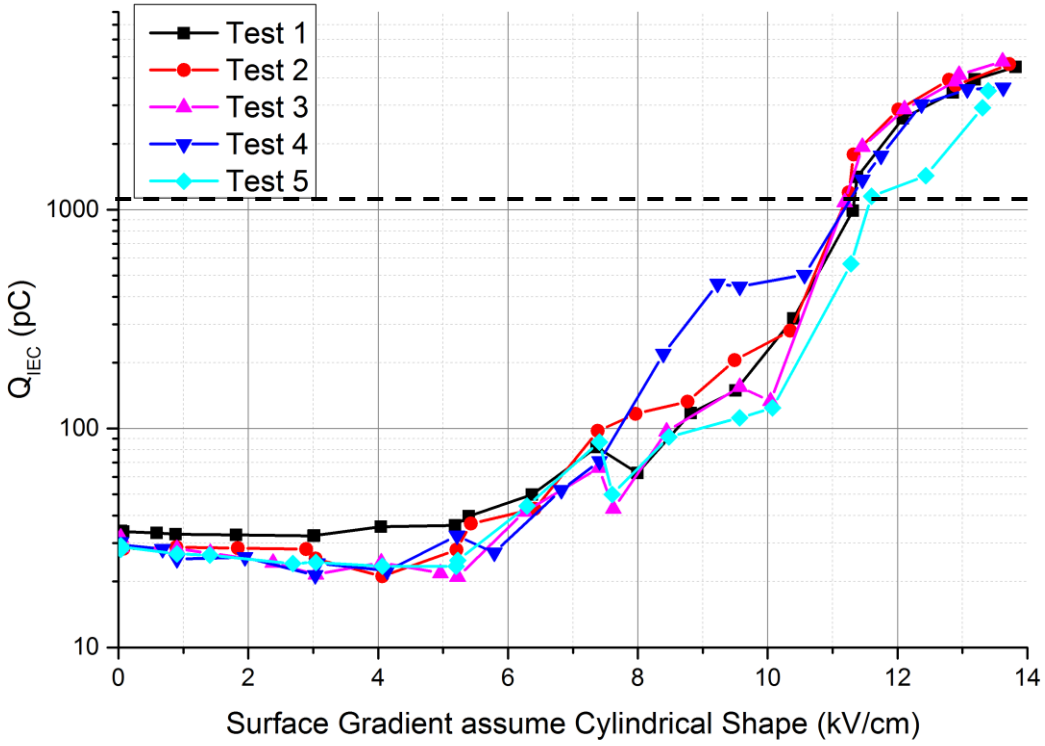

Figure 6-3 PD Detection for Aged Matthew Conductor under Light Spray Condition

6.4.2 Corona Inception and Extinguishing for Different Samples

Average value over five measurements is taken as the corona inception level. Table 6-4 summarized the corona inception value related to electric field.

Table 6-4 Corona Inception Field Strength for conductors (surface gradient assuming cylindrical shape)

	Dry		Manual Spray		Light Spray	
	Inception (kV/cm)	Extinction (kV/cm)	Inception (kV/cm)	Extinction (kV/cm)	Inception (kV/cm)	Extinction (kV/cm)
Old GAP Matthew	15.3	12.3	10.1	11.4	11.2	11.8
AAAC 'Sorbus'	21.6	19.8	10.1	12.6	10.5	12.9
ACCC 'London'	22.1	21.0	9.4	12.0	7.9	8.1

It is concluded that:

- Under dry condition, extinction level is lower than the inception level while under wet condition, it reversed. This is due to the reduced volume of water droplets on the surface of conductors after energizing.

- Both Old GAP and AAAC are aged conductor and with contaminations on the surface. However, under dry, Old GAP has much lower inception gradient than AAAC. This is due to effect of stranding shape as shown in Section 3.3.2.

6.5 Results Comparison and Discussion for AN

As introduced in Section 6.3.2, the sound pressure level result is compared among various types of conductor samples through the post-process of recorded signal. As an example, Figure 6-4 is one of the comparisons for 100 Hz SPL under light spray condition and 18 kV/cm stress. A full set of results is given in the appendix.

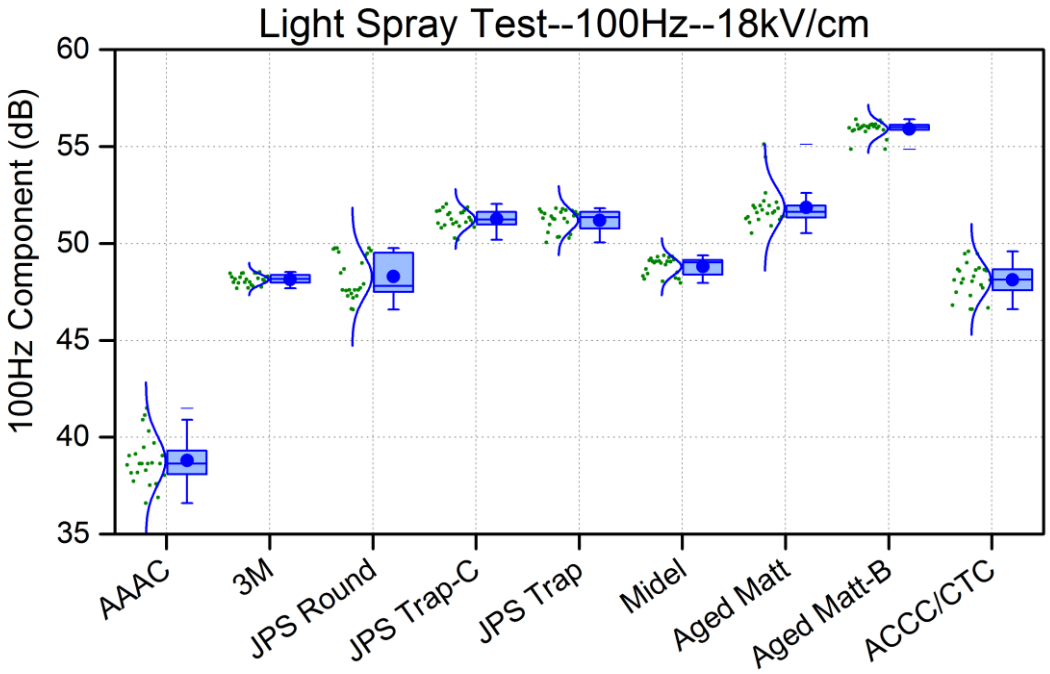

Figure 6-4 100 Hz Sound Pressure Level at 18 kV/cm Stress for Light Spray Tests

6.5.1 Comparison between Manual Spray and Light Spray

Within the experiments, manual spray and light spray are simulating different types of rain. As described in Section 5.3.7, manual spray condition applies voltage when the spray is stopped while light spray condition applies voltage when the spray is continued. As a result, manual spray tests study the noise characteristics for post-rain condition while light spray tests study for during-rain condition.

As introduced in Chapter 3 the surface gradient for different overhead line designs varied from 13 kV/cm to 19 kV/cm. To allow for this, the average value is taken from 13 kV/cm to 19 kV/cm for each conductor sample. These average values for 100 Hz are compared in Figure 6-5.

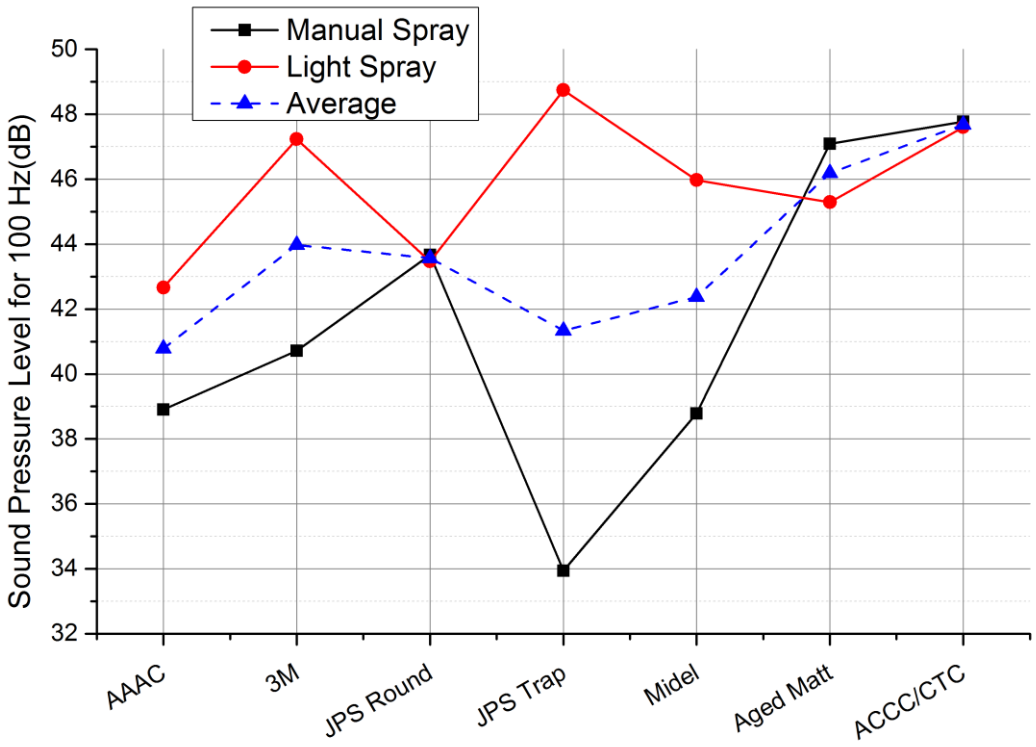

Figure 6-5 Comparison for Spray Condition-100 Hz

It is observed that:

- In general, the 100 Hz SPL for manual spray is substantially lower than for light spry
- Only on the Aged Matthew conductor, is SPL for manual spray distinctly higher than light spray
- There are two types of conductors (JPS Round and ACCC/CTC) have similar SPLs for both manual spray and light spray
- Significant difference (approximately 15 dB) has been observed for JPS Trapezoidal between these two different spray conditions

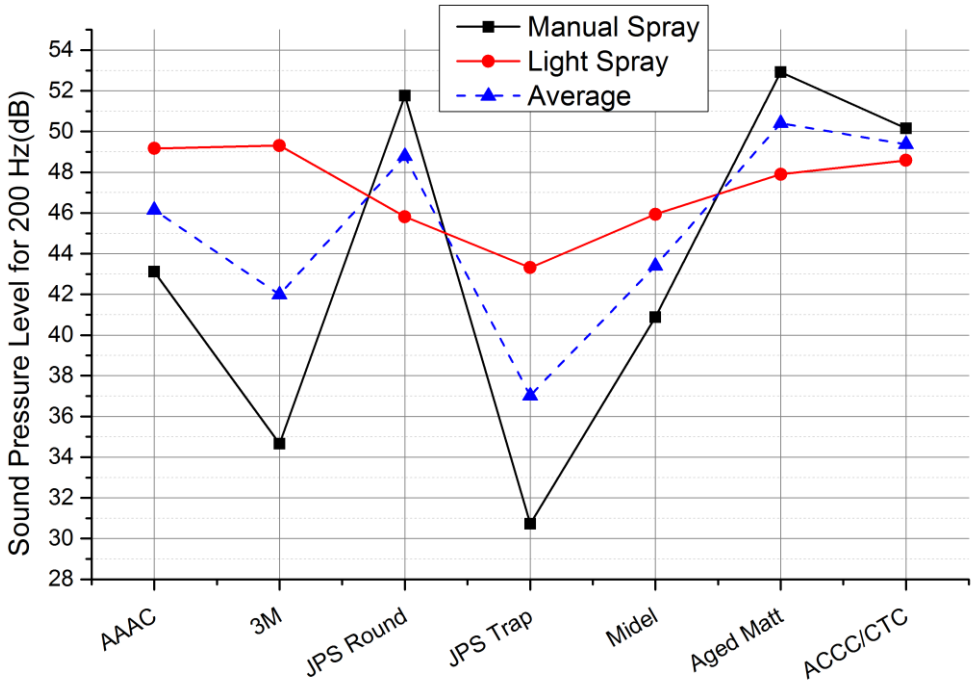

Figure 6-6 Comparison for Spray Condition-200 Hz

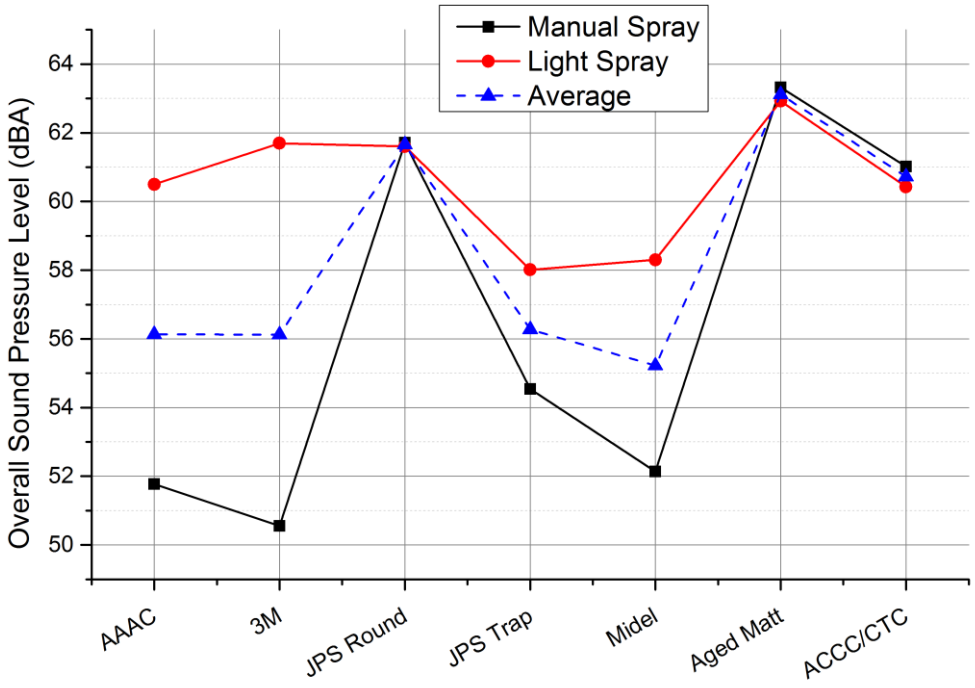

Figure 6-7 Comparison for Spray Condition-A-weighting

A similar plot for 200 Hz SPL is shown in Figure 6-6, the increase of SPL from manual spray to light spray is different compared to 100 Hz results. Three samples

generate higher level of 200 Hz noise in manual spray tests, such as: JPS Round, Aged Matthew and ACCC/CTC. By contrast, four other samples generate lower level of 200 Hz noise in manual spray tests, such as: AAAC, 3M, JPS-Trap, and Midel.

In Figure 6-7, the A-weighted overall SPL is plotted against different types of conductors. In general, the overall level for light spray is higher than for the manual spray. If manual spray is compared against light spray, JPS round, aged Matthew and ACCC/CTC have either similar levels or slightly higher levels of SPL while all other types of samples (AAAC, 3M, JPS Trapezoidal, and Midel) have lower level of SPL.

Summarizing the results for 100 Hz, 200 Hz, and A-weighting, the following conclusions are drawn:

- SPL results vary substantially from the manual spray condition to the light spray condition
- In a majority of the cases, manual spray generates lower SPLs (100 Hz, 200 Hz, and A-weighting) than light spray. However, there are situations where manual spray has higher SPLs than light spray (typically JPS Round, aged Matthew and ACCC/CTC)
- The conductor behave differently from each other and the noise level is hard to predict
- Results from individual conductor types are very reproducible

6.5.2 Noise Rating for Different Samples

When comparing the noise performance of two different conductors, it is important to select the key index for sound pressure level. As introduced in the literature review in Chapter 2, the human ear is more sensitive to high frequency components while low frequency components can transmit over longer distances, and can be more annoying. Within this part of analysis, a rating stratagem comprising both low frequency (tonal noise) and high frequency (crackling noise) components is utilized. It is designed to help power utilities like National Grid in choosing conductors for overhead line and has been presented to National Grid engineers.

a) Scores for Sound Pressure Level at a Certain Surface Gradient

After statistical analysis, data from Figure 6-4 is averaged and shown in Table 6-5. For convenience, scores are displayed instead of sound pressure levels. The rules for transferring sound pressure level to scores are:

- each score equals to 3 dB in SPL
- the reference is selected as AAAC (all scores for AAAC are set to 0)
- positive score means louder than AAAC while negative score means quieter than AAAC

In Table 6-5, scores are marked for noise levels at 18 kV/cm stress. These scores are displayed for both manual spray and light spray conditions.

Table 6-5 SPL Levels and Scores for 18 kV/cm Stress

SPL (dB)		AAAC	3M	JPS Round	JPS Trap	Midel	Aged Matt	ACCC/CTC
Manual Spray	**100 Hz**	45.58	49.95	50.60	40.93	46.69	51.44	50.78
	200 Hz	49.89	46.31	55.67	40.97	48.44	55.23	55.89
	A-Weighting	58.63	58.03	65.95	61.52	58.85	66.49	66.40
SPL (dB)		AAAC	3M	JPS Round	JPS Trap	Midel	Aged Matt	ACCC/CTC
Light Spray	**100 Hz**	38.97	48.15	48.43	51.23	48.84	51.99	48.21
	200 Hz	51.74	52.98	48.24	47.05	49.69	51.00	52.50
	A-Weighting	64.40	65.03	63.96	61.98	61.40	65.55	64.52
Score		AAAC	3M	JPS Round	JPS Trap	Midel	Aged Matt	ACCC/CTC
Manual Spray	**100 Hz**	0	1	1	-2	0	1	1
	200 Hz	0	-2	1	-3	-1	1	2
	A-Weighting	0	-1	2	0	0	2	2
Score		AAAC	3M	JPS Round	JPS Trap	Midel	Aged Matt	ACCC/CTC
Light Spray	**100 Hz**	0	3	3	4	3	4	3
	200 Hz	0	0	-2	-2	-1	-1	0
	A-Weighting	0	0	-1	-1	-2	0	0

Similar tables can be generated for other surface gradient values from data which is illustrated in Appendix I.

b) Scores for a Specific Design of Overhead Line

As explained in Section 6.3.1, the electric field reference for lab tests is calculated assuming the conductor is a cylinder, and the whole set-up is an axis-symmetrical geometry. This then gives a uniform distribution of electric field around the surface of conductors. However, in the reality, the electric field distribution is not uniform around each sub-conductor even we make the cylindrical assumption. This has been discussed in Section 3.3.5 when considering the effect of bundle arrangements. In

order to examine the noise performance of the conductor in the real bundle arrangements (for example: twin bundle), the proportion of the cylindrical surface at a giving electric field (i.e. the surface field distribution) is used as an input to generate the scores.

Taking an existing tower configuration in National Grid as an example:

- tower type: L2
- bundle arrangement: twin bundle with 400 mm spacing
- phase arrangement: un-transposed

The electric field distribution (assuming the conductors are cylinders) for various types of conductors is shown in Figure 6-8.

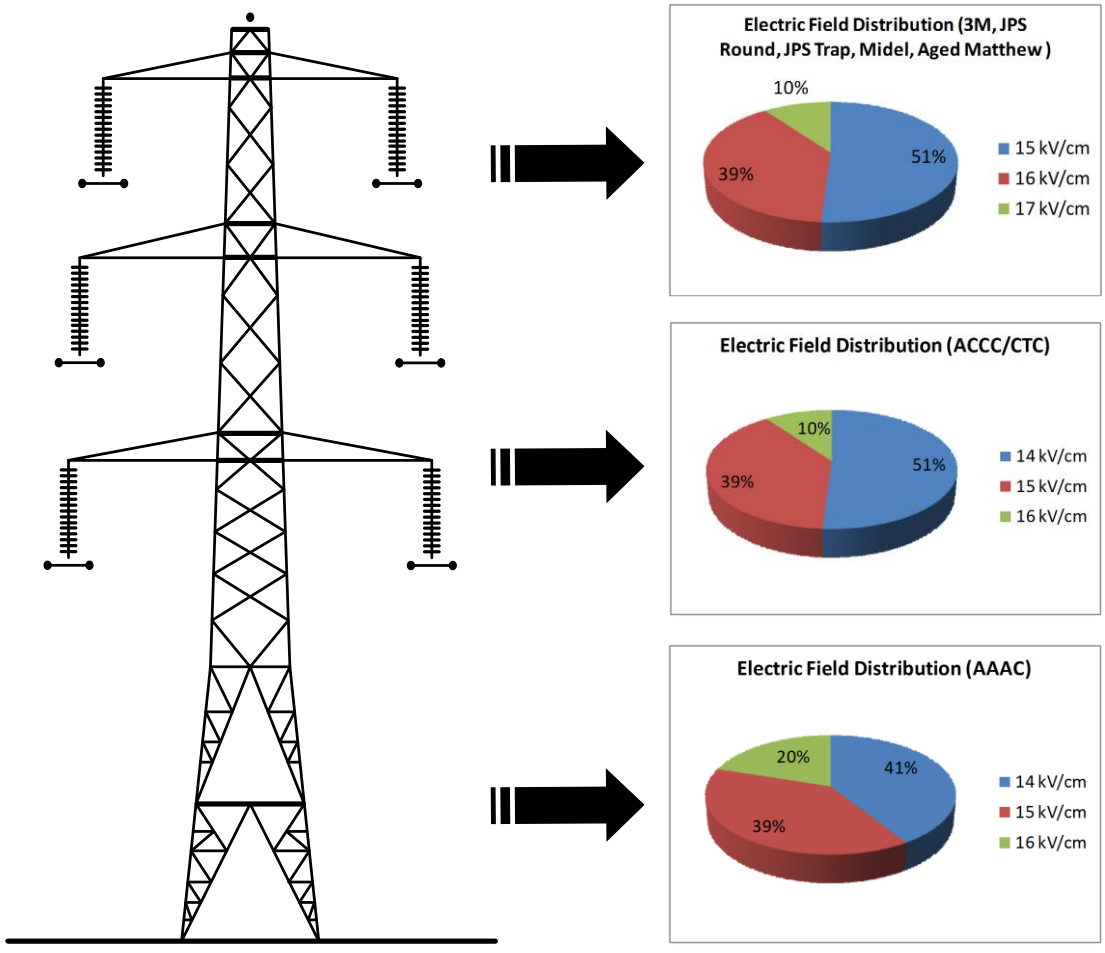

Figure 6-8 Surface Gradient Distribution for Various Types of Conductors on L2 Tower

The difference observed in Figure 6-8 is due to different types of conductors having different radius. For example, ACCC/CTC and AAAC have larger radius than the other five types of conductor, which results lower surface gradient values.

Figure 6-8 generates percentages of area have a certain level of surface gradient. For example, for AAAC conductor, there are 41% of the surface area has electric field between 13.5 kV/cm and 14.4 kV/cm (rounded-off). This factor is utilized to weight the measured noise scores as shown in Table 6-5. As explained in Section 6.5.1, different spray conditions give different results in the measurements. For this reason, manual spray and light spray are considered separately in the score analysis. Manual spray is considered first. After adding the weighted results together, the score indexes for 100 Hz (Figure 6-9), 200 Hz (Figure 6-10) and overall level (Figure 6-11) are generated. These score plots give prediction of noise levels if a certain type of conductor was installed on a L2 tower subject to conditions after rain stopped (manual spray).

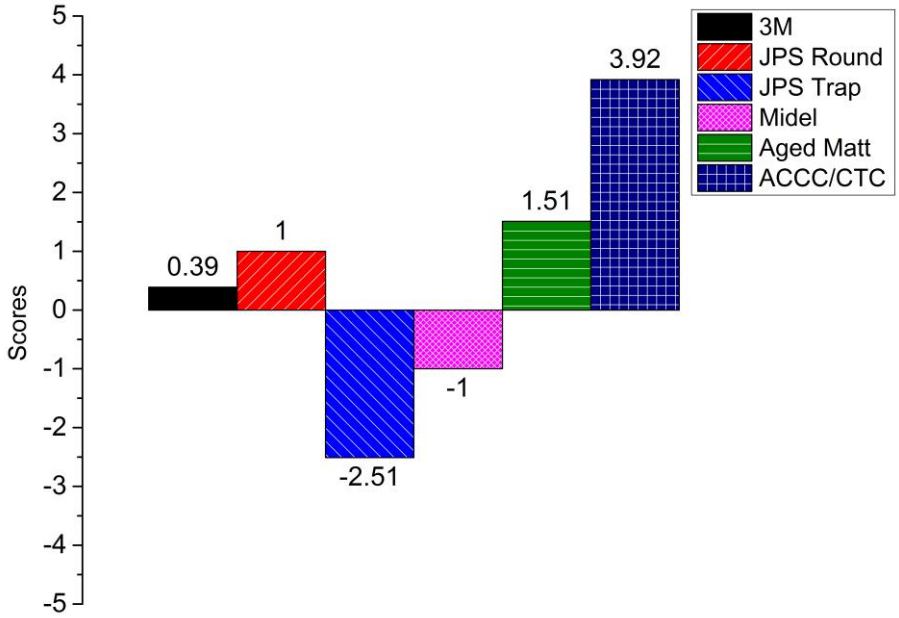

Figure 6-9 100 Hz Noise Emission Index for Manual Spray

Following conclusions are obtained from these index plots for manual spray:

- In the order of increased level of noise emission, these conductors are ranked as: JPS Trap, Midel-3M, AAAC, JPS Round, Aged Matthew, and ACCC/CTC.

- In different frequency ranges, the predicted level of noise varies. For example, 3M is noisier than AAAC in 100 Hz but quieter in both 200 Hz and overall level

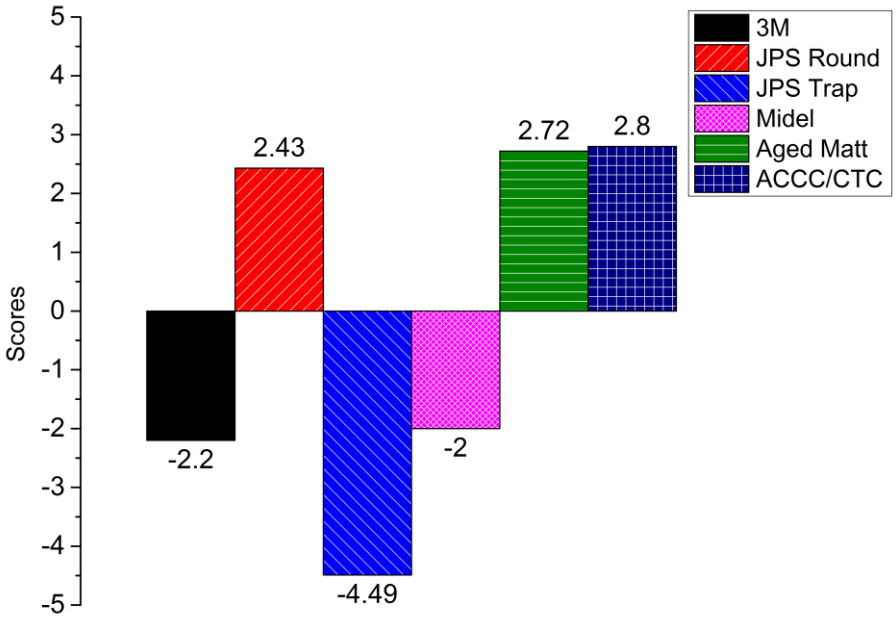

Figure 6-10 200 Hz Noise Emission Index for Manual Spray

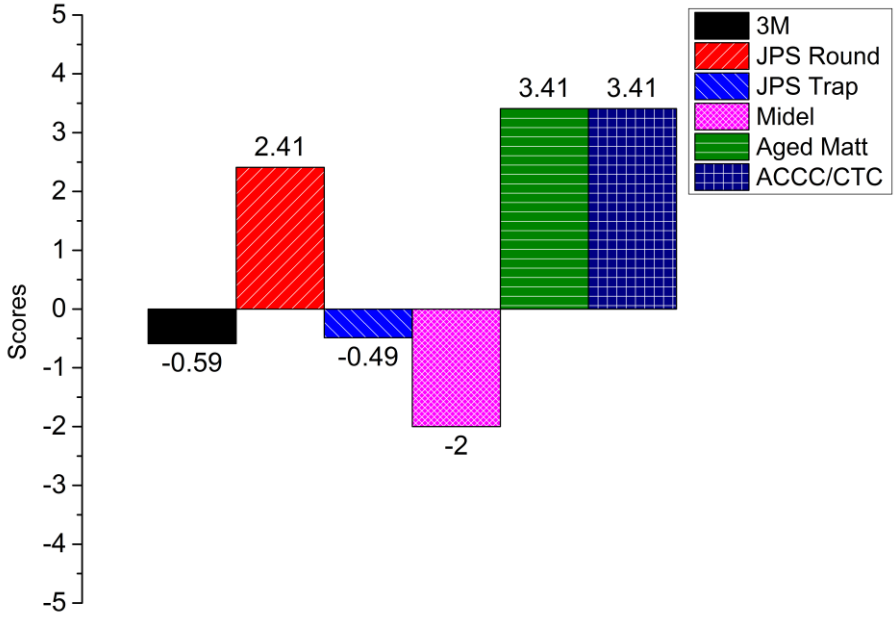

Figure 6-11 Overall (A-weighting) Noise Emission Index for Manual Spray

The same process is utilized to obtain the noise indexes for the light spray test. Results for 100 Hz (Figure 6-12), 200 Hz (Figure 6-13) and A-weighting (Figure 6-14)

indicate a different trend of noise emission compared to manual spray. A significant increase of noise level for JPS Trapezoidal is observed at 100 Hz. However, the 200 Hz and A-weighting index for JPS Trapezoidal remain lowest. The other difference is ACCC/CTC becomes quieter for 200 Hz and A-weighting indexes.

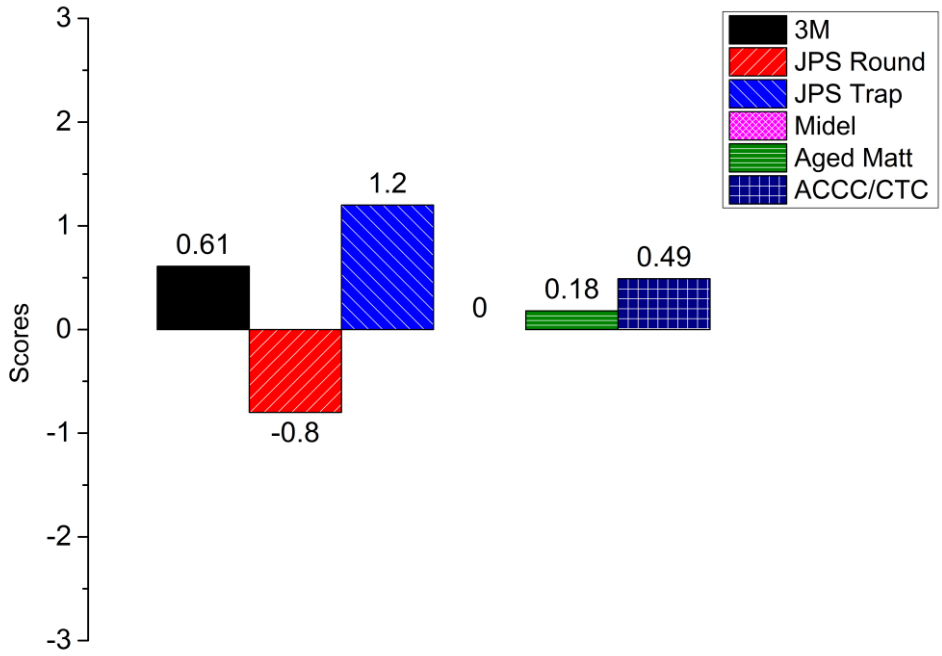

Figure 6-12 100 Hz Noise Emission Index for Light Spray

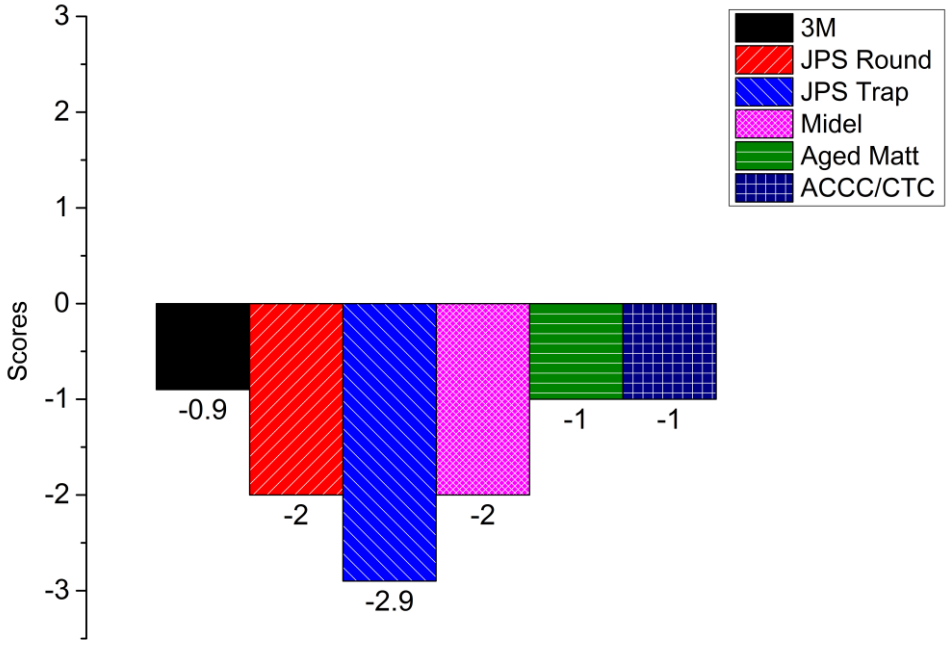

Figure 6-13 200 Hz Noise Emission Index for Light Spray

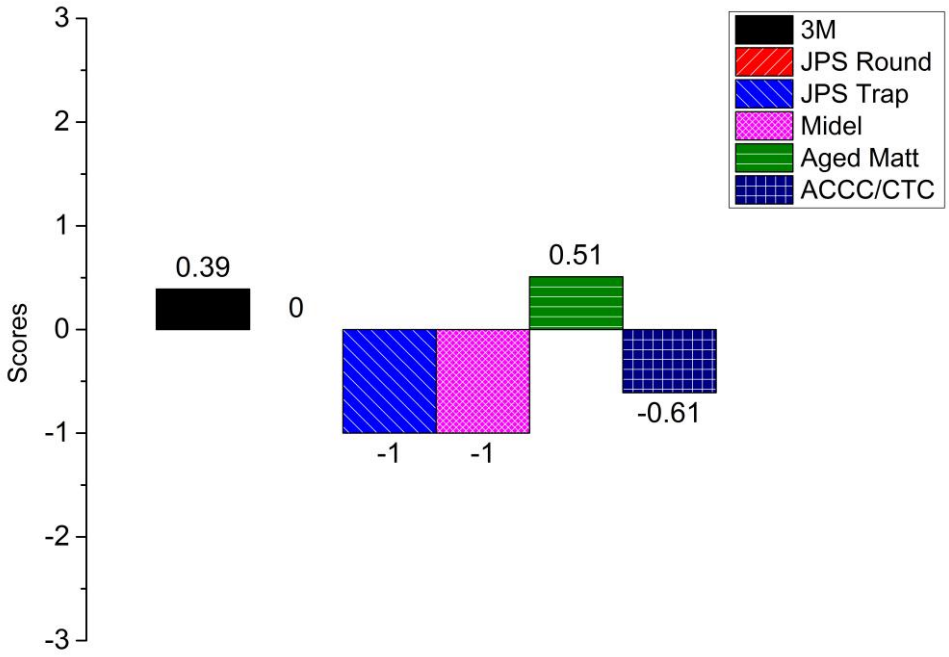

Figure 6-14 Overall (A-weighting) Noise Emission Index for Light Spray

In the real situation, both during-rain and post-rain conditions exist. In order to give a comprehensive rating for different conductor samples, manual spray and light spray indexes are added up to generate a overall score table (Table 6-6). Within this table, highest scores for each frequency span is marked red while lowest marked green.

Table 6-6 Overall Noise Index Combining Manual Spray and Light Spray

Overall Score	AAAC	3M	JPS Round	JPS Trap	Midel	Aged Matt	ACCC/CTC
100 Hz	0	1	0.2	**-1.31**	-1	1.69	**4.41**
200 Hz	0	-3.1	0.43	**-7.39**	-4	1.72	**1.8**
A-Weighting	0	-0.2	2.41	-1.49	**-3**	**3.92**	2.8

It is observed that:

- ACCC/CTC performs worst in both 100 Hz and 200 Hz indexes while Aged Matthew generates the highest noise level in A-weighting index
- JPS Trapezoidal conductor is quietest in both 100 Hz and 200 Hz indexes while Midel performs best in A-weighting level
- Aged Matthew conductor produces a relatively high level of noise in all three cases (above 1.5 score) while JPS Trapezoidal and Midel conductors produce relatively low level of noise in all frequencies (below -1)

- Depending on the frequencies, 3M conductor produces a wide range of noise levels (from -3 to 1)
- JPS Round conductor produces sufficient high level for A-weighting noise but low level for both 100 Hz and 200 Hz noise

6.6 Conclusion

This chapter proposed a standardized procedure to measure audible noise level and PD level from overhead line conductors. By following the same procedure, such as sample preparation, measurement procedure and results analysis, reproducibility is maintained. In the final part of this chapter, a rating method for audible noise assessment is developed. This method is considers both low and high frequency components, and allows direct comparison among various samples.

As a set of samples, with various surface conditions, ages and surface geometries, have been measured, discussion on the noise levels respect to these characteristics is conducted in the next chapter.

Chapter 7 Discussion

7.1 Introduction

In Section 6.5.2, a procedure was developed to compare the noise performance of different types of conductors. This chapter integrates the comparison of results with the surface characteristics of various types of conductors to discuss the mechanisms of noise generation.

7.2 Shape of Strands

As explained in Section 6.2.1, two types of strands exist in the samples tested: trapezoidal cross-section and round cross-section (shown in Figure 7-1, Figure 3-30 and Figure 3-31).

Table 7-1 Shape of Strands for Different Samples

Conductor Sample	AAAC	3M	JPS Round	JPS Trap	Midel	Aged Matt	ACCC/CTC
Shape of Strands	R	R	R	T	T	T	T

The shapes of strands are listed in Table 7-1, where 'R' refers to round cross-sections while 'T' refers to trapezoidal cross-sections.

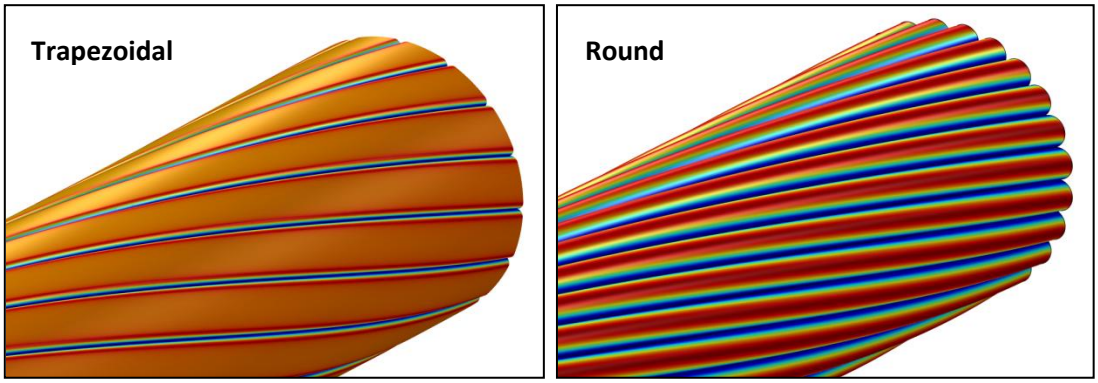

Figure 7-1 Shape of Strands (the colour shows the electric field distribution on the surface)

7.3 Contact Angle Measurements

The contact angle for water droplets has been measured for each type of conductor on a precise instrument (Figure 7-2). However, this equipment is designed for planar surfaces. A difficulty of contact angle measurements results from the round stranded conductors, when the surface has a large curvature. A micro-volume droplet is applied in order to obtain the accurate measurement results. However, the stranding shape still has effect on the measured results on contact angles. Contact angle is also affected by surface roughness, and the history of the surface. So while contact angle is indicative of droplet behaviour, it is not the entire picture concerning moisture movement on the surface.

With these reservations in mind surface condition is defined as:

- Hydrophilic ('I' in Table 7-2): contact angle is lower than 90°C
- Hydrophobic ('O' in Table 7-2): contact angle is higher than 90°C

Table 7-2 summarized the surface condition for all samples under tests.

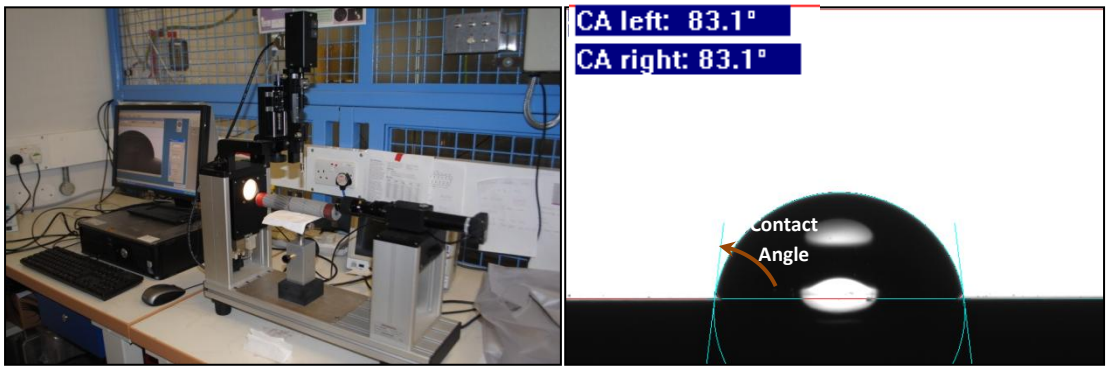

Figure 7-2 Contact Angle Measurement

Table 7-2 Surface Condition for Different Samples

Sample	AAAC	3M	JPS Round	JPS Trap-C	JPS Trap	Midel	Aged Matt	Aged Matt-B	ACCC/CTC
CA	86.0	82.0	103.5	95.3	69.5	85.3	104.1	83.1	78.0
SC	I	I	O	O	I	I	O	I	I

Note: CA-contact angle; SC-surface condition; 'I'-hydrophilic; 'O'-hydrophobic.

7.4 Noise and Surface Condition

As discussed in Section 6.5.1, manual spray and light spray give different conclusions in terms of noise performance. These two spray conditions are discussed separately in the following.

Within Figure 7-3 and Figure 7-4, only the first three samples (AAAC, 3M and JPS Round) have round strands, and the other six samples have trapezoidal strands. Results indicate that shape of strands is not a definitive factor in terms of noise emission. In other words, it is not always the case that round shape strands perform better or worse than trapezoidal shape strands.

In order to evaluate the effect of surface condition (contact angle), conductors which have the same geometries are summarized here:

- 3M; JPS Round: they have the same surface geometry but different surface condition. JPS Round is hydrophobic while 3M is hydrophilic. In terms of the noise emission, all three frequencies in manual spray indicate that JPS Round is noisier
- JPS Trapezoidal (coated with silicon); JPS Trapezoidal; Midel; Aged Matthew; Aged Matthew (sandblasted): these five samples have same surface geometry but different surface conditions. Referring to Table 7-2 and Figure 7-3, hydrophobic samples have higher noise level than hydrophilic samples. It is also observed that silicone coating makes the sample noisier while sandblasting reduces the sound emission for manual spray tests.

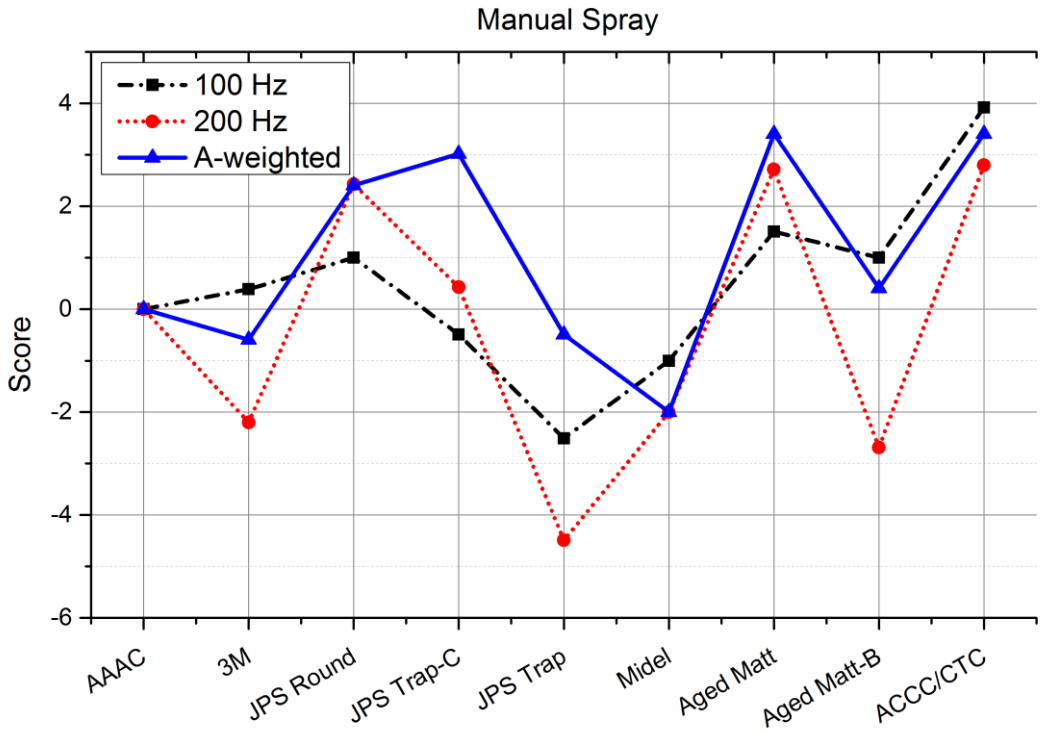

Figure 7-3 Noise Emission Index for Manual Spray

Under the light spray tests, it is observed that:

- If 3M is compared with JPS Round, hydrophobic sample generates lower noise level which is the opposite to the manual spray results
- For 100 Hz noise level, it is observed that silicon coating reduces the noise level while sandblast increases the noise emission

These conclusions contradict the results generated from the manual spray tests. Given this evidence, it is concluded that surface condition (contact angle) dominates the noise emission in manual spray condition but not in light spray condition. There are further factors could affect the performance of conductors under light spray conditions such as roughness.

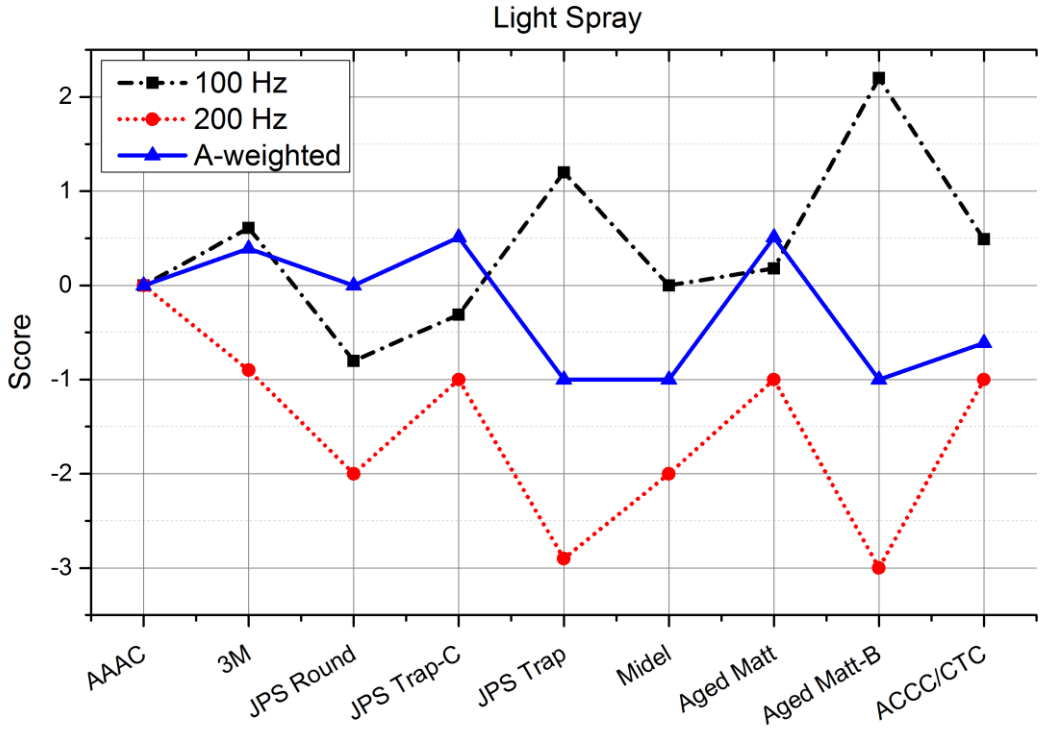

Figure 7-4 Noise Emission Index for Light Spray

To understand the consequences of surface conditions on noise generation, a controlled experiment is carried out to evaluate water droplets' behaviour on different surface conditions. As shown in Figure 7-5, within a short length of a conductor sample, different surface treatments (silicone coated, without treatment and sandblasted) generated different surface conditions (hydrophobic, normal and hydrophilic). Simulated rain conditions (light spray) and high voltage (to reproduce the operational condition with 18 kV/cm surface stress assuming a cylindrical shape) are applied, and different appearances of water droplets are observed.

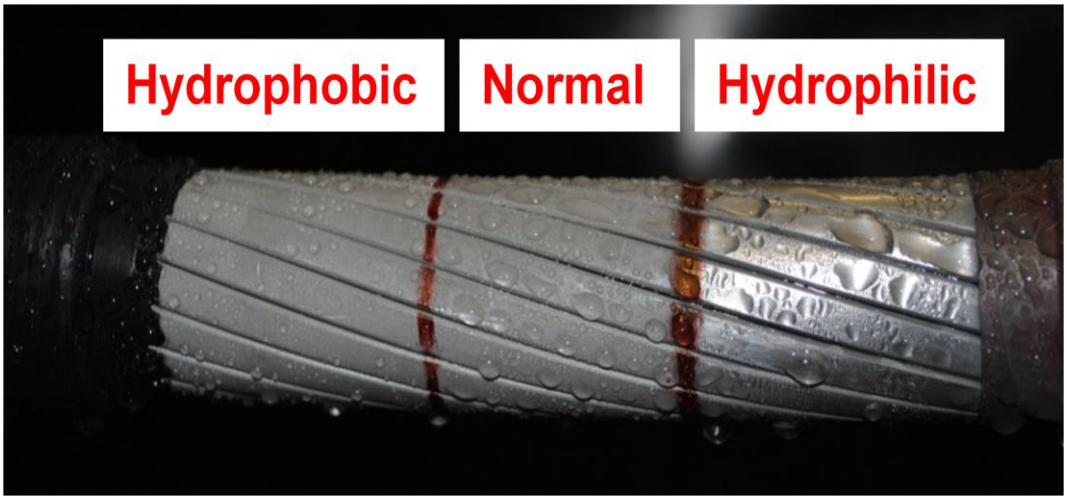

Figure 7-5 Formation of water droplets on the surface of different hydrophobicities

It is concluded that:

- The size of droplets is highest on the hydrophilic surface while lowest on the hydrophobic surface.
- For the hydrophobic surface, the droplets accumulate to a certain size until they start to slip along the stranding edge. Because the minimum droplet size needed to start slip is relatively small (this is due to the surface contact angle), we observe a large number of small droplets moving quickly compared to the other surfaces.
- For the hydrophilic surface, the droplet can grow to become relatively large before slipping down. We can observe a very slow slip with large droplets along the stranding.

The key outcome of analysis on noise level and water droplets' appearance demonstrated that 100 Hz, 200 Hz and A-weighted noise levels change differently with wetting types (like manual spray and light spray). This key conclusion indicates that the noise generation of 100 Hz, 200 Hz and A-weighted has different physical mechanisms.

It has been explained in Chapter 4 that trapezoidal shape strands in a hydrophobic condition lead to more droplets with smaller size while round strands with hydrophilic condition leads to fewer droplets with larger size. The frequency of vibrating droplets is also shown in Figure 4-17 with the conclusion that smaller droplets experience

higher vibrating frequencies than larger droplets. These different frequency characteristics determined the different output of noise at 100 Hz, 200 Hz and A-weighted.

In conclusion, surface condition (hydrohpobicity), surface roughness, stranding shape (round strands or trapezoidal strands), surface electric field strength and wetting procedures (manual spray or light spray) together determine the size, distribution and vibrating frequencies of surface droplets which affect 100 Hz, 200 Hz and A-weighted noise levels in different ways. So predicting noise emission levels from overhead line conductors is not straightforward and can cause large variations in the results due to this complex nature.

7.5 Comments on Procedures in Evaluating Noise from Conductors

As the flow chart (Figure 7-6) explained, existing noise prediction methods first compute a single maximum electric field value on surface of conductor. This method ignores the conductor stranding shape, proximity effect of the tower and the potential protrusions on the surface of conductor (Section 2.2.1). The outcome of the simplified model is a single maximum value of electric field. This value is then utilized as an input parameter to compute the noise level. Empirical equations generated from experimental data (Section 2.3.3) are then utilized to compute an A-weighted noise level. Depending on whether this noise level is acceptable or unacceptable, the power utility then makes the decision concerning the conductor type to be installed.

Within the research work of this thesis, these following comments are developed on this existing method:

- The existing method in calculating the surface gradient is not accurate as it does not take into consideration stranding shape.
- A single maximum value is not sufficient to represent the distribution of electric field
- Existing empirical equations are based on the data generated in 1950s and 1960s when newly designed conductors (HTLS) were not considered, so there is a lack of information when trying to evaluate new types of conductors

- The index selected to present noise emission is A-weighted while the specific contribution of low frequency noise (especially 100 Hz and 200 Hz) is not taken into consideration

With all these concerns listed above, detailed prediction of noise level from overhead line is not realistic as the large variation of results and complex physical mechanisms behind this. An assessment-based evaluating strategy is believed to give more useful information when supporting utilities to select conductor or evaluate noise performances. This strategy includes the consideration of protrusions, and shape of strands when computing the surface gradient. It generates the natural of distribution of surface electric field rather than a single maximum value. A cage experiment with controlled background noise and electric field distribution has been developed as a reproducible tool for various types of conductors. Different wetting conditions, include manual spray and light spray, are reproduced in the experiment. A rating strategy analyzing frequency characteristics is thus necessary and developed to give information on the noise performance for different conductors, as discussed in Section 6.5.

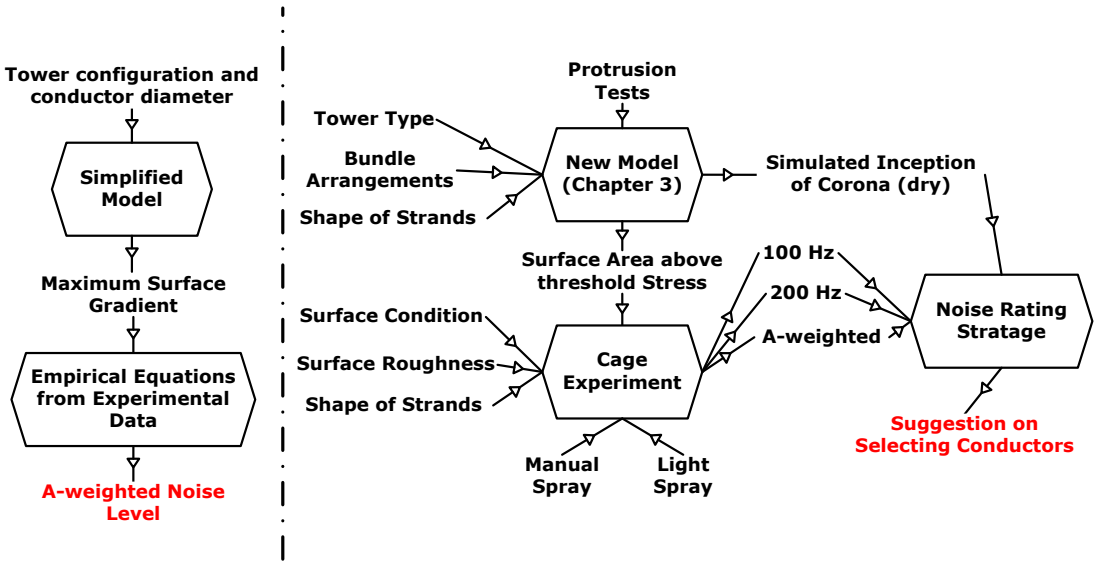

Figure 7-6 Procedures in Noise Prediction (left: existing method; right: method developed in this thesis)

Chapter 8 Conclusions and Future Work

8.1 Achievements

A methodology for modelling surface fields on conductors has been established.

This method employs both Charge Simulation Method and Finite Element Method to calculate the electric field distribution for various stranding shapes (round strands and trapezoidal strands are considered) as well as the presence of protrusions. Results have shown that although the round strands have a higher maximum value of electric field, the trapezoidal strands have a larger area which could potentially generate corona discharges.

With specific treatment on boundary conditions and meshes, a large scale FEA model has been developed to simulate the electric field distribution around conductors when they pass a tower. The enhancement of electric field is evaluated. The effect of bundle geometry on surface electric field is also predicted. This has also been applied to the National Grid's new T-Pylon structure.

A test regime and instrumentation for audible noise evaluation for overhead line conductors has been established.

An anechoic chamber has been built to isolate the background noise including the hum noise from the testing transformer. A cage experiment which is capable of testing a three meter long conductor has been designed and commissioned. Electrical design procedures include optimising the dimensions of the cage experiment, designing end fittings to mitigate end effects, corona inspection, selection of a bushing and partial discharge evaluation for joints and bushings. A tensioning system to apply tension to the conductor was designed to reduce the sag level to a negligible level. A spray system has been designed and implemented to simulate both the heavy and light rain conditions.

UV cameras have been employed to visually detect the corona discharges. They are also important tools when carrying out corona inspection in the field. Two high accuracy microphones were introduced for acoustic measurements. Sound signals are processed through an integrated platform which enables FFT analysis and overall

level analysis. A high speed camera was employed to observe the motion of a section of droplets on surface of conductor when AC voltage is applied. An Omicron PD detection system is utilized to detect the discharge level of bushing.

Measurements have been shown to be reproducible.

Seven conductor samples tested under the test arrangement have shown consistent results allowing direct comparison of performance.

A strategy has been developed to compare the performance of different types of conductors, and it has been utilized in National Grid as tool to select conductors.

This stratagem takes into consideration both the low frequency pure tones (100 Hz, 200 Hz and their harmonics) and the high frequency wide band noise (typically 1 kHz to 10 kHz). Results are different compared to the A-weighted results because low frequency noise level does not correlate well with high frequency noise. This also demonstrated the importance of assessing the low frequency noise separately in future line designs.

A data base has been generated for the noise performance on various types of conductors.

This has been provided in the Appendix I and can be utilized for predicting noise from conductors in the future.

It has been shown that the nature of the surface wetting changes the relative noise generation from the conductors.

From observation, the formation of moisture varies among different types of samples. This depends on hydrophobicity, surface roughness, geometry of strands and the spray condition. It has been demonstrated that by changing the surface condition of a conductor sample, the noise performance can be changed. This difference is identified not only by the overall level increasing or reducing but also by the frequency distribution changing.

Detailed measurements have shown that there is more than one mechanism present in noise production.

The independence between hum and crackling noise levels proved that the physical mechanisms behind them are different. The 100 Hz, 200 Hz and A weighted noise levels do not change in the same way with different wetting conditions. Light spray and manual spray give different noise outputs for same sample. This indicates that the emissions of noise from overhead line conductors are different when they are under rain condition or post rain condition.

Trapezoidal strands do not necessarily produce more noise than round strands under wet conditions. Unlike the protrusion analysis for dry conditions, noise levels generated from the trapezoidal stranded conductor are not always above those from the round-strand conductor. This is due to the complexity of moisture formation and movement during rain condition which can modify the noise output.

Low levels of hydrophobicity reduce noise generation. Grit-blasting has been employed as an efficient method to reduce the surface hydrophobicity by removing the silicon components on the surface of conductors, and modifying surface roughness. A grit-blasted sample was tested before and after treatment, and result compared. It is found that reducing the hydrophobicity is an effective way to reduce the noise level. This has been submitted to National Grid as a general comment and as a potential method in reducing noise emissions, but this needs further work to verify consistency and the importance of grit type etc.

8.2 Potential Future Work

Work related to audible noise emitted from overhead line conductors should continue. Potential research topics are summarized below.

Mechanism of Hum Noise

As described in Chapter 1, the physical mechanism of hum noise from overhead line conductors is difficult to understand. This is due to the complex physical phenomena involved in the noise generation, such as corona discharge (Chapter 5), droplet vibration and movement of ejected charged particles (Chapter 4). Due to the related nature of these phenomena it is difficult to design an experiment to identify the main source of hum noise. Preliminary research has been carried out through this project, and several hypotheses have been drawn:

1. Oscillation of fine particles:

   When the voltage increased to a certain level, the droplets start to eject smaller sub-droplets. After separation from the main body of water drop, these small parcels vibrate under AC electric field. This reciprocate movement of mass generates 100 Hz hum noise.

2. Vibration of charged water droplets getting trapped in high electric field regions:

   Due to the physical constraints and time limitations, experiments on twin bundles were not carried out. However, the different field distribution on a twin bundle could potentially create a high electric field region where charged droplets can vibrate in equilibrium state (as shown in Figure 8-1). This mechanism can generate a large mass vibrating at 100 Hz and thus acoustic noise as well.

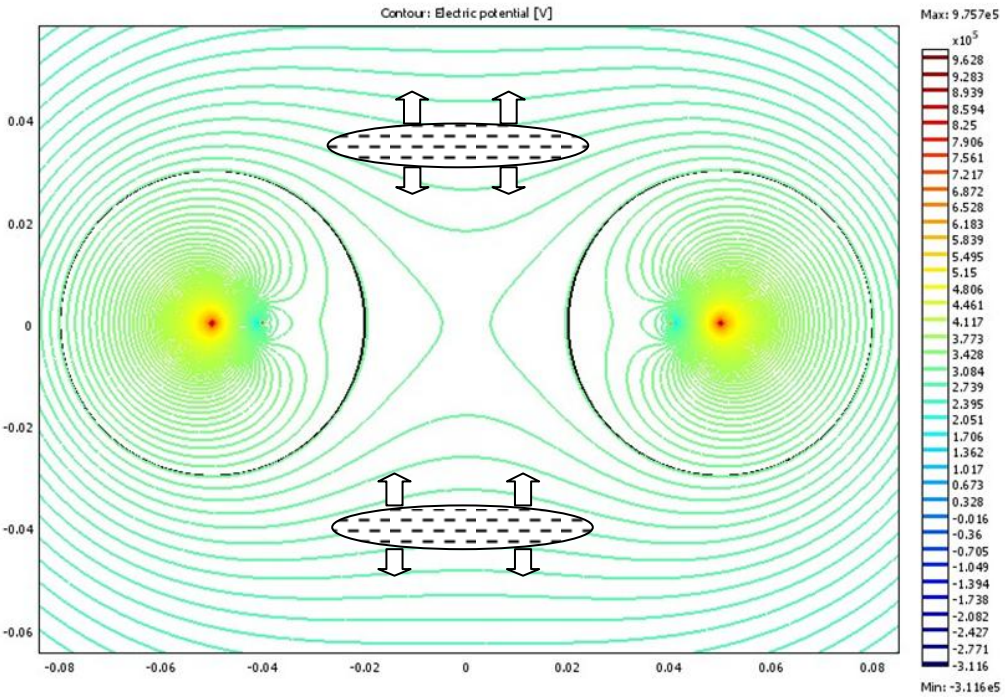

Figure 8-1 Voltage Potential Contour for a Twin Bundle Arrangement (spacing between sub-conductors is selected small to give a better picture, but not the real bundle spacing distance)

3. Vibration of droplets

   From the evidence of experiments, the GAP conductor tends to form large population of similar size drops. If these droplets are vibrating around resonance frequency, the magnitude will be enhanced. This mechanical

vibration of water droplet can create pressure difference which then generates acoustic waves with 100 Hz frequency.

APPENDIX

Acoustic Emission Database for Various Conductors

These plots are the measured noise levels for different types of conductors. Resutls are presented at 100 Hz, 200 Hz and A-weighted. Each green dot represents a single measurement, while the blue curve is the best-fit normal distribution of the data. The blue box provides: a blue dot at the centre for the mean, the maximum and minimum obervations, whilst the box top and bottom give the 90 and 10 percentiles.

Details of the conductors are given in Table 6-1.

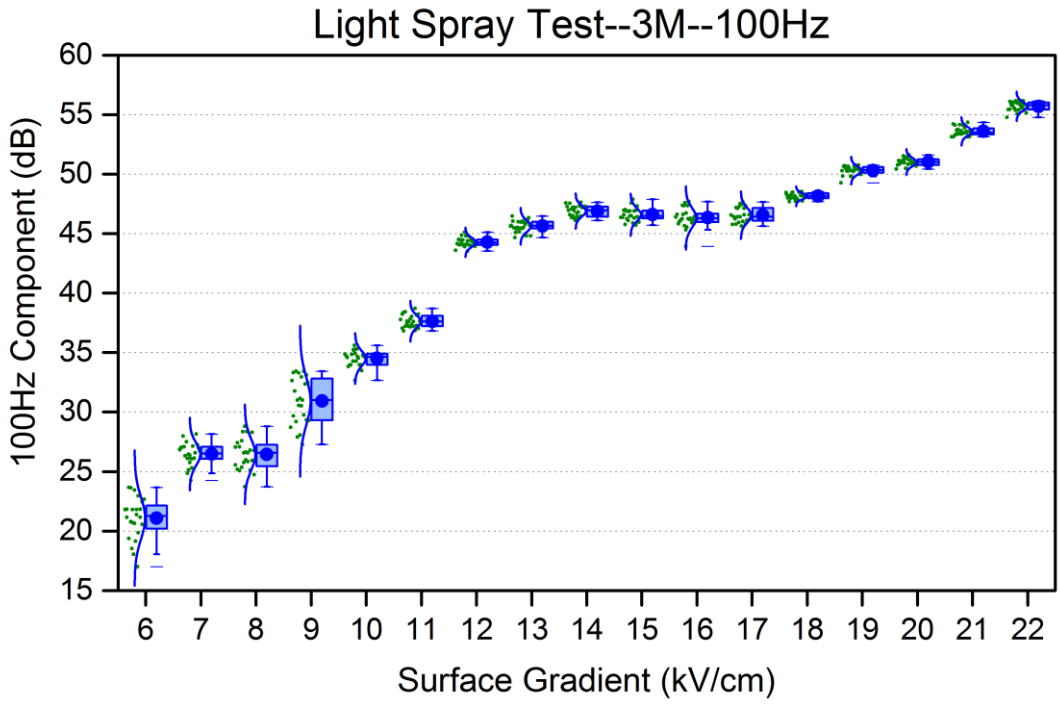

Figure 1 Light Spray Test 100 Hz Results on 3M Conductor

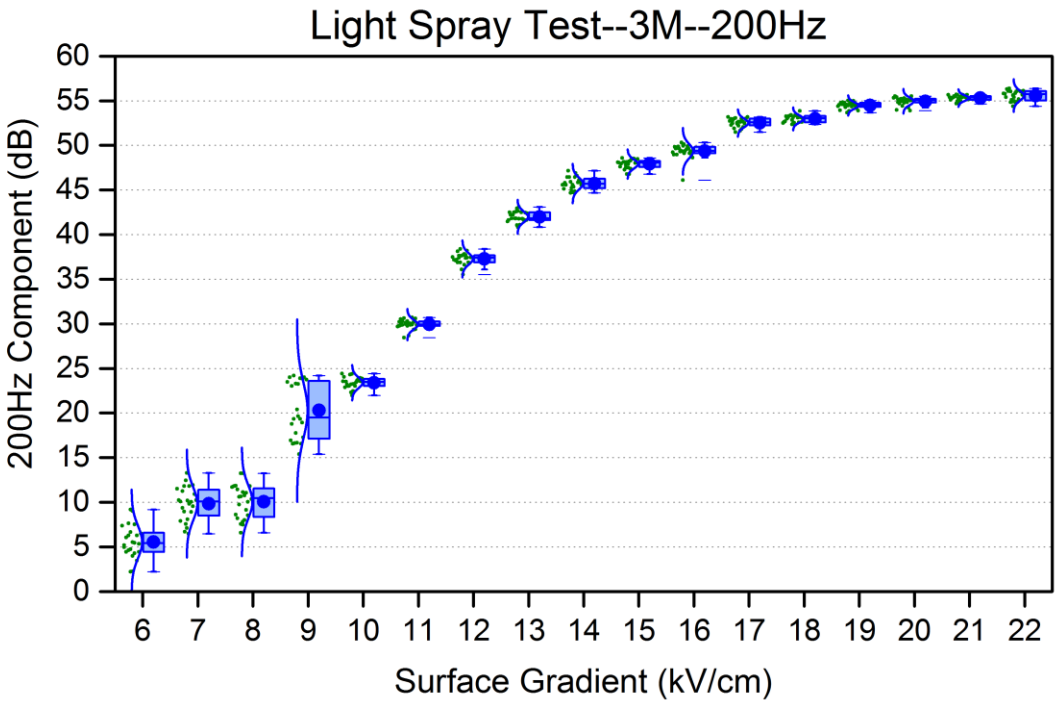

Figure 2 Light Spray Test 200 Hz Results on 3M Conductor

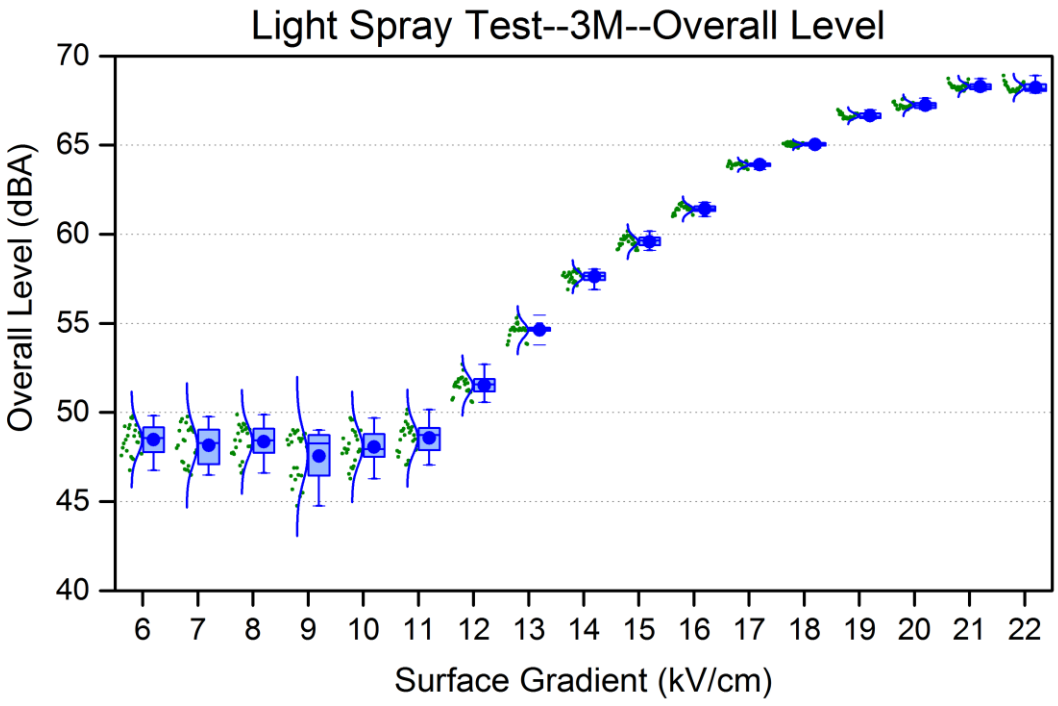

Figure 3 Light Spray Test Overall Level Results on 3M Conductor

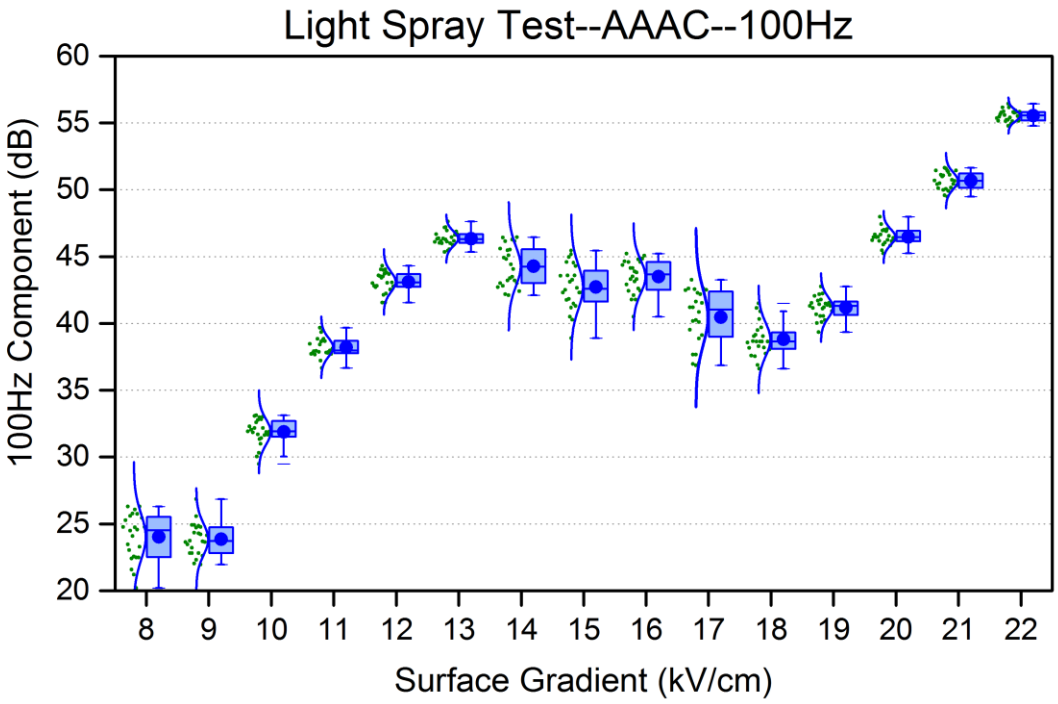

Figure 4 Light Spray Test 100 Hz Results on AAAC Conductor

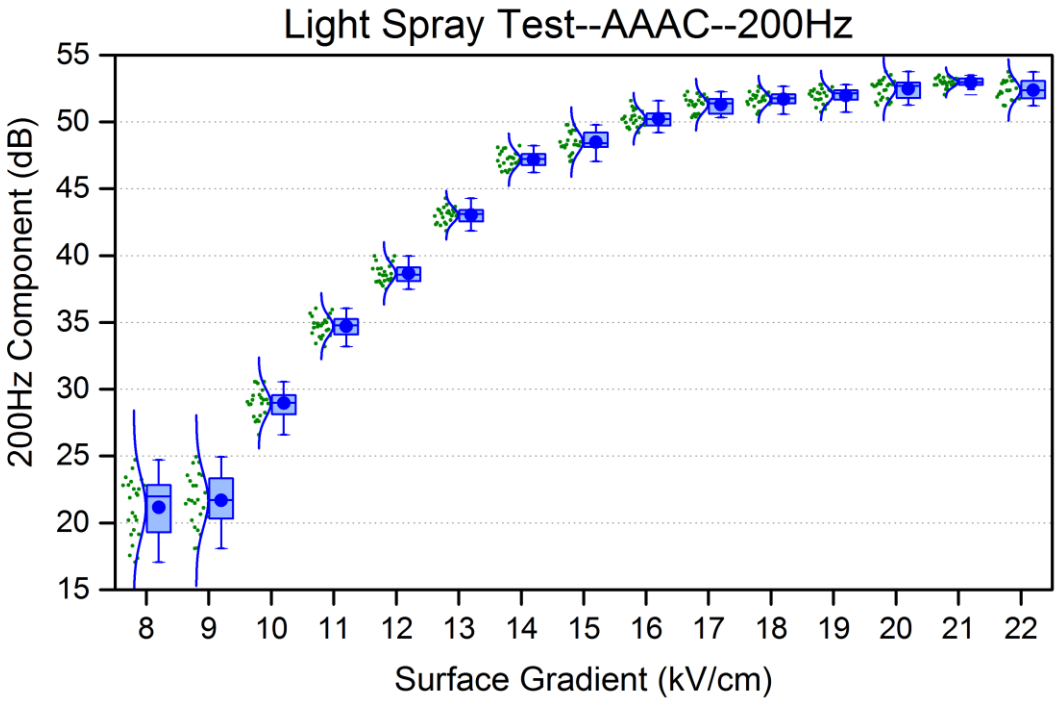

Figure 5 Light Spray Test 200 Hz Results on AAAC Conductor

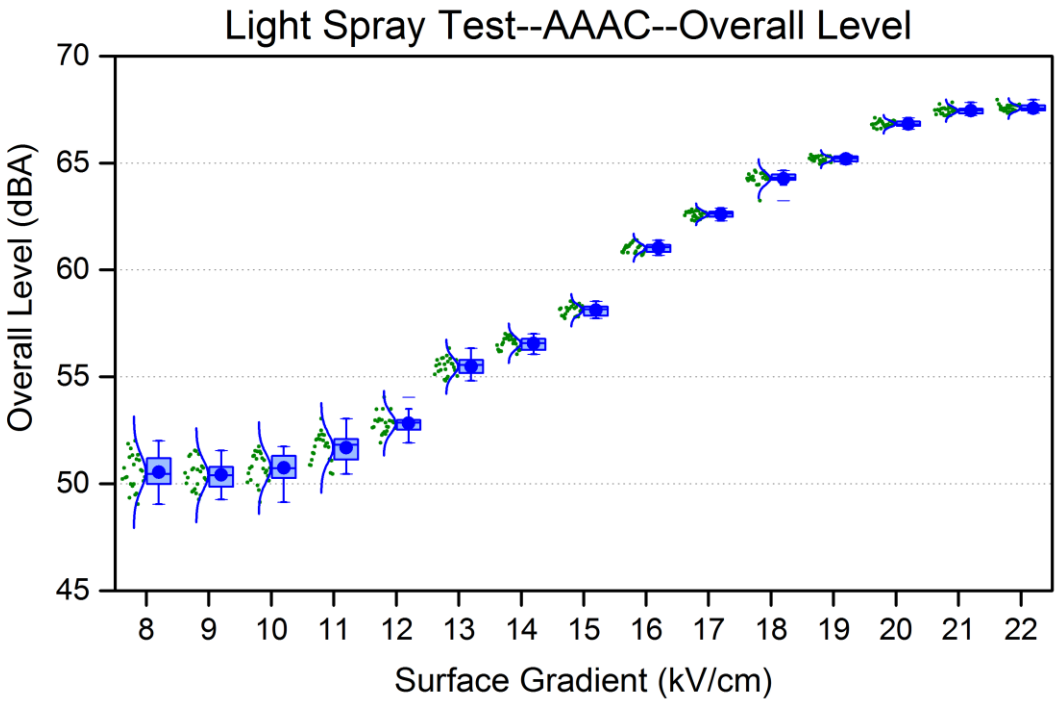

Figure 6 Light Spray Test Overall Level Results on AAAC Conductor

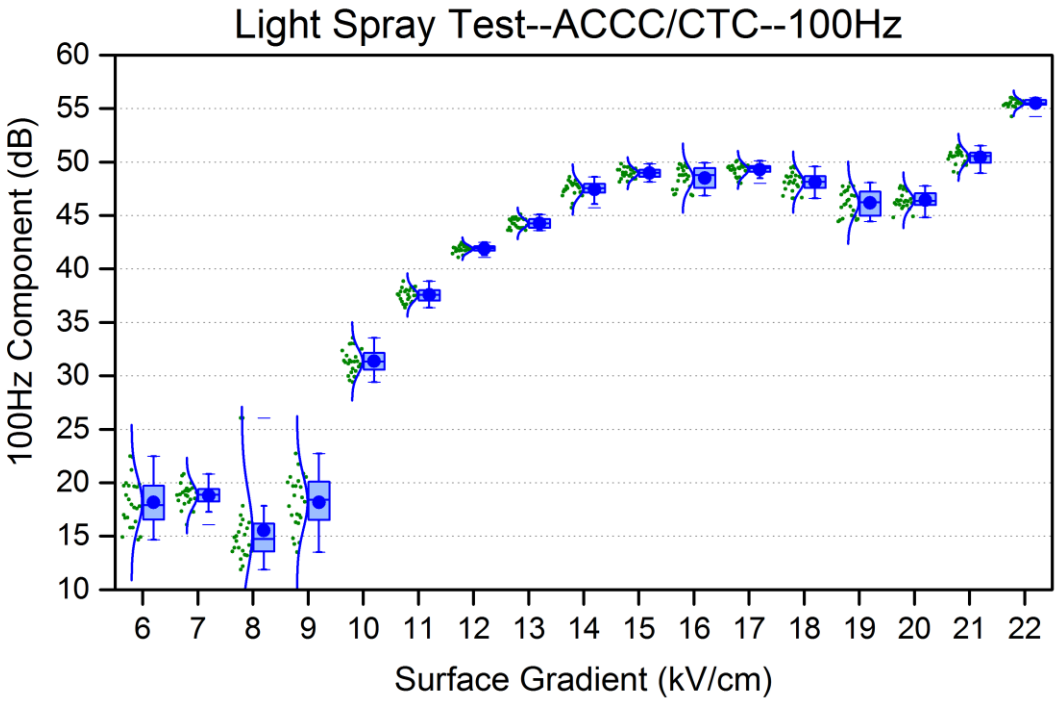

Figure 7 Light Spray Test 100 Hz Results on ACCC/CTC Conductor

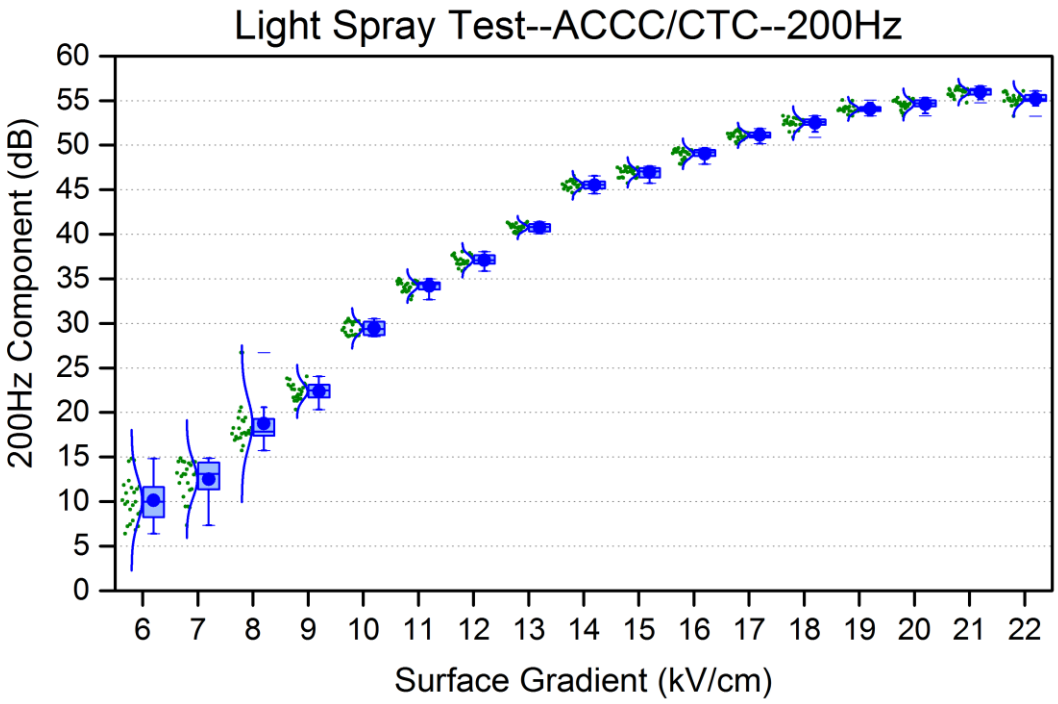

Figure 8 Light Spray Test 200 Hz Results on ACCC/CTC Conductor

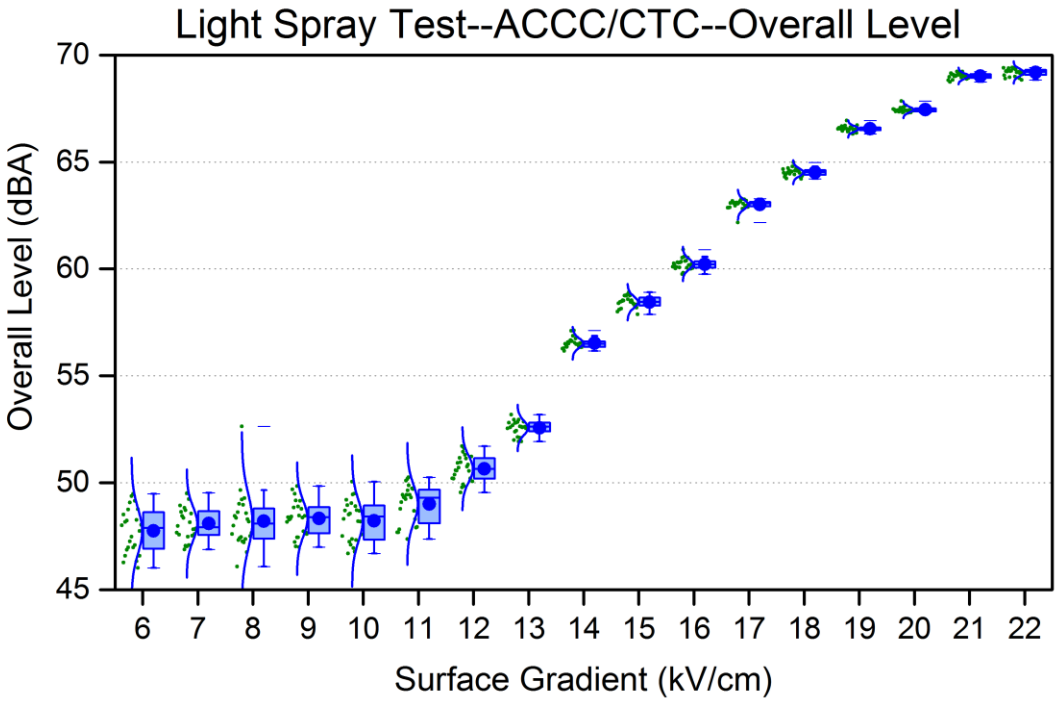

Figure 9 Light Spray Test Overall Level Results on ACCC/CTC Conductor

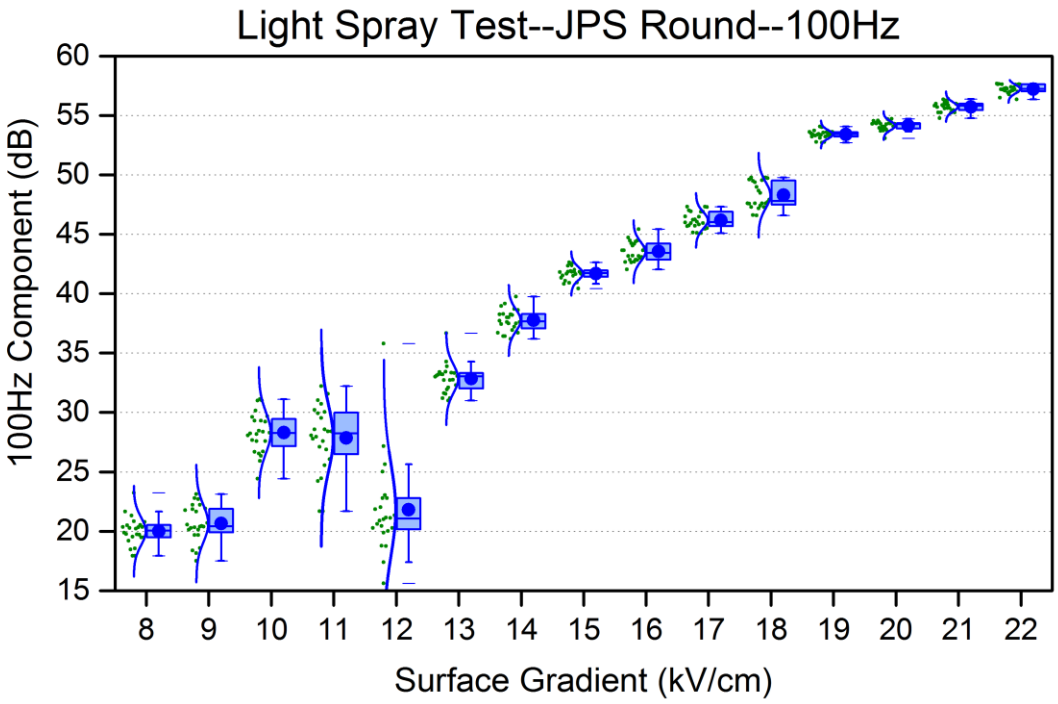

Figure 10 Light Spray Test 100 Hz Results on JPS Round Conductor

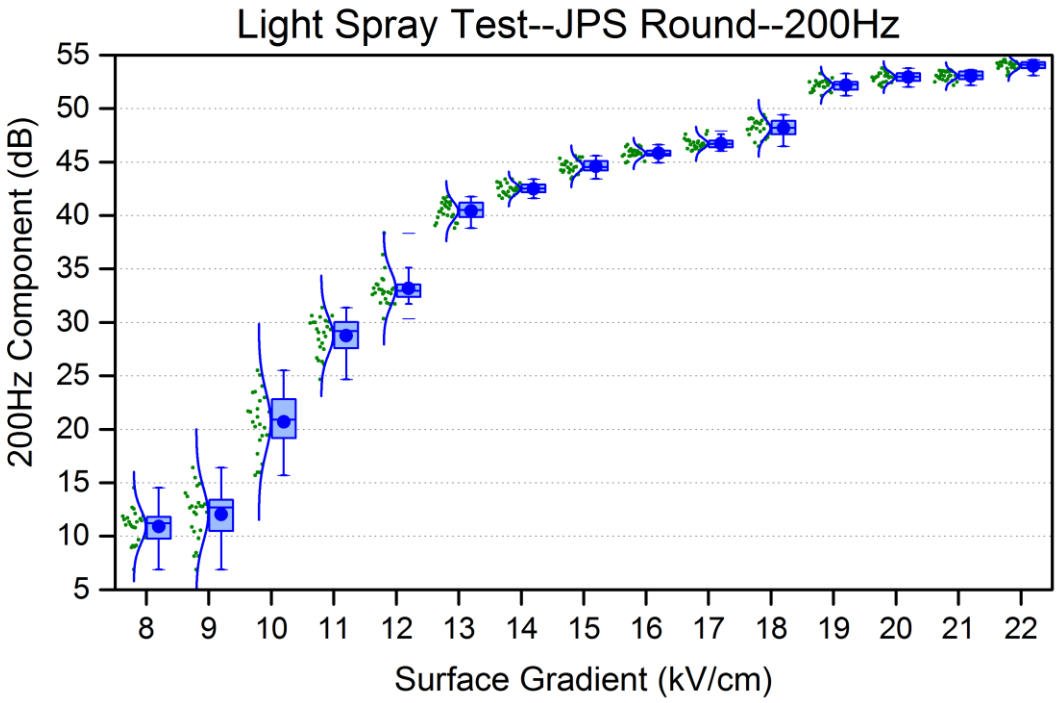

Figure 11 Light Spray Test 200 Hz Results on JPS Round Conductor

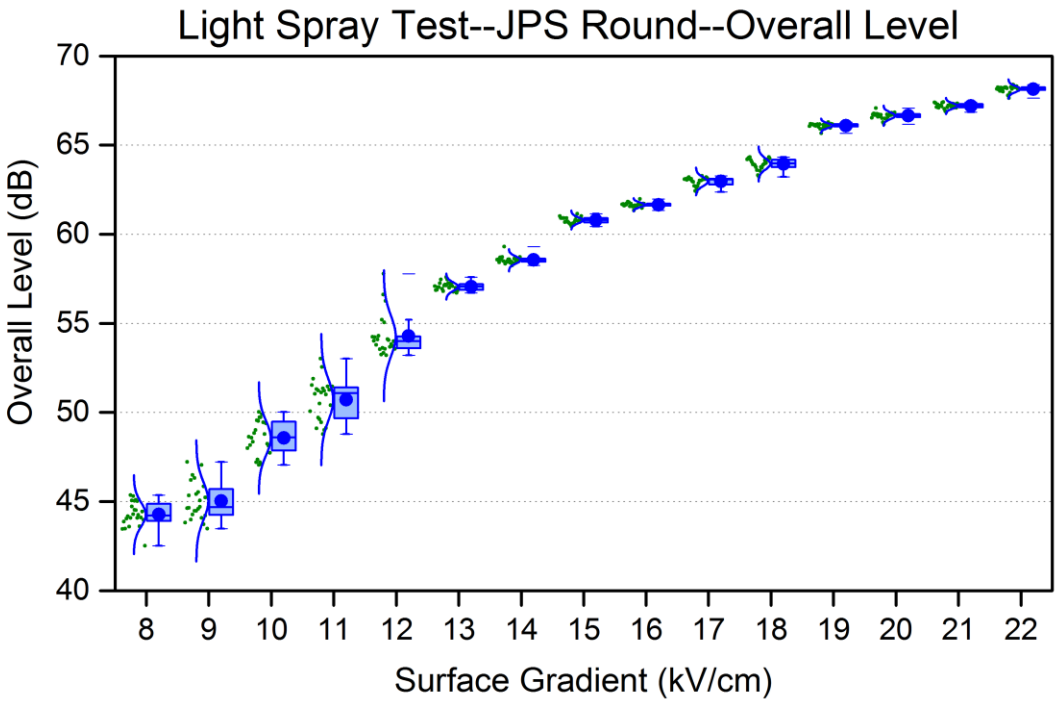

Figure 12 Light Spray Test Overall Level Results on JPS Round Conductor

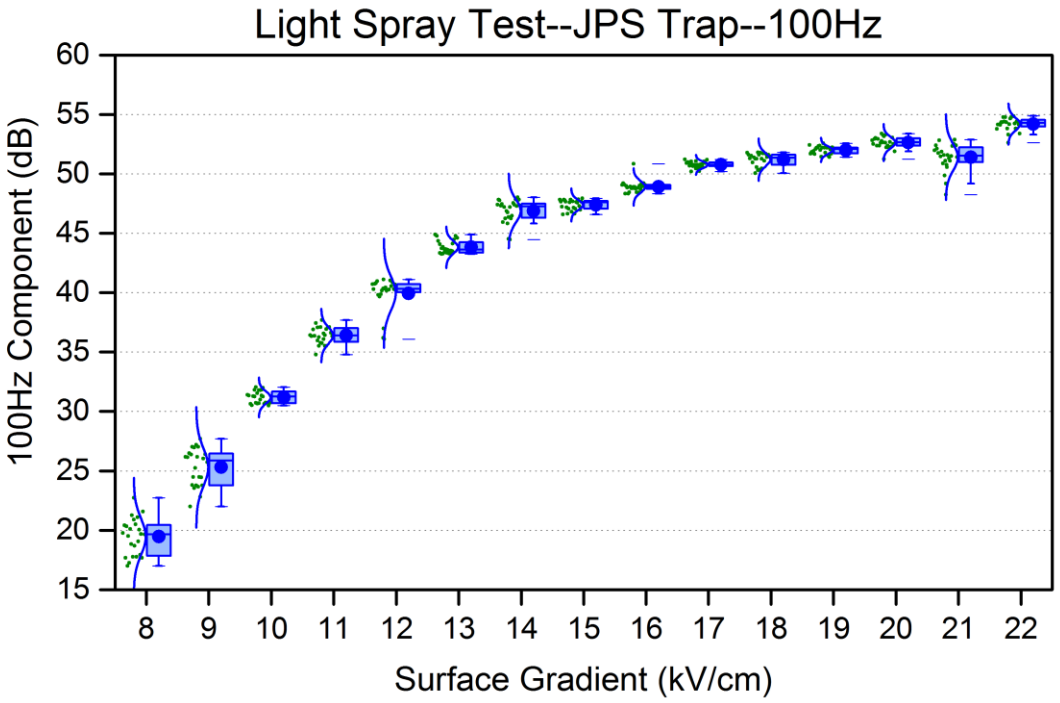

Figure 13 Light Spray Test 100 Hz Results on JPS Trap Conductor

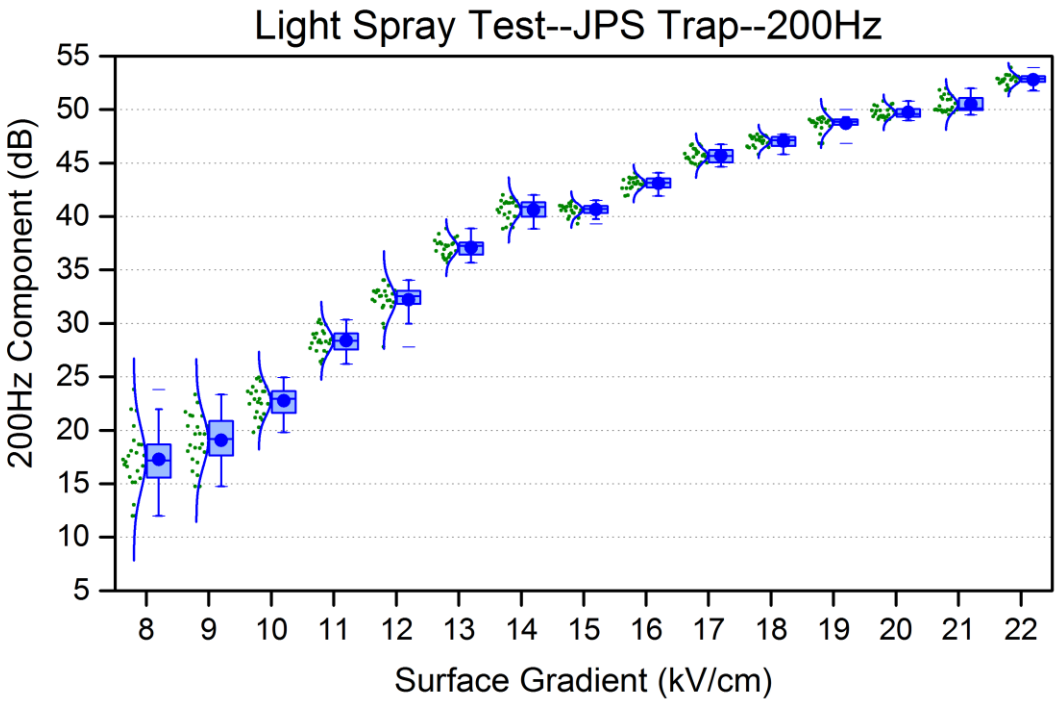

Figure 14 Light Spray Test 200 Hz Results on JPS Trap Conductor

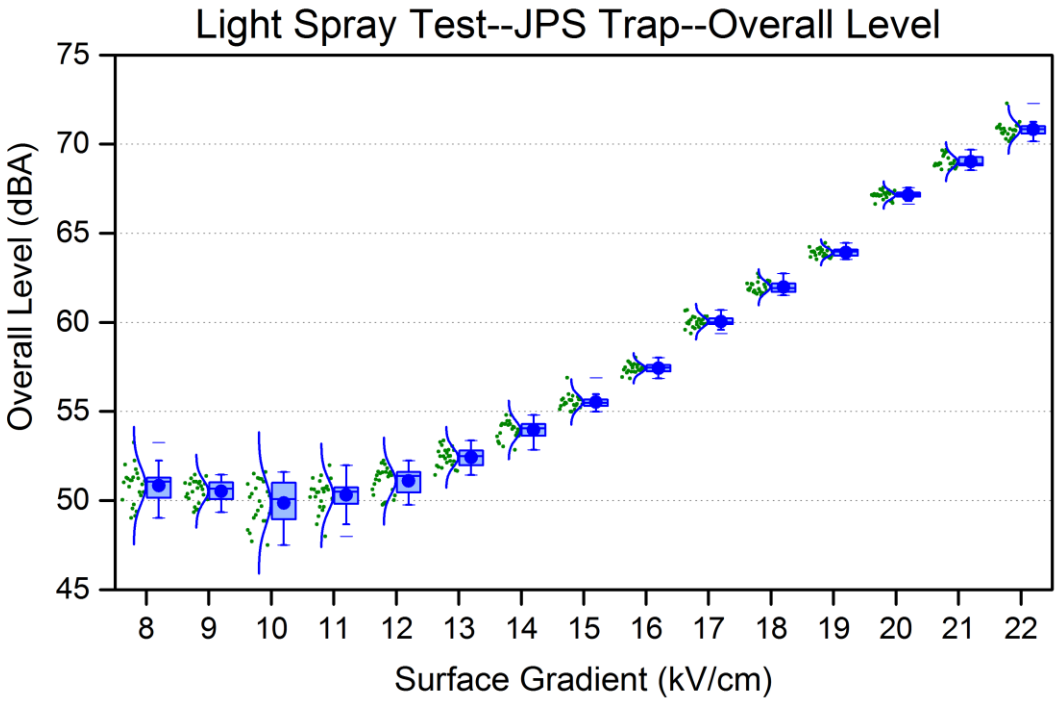

Figure 15 Light Spray Test Overall Level Results on JPS Trap Conductor

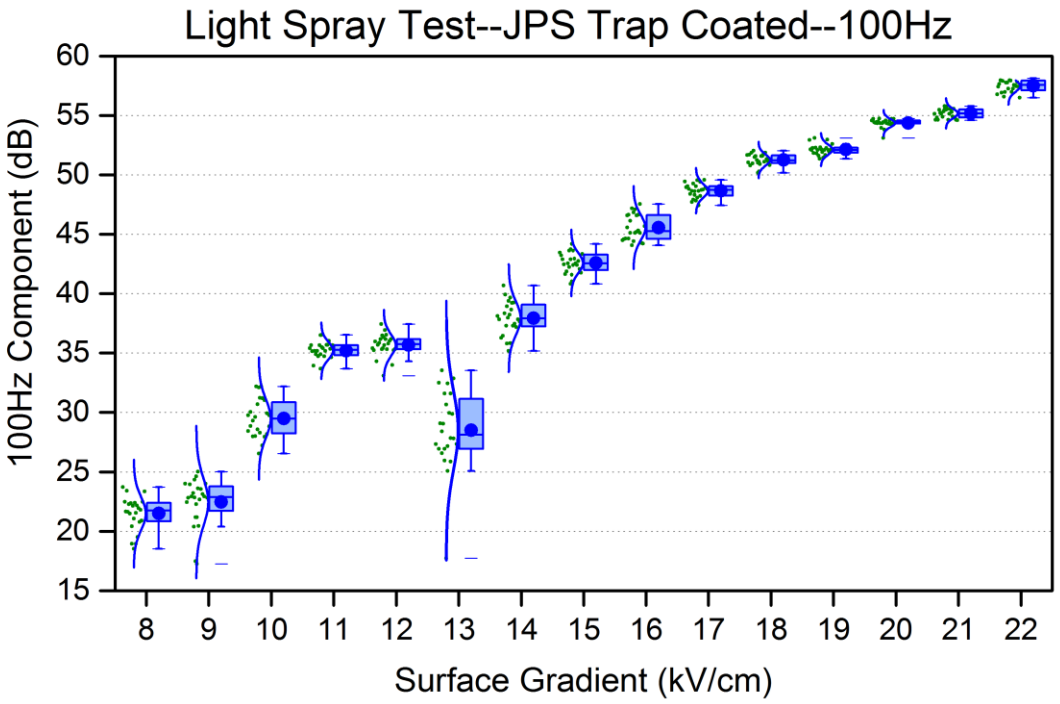

Figure 16 Light Spray Test 100 Hz Results on JPS Trap Coated Conductor

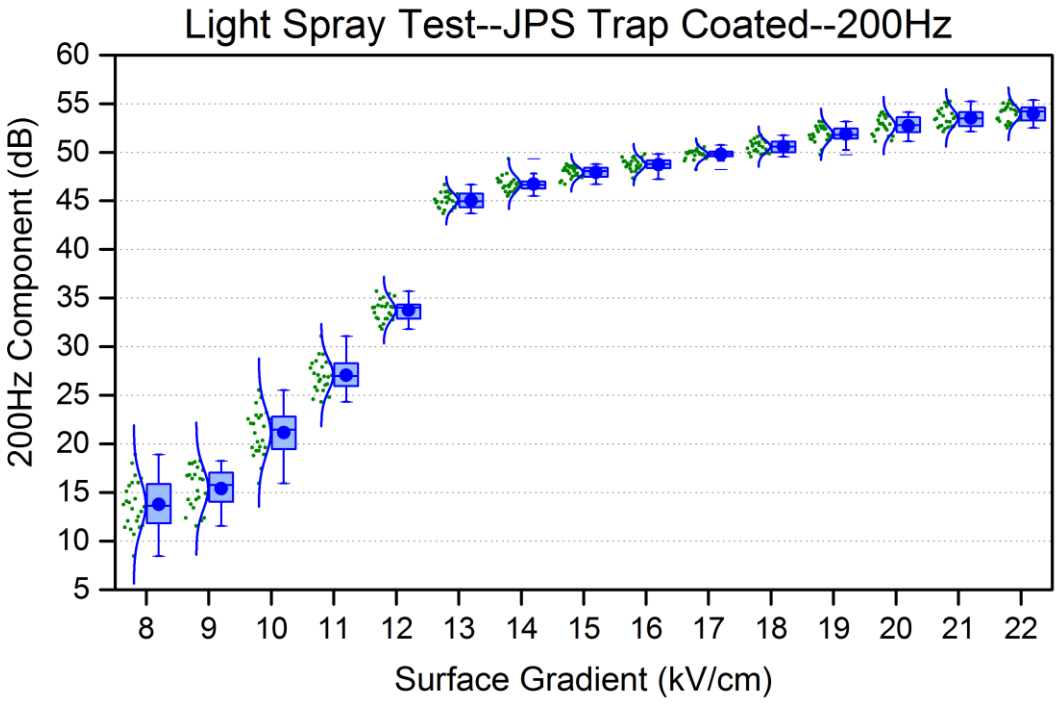

Figure 17 Light Spray Test 200 Hz Results on JPS Trap Coated Conductor

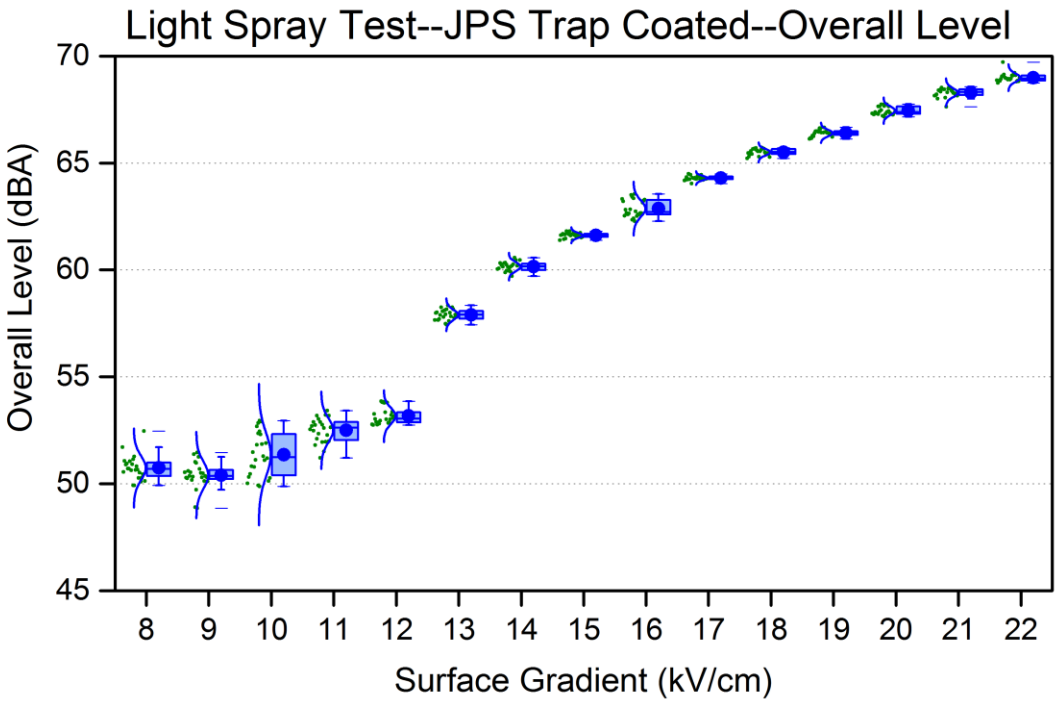

Figure 18 Light Spray Test Overall Level Results on JPS Trap Coated Conductor

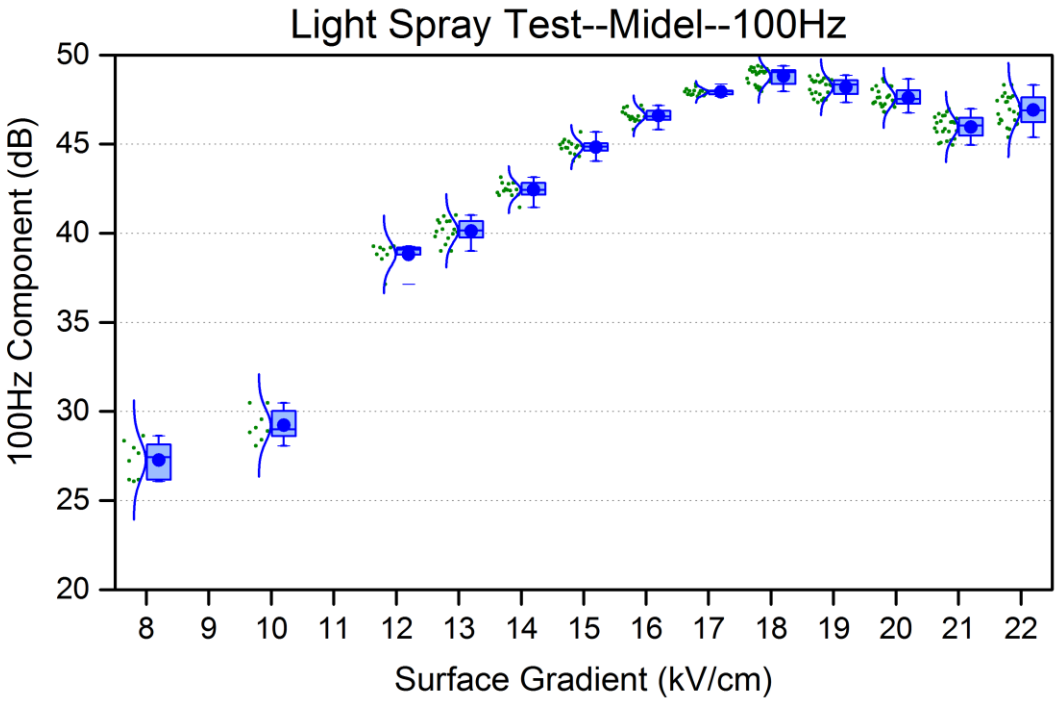

Figure 19 Light Spray Test 100 Hz Results on Midel Conductor

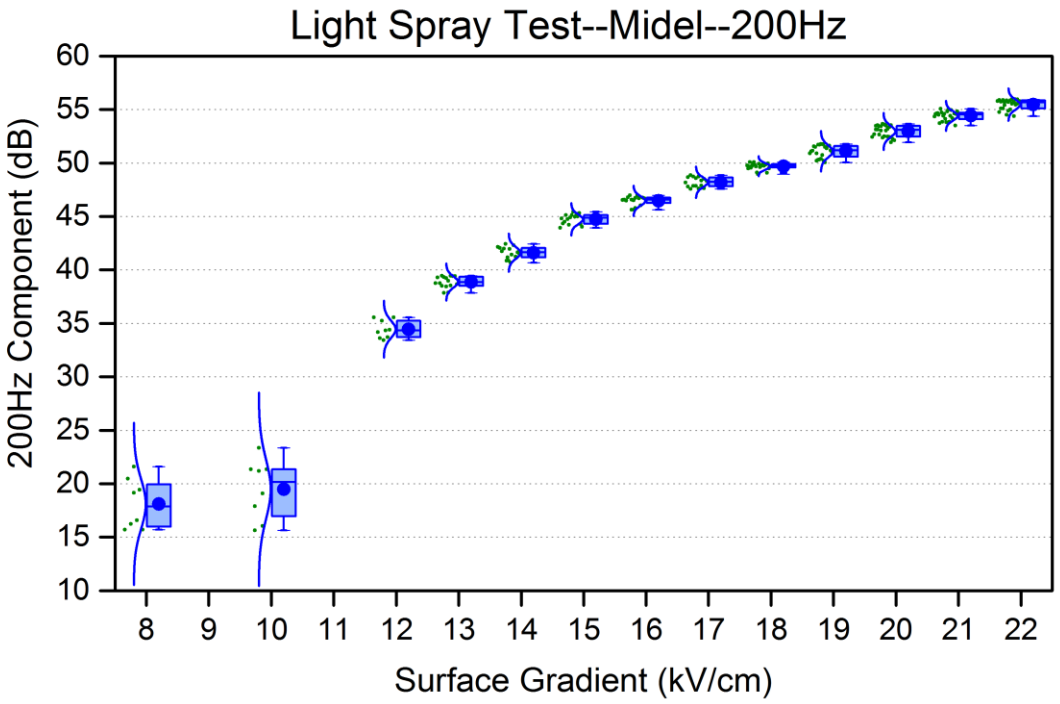

Figure 20 Light Spray Test 200 Hz Results on Midel Conductor

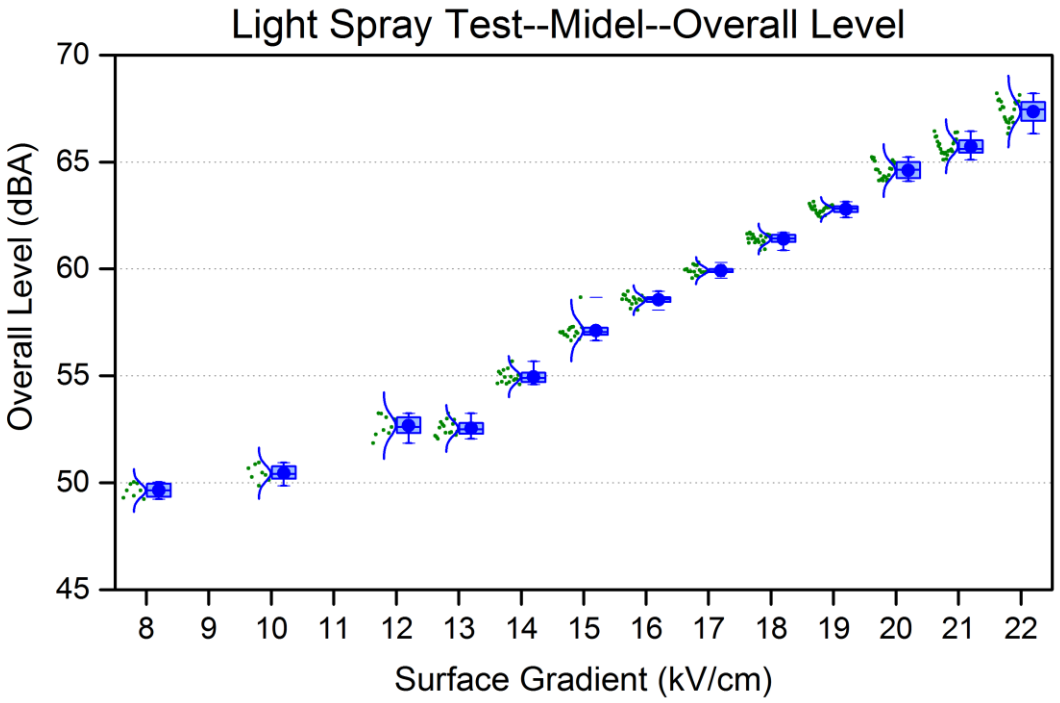

Figure 21 Light Spray Test Overall Level Results on Midel Conductor

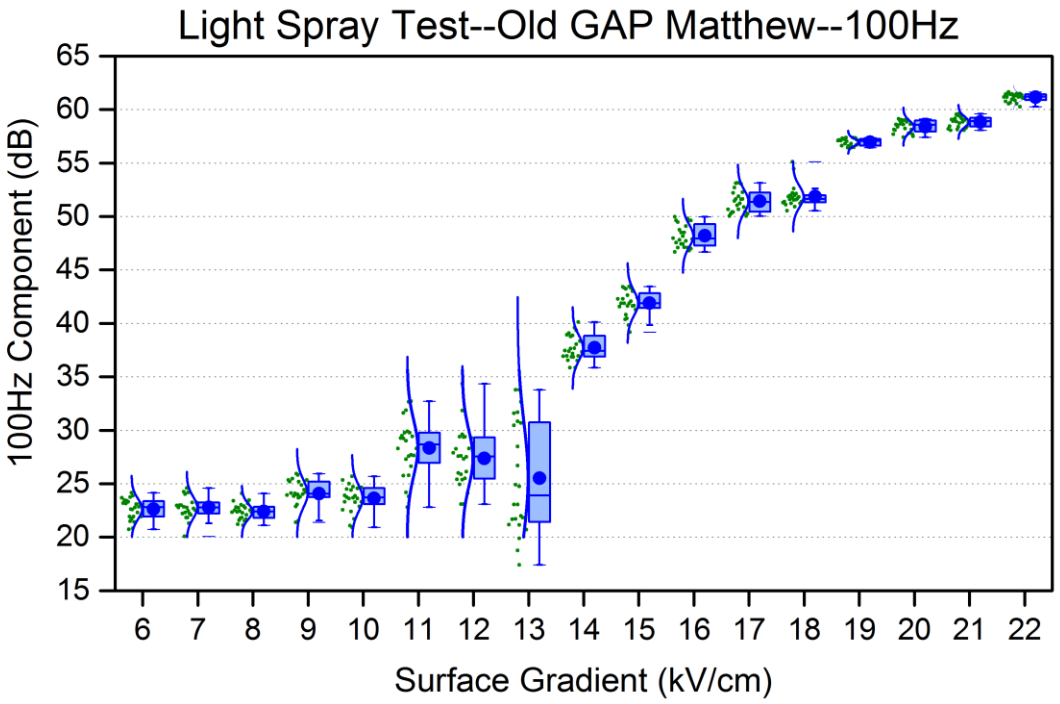

Figure 22 Light Spray Test 100 Hz Results on Aged Matthew Conductor

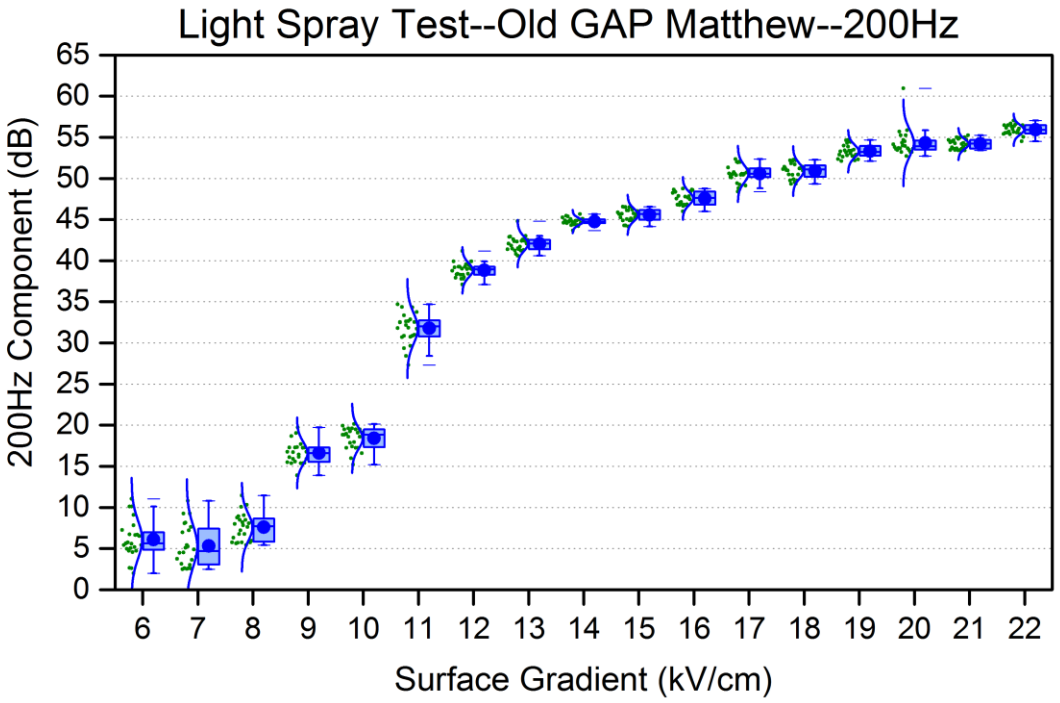

Figure 23 Light Spray Test 200 Hz Results on Aged Matthew Conductor

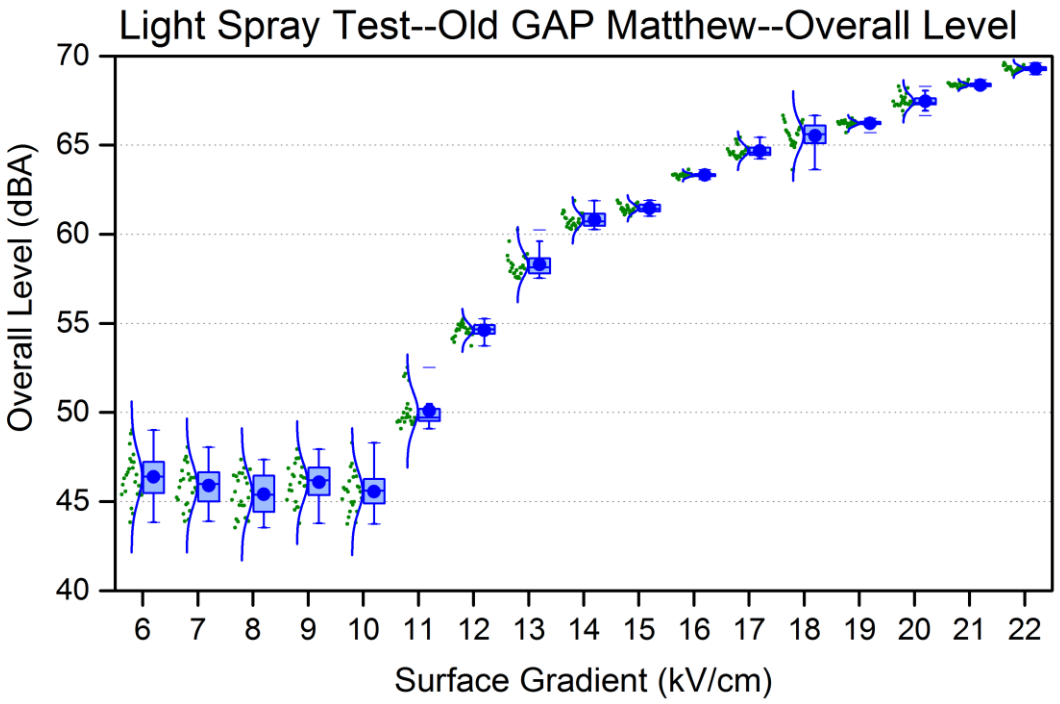

Figure 24 Light Spray Test Overall Level Results on Aged Matthew Conductor

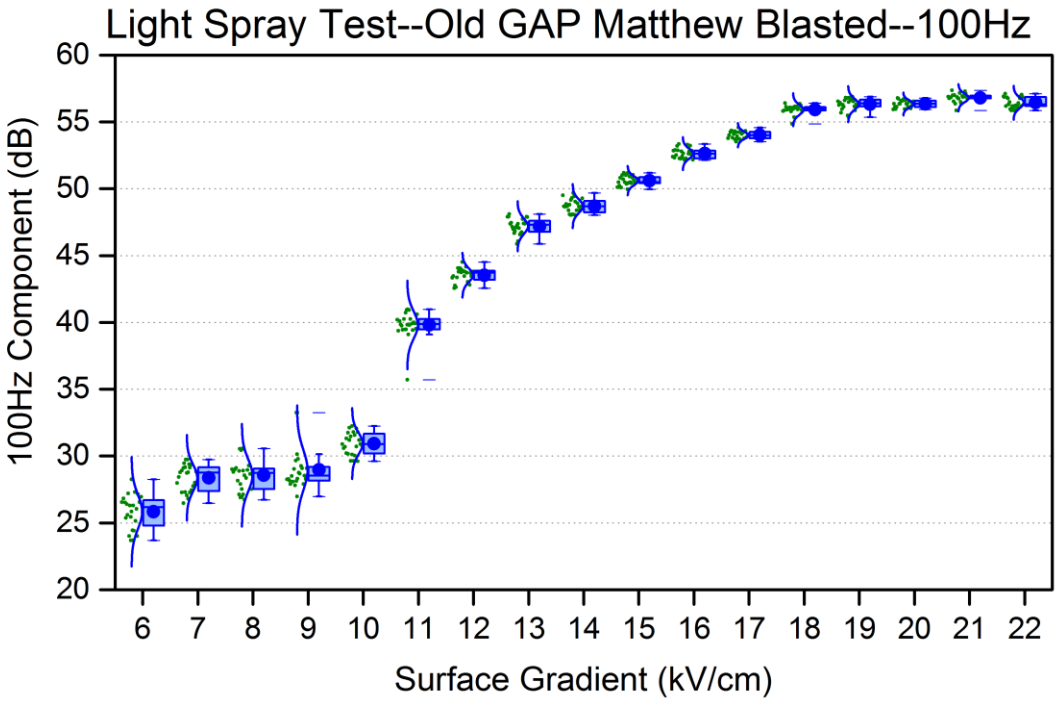

Figure 25 Light Spray Test 100 Hz Results on Aged Matthew Blasted Conductor

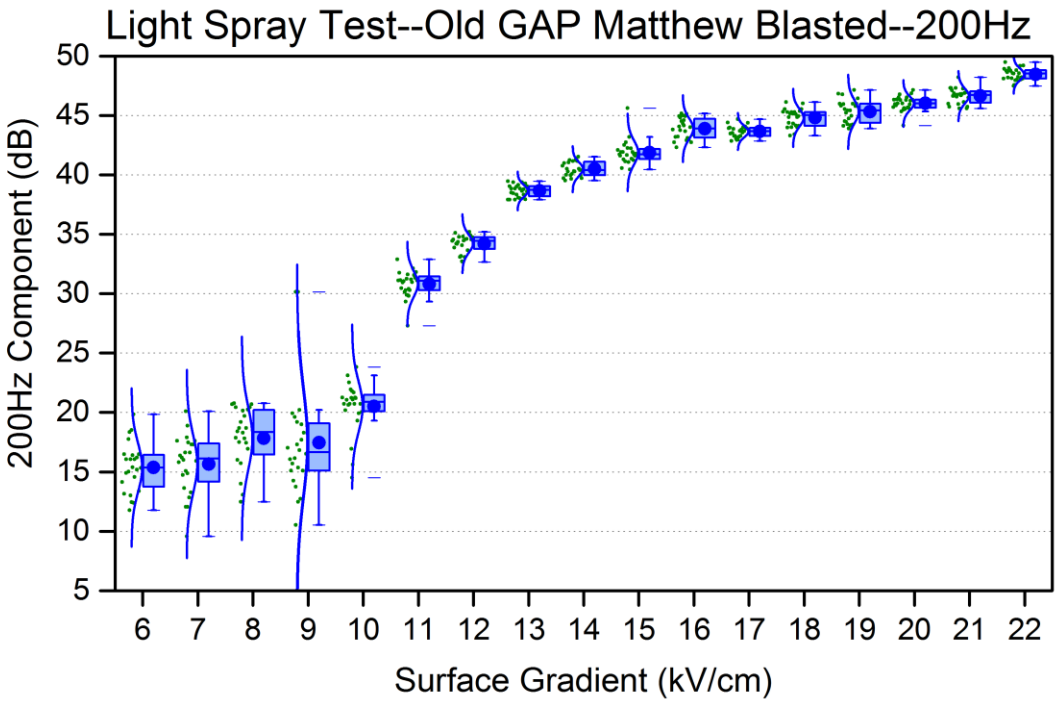

Figure 26 Light Spray Test 200 Hz Results on Aged Matthew Blasted Conductor

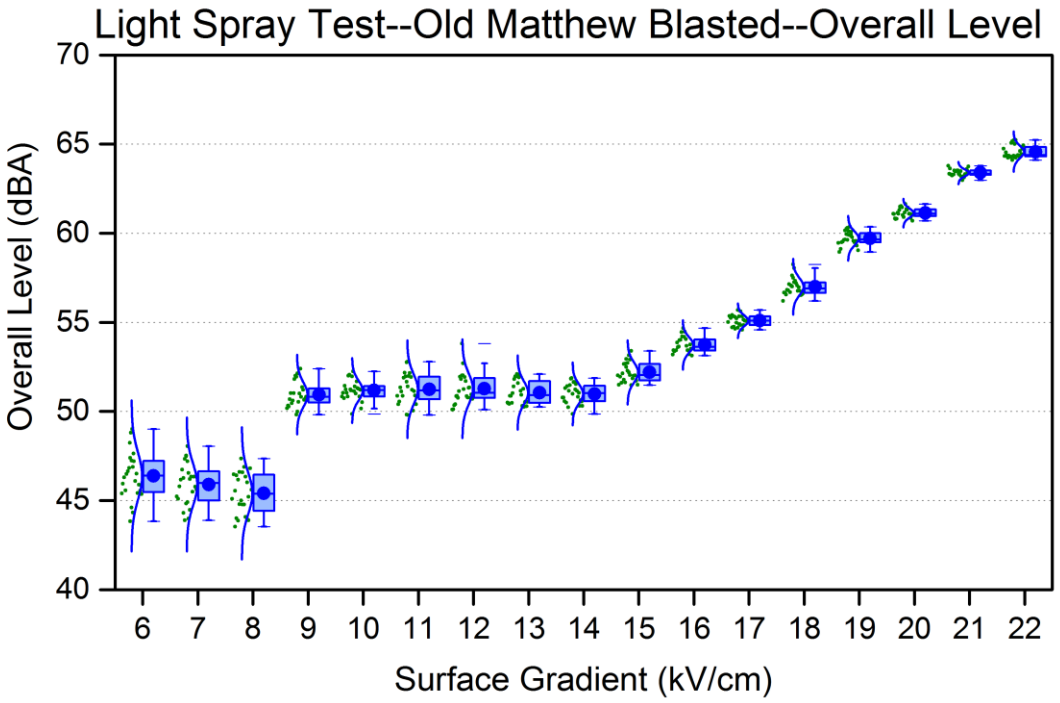

Figure 27 Light Spray Test Overall Level Results on Aged Matthew Blasted Conductor

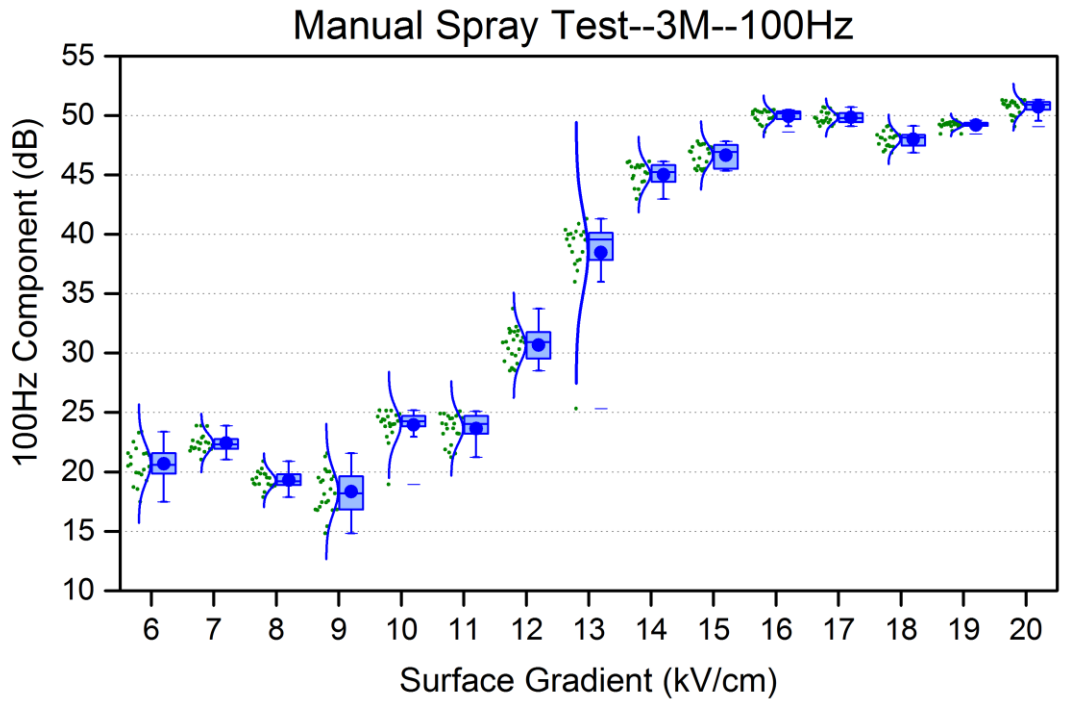

Figure 28 Manual Spray Test 100 Hz Results on 3M Conductor

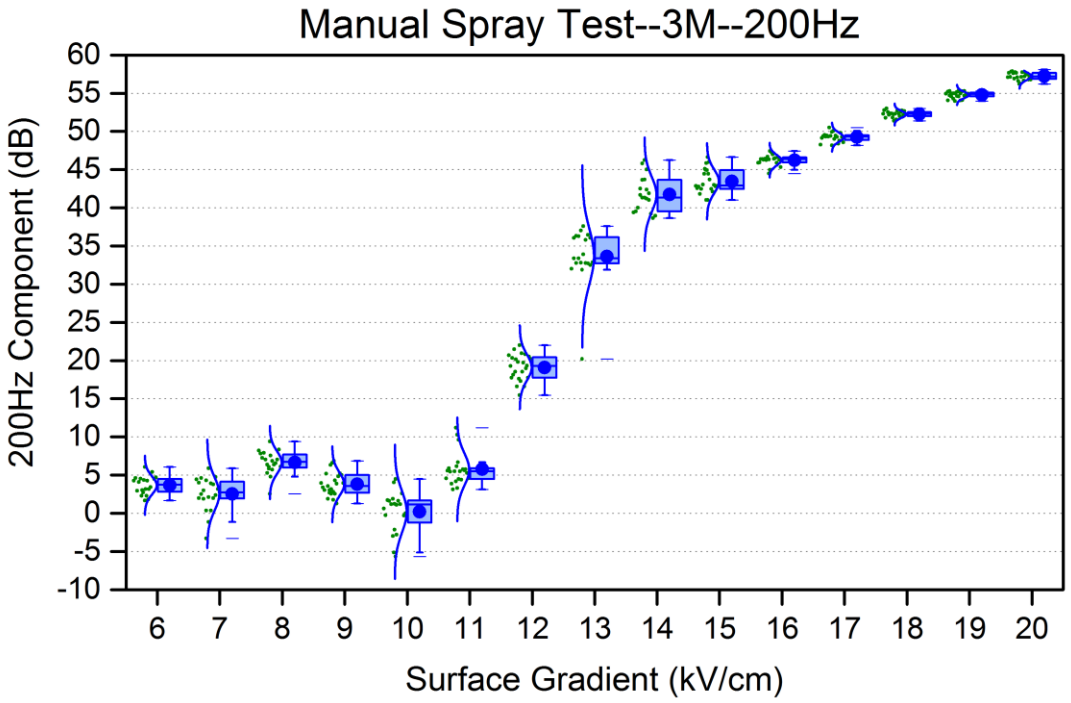

Figure 29 Manual Spray Test 200 Hz Results on 3M Conductor

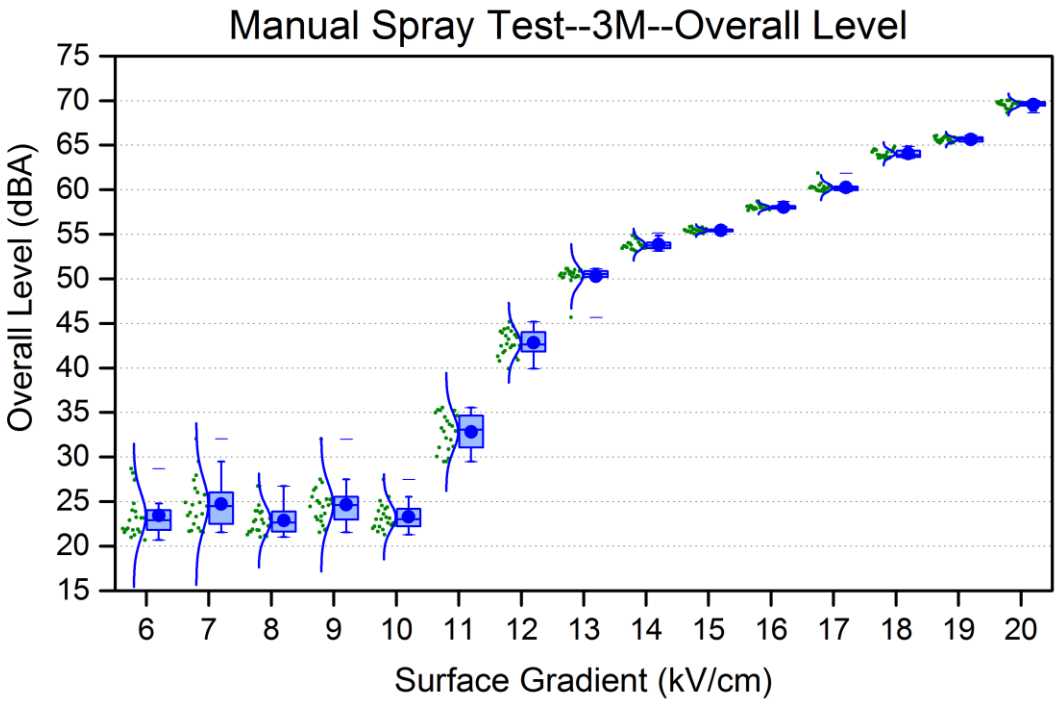

Figure 30 Manual Spray Test Overall Level Results on 3M Conductor

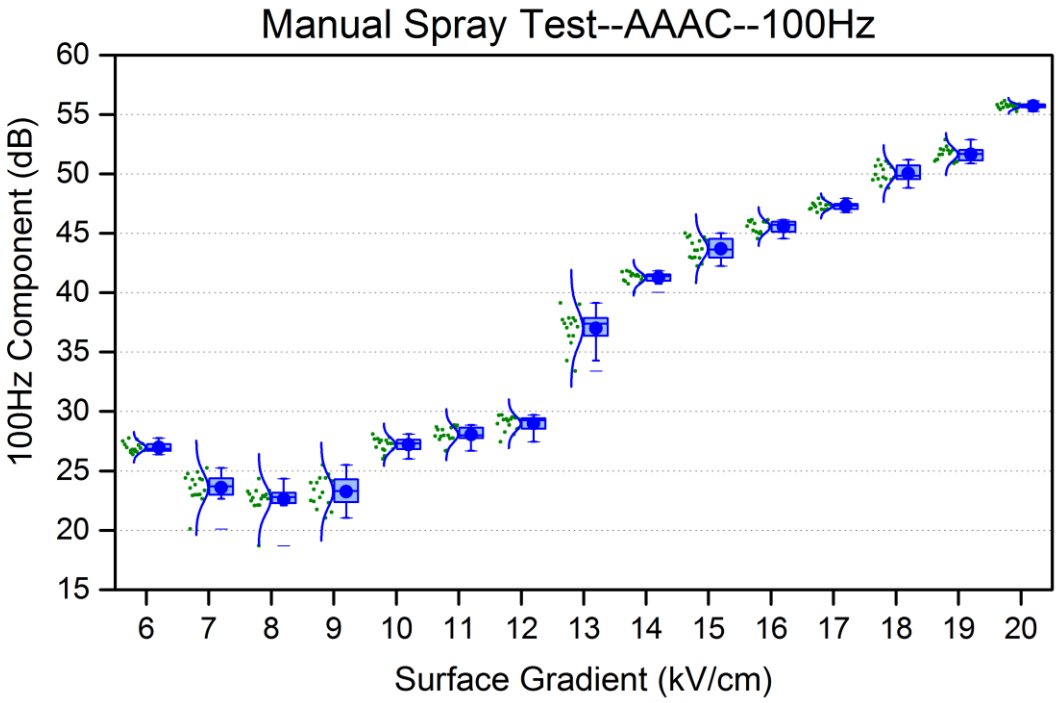

Figure 31 Manual Spray Test 100 Hz Results on AAAC Conductor

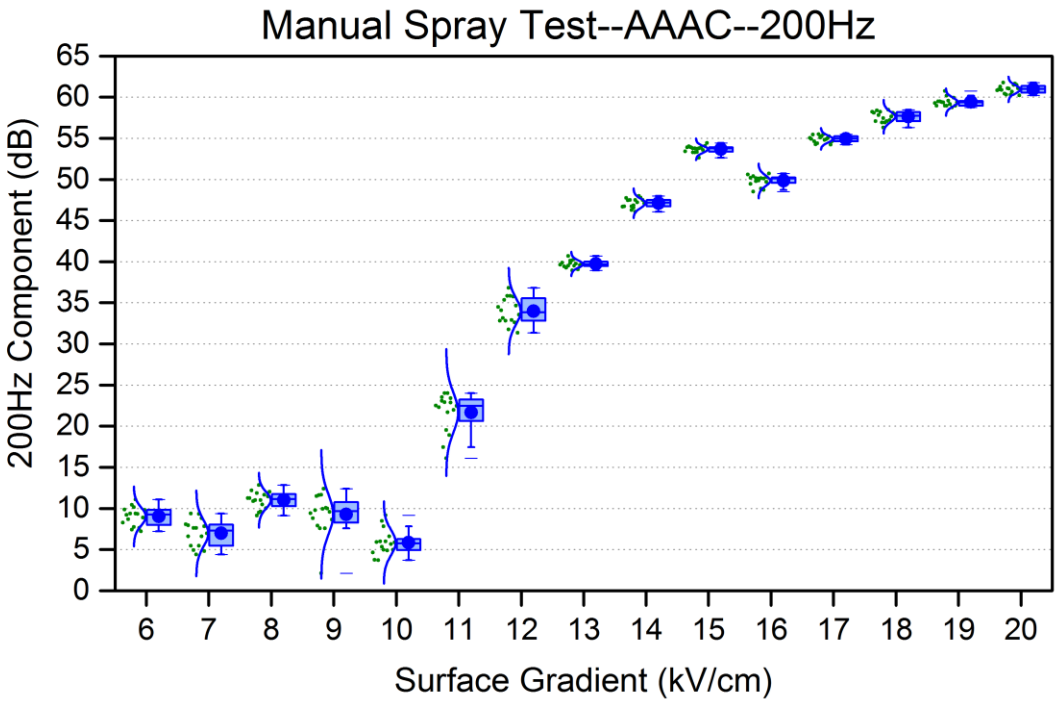

Figure 32 Manual Spray Test 200 Hz Results on AAAC Conductor

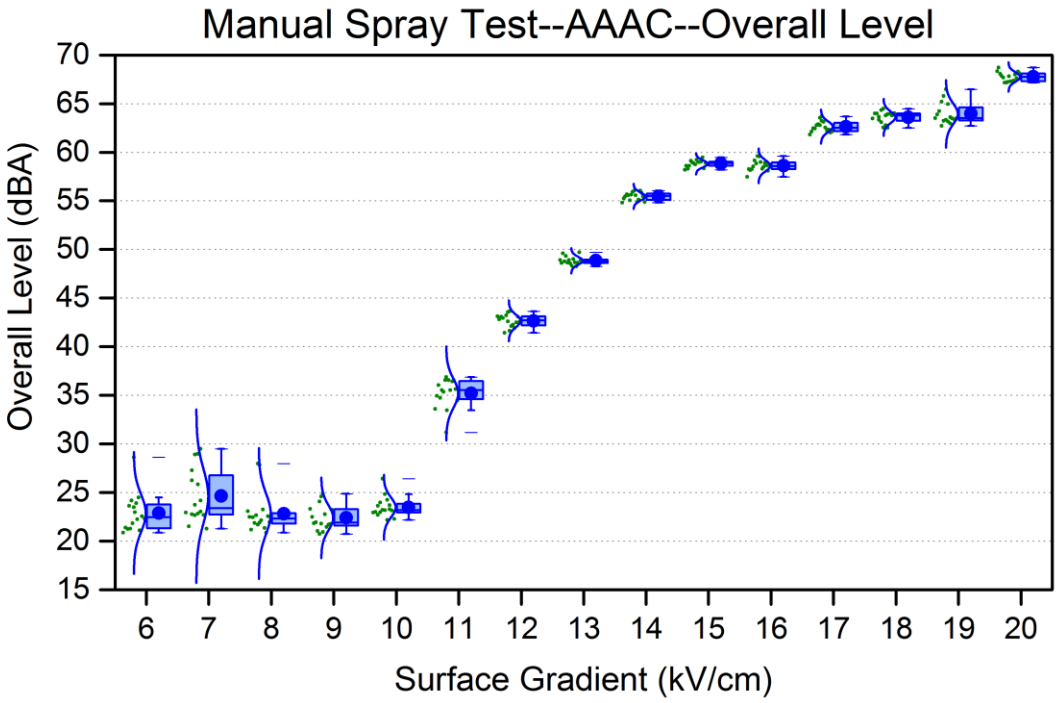

Figure 33 Manual Spray Test Overall Level Results on AAAC Conductor

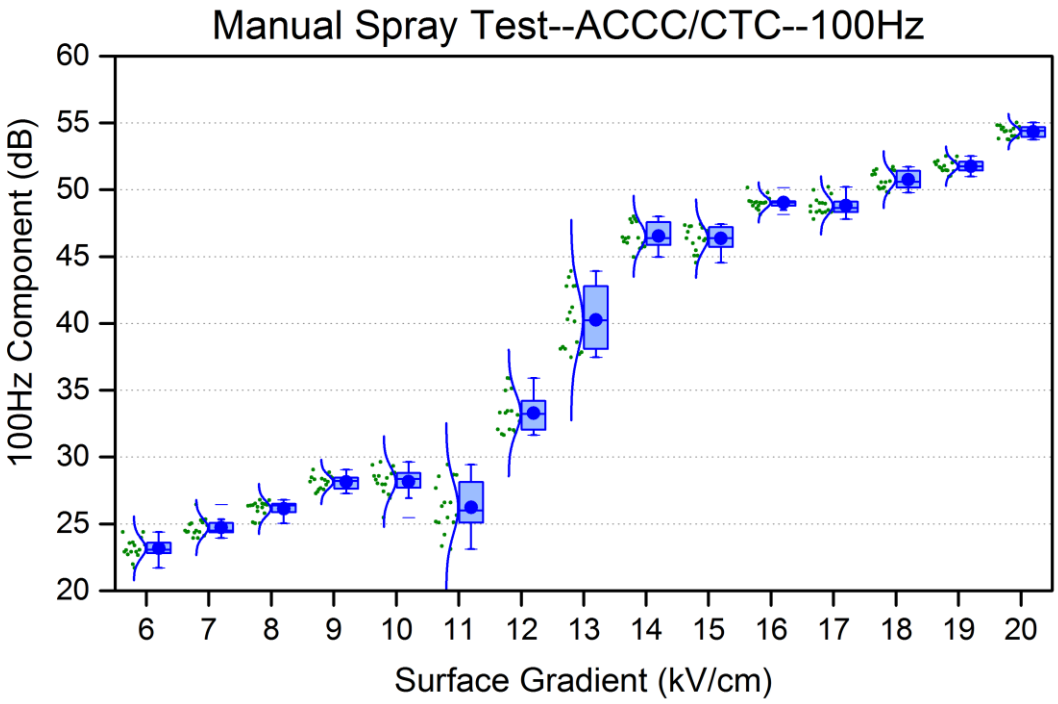

Figure 34 0Manual Spray Test 100 Hz Results on ACCC/CTC Conductor

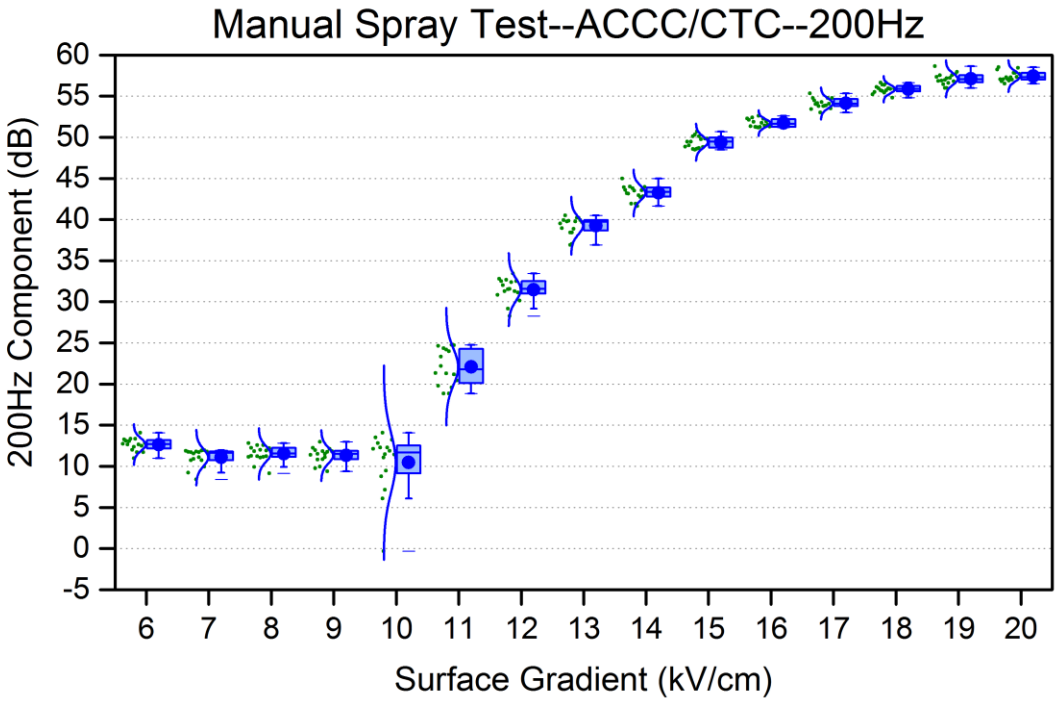

Figure 35 Manual Spray Test 200 Hz Results on ACCC/CTC Conductor

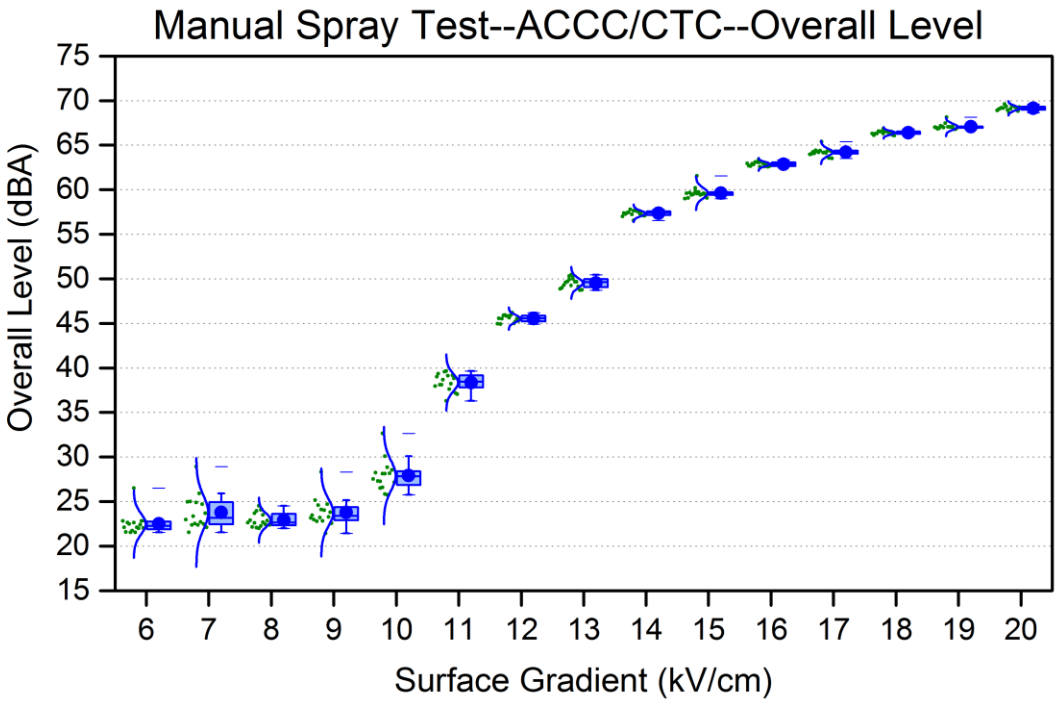

Figure 36 Manual Spray Test Overall Level Results on ACCC/CTC Conductor

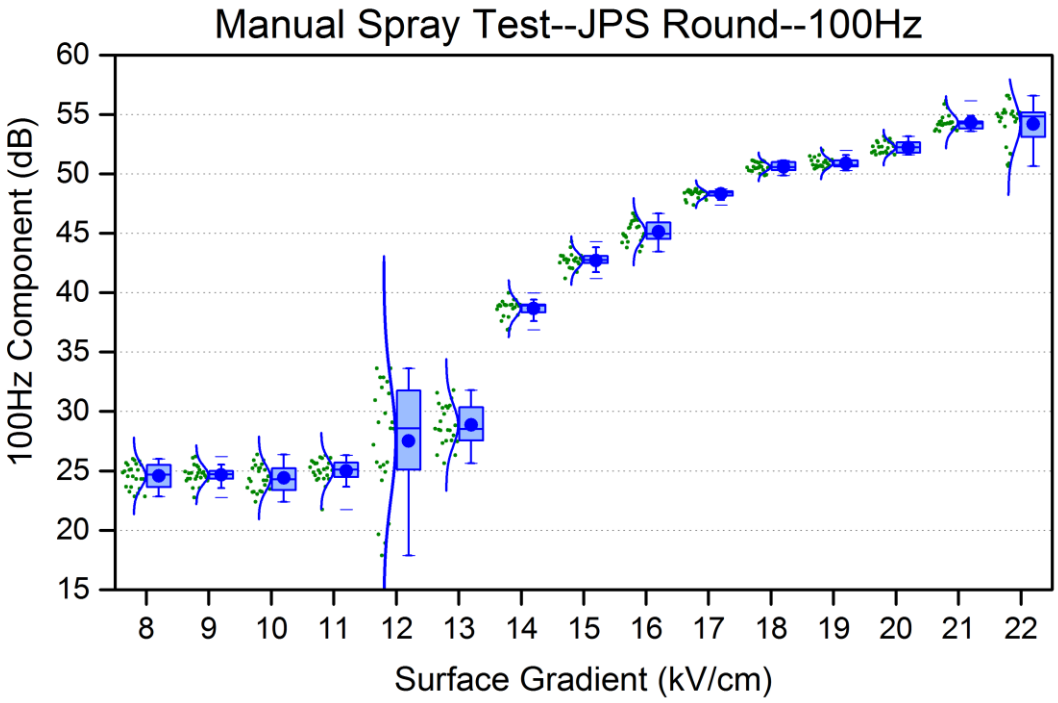

Figure 37 Manual Spray Test 100 Hz Results on JPS Round Conductor

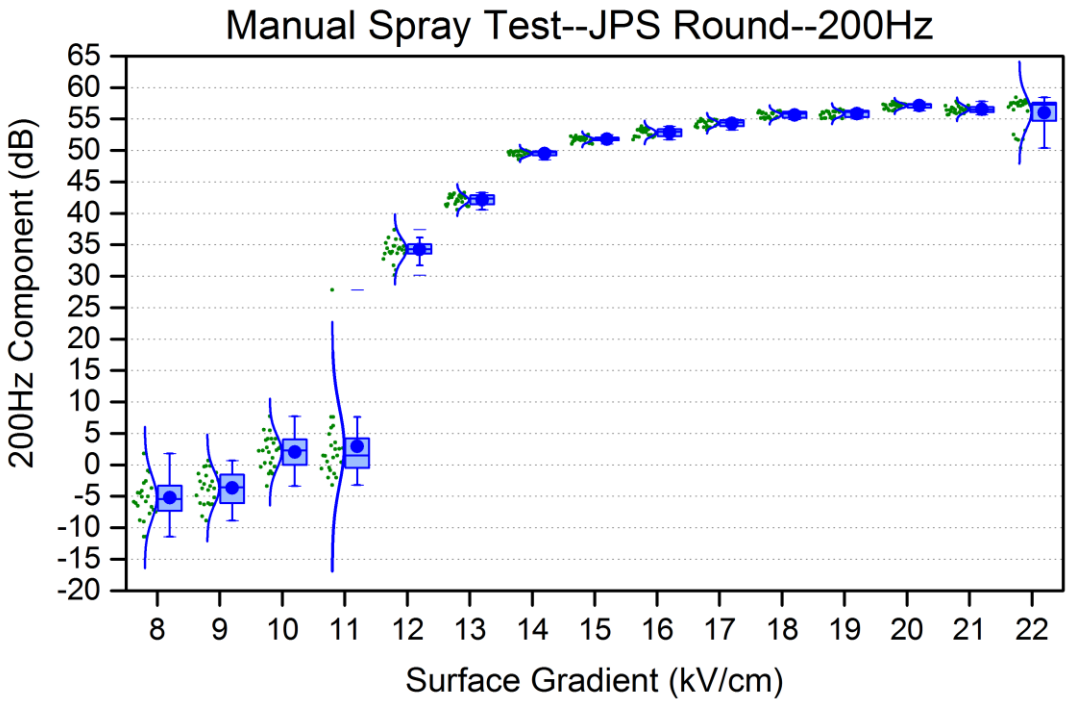

Figure 38 Manual Spray Test 200 Hz Results on JPS Round Conductor

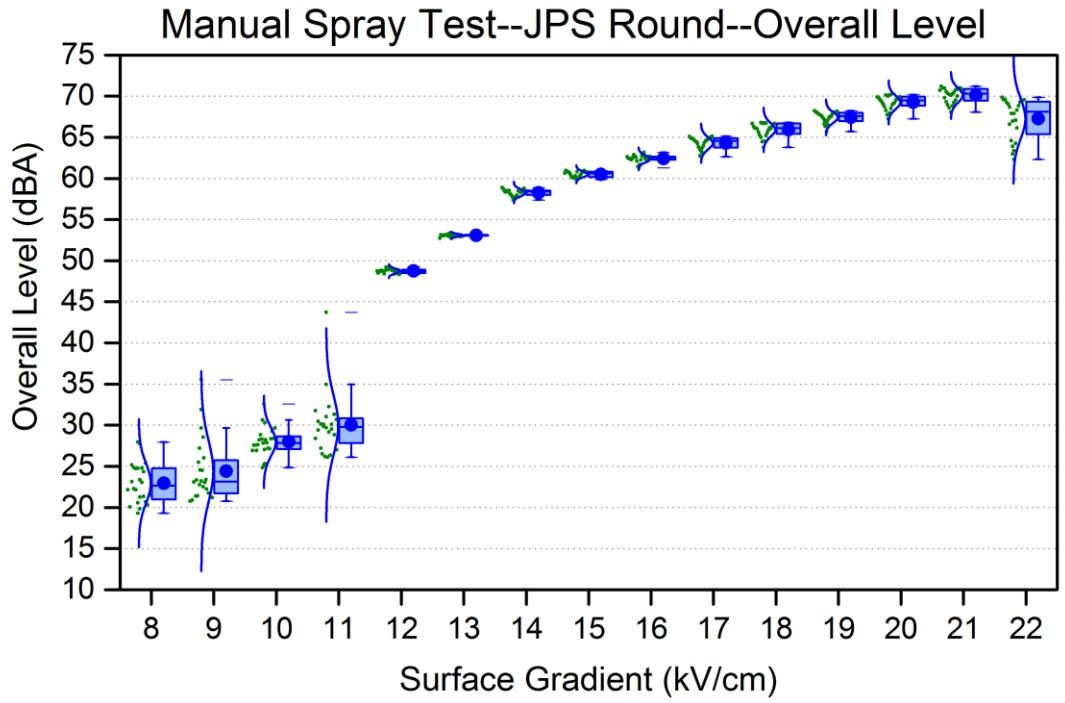

Figure 39 Manual Spray Test Overall Level Results on JPS Round Conductor

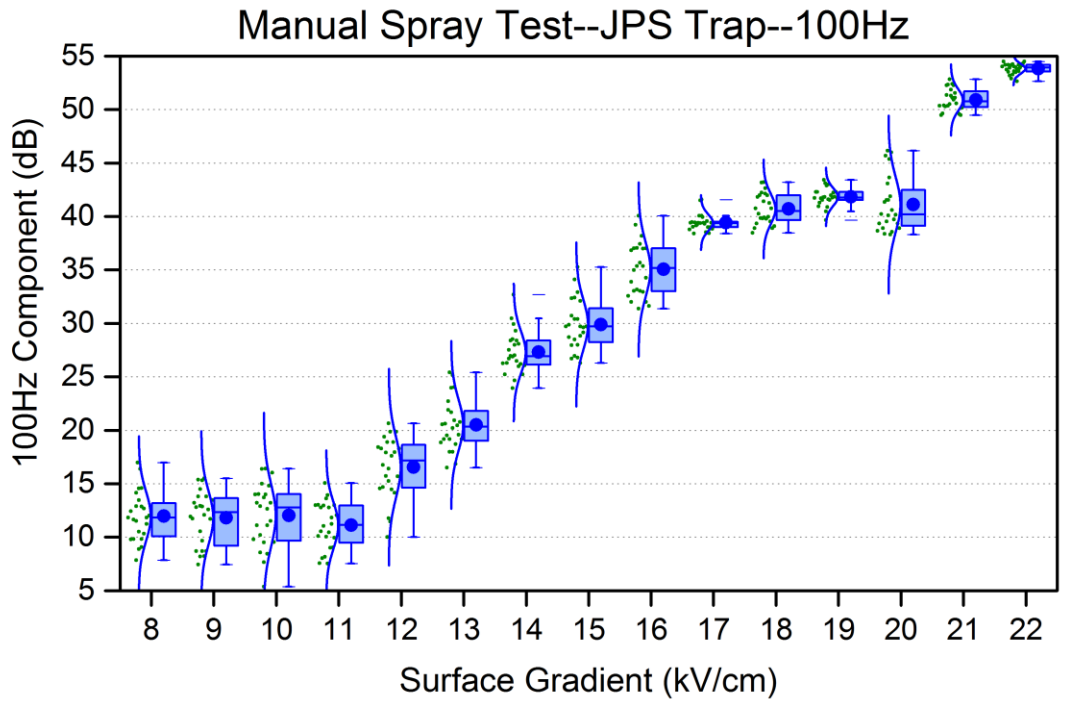

Figure 40 Manual Spray Test 100 Hz Results on JPS Trap Conductor

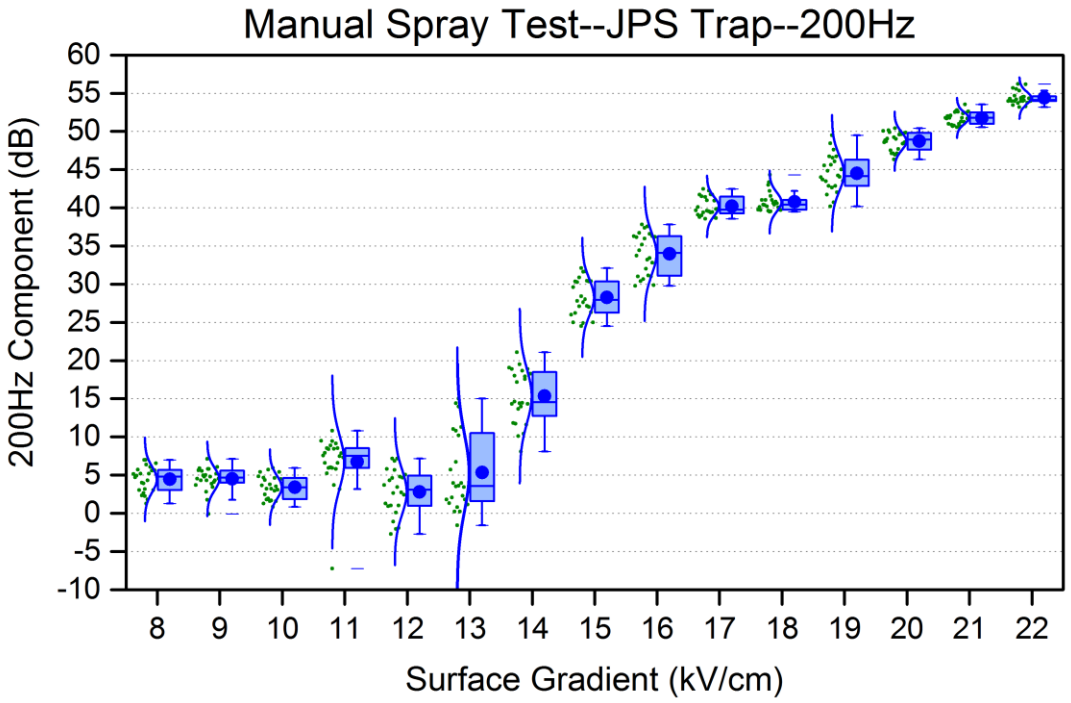

Figure 41 Manual Spray Test 200 Hz Results on JPS Trap Conductor

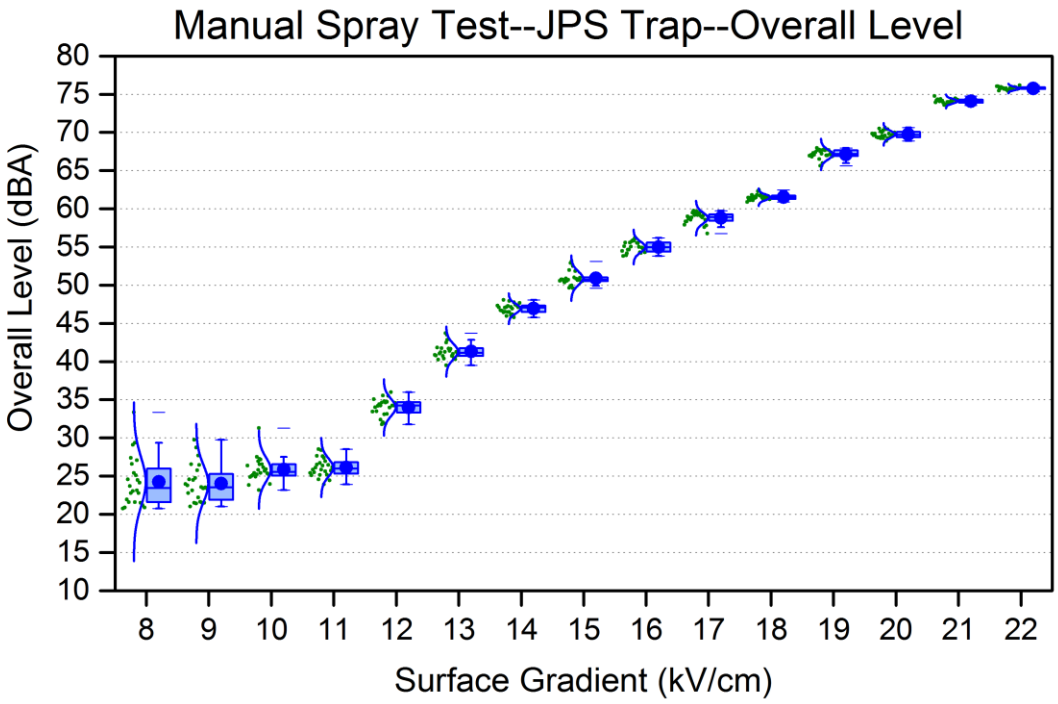

Figure 42 Manual Spray Test Overall Level Results on JPS Trap Conductor

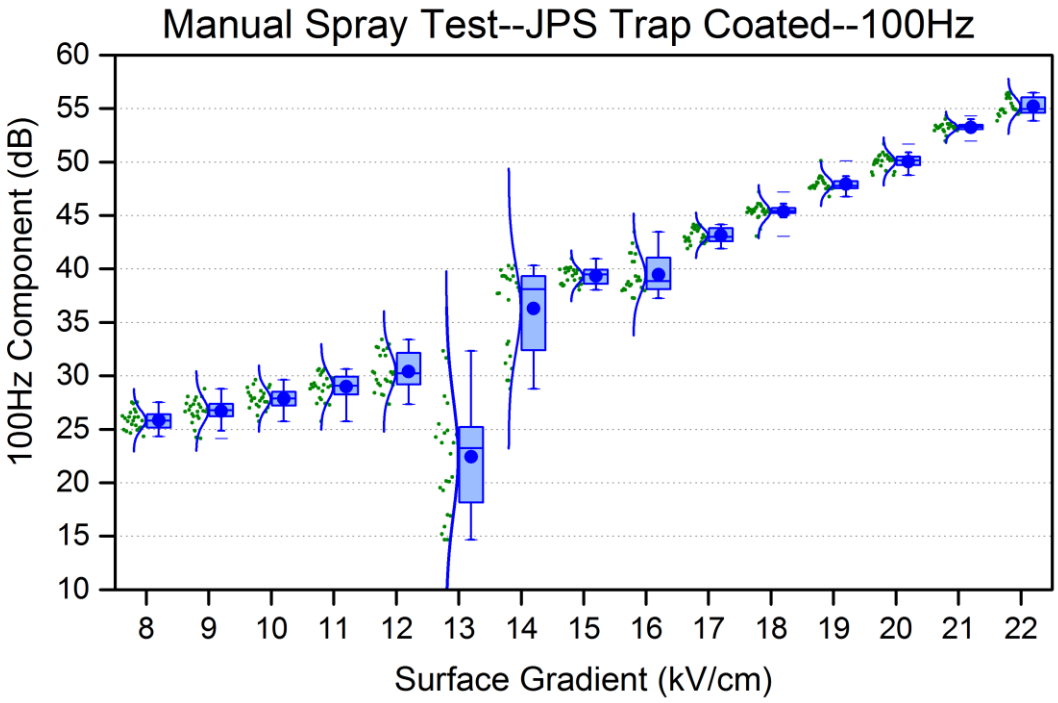

Figure 43 Manual Spray Test 100 Hz Results on JPS Trap Coated Conductor

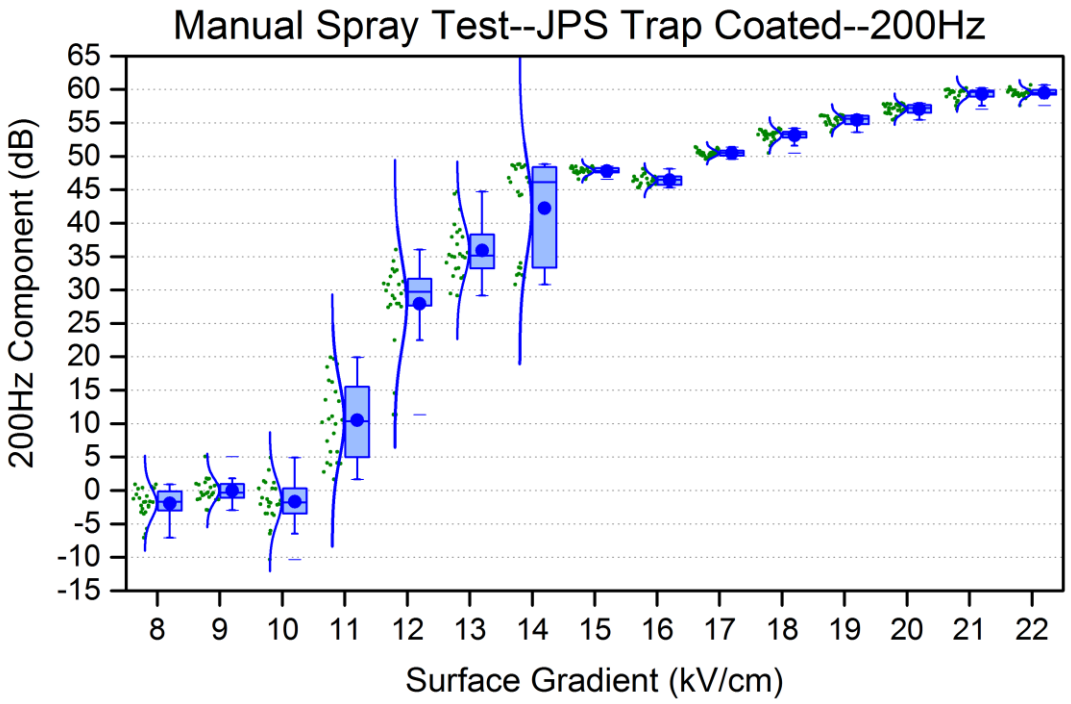

Figure 44 Manual Spray Test 200 Hz Results on JPS Trap Coated Conductor

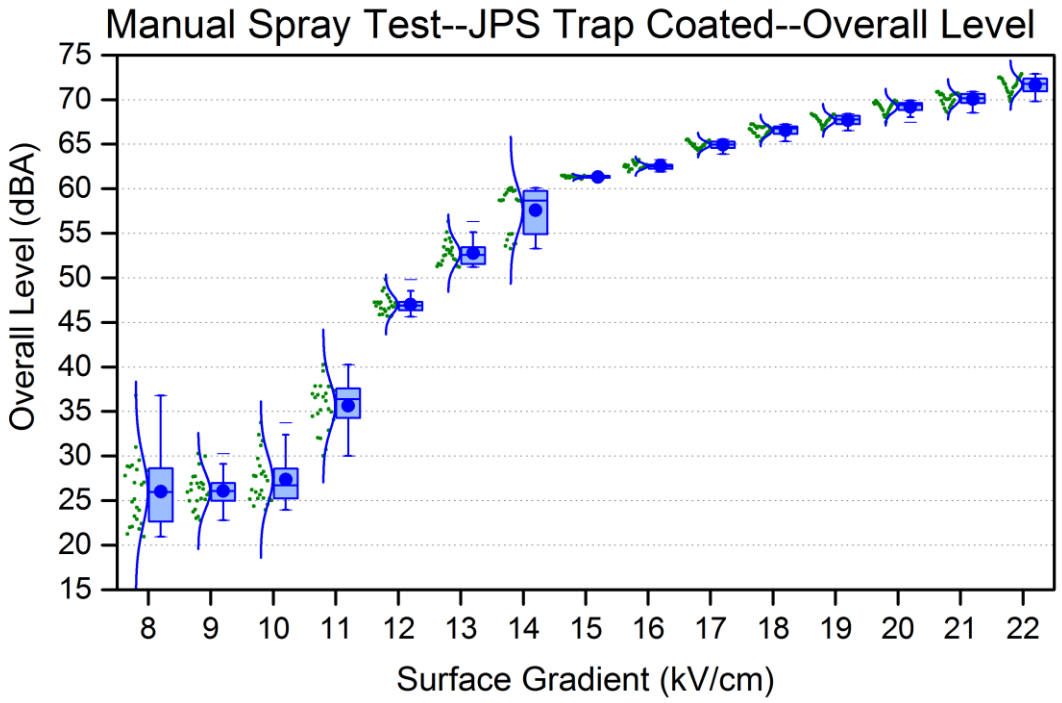

Figure 45 Manual Spray Test Overall Level Results on JPS Trap Coated Conductor

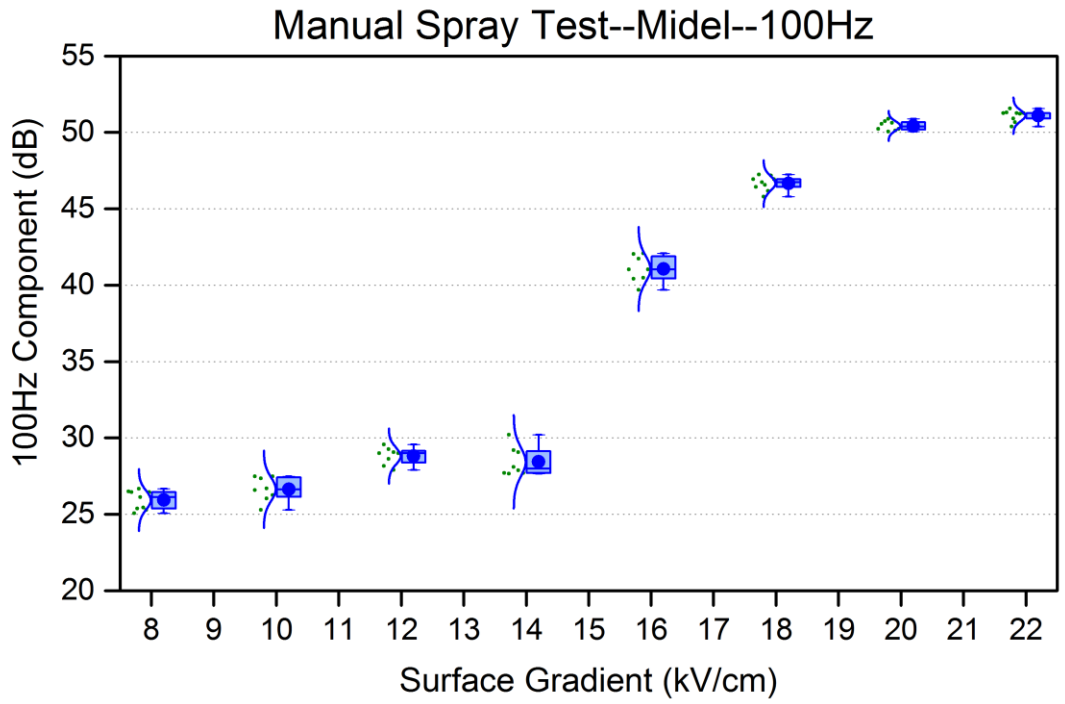

Figure 46 Manual Spray Test 100 Hz Results on Midel Conductor

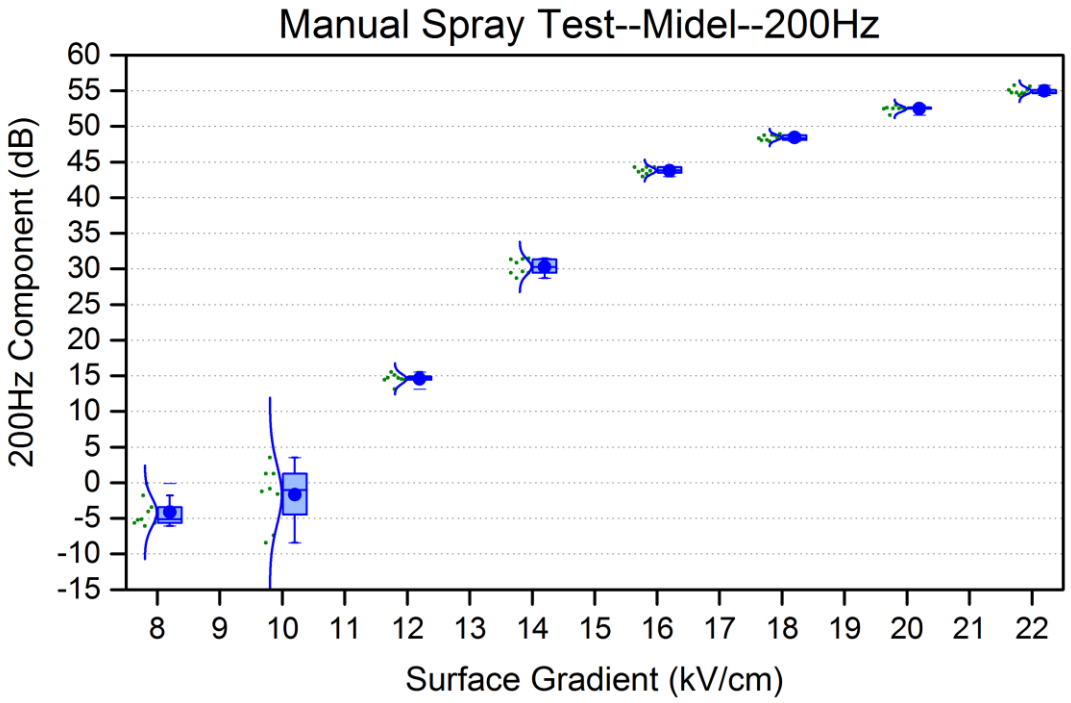

Figure 47 Manual Spray Test 200 Hz Results on Midel Conductor

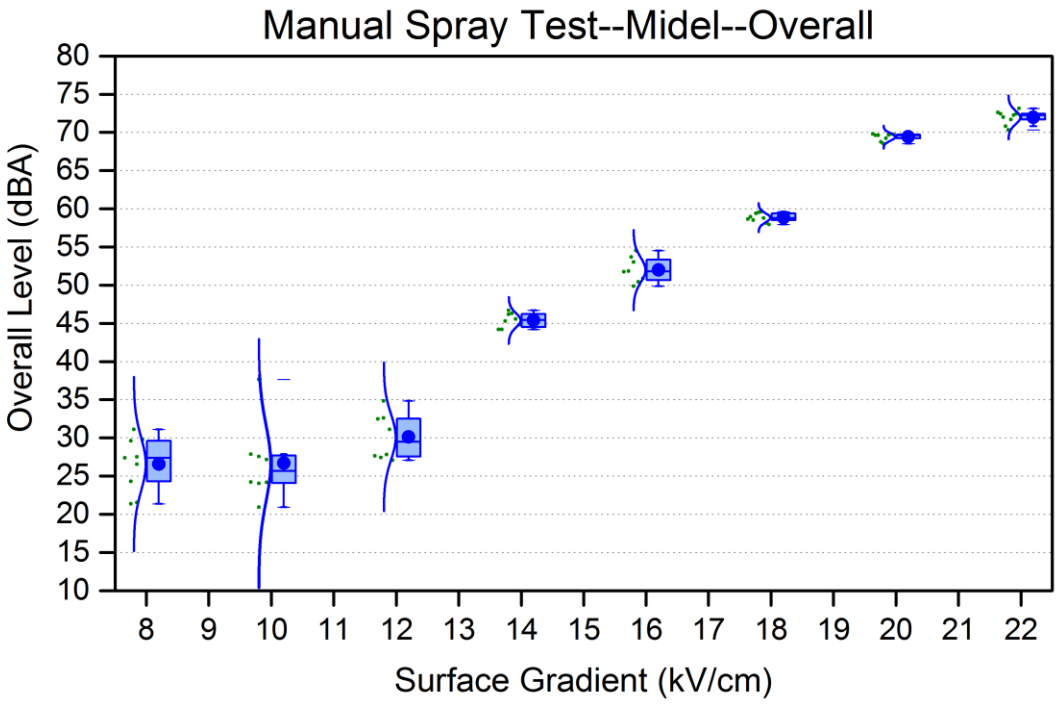

Figure 48 Manual Spray Test Overall Level Results on Midel Conductor

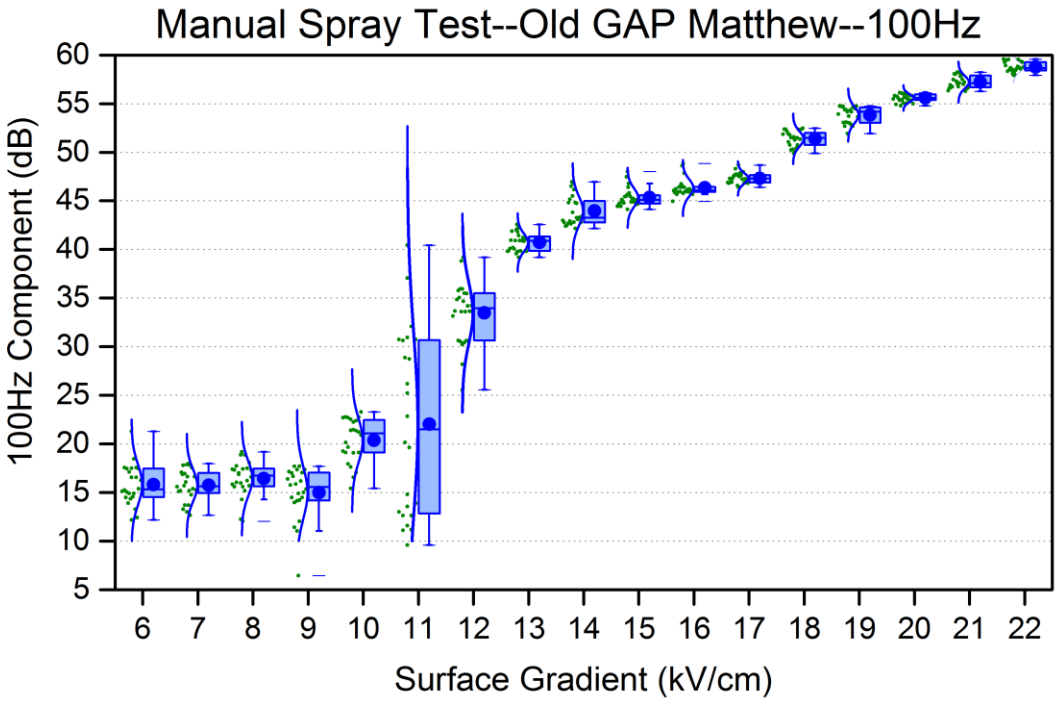

Figure 49 Manual Spray Test 100 Hz Results on Aged Matthew Conductor

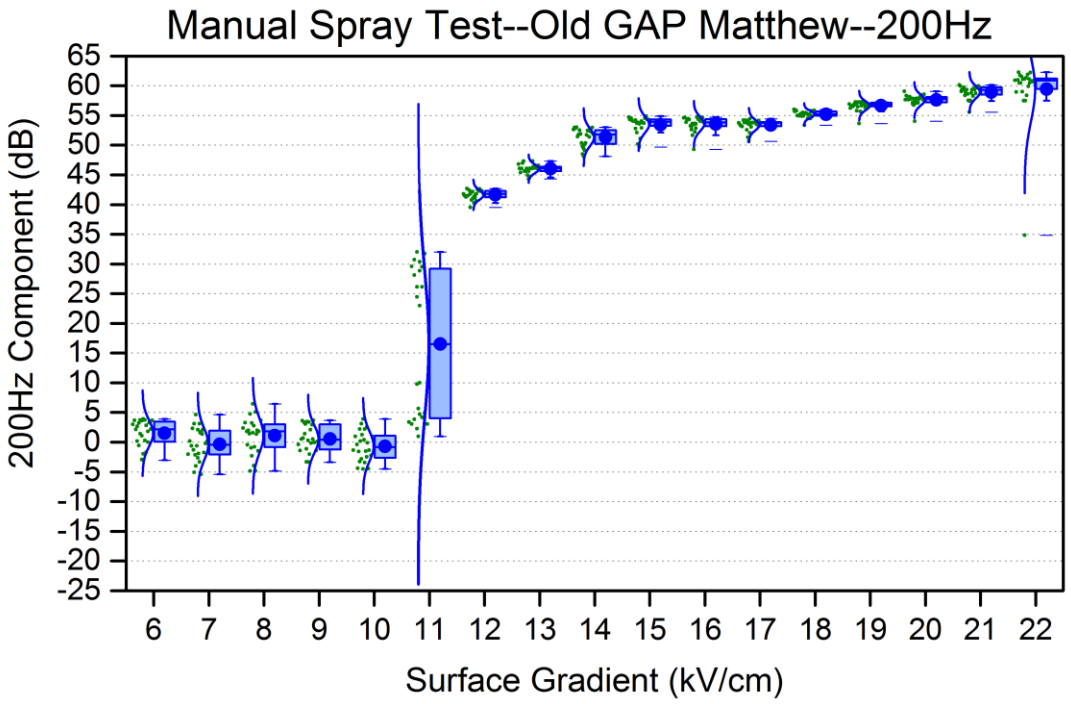

Figure 50 Manual Spray Test 200 Hz Results on Aged Matthew Conductor

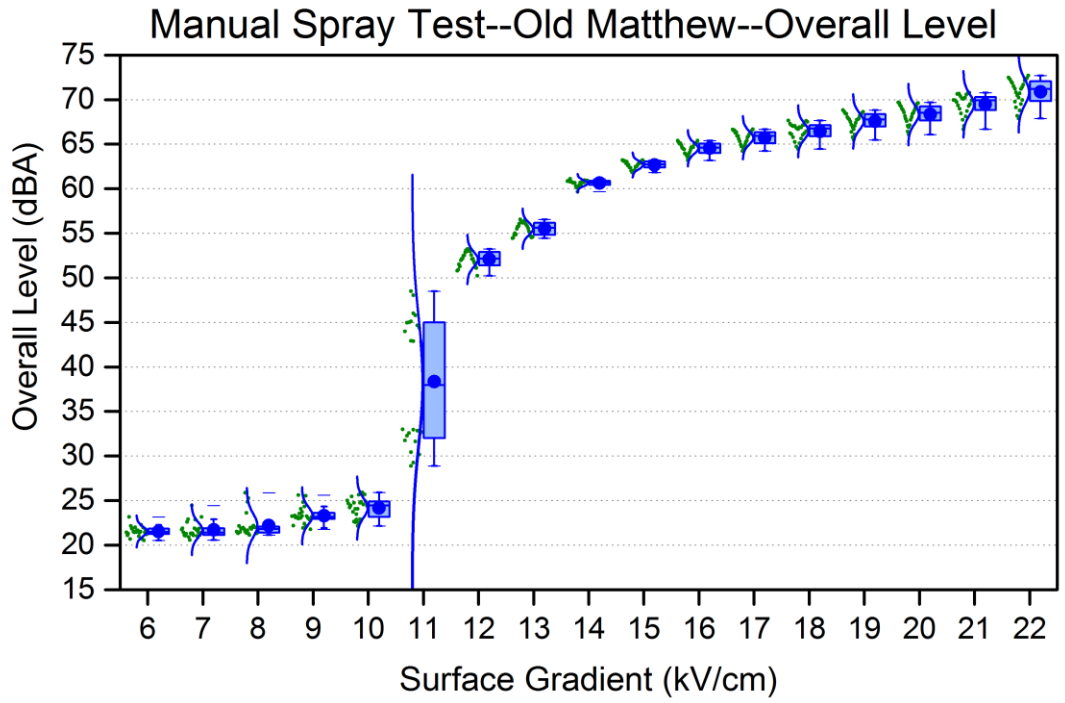

Figure 51 Manual Spray Test Overall Level Results on Aged Matthew Conductor

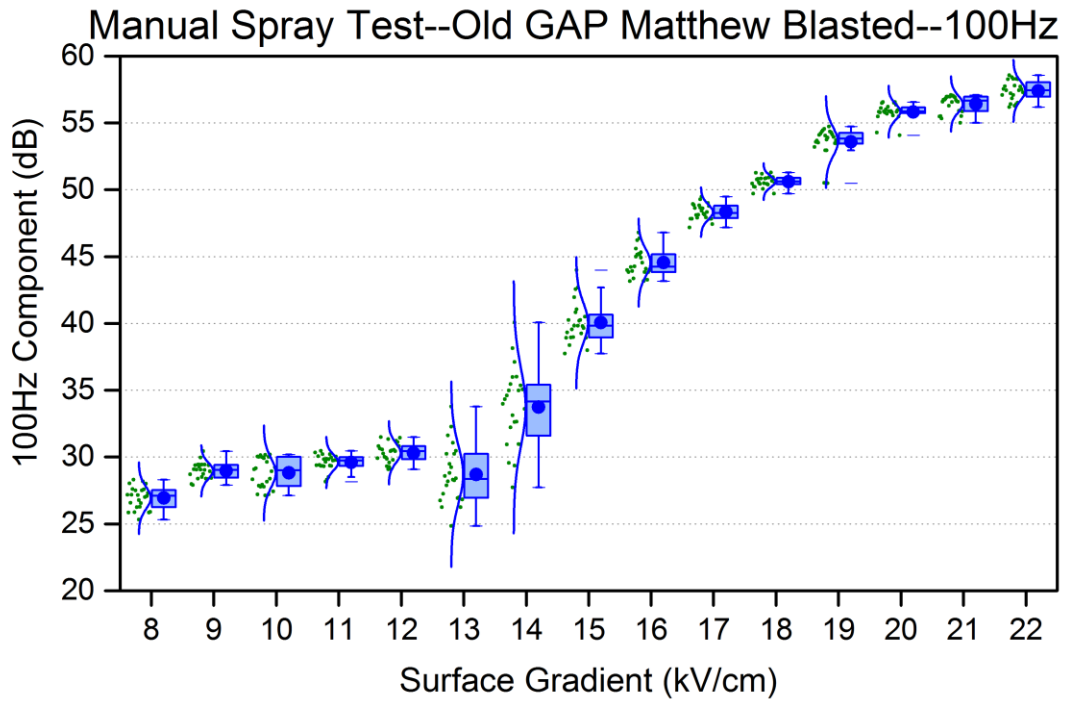

Figure 52 Manual Spray Test 100 Hz Results on Aged Matthew Blasted Conductor

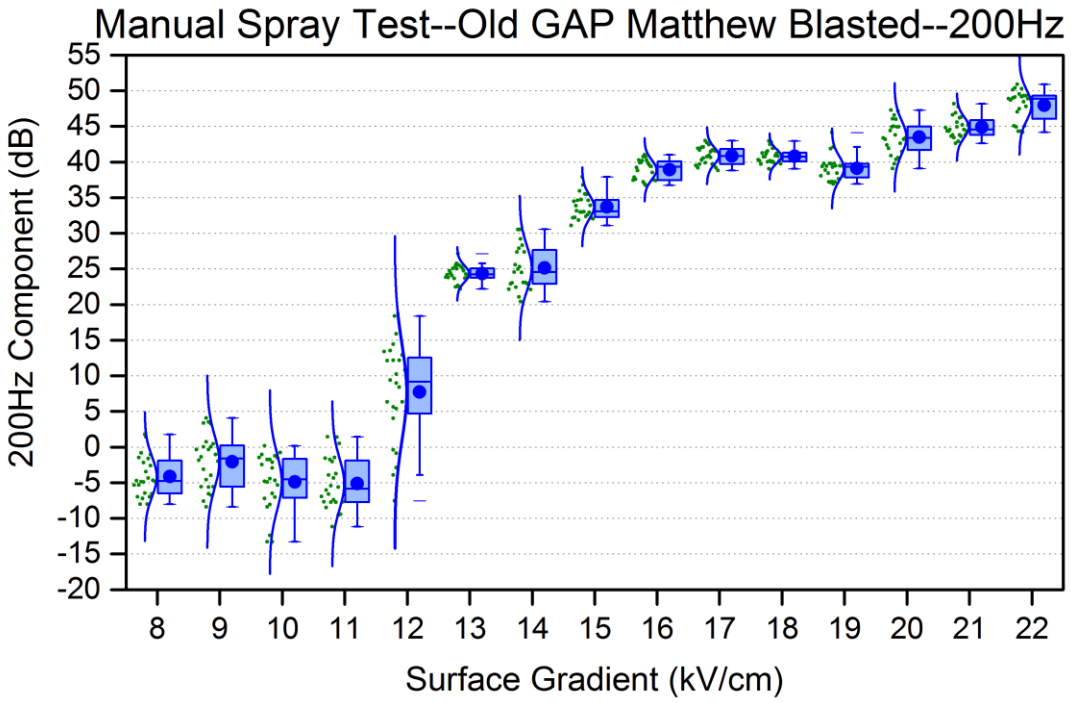

Figure 53 Manual Spray Test 200 Hz Results on Aged Matthew Blasted Conductor

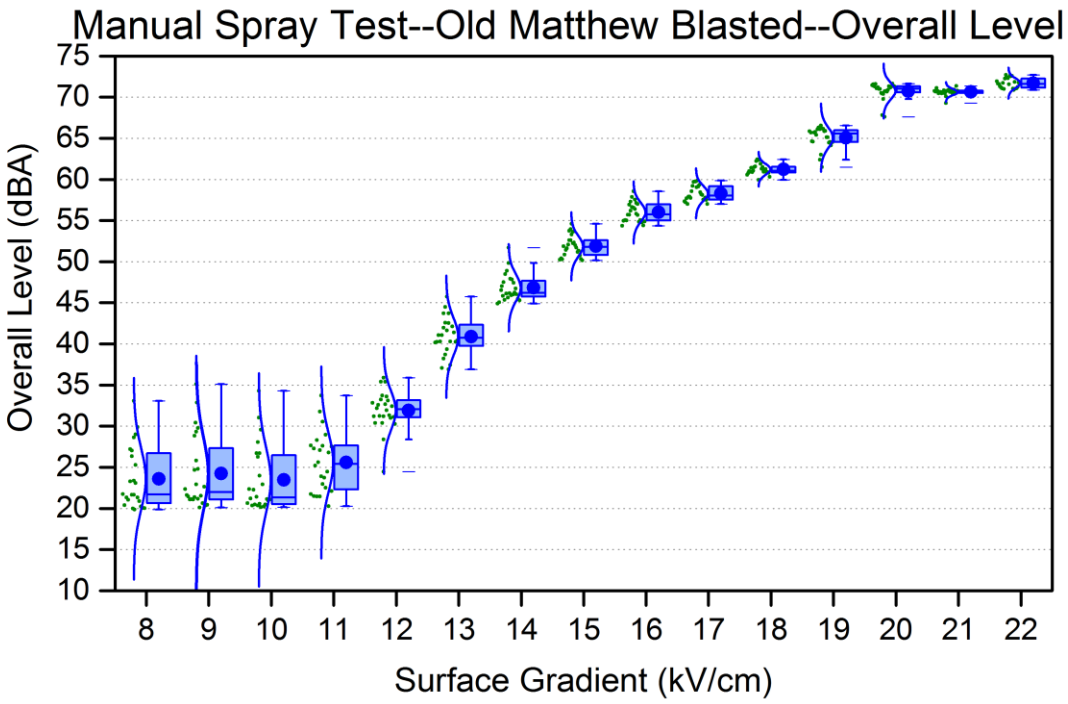

Figure 54 Manual Spray Test Overall Level Results on Aged Matthew Blasted

REFERENCE

[1] "Product Brochure-GTACSR & GZTACSR," 2005, from http://www.jpowers.co.jp/english/product/oerhead_alum.html.

[2] "shorter, lighter pylon wins design competiition," 2011, from http://eandt.theiet.org/news/2013/jul/t-pylon.cfm.

[3] E. R. Taylor, V. L. Chartier, and D. N. Rice, "Audible Noise and Visual Corona from HV and EHV Transmission Lines and Substation Conductors - Laboratory Tests," *Power Apparatus and Systems, IEEE Transactions on,* vol. PAS-88, pp. 666-679, 1969.

[4] F. Bastien, "Acoustics and gas discharges: applications to loudspeakers," *Journal of Physics D: Applied Physics,* vol. 20, p. 1547, 1987.

[5] U. Ingard, "Acoustic wave generation and amplification in a plasma," *Physical Review,* vol. 145, p. 41, 1966.

[6] R. J. Lings and E. P. R. Institute, *EPRI AC Transmission Line Reference Book: 200 KV and Above, Third Edition*: Electric Power Research Institute, 2005.

[7] P. S. Maruvada, *Corona performance of high-voltage transmission lines*: Research Studies Press, 2000.

[8] U. Straumann, "Mechanism of the tonal emission from ac high voltage overhead transmission lines," *Journal of Physics D: Applied Physics,* vol. 44, p. 075501, 2011.

[9] U. Straumann, "Simulation of the space charge near coronating conductors of ac overhead transmission lines," *Journal of Physics D: Applied Physics,* vol. 44, p. 075502, 2011.

[10] U. Straumann and J. Fan, "Audible Noise from AC-UHV Transmission Lines– Theoretical Comparison of Broadband and Tonal Components," *Electronic Resource accessed at: http://www. eeh. ee. ethz. ch/uploads/tx_ethpublications/UHV09_StraumannFan_Ap ril09__2_. pdf*, 2009.

[11] U. Straumann and M. Semmler, "About the mechanism of tonal emission from high voltage transmission lines," in *Proc. XV Int. Conference on Gas Discharges GD, Toulouse*, 2004, pp. 363-366.

[12] T. Teich and H. Weber, "Tonal emission from high voltage lines," in *Proc. of 14th Int. Conf. on Gas Discharges and Their Applications, Liverpool, UK*, 2002, pp. 259-262.

[13] M. Temoshok, "Relative Surface voltage Gradients of Grouped Conductors," *American Institute of Electrical Engineers, Transactions of the*, vol. 67, pp. 1583-1591, 1948.

[14] G. E. Adams, "Voltage Gradients on High-Voltage Transmission Lines," *Power Apparatus and Systems, Part III. Transactions of the American Institute of Electrical Engineers*, vol. 74, pp. 5-11, 1955.

[15] E. Weber, *Electromagnetic Theory: Static Fields and Their Mapping*: Dover, 1950.

[16] W. v. Mangoldt, "Electrical fundamentals of bundle conductors," presented at the Siemens-Schuckert-Werke AG, Berlin, Germany, 1942.

[17] IEEE, "A Survey of Methods for Calculating Transmission Line Conductor Surface Voltage Gradients," *Power Apparatus and Systems, IEEE Transactions on*, vol. PAS-98, pp. 1996-2014, 1979.

[18] S. Y. King, "The electric field near bundle conductors," *Proceedings of the IEE - Part C: Monographs*, vol. 106, pp. 200-206, 1959.

[19] S. Y. King, "An improved solution for the field near bundle conductors," *Electrical Engineers, Proceedings of the Institution of,* vol. 110, pp. 1044-1050, 1963.

[20] W. Thomson, *Reprint of papers on electrostatics and magnetism*: Macmillan & Company, 1872.

[21] P. Hammond, "Electric and magnetic images," *Proceedings of the IEE - Part C: Monographs,* vol. 107, pp. 306-313, 1960.

[22] M. P. Sarma and W. Janischewskyj, "Electrostatic Field of a System of Parallel Cylindrical Conductors," *Power Apparatus and Systems, IEEE Transactions on,* vol. PAS-88, pp. 1069-1079, 1969.

[23] J. A. Stratton, *Electromagnetic Theory*: Wiley, 2007.

[24] Q. S. Min Sun, Qizheng Ye, *Engineering Electromagnetism*: Tech Publication, 2001.

[25] A. S. Timascheff, "Field Patterns of Bundle Conductors and Their Electrostatic Properties," *Power Apparatus and Systems, Part III. Transactions of the American Institute of Electrical Engineers,* vol. 80, pp. 590-596, 1961.

[26] P. Thanassoulis and R. P. Comsa, "Calculation of Maximum Voltage Gradients, Part I: Bundle Conductors," *Power Apparatus and Systems, IEEE Transactions on,* vol. PAS-90, pp. 145-150, 1971.

[27] A. S. Timascheff, "Fast Calculation of Gradients for the Center Phase of a Three-Phase Bundle Conductor Line with Any Number of Subconductors," *Power Apparatus and Systems, IEEE Transactions on,* vol. PAS-90, pp. 157-164, 1971.

[28] M. S. Abou-Seada and E. Nasser, "Digital Computer Calculation of the Potential and Its Gradient of a Twin Cylindrical Conductor," *Power Apparatus and Systems, IEEE Transactions on*, vol. PAS-88, pp. 1802-1814, 1969.

[29] H. Singer, H. Steinbigler, and P. Weiss, "A Charge Simulation Method for the Calculation of High Voltage Fields," *Power Apparatus and Systems, IEEE Transactions on*, vol. PAS-93, pp. 1660-1668, 1974.

[30] A. Yializis, E. Kuffel, and P. H. Alexander, "An Optimized Charge Simulation Method for the Calculation of High Voltage Fields," *Power Apparatus and Systems, IEEE Transactions on*, vol. PAS-97, pp. 2434-2440, 1978.

[31] H. Qin, S. Lichun, J. Xingliang, X. Rong, Y. Qianfei, and S. Zhang, "Calculation of Conductors' Surface Electric Field of Â±800kV UHVDC Transmission Lines with Optimized Charge Simulation Method," in *High Voltage Engineering and Application, 2008. ICHVE 2008. International Conference on*, 2008, pp. 362-365.

[32] N. Kolcio, B. J. Ware, R. L. Zagier, V. L. Chartier, and F. M. Dietrich, "The Apple Grove 750 kV Project Statistical Analysis of Audible Noise Performance of Conductors at 775 kv," *Power Apparatus and Systems, IEEE Transactions on*, vol. PAS-93, pp. 831-840, 1974.

[33] T. H. Teich and H. J. Weber, "Origin and abatement of tonal emission from high voltage transmission lines," *Elektrotechnik und Informationstechnik*, vol. 119, pp. 22-7, / 2002.

[34] G. W. Juette and L. E. Zaffanella, "Radio noise currents and audible noise on short sections of UHV bundle conductors," *IEEE Transactions on Power Apparatus and Systems*, vol. PAS-89, pp. 902-13, 05/ 1970.

[35] G. W. Juette and L. E. Zaffanella, "Radio Noise, Audible Noise, and Corona Loss of EHV and UHV Transmission Lines Under Rain: Predetermination

Based on Cage Tests," *Power Apparatus and Systems, IEEE Transactions on,* vol. PAS-89, pp. 1168-1178, 1970.

[36] J. J. LaForest, "Transmission-line reference book. 345 kV and above. Second edition," EPRI-EL-2500; Other: ON: DE82905265 United StatesOther: ON: DE82905265Wed Feb 06 19:11:53 EST 2008NTIS, PC A99/MF A01.ERA-07-046634; EDB-82-124397English, 1981.

[37] D. E. Perry, "An Analysis of Transmission, Line Audible Noise Levels Based Upon Field and Three-Phase Test Line Measurements," *Power Apparatus and Systems, IEEE Transactions on,* vol. PAS-91, pp. 857-865, 1972.

[38] M. G. Comber and R. J. Nigbor, "Audible noise performance of the first three-phase ultra-high voltage transmission test line at EPRI's project UHV," *Power Apparatus and Systems, IEEE Transactions on,* vol. 95, pp. 1105-1114, 1976.

[39] M. G. Comber and R. J. Nigbor, "Audible Noise Performance of Regular and Asymmetric Bundles and effect of Conductor Aging on Project UHV's Three-Phase Test Line," *Power Apparatus and Systems, IEEE Transactions on,* vol. PAS-98, pp. 561-572, 1979.

[40] W. C. Pokorny, R. H. Schlomann, C. J. Miller, and H. C. Barnes, "Investigation of Corona Effects from Wet Bundle Conductions for Application to UHV Configurations," *Power Apparatus and Systems, IEEE Transactions on,* vol. PAS-91, pp. 211-222, 1972.

[41] M. G. Comber and L. E. Zaffanella, "The Use of Single-Phase Overhead Test Lines and Test Cages to Evaluate the Corona Effects of EHV and UHV Transmission Lines," *Power Apparatus and Systems, IEEE Transactions on,* vol. PAS-93, pp. 81-90, 1974.

[42] M. O. Comber and L. E. Zaffanella, "Audible-Noise Reduction by Bundle Geometry Optimization," *Power Apparatus and Systems, IEEE Transactions on,* vol. PAS-92, pp. 1782-1791, 1973.

[43] N. G. Trinh, P. S. Maruvada, and B. Poirier, "A Comparative Study of the Corona Performance of Conductor Bundles for 1200 KV Transmission Lines," *Power Apparatus and Systems, IEEE Transactions on,* vol. PAS-93, pp. 940-949, 1974.

[44] M. Sforzini, R. Cortina, G. Sacerdote, and R. Piazza, "Acoustic noise caused by a.c. corona on conductors: Results of an experimental investigation in the anechoic chamber," *Power Apparatus and Systems, IEEE Transactions on,* vol. 94, pp. 591-601, 1975.

[45] A. C. Baker, M. G. Comber, and K. E. Ottosen, "Investigation of the corona performance of conductor bundles for 800-kV transmission," *Power Apparatus and Systems, IEEE Transactions on,* vol. 94, pp. 1117-1130, 1975.

[46] M. G. Comber and R. Cortina, "Audible noise generation of individual subconductors of transmission line conductor bundles," *Power Apparatus and Systems, IEEE Transactions on,* vol. 95, pp. 525-535, 1976.

[47] X. B. Bian, D. Y. Yu, L. C. Chen, J. M. K. MacAlpine, W. Liming, G. Zhicheng, *et al.*, "Influence of aged conductor surface conditions on AC corona discharge with a corona cage," *Dielectrics and Electrical Insulation, IEEE Transactions on,* vol. 18, pp. 809-818, 2011.

[48] X. B. Bian, D. Y. Yu, M. Xiaobo, M. Macalpine, W. Liming, G. Zhicheng, *et al.*, "Corona-generated space charge effects on electric field distribution for an indoor corona cage and a monopolar test line," *Dielectrics and Electrical Insulation, IEEE Transactions on,* vol. 18, pp. 1767-1778, 2011.

[49] U. Straumann and J. Fan, "Tonal component of the audible noise from UHV-AC Transmission Lines," in *16th International Symposium on High Voltage Engineering ISH, Cape Town, South Africa*, 2009, pp. 516-520.

[50] U. Straumann and H. Weber, "Potential reduction of audible noise from new and aged overhead transmission line conductors by increasing their hydrophilicity," in *Cigré Session*, 2010.

[51] A. Britten, E. Clarke, and H. Konkel, "Radio Interference, Corona Losses, Audible Noise and Power Frequency Electric Fields as Factors in the Design of ESCOM's 765 kV Lines," in *Open Conference on EHV Transmission Systems. Eskom Megawatt Park Auditorium*, 1987.

[52] M. Fukushima, K. Tanabe, and Y. Nakano, "Prediction Method and Subjective Evaluation of Audible Noise Based on Results at the Shiobara HVDC Test Line," *Power Delivery, IEEE Transactions on*, vol. 2, pp. 1170-1176, 1987.

[53] M. Fukushima, K. Tanabe, and Y. Nakano, "Prediction Method and Subjective Evaluation of Audible Noise Based on Results at the Shiobara HVDC Test Line," *Power Engineering Review, IEEE*, vol. PER-7, pp. 56-57, 1987.

[54] K. Tanabe, "Second harmonics of audible noise from AC transmission lines-Random walk model on space distribution," *Power Delivery, IEEE Transactions on*, vol. 6, pp. 216-222, 1991.

[55] K. Tanabe, "Hum noise performance of 6, 8, 10 conductor bundles for 1000 kV transmission lines at the Akagi test site: a comparative study with cage data," *Power Delivery, IEEE Transactions on*, vol. 6, pp. 1799-1804, 1991.

[56] K. Tanabe, T. Takebe, and M. Isozaki, "Reduction of audible noise using asymmetrical bundles for 1000 kV transmission lines: full-scale test results of Akagi test line," *Power Delivery, IEEE Transactions on*, vol. 11, pp. 1482-1491, 1996.

[57] V. L. Chartier, S. H. Sarkinen, R. D. Stearns, and A. L. Burns, "Investigation of Corona and Field Effects of AC/DC Hybrid Transmission Lines," *Power Apparatus and Systems, IEEE Transactions on*, vol. PAS-100, pp. 72-80, 1981.

[58] R. H. Warring and G. Atherley, *Handbook of noise and vibration control*: Trade and technical Press, 1970.

[59] U. Guide, "Maxwell 3D, version 9.0," *Ansoft Co,* 2002.